DEPARTAMENT DE FÍSICA APLICADA I
ELECTROMAGNETISME

ELECTRONIC STRUCTURE AND OPTICAL PROPERTIES OF III-N NANOWIRES.

ALEJANDRO MOLINA SÁNCHEZ

UNIVERSITAT DE VALÈNCIA
Servei de Publicacions
2011

Aquesta Tesi Doctoral va ser presentada a València el dia 18 de gener de 2011 davant un tribunal format per:

- Dr. Enrique Louis Cereceda
- Dr. Giancarlo Cicero
- Dr. Antonio Justino Ruas Madureira
- Dr. Andrés Ayuela Fernández
- Dra. Ana Cros Stötter

Va ser dirigida per:
Dr. Alberto García Cristóbal
Dr. Andrés Cantarero Sáez

Dipòsit legal: V-4121-2011
I.S.B.N.: 978-84-370-8072-7
Edita: Universitat de València
Servei de Publicacions
C/ Arts Gràfiques, 13 baix
46010 València
Spain
Telèfon:(0034)963864115

UNIVERSITAT DE VALÈNCIA
Departamento de Física Aplicada y Electromagnetismo

Electronic Structure and Optical Properties of III-N Nanowires

by

Alejandro Molina Sánchez

Supervised by
Alberto García Cristóbal
and
Andrés Cantarero Sáez

VALÈNCIA
December 2010

A Desirée y a mi familia por su apoyo, y a la memoria de mis abuelos

Agradecimientos

Quisiera en primer lugar agradecer a mis directores de tesis, Alberto García y Andrés Cantarero, por la confianza depositada en mí durante todos estos años. Sin su ayuda y dedicación no habría sido posible llegar hasta aquí. Han sido muchas las horas que hemos pasado juntos, y muchos los conocimientos que me han trasmitido. Agradezco enormemente que su puerta siempre estuviera abierta para contestar a cualquier duda que me viniera a la cabeza. Me considero muy afortunado por haber aprendido Ciencia con ellos. Espero aprovechar todo lo aprendido en el futuro. También quiero agradecer a los demás profesores del grupo de espectroscopia de sólidos, Ana Cros, Nuria Garro y Mauricio Morais, su ayuda y ánimo para la realización de este trabajo. A Nuria en especial le agradezco la ayuda en la redacción de este trabajo. También creo que a Mauricio este trabajo le ha costado más cápsulas de Nespresso de las deseadas.

De los demás compañeros del grupo de espectroscopia de sólidos, también guardo un grato recuerdo, Maribel, Jaime, Juan, Jorge, Michael, Rafa, Dora, Pascual, Jose, David, Oscar, Dora, Jose María y Antonio. Especial mención merece Maribel, que ha tenido que compartir despacho conmigo durante más tiempo del saludable, Jaime, colaborador directo en este trabajo, Juan, que me ayudó a aterrizar en Valencia. Cómo echaré de menos las cervecitas del oficinista compartidas durante todos estos años. También agradezco a Jose su ayuda desinteresada durante estos años, cualquiera que fuera el tipo de problema, ya fuera con Fortran, linux, y un largo etcétera. Quiero también agradecerle a Volker haberme presentado a quienes más tarde serían mis directores de tesis. Tampoco puedo olvidarme de los brasileños que le han dado alegría a este grupo durante sus estancias investigadoras, Luis Ogando, Justino Madureira, y más recientemente Everton Gadret. En especial quiero agradecerle a Justino sus oportunas sugerencias durante la redacción de este trabajo. También quiero mencionar a mis compañeros de despacho, Sandra, Raúl, Esteban, David, Henry, y Kamal por hacerme más agradable mi estancia aquí. Siempre me he sentido afortunado de compartir mi tiempo en Valencia con este grupo de compañeros, que se han portado conmigo como una

gran familia.

Ich möchte mich auch bei Dr. Gabriel Bester für seine Gastfreundschaft und seine stetige Unterstützung während meiner Zeitam Max-Planck-Institut in Stuttgart bedanken. Mit seinem Beitrag ist ein wichtiger Teil dieser Doktorarbeit entstanden. Ich bedanke mich auch bei den Mitarbeitern seiner Gruppe, Linas, Kit, Peng und Ranber, die mir eine angenehme Zeit in Deutschland ermöglichten.

Además, parte de este trabajo ha sido posible gracias la colaboración con los Drs. Alexander Terentjevs y Giancarlo Cicero. El tiempo en Torino me sirvió para descubrir una bella ciudad, disfrutar de la excelente cocina italiana, y aprender gran parte de lo que sé sobre los métodos *ab initio*, además de haber plasmado nuestro trabajo conjunto en una publicación. Tampoco puedo olvidar al grupo de la Dra. Angela Rizzi, en la Universidad de Göttingen, crecedores de las muestras de nanohilos de InN de las que tanto hemos hablado durante este tiempo, y que nos han dado tanto trabajo.

Por otro lado quiero agradecer a las diferentes entidades que me han dado el apoyo económico necesario para la realización de este trabajo. En primer lugar, a la Unión Europea, que a través de los proyectos SANDIE, ACDET-II y NANOLICHT, ha sufragado gran parte de esta tesis. También a la agencia alemana Deutscher Akademischer Austausch Dienst (DAAD), que financió mi estancia investigadora en Stuttgart. También me gustaría mencionar a las organizaciones que hacen posible el acceso libre a software de calidad. Esta tesis no habría podido ser escrita sin el desarrollo de las diferentes versiones de linux, pdflatex, gnuplot, xmgrace, LAPACK, ARPACK y un largo etcétera.

Por último tengo que agradecer a las personas que fuera del mundo académico, son partícipes de este proyecto, y que sin ellos, no hubiera sido posible llevarlo a cabo. A Desirée tengo que agradecerle de corazón su apoyo diario e infinita paciencia, que han hecho el camino hasta aquí mucho más llevadero. Tengo mucho que agradecer a mi madre, mi padre, y mi familia. Entre todas las cosas que les agradezco (que son bastantes), destaca su apoyo incondicional durante toda mi carrera académica.

List of publications

Parts of the work contained in this thesis have been reported in the following publications:

1. A. Molina-Sánchez, A. García-Cristóbal, A. Cantarero. *Tight-binding study of the optical properties of GaN/AlN polar and nonpolar quantum wells.* Microelectronics Journal, **40**, 418 (2009).

2. R. Mata, A. Cros, J. Budagosky, A. Molina-Sánchez, N. Garro, A. García-Cristóbal, J. Renard, S. Founta, B. Gayral, E. Bellet-Almaric, C. Bougerol, and B. Daudin. *Reversed polarized emission in highly strained a-plane GaN-AlN multiple quantum wells.* Phys. Rev. B, **82**, 125405 (2010).

3. J. Segura-Ruiz, A. Molina-Sánchez, N. Garro, A. García-Cristóbal, A. Cantarero, F. Iikawa, C. Denker, J. Malindretos, and A. Rizzi. *Inhomogeneous free-electron distribution in InN nanowires: Photoluminescence excitation experiments.* Phys. Rev. B, **82**, 125319 (2010).

4. A. Molina-Sánchez, A. García-Cristóbal, A. Cantarero, A. Terentjevs, and G. Cicero. *LDA+U and tight-binding electronic structure of InN nanowires.* Phys. Rev. B, **82**, 165324 (2010).

5. A. Molina-Sánchez, A. García-Cristóbal, and A. Cantarero. *Anisotropy in the optical response of GaN and AlN nanowires. In preparation.*

6. A. Molina-Sánchez, A. García-Cristóbal, A. Cantarero, and G. Bester. *Semi-empirical pseudopotential method in GaN nanowires: Method for the passivation of free-surfaces and electronic structure. In preparation.*

Parts of the work contained in this thesis have been presented in the following Workshops and Conferences:

1. *Tight-binding study of the optical properties of GaN/AlN polar and nonpolar quantum wells.* A. Molina-Sánchez, A. García-Cristóbal, and A. Cantarero. Workshop on Recent Advances of Low Dimensional Structures and Devices. 7-9 April 2008, Nottingham (UK).

2. *Self-consistent modeling of the electron accumulation in InN nanowires.* A. Molina-Sánchez, A. García-Cristóbal, and A. Cantarero. Advanced school on hybrid nanostructured materials for photovoltaic applications. 9-11 March 2009, Valencia (Spain).

3. *Study of the optical transitions in InN-based nanocolumns.* A. Molina-Sánchez and A. García-Cristóbal. Optics of Excitons in Confined Systems (OECS 11) 7-11 September 2009, Madrid (Spain).

4. *Reversed optical polarization in nonpolar GaN/AlN quantum wells: Role of strain and confinement* . R. Mata, A. Cros, N. Garro, J. A. Budagosky, A. Molina-Sánchez, A. García-Cristóbal, J. Renard, S. Founta, B. Gayral, E. Bellet-Amalric, B. Daudin. International Conference on Nitride Semiconductors (ICNS-8) 18-23 Octubre 2009, Jeju (South Korea).

5. *Self-consistent modeling of electron surface accumulation in InN nanocolumns and photoluminescence excitation experiments.* A. Molina-Sánchez, J. Segura-Ruiz, N. Garro, A. García-Cristóbal, and A. Cantarero. VI Meeting of the Solid State Physics Group of the Royal Spanish Physics Society. 3-5 February 2010, Zaragoza (Spain).

6. *Optical properties of InN and InGaN nanowires.* J. Segura-Ruiz, A. Molina-Sánchez, N. Garro, A. García-Cristóbal, and A. Cantarero. Electronic, transport, and optical properties of low-dimensional systems (WS10-ETOLDs). 31 May-2 June 2010, Valencia (Spain).

7. *Atomistic modeling of InN nanowires.* A. Molina-Sánchez, A. García-Cristóbal, A. Cantarero, A. Terentjevs, and G. Cicero. Empirical Methods in Semiconductor Nano-Structures: Design and Modeling. 23-25 June 2010, Manchester (UK).

Contents

Preface

The term III-N nanowire (NW) will refer throughout this work to the free-standing nanowires made of group-III-nitrides semiconductors, namely InN, GaN and AlN [1]. These nanostructures have a large length/diameter ratio, of the order of 100 (several micrometers versus tenths of nanometers). The term free-standing highlights the fact that the NWs are not embedded in another material. The improvement of the epitaxial techniques [2], and in particular, those based on III-N semiconductors [3], has lead an important part of the Solid State Physics community to concentrate the attention in the last years towards a better understanding of the physical properties of those NWs, and their application in the development of novel devices [4, 5].

Nanowires present several differences with respect to the still widely investigated two-dimensional layers and the zero-dimensional nanostructures (quantum dots). We would like to highlight the following: (i) Nanowires grow strain-free (except maybe at their base), and thus with a minimal presence of dislocations or defects along the main structure. This fact opens the possibility of growing high-quality materials with an important lattice mismatch with the substrate, contrary to the situation found in quantum dots or superlattices. (ii) Depending on the NW lateral dimensions, two types of NWs can be distinguished. When the diameter is larger than $\sim$ 20 nm, the electronic properties of the NWs can be considered as that of a bulk material, thus making them a suitable platform to study the bulk optical and transport properties, which can be hardly investigated in bulk samples (thin films), that grow with a high density of defects, when there is a high lattice mismatch with the substrate [6]. (iii) For NWs of smaller diameters ($\lesssim$ 20 nm), on the other hand, the effects of quantum confinement can lead to important changes in the optical and transport properties, which can open the possibility of tuning the NW properties by controlling their size [7]. (iv) Moreover, contrary to quantum dots, that are usually immersed in a matrix of another material, the free-standing NWs have the advantage that they can be easily separated from the substrate and dispersed on a surface. Thus, transport measurements in single NWs

can be performed [8].

One can roughly classify the investigations on nanowires into three main research lines. The first one concerns the fabrication, being the molecular beam epitaxy or/and the metal organic chemical vapor deposition (MOCVD) the two techniques that allow the growth of higher quality NWs. This research area is in constant development, and is not limited only to the growth of pure compound NWs, but also alloy-based NWs, which extend the possibilities of allowing beyond those possible in standard bulk growth, or axially and radially structured NWs [9]. New physical phenomena arise which must be tacked by the physical community, in particular the effect of the surface in the optical and transport properties of the NWs. Another focus of research is based on applications to optoelectronics devices and photovoltaic cells. In particular, III-N NWs, as InN, GaN and AlN, have attracted a special interest of the scientific community, due to the band gap engineering. InN has a band gap of 0.67 eV (1852 nm), in the infrared, whereas GaN and AlN have a band gap of 3.5 eV (355 nm) and 6.2 eV (200 nm), respectively, in the ultraviolet. This opens the possibility of covering the whole solar spectrum by an appropriate alloying [10]. Also, each material shows a different degree of anisotropy in the optical response due to its specific band structure, being useful for polarization-sensitive devices [11].

In this context, the theory and numerical simulations play a crucial role in the explanation of NWs properties and a better understanding of the observed phenomena. The predictions offered by the theory can also drive the fabrication of new heterostructures and the design of devices. In this work, we have studied theoretically by using several models, the fundamental aspects of the electronic structure and optical properties of the III-N bulk semiconductors in the first place, and have applied afterwards such models to the investigation of the III-N nanowires physical properties.

The thesis has been structured as follows:

- In Chapter 1 we have included a brief summary of the properties of the group III nitride bulk semiconductors and nanowires. We have focused on the structural and optical properties of free-standing NWs, giving a brief account of the state-of-the-art of the field concerning the main achievements of the growth techniques, together with spectroscopic results and potential applications. The Chapter is ended with the presentation of the different theoretical methods used in this work to calculate the electronic and optical properties of the NWs. We have also discussed the state-of-the-art of the main techniques used to study NW system as well.

- In Chapter 2 we describe the theoretical models employed in this thesis for the study of the bulk electronic structure. We have complemented the discussion with our own calculations of the band structure of III-N bulk semiconductors, with the aim of highlighting the differences between the electronic structures of InN, GaN and AlN. We devote also this Chapter to introduce several concepts necessary to understand the results related to III-N nanowires, to be presented later. The methods have been ordered hierarchically, the *ab initio* formulation, being presented first, followed by the formulation of the semi-empirical methods, based on the pseudopotential and tight-binding approaches.

- In Chapter 3 we have calculated the electronic structure and the optical properties of the III-N free-standing nanowires from an atomistic point of view. Due to the limitation of the *ab initio* methods to system with few atoms, *i. e.*, long computational time, the semi-empirical pseudopotential and the tight-binding methods have been used. Moreover, the model used for the lateral free surfaces of nanowires has been discussed.

- Finally, Chapter 4 is devoted to the study of the inhomogeneous distribution of electrons in large InN nanowires, which has been studied within the framework of the effective mass approximation, by means of a self-consistent procedure designed to find simultaneously the electrostatic potential and the charge density. We study the optical absorption and its different dependencies. We show also the excellent agreement of our numerical results with the experiments, which has been performed with high quality sample.

Chapter 1

Introduction

In this Chapter we will present an overview of the main physical properties of the nanowires based on group III nitrides (InN, GaN and AlN). We start in Section 1.1 with a summary of the bulk crystalline structure and electronic structure. In Section 1.2 we give a brief overview of the growth techniques and analyze some experiments on the optical properties of III-N NWs. Finally, in Section 1.3 we present the theoretical models used in this thesis for the calculations of the electronic structure and the optical properties of III-N NWs.

1.1 Bulk III-N semiconductors

1.1.1 Crystal structure

Under the denomination on group III nitride (or more briefly, III-N) semiconductors, we refer the binary compounds InN, GaN and AlN [1], where the nitrogen atom plays the role of anion, and the group III element is the cation. III-N semiconductors crystallize, under ambient pressure and room temperature conditions, in the thermodynamically stable wurtzite structure. In this structure, each atom of one type is tetrahedrally bonded to four atoms of the other type [12]. III-N semiconductors can be grown also in the meta-stable zinc-blende structure, by taking advantage of epitaxial growth on cubic substrates such as GaAs [13] or 3C-SiC [14]. Under certain growth conditions, both crystal structures can coexist, as observed recently in GaN [15] and InP nanowires [16]. In a reciprocal trend, in the last years, it has emerged an increasing interest in synthesizing other zincblende semiconductors, such as GaAs and InAs, in the wurzite phase [17].

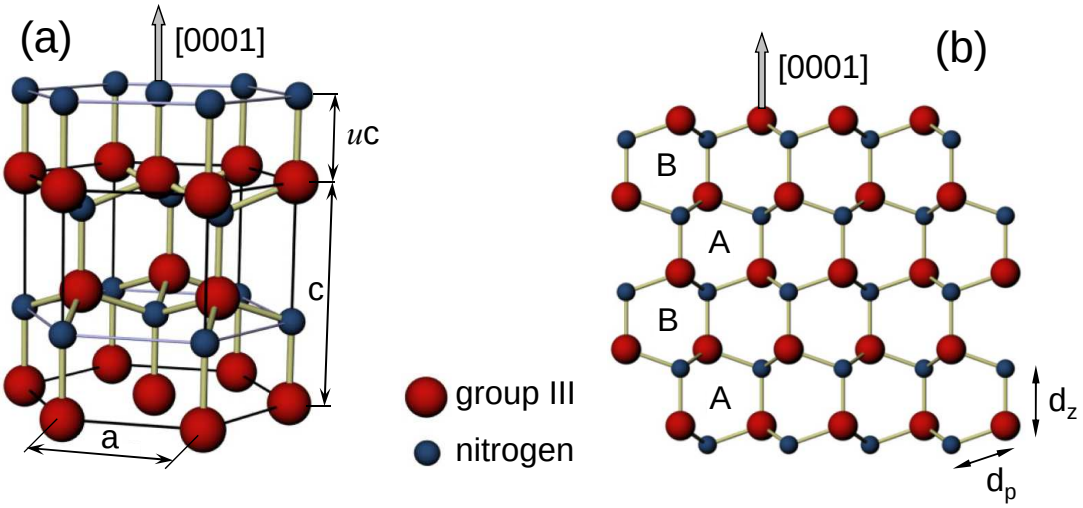

Figure 1.1: (a) Representation of the wurtzite unit cell of parameters a and c of a III-N compound. (b) Stacking sequence of wurtzite.

The space group of the wurtzite crystal structure is denoted by $P6_3mc$ in the Hermann-Mauguin notation and C_{6v}^4 in the Schönflies notation. The point group symmetry is $6mm$ in the Hermann-Mauguin notation and C_{6v} in the Schönflies notation [18]. The wurtzite structure consists of two hexagonal sublattices of parameters a and c, displaced relative to each other a distance uc along the [0001] direction (c-axis) (u is called the internal parameter), as shown in Fig. 1.1(a). The resultant atom arrangement is such that each atom of one sublattice is tetrahedrally bound to the atoms of the other sublattice, giving a stacking sequence ABAB... along c-axis, as depicted in Fig. 1.1(b). The distances between one atom and its nearest neighbors are specified in terms of a, c and u,

$$d_z = uc, \qquad d_p = \sqrt{\frac{a^2}{3} + \left(\frac{1}{2} - u\right)^2 c^2}, \tag{1.1}$$

where d_z is the bond distance along the c-axis, and d_p the bond distance between an atom and its nearest neighbors in the basal plane. In the ideal wurtzite structure, the lattice parameters c, a and the internal parameter u follow the relation $c/a = \sqrt{8/3} \simeq 1.633$, $u = 3/8 = 0.375$, and $d_z = d_\perp = 3c/8$. However, in most of the III-N semiconductors, there is a distortion of the tetrahedral bond being $d_z \neq d_\perp$, which leads to deviations in the lattice parameter relations from the ideal one. In Table 1.1 we show the experimental lattice parameters of III-N semiconductors, where the deviation from the ideal wurtzite structure can be noticed. This leads to important effects in the electronic structure of wurtzite III-N semiconductors

	a (Å)	c (Å)	u	c/a
InN	3.538	5.703	0.377	1.612
GaN	3.189	5.185	0.375	1.626
AlN	3.112	4.982	0.382	1.601

Table 1.1: Lattice parameters of III-N wurtzite semiconductors as reported in Refs. [19] and [20].

as compared to their zinc-blende counterparts, which will be described later.

The choice of the primitive vectors of the Bravais hexagonal lattice, that we have adopted in this work is:

$$\begin{aligned} \boldsymbol{a}_1 &= \left(\frac{a}{2}, \frac{\sqrt{3}a}{2}, 0\right), \\ \boldsymbol{a}_2 &= \left(-\frac{a}{2}, \frac{\sqrt{3}a}{2}, 0\right), \\ \boldsymbol{a}_3 &= (0, 0, c), \end{aligned} \tag{1.2}$$

with the vector components referred to a rectangular reference system. The vector $\boldsymbol{a}_3$ is orthogonal to both vectors $\boldsymbol{a}_1$ and $\boldsymbol{a}_2$, which form a 60° angle. The lengths are $|\boldsymbol{a}_1| = |\boldsymbol{a}_2| = a \neq c = |\boldsymbol{a}_3|$. Any unit cell of the lattice is specified by a lattice vector as:

$$\boldsymbol{R}_n = n_1\boldsymbol{a}_1 + n_2\boldsymbol{a}_2 + n_3\boldsymbol{a}_3, \tag{1.3}$$

with n_1, n_2 and n_3 integers. The position vectors of the four atoms, $\boldsymbol{\tau}_i$ ($i = 1, \ldots, 4$), inside the unit cell, are given by

$$\begin{aligned} \boldsymbol{\tau}_1 &= (0, 0, 0), \\ \boldsymbol{\tau}_2 &= (0, 0, uc), \\ \boldsymbol{\tau}_3 &= \left(0, \frac{a}{\sqrt{3}}, \frac{c}{2}\right), \\ \boldsymbol{\tau}_4 &= \left(0, \frac{a}{\sqrt{3}}, (1-u)c\right), \end{aligned} \tag{1.4}$$

where $\boldsymbol{\tau}_1$ and $\boldsymbol{\tau}_3$ denote the vector position of the group III atoms (In, Ga or Al), while $\boldsymbol{\tau}_2$ and $\boldsymbol{\tau}_4$ the nitrogen atoms. Due to the hexagonal arrangement of the atoms, the directions and crystallographic planes of the wurtzite structure

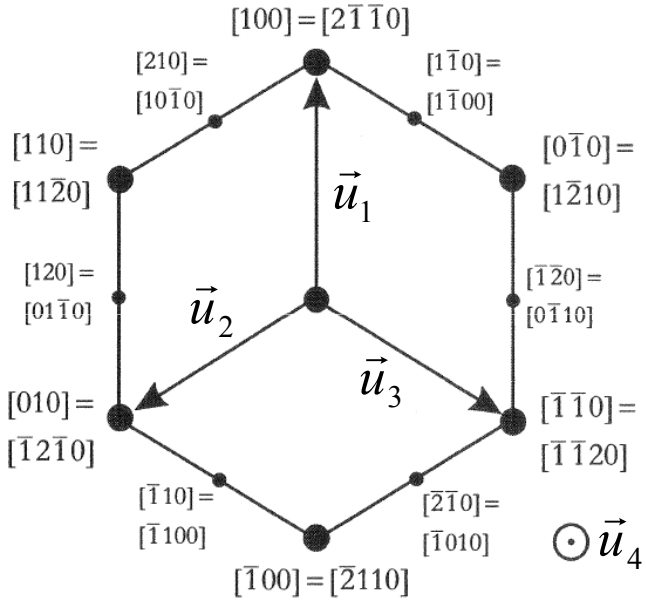

Figure 1.2: Crystallographic orientations in the hexagonal system, indicated by the Miller $[hkl]$ and the Miller-Bravais $[hkjl]$ index. Note that in the latter $j = -(h + k)$. The Miller-Bravais indexing system uses three coplanar vectors $\boldsymbol{u}_1, \boldsymbol{u}_2, \boldsymbol{u}_3$, besides $\boldsymbol{u}_4$, which coincides with the vector $\boldsymbol{a}_3$.

are commonly written in terms of the Miller-Bravais indices in the specialized literature, instead of the usual Miller indices. In Fig. 1.2 we have represented the correspondence between both indexing nomenclature. The orientation [0001] is generally referred as polar direction and the perpendicular plane, (0001), as polar surface, due to the spontaneous polarization developed by the wurtzite crystals along the c-axis [21]. The planes perpendicular to (0001), are consequently called nonpolar surfaces. The nonpolar planes are denominated M-plane for $(1\bar{1}00)$ and A-plane for $(11\bar{2}0)$. The associated nonpolar directions are denoted by a small letter, *i. e.*, the m-direction or a-direction. This terminology will be kept through out this thesis.

Besides the direct lattice, defined by the primitive translations of Eq. (1.2), it is also important to introduce the reciprocal lattice, generated by three primitive translation vectors $\boldsymbol{b}_1$, $\boldsymbol{b}_2$ and $\boldsymbol{b}_3$ in the reciprocal space, satisfying the relation

$$\boldsymbol{a}_i \cdot \boldsymbol{b}_j = 2\pi\delta_{ij}. \tag{1.5}$$

In the case of the hexagonal Bravais lattice, the reciprocal lattice primitive translations are:

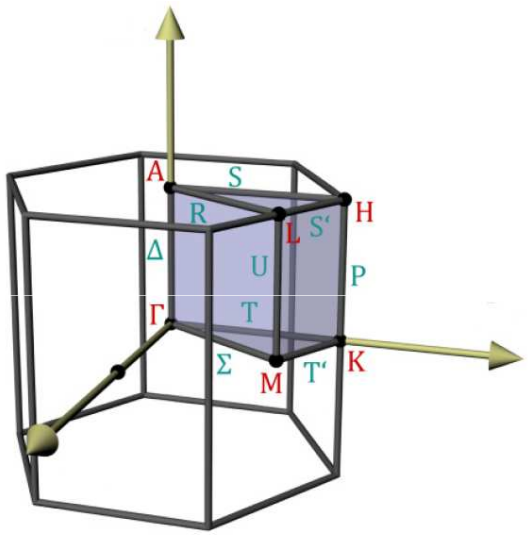

Figure 1.3: First Brillouin zone of the wurtzite structure showing some of the high-symmetry points and directions according to the Koster notation [22].

$$\begin{aligned} \boldsymbol{b}_1 &= \frac{2\pi}{a}(1, \frac{1}{\sqrt{3}}, 0), \\ \boldsymbol{b}_2 &= \frac{2\pi}{a}(-1, \frac{1}{\sqrt{3}}, 0), \\ \boldsymbol{b}_3 &= \frac{2\pi}{c}(0, 0, 1). \end{aligned} \tag{1.6}$$

All the sites of the reciprocal lattice are obtained by:

$$\boldsymbol{K}_m = m_1\boldsymbol{b}_1 + m_2\boldsymbol{b}_2 + m_3\boldsymbol{b}_3, \tag{1.7}$$

with m_1, m_2 and m_3 integers.

One convenient choice of primitive unit cell of the reciprocal lattice is the so-called first Brillouin zone [23]. In Fig. 1.3 we show the first Brillouin zone (primitive unit cell) of the reciprocal lattice of the hexagonal Bravais lattice, labeling the high symmetry points (Γ, A, M, K, L, M) and directions (Σ, Δ, T,...) according to the Koster notation [22].

1.1.2 Electronic structure of III-N semiconductors

The band structure of a semiconductor is of pivotal importance in the understanding the properties of the material in response to applied fields and to determine its potential applications. In this Subsection, we summarize the main features of the band structure of the III-N semiconductors. Figure 1.4 shows the band structure of GaN, as calculated within the density functional theory. Since all the group III nitrides are direct band gap semiconductors, the most important region of the band structure is in the vicinity of the Γ point ($\boldsymbol{k} = 0$), that has been marked with a red rectangle in Fig. 1.4. Most of the fundamental optical properties, such as the optical absorption or the photoluminescence, are basically determined by the features of the bands adjacent to the band gap, near the Γ point. The proper description of this region is therefore of crucial importance for realistic predictions about the optical properties of the wurtzites semiconductors. The bands far from the center of the Brillouin zone can be accessible by, for instance, angle-resolved photoemission spectroscopy [24], but their influence in the optical properties of the III-N nanowires studied in this work is marginal. Thus, although the theoretical methods used in this thesis are able to calculate accurately the bands in the whole Brillouin zone, our calculations below will be in general biased towards an accurate detailed description of this part of the band structure.

On the other hand, the electron wave functions can be classified (in the so-called representations) according to their transformation under symmetry operations of the crystal point group (C_{6v}^4 in wurtzite crystals). In addition, optical selection rules can be deduced from the wave functions symmetry. The group theory is the mathematical tool that deals with this issue and we will complete our discussion of the electronic structure with some notions of group theory [25]. Table 1.2 presents the character of the group C_{6v}^4 (without spin), $\Gamma_1, \ldots \Gamma_6$, and for the double group (relevant when the spin-orbit interaction is considered), that introduces the representations Γ_7, Γ_8, and Γ_9. The basis functions for each representation are also given. The states belonging to the Γ_1 representation are either spherically symmetric or axially symmetric around the $\hat{z}$-axis (c-axis), *i. e.*, they have the same symmetry as the atomic orbitals s and p_z. On the contrary, the states labeled as Γ_5, are symmetric with respect to rotations around the $\hat{x}$- and $\hat{y}$-axis, as the orbital p_x and p_y are. The other representations can be also related to other orbitals or combination of them, $d_{x^2-y^2}$, d_{yz}, $f_{x^3-3xy^2}$, etc.

Due to the electronic configuration of group III and nitrogen atoms, with s and p valence electron symmetry, the electron wave functions are essentially dominated by those orbitals. In the case of atoms of larger atomic number, Ga ($Z = 13$)

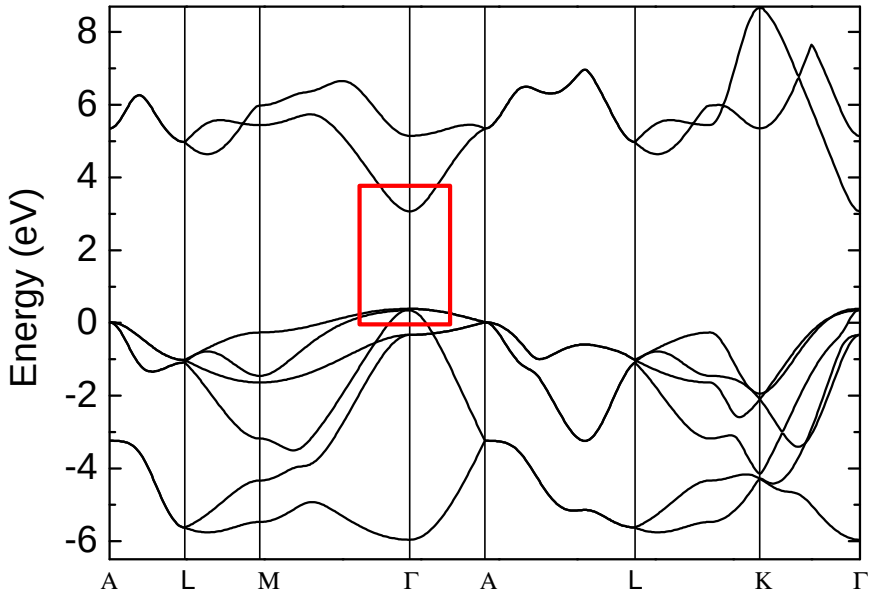

Figure 1.4: Band structure of GaN calculated within the density functional theory in the local density approximation (see Chapter 2 for details of the calculation). The zero of energy is placed arbitrarily at the valence band maximum. The important portion of the band structure, near the fundamental energy gap is framed with a red rectangle.

and In ($Z = 49$), the d orbitals can also play an important role for an accurate description of the electronic structure, as discussed later. The wave functions of the lowest conduction band in the vicinity of the Γ point are mostly formed by a combination of atomic-like s orbitals and a spin function, belonging to the Γ_7 representation of the double group [26]. This band can be considered to be essentially 2-fold degenerate (the Dresselhaus effect can be neglected [27]), and can be well approximated by a parabolic dispersion with an anisotropic effective mass. This parabolic picture of the conduction band works well for GaN and AlN, where the wide band gap prevents a sizeable coupling with the valence bands. By the same token, in the case of InN, the narrow band gap leads a strong coupling between conduction band and valence band manifold, resulting in a considerable deviation from the parabolic approximation of the conduction band [28]. The topmost valence band states are mostly a combination of orbitals of p symmetry (p_x, p_y, and p_z-like) orbitals with spin functions (spinors). These valence bands cannot be simply represented by parabolic dispersion curves as they exhibit a complicated dependence with $\boldsymbol{k}$, as we will shown in detail.

While the conduction band near the Γ point is similar to that of zinc-blende semiconductors, the valence bands are the hallmark of wurtzite semiconductors. Figure 1.5 shows: (a) a schematic representation of the splitting of the valence

C_{6v}	E	C_2	$2C_3$	$2C_6$	$3\sigma_v$	$3\sigma_d$	Basis
Γ_1	1	1	1	1	1	1	$s, z, 3z^2 - r^2$
Γ_2	1	1	1	1	-1	-1	R_z
Γ_3	1	-1	1	-1	-1	1	$x^3 - 3xy^2$
Γ_4	1	-1	1	-1	1	-1	$y^3 - 3yz^2$
Γ_5	2	-2	-1	1	0	0	$(R_x, R_y), (x, y), (zx, yz)$
Γ_6	2	2	-1	-1	0	0	$(x^2 - y^2, yz)$

	E	$\bar{E}$	$C_2, \bar{C}_2$	$2C_3$	$2\bar{C}_3$	$2C_6$	$2\bar{C}_6$	$3\sigma_v, 3\bar{\sigma}_v$	$3\sigma_d, 3\bar{\sigma}_d$
Γ_7	2	-2	0	1	-1	$\sqrt{3}$	$-\sqrt{3}$	0	0
Γ_8	2	-2	0	1	-1	$-\sqrt{3}$	$\sqrt{3}$	0	0
Γ_9	2	-2	0	-2	2	0	0	0	0

Table 1.2: Character table for the wurtzite single group C_{6v}^4 at the BZ center (Γ point). The representations are labeled as Γ_1,...,Γ_6. The double group results due to the introduction of the spin-orbit interaction, with representations Γ_7, Γ_8 and Γ_9. Adapted from Ref. [29].

bands at the Γ point, and (b), the band dispersion as calculated with the tight-binding method for InN, taking into account the crystal-field (Δ_{cf}) and the spin-orbit (Δ_{so}) interactions (see more details in Chapter 2). The crystal-field splitting is a direct consequence of the anisotropy of wurtzite crystals and is one of their most relevant characteristic. The spin-orbit interaction is a relativistic effect caused by the coupling of the spin with the angular momentum, being more important in heavier atoms. In our case, more important in InN than in GaN and AlN. An explanation of the wurtzite valence band structure can be constructed by considering the effect caused by the crystal-field interaction in a virtual cubic crystal, where the six valence bands are degenerate (in absence of spin-orbit interaction), as shown in the left side of Fig. 1.5(a). The crystal-field interaction breaks this degeneracy (as well as changes the space group), and now the states belong either to the representation Γ_5 (4-fold degenerate and with the same symmetry as $p_x - p_y$ orbitals), or to the representation Γ_1 (2-fold degenerate and with the same symmetry as p_z orbitals). If one now switches on the spin-orbit interaction, the states are further mixed to form three doublets, Γ_9, $\Gamma_{7,+}$ and $\Gamma_{7,-}$, now labeled according to the irreducible representation of the double space group. Considering both effects the valence band wave functions in the Γ point are two-fold degenerate and belong to the representations Γ_9 and Γ_7 [26]. A more detailed explanation in terms of group theory can be found in Ref. [30]. The 2-fold degeneracy is lifted for directions perpendicular to the c-axis due to the spin-orbit interaction (see Fig. 1.5). This is known as Dresselhaus effect [27].

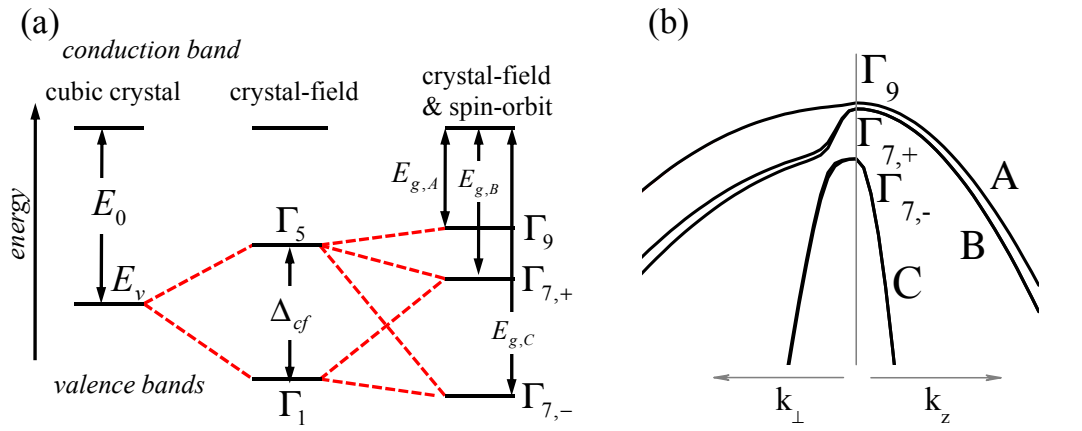

Figure 1.5: (a) Splitting of the Γ-point valence band states, for wurtzite III-N semiconductors, interpreted as a result of the influence of the crystal-field and the spin-orbit coupling (after Ref. [31]). (b) Schematic representation of the top of the InN valence band in the vicinity of the Γ point (calculated with the tight-binding model, see Chapter 2).

An analytical expression of their energies as a function of Δ_{cf} and Δ_{so} can be obtained by the $\boldsymbol{k}\cdot\boldsymbol{p}$ method [32], written as follows:[1]

$$\begin{aligned} E_{\Gamma_9} &= E_v + \Delta_{cf} + \frac{1}{3}\Delta_{so}, \\ E_{\Gamma_{7,+}} &= E_v + \frac{1}{2}\left\{\Delta_{cf} - \frac{1}{3}\Delta_{so} + \sqrt{\left(\Delta_{cf}+\Delta_{so}\right)^2 - \frac{8}{3}\Delta_{cf}\Delta_{so}}\right\}, \\ E_{\Gamma_{7,-}} &= E_v + \frac{1}{2}\left\{\Delta_{cf} - \frac{1}{3}\Delta_{so} - \sqrt{\left(\Delta_{cf}+\Delta_{so}\right)^2 - \frac{8}{3}\Delta_{cf}\Delta_{so}}\right\}, \end{aligned} \tag{1.8}$$

where E_v is the valence band edge (in the absence of Δ_{cf} and Δ_{so}). In the case of $\Delta_{so} = 0$, we get $E_{\Gamma_9} = E_{\Gamma_{7,+}} \equiv E_{\Gamma_5}$, and $E_{\Gamma_{7,-}} \equiv E_{\Gamma_1}$ (see Fig. 1.5). The magnitude and sign of the parameters Δ_{cf} and Δ_{so} determine the ordering of the Γ point valence band states, as well as the off-Γ band anticrossings. In Table 1.3 we show the band gaps, Δ_{cf} and Δ_{so} of the III-N semiconductors. Hence, for InN and GaN, the Δ_{cf} and Δ_{so} splittings are both positive and smaller than 40 meV. On the opposite, in the case of AlN, Δ_{so} is negligible and Δ_{cf} has a large negative value (hundreds of meV), which is responsible for the different photoluminescence

[1] Another notation for the valence bands can be found in the literature, labeling the bands as *A*, *B* and *C*, starting from the valence band edge [33]. Those labels do not give any information about the symmetry of the states and can lead to a misunderstanding when dealing with different material symmetries. In this thesis, we will use both notations in our discussion of the electronic structure of III-N semiconductors, but always with a precise specification of the symmetry of each state.

	E_g(eV)	Δ_{cf} (meV)	Δ_{so} (meV)
InN	0.67	20-80	8-25
GaN	3.5	9-50	8-20
AlN	6.2	$-$(104-300)	5-20

Table 1.3: Band gap E_g, and parameters Δ_{cf} and Δ_{so} of III-N semiconductors, summarized from Refs. [19, 35–39].

features of AlN crystals as compared with the other III-N semiconductors [34]. Measuring accurately the valence band splittings (Δ_{cf} and Δ_{so}) is rather difficult and therefore these values are constantly revised.

One very interesting characteristic of III-N semiconductors is the wide range spanned by their band gap value. In Fig. 1.6 we show the band gap energy of the III-N semiconductors versus the lattice constant a. The band gaps of AlN and GaN are in the ultraviolet part of the spectrum, whereas that of InN lies in the infrared spectrum [40]. As we see, GaN and InN reside in the opposite sides of the electromagnetic visible spectrum, and the ternary $Ga_xIn_{1-x}N$ compound could in principle cover completely it by changing the alloy composition x. This property converts $Ga_xIn_{1-x}N$ in one of the most appealing one in the field of photovoltaic technology [10, 41]. The AlN and GaN semiconductors are commonly termed as wide band gap (or wide-gap) semiconductors. Probably one of the most recognized applications of GaN is the blue laser diode [31]. Other relevant applications are as active material of field-effect transistor or single electron transistors [42]. The AlGaN alloys are widely used, for instance, as ultraviolet detectors [43].

In the case of InN, the exact value of its band gap has been the object of a notorious controversy. Nowadays, it seems to be solved with the current accepted value of 0.67 ± 0.05 eV [1]. However, in the earliest 80's, due to the poor quality of the InN layers available (usually grown by the sputtering technique), the assigned value of the band gap was around 1.9 eV [44]. The ultimate reason of this overestimation was the high density of impurities, leads to a very hight occupancy of the conduction band by free electrons. The resulting degenerate semiconductor sample, exhibited a sizeable Burstein shift that manifested in the absorption spectra, as an apparent higher value of the band gap. The improvement of the growth procedures, and notably the molecular beam epitaxy technique, has allowed to obtain better samples, with a much smaller impurity concentration, and finally has lead to the update of the band gap value to the current value of 0.67 eV, reported almost simultaneously by the authors of Refs. [45] and [46]. This update places

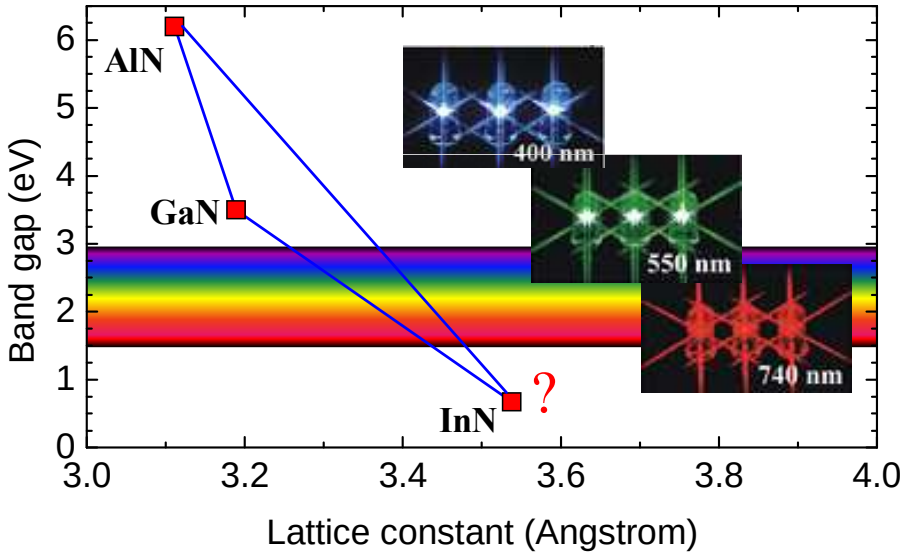

Figure 1.6: Representation of the band gap of AlN, GaN and InN versus the a lattice constant. The question symbol asks if the controversy around the InN band gap (extracted from Ref. [47]).

the InN band gap in the infrared spectrum, and has situated the material at the top of the list of the most investigated materials for the optoelectronic and solar energy applications, as we have commented before.

Despite of the improvements in the growth techniques, indium nitride still exhibit a propensity to the n-doping. Moreover, their surface states are mainly donor-type [48], giving rise to an electron accumulation layer at the surfaces, associated with a transfer of electrons from the surface states to the bulk. It is still under debate the character, intrinsic or not, of the electron accumulation in InN surfaces. While there is a general agreement on the existence of an accumulation layer on polar surfaces, the situation at nonpolar surfaces, such as the $(11\bar{2}0)$-plane layers, is still controverted. In this sense, optical studies have shown that this accumulation layer can depend on the growth conditions [49]. The study of nonpolar surfaces is difficult because of the high density of defects and the metalic indium coverage exhibited by the state-of-the-art samples. A recent study suggest that the origin of the accumulation layer in nonpolar surfaces is related to the adsorption of oxygen at InN surface [50]. However, the high density of basal-plane stacking faults of the studied samples prevents a definitive conclusion. As we explain in Subsection 1.2, the studies performed on InN nanowires seem to be more conclusive due to the absence of defects and strain in such structures.

From a theoretical point of view, the computation effort has been mostly di-

rected to the elucidation of the band structure from *first principles*. It is well known that the indium d orbitals cannot be disregarded and that *ab initio* calculations based on the local density approximations (LDA) give an incorrect estimation of the p-d orbital coupling. This results in a zero or even negative band gap. The refinement of the local density approximation by including the Hubbard model [51], or calculations beyond density functional theory (DFT), such as the GW approximation [39, 52], have shown themselves to be able to solve, at least partially, the InN band gap problem. Concerning the indium nitride surface properties, the calculations of Van de Walle's group have concluded a tendency of the polar surfaces to develop an accumulation layer, but suggest the absence of such accumulation layer in $(11\bar{2}0)$ and $(1\bar{1}00)$ surfaces under certain conditions [53].

1.2 Properties of III-N semiconductor nanowires

Nanowires (NWs) are characterized by a much larger longitudinal length (range 1-10 μm) than the cross-section dimension (range 10-70 nm). When the nanowire cross-section reaches such dimensions that the effects of the quantum confinement on the electron states are appreciable, they can legitimately called as quantum wires. In addition, the longitudinal direction of the NW can be used to direct the conduction of the electrons, phonons, and photons. Thus, many physical properties of semiconductors have stronger dependence on the geometry when grown as a nanowire than as a bulk [54]. Contrary to the early realization of the quantum wire concept, which were based on the formation of elongated structures, lying on the substrate and covered with another semiconductor [55], the nanowires under study here adopt a columnar shape, which are also called nanocolumns in the literature [56].

Among the variety of growth techniques to fabricate group III nitride NWs, the molecular beam epitaxy (MBE) is one of the most successful tools to obtain NWs with high crystalline quality. It is also noteworthy the crystalline quality achieved by another technique such as metal organic chemical vapor deposition (MOCVD) [3, 57]. This methods typically use a catalyst that defines the position and diameter of NWs and enhances the NW growth locally. Unfortunately, the catalyst can also be a source of contamination of the sample. In the following we describe succinctly the growth of NWs by MBE.

Molecular beam epitaxy is a growth technique based in a controlled slow deposition of a thin crystalline layer on a monocrystalline substrate, in such a way that the crystal structure of the new layer replicates that of the substrate. To achieve

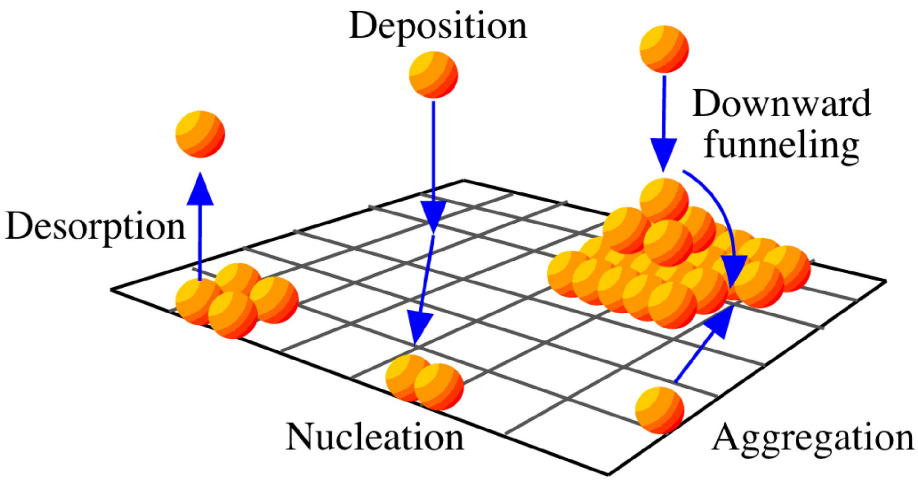

Figure 1.7: Illustration of the elemental processes taking place on growing surface during MBE.

the crystalline deposition, molecules or atoms of the constituent species are evaporated from elemental beam sources (effusion cells), depositing on the surface. Once on the surface, the atoms move by diffusion until they reach a thermodynamically favorable location to bond to the substrate. The main possible processes involved in the MBE are shown in Fig. 1.7 and explained as follows:

- Deposition: The atoms arrive to the surface but they are not attached yet and are free to move.
- Desorption: Adatoms of sufficient kinetic energy do not aggregate and leave the substrate surface.
- Diffusion: The adatoms move on the surface to reach a energetically favorable location.
- Nucleation: The adatoms are attached to the substrate or to the grown layer.

Because the atoms require time to diffuse across the surface, the quality of the film will improve with slower growth rate. Typically growth rates of about one monolayer per second provide sufficient high quality layers. The dynamics of the growth processes is controlled mainly by the substrate temperature and the flux of beam source. The chemical elements are commonly provided by effusion cell sources (typically knowing Knudsen cells), that contain the elemental form of the constituents in very high purity. The cells are heated in a controlled manner to encourage evaporation, in the required amounts or fluxes. The material flux

is measured by means of the beam equivalent pressure (BEP) of the atomic or molecular beams, and it is used to quantify flux ratios and growth rates.

Some relevant advantages of MBE are:

- The high vacuum atmosphere allows a minimization of the appearance of non-intentional impurities, and perform an accurate doping process.
- The samples can be analyzed *in-situ* by reflection high energy electron diffraction (RHEED). In this technique a beam of electrons of energy 5-40 keV is focused into the substrate. They are reflected from the surface at a very small angle (less than 3°) and directed onto a recording screen. These electrons interact with only the top few atomic layers and thus provide valuable information about the surface. The obtained diffraction pattern can be used to establish the surface geometry and morphology.

Some disadvantages of MBE can be mentioned:

- Epitaxial growth techniques require a high crystalline quality substrate having a small lattice mismatch compared to the material to be grown. This is not always possible and a buffer layer must be grown to avoid a high density of defects.
- In order to avoid the contamination of the growing material, each MBE system must in principle be dedicated to fabricate only one class of materials: arsenides, nitrides, etc.
- The slow growth velocities and long growth times imply that this technique is not appropriate to grow bulk materials. Typical thicknesses obtained by this technique are around the micrometer.

After this brief introduction to the MBE technique, we turn to study the actual growth procedure that generates the NWs. The procedure starts with deposition of atoms forming a two-dimensional layer. This so-called wetting layer epitaxial layer presents a lattice mismatch with the substrate. Therefore, the associated strain energy increases with the thickness of the wetting layer and can be elastically relieved by the formation of islands with dimensions of nanometers (Stranski-Krastanov mode) [59]. This method has revealed itself as a very efficient way to obtain semiconductor quantum dots, free of defects. However, this process is essentially spontaneous, and it remains difficult to control the size and shape of

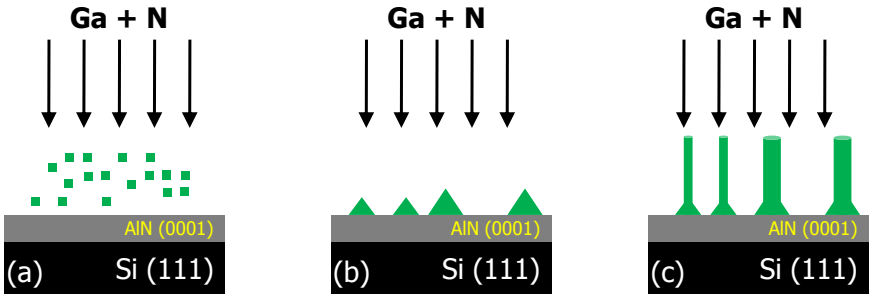

Figure 1.8: Steps of the nanowire growth process described in Ref. [58]. (a) Diffusion of gallium and nitrogen atoms over the AlN-(0001) surface. (b) Formation of islands of GaN. (c) Growth of the nanowires.

the dots, and their separation. The reader can find more details about the growth of self-organized quantum dots, and their main electronic and optical properties [60, 61].

We focus from now on the growth process of GaN NWs. In Fig. 1.8 we have represented a scheme of the NW formation, as described in Ref. [58]. The first step is to diffuse the gallium and nitrogen atoms on an partially relaxed AlN thin layer on Si (001), for a fixed temperature of the substrate (step (a) in Fig. 1.8), following the deposition of gallium and nitrogen atoms. The formation of nanometer-sized GaN islands takes places (step (b) in Fig. 1.8). These islands are preferential sites for further GaN growth due to strain minimization, and act as a collector of material, becoming the seeds of the NW growth. In this step, it is also observed the generation of a low density of columnar structures together with a high density of GaN islands. Keeping the effusion of atoms from the Knudsen cells, one observes that most of the NWs grow directly on top of the three-dimension islands (step (c) in Fig. 1.8). These NWs grow without dislocations or staking faults, being essentialy strain-free structures. The morphology, density, and size of the NW can be controlled to some extent by the ratio of gallium and nitrogen atoms, denoted as III/V ratio, and substrate temperature. It is well established that the grow of III-N NWs takes place under nitrogen-rich conditions [62], depending the temperature on the material.[2] It is important to notice the absence of catalyst elements in this growth mode, and therefore, the absence of unintentional contamination.

Concerning the morphology of the NWs, it is important to mention that in many of the existing samples, the NWs present a hexagonal cross-section, faceted at $(10\bar{1}0)$ planes. This characteristic is common to all III-N nanowires. In Fig. 1.9 we show microscopy images of (a) GaN and (b) InN NWs. In both cases we appreciate

[2]In the NW literature it is common to find the term plasma-assisted MBE (sometimes one can find this technique in the literature as PAMBE) [63].

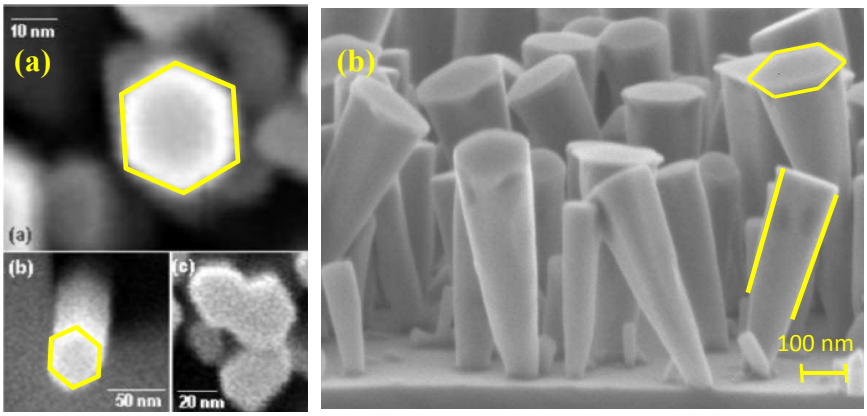

Figure 1.9: (a) Top view scanning electron microscopy image of GaN NWs [65], and (b) lateral view of InN NWs [67].

the hexagonal cross-sections. Theoretical studies based on *ab initio* calculations for free-standing GaN surfaces, have shown a lower formation energy for $(1\bar{1}00)$ surfaces than for $(11\bar{2}0)$ surfaces [64]. As the NWs free surfaces are nonpolar, it is logic to think that the structure choses the $(1\bar{1}00)$ planes to minimize the energy. The X-ray studies diffraction of Refs. [65] and [66] also point in that particular morphology.

The method described here for the growth GaN NWs can and has been extended to the other III-N semiconductors by the pertinent modifications. Therefore, by an appropriate choice of the substrate, flux ratio, and substrate temperature, it has been shown feasible to grow NWs made of any III-N semiconductor [68]. The techniques to grow InN and GaN nanowires are well established and these system are nowadays a robust field of research. In the case of AlN nanowires, only recently there have appeared preliminary works showing the growth with sufficient crystalline quality and an acceptable columnar morphology [69, 70]. Table 1.10 summarizes the most important groups active in the study of III-N NWs present as well as the main characteristics of their samples.

1.2.1 InN nanowires

The InN NWs usually grow at temperatures ranging from 400 to 600 °C, due to the low decomposition temperature of InN. At these low temperatures the desorption of indium (see Fig. 1.7) can be neglected, while the decomposition of nitrogen by effusion is a process which strongly affects the InN growth. The nitrogen decomposition induces a segregation of indium atoms at the surface. To avoid the formation

Group	Material	Substrate	Diameter (nm)	Technique	Tsubs (ºC)	Refs.
A. Rizzi	InN	Sapphire	20-80	MBE	450	[67]
E. Calleja	InN	AlN/Si	80-120	MBE	475	[73]
R. Calarco	InN	Si	50-150	MBE	440-525	[71]
B. Daudin	GaN	AlN/Si	40-80	MBE	720	[58]
R. Calarco	GaN	Si	20-50	MBE	785	[63]
E. Calleja	GaN	Si	65-150	MBE	660-770	[65]
V. Naraynamurti	GaN	Si	20-80	MOVCD (nickel)	700	[57]
B. Daudin	AlN	SiO2/Si	80-120	MBE	900-950	[69]
J. Jian	AlN	Graphite, Si, Mo	80-150	MOVCD	900	[70]

Table 1.10: Summary of the growth conditions, material, size and substrate of the III-N nanowires studied by the most relevant research groups.

of defects during MBE growth, the nitrogen flux must balance the indium accumulation. Therefore, nitrogen-rich conditions are necessary for obtaining the InN NWs with the characteristic columnar morphology [71, 72].

The most commonly used substrate is Si (111), that offers the advantages with respect to sapphire substrates of having a low cost, high crystal quality, doping capabilities, cleavability, and thermal conductivity [73]. The covering of the Si (111) substrate by a thin layer of AlN has also shown the capability of the columnar growth of InN. In Fig. 1.11 we show one of the first samples of InN NWs obtained by the group of R. Calarco in 2006 [71].

Concerning the physical properties of InN NWs, the presence of an electron accumulation at the surface, analogously to the case of InN layers is a notorious property that is receiving a great attention [74]. The first evidence of an electron accumulation layer in nonpolar surfaces were reported by the group of E. Calleja in Ref. [75], where the measurements of the transport along the NWs indicate a strong surface conductivity. Other studies based on Raman spectroscopy and photoluminescence also point to the presence of a surface accumulation layer [49]. One of the aims of this thesis is to provide a theoretical model capable of explaining the influence of this electron accumulation layer in the optical properties of InN NWs. The Chapter 4 is devoted to the presentation of the model and the comparison between the theoretical and experimental results.

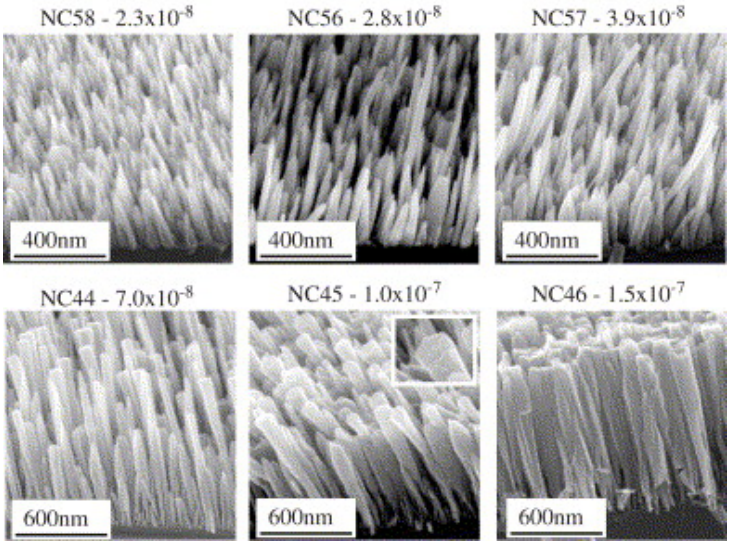

Figure 1.11: Scanning electron microscopy image of InN nanowires grown at substrate temperature of 475 °C. Together with the name of the sample, the In-flux in mbar. Extracted from Ref. [71]

1.2.2 GaN nanowires

Because of the prospective applications of GaN, due to its near ultraviolet band gap, the GaN nanowires have received an enormous attention [76]. The substrate temperature is around 700 °C, much higher than in the case of InN NWs. In principle, the difference between the substrate temperatures for the growth of these types of NWs could represent a problem to grow NWs based on the ternary alloy GaInN. An alternative technique to the growths of GaN NWs by MBE is the self-catalyst vapor-liquid-solid (VLS) process [77]. Here, the GaN nanowires nucleate and grow from Ga droplets formed during thermal decomposition of GaN at very high temperatures in vacuum atmosphere. The disadvantages of the VLS mode is a low control of the growth, and a larger dispersion in the sizes. In Fig. 1.12 we show a picture of GaN NWs, highlighting the hexagonal cross-section of the structures.

Differently to the reported electron accumulation layer behavior at the surfaces of InN NWs, the observed experimental transport indicates a depletion of electrons near the surface of GaN NWs. In principle, below a critical diameter, the current flow is only possible with illumination by ultraviolet light that generates electron-hole pairs. The determination of the critical diameter was achieved by performing current voltage measurements. Such behavior has been reported in silicon-doped GaN NWs, with the critical diameter depending on the amount of doping [78]. An

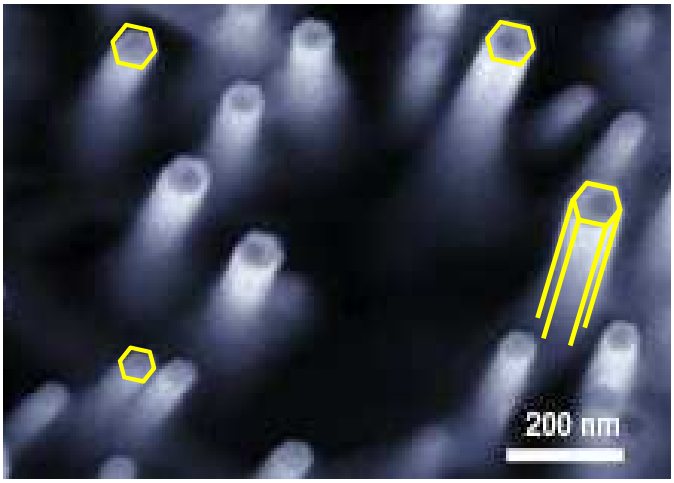

Figure 1.12: Scanning electron microscopy image of GaN NWs oriented along the *c*-axis, as grown by MOCVD over a substrate of MgO (from Ref. [80]).

atomic force microscopy point also out to the existence of such electron depletion layer. However, there is not nowadays a definitive explanation of the phenomenon [79].

1.2.3 AlN nanowires

The AlN NWs are probably the less investigated member of the family of III-N NWs. The InN and GaN NWs have concentrated until now the major efforts of the scientific community as we have reported in the previous Subsections. However, the band gap in the far ultraviolet (UV) of AlN makes this material very interesting for optoelectronic applications. The Si (111) substrate used in the growth of InN NWs is unsuitable here, since no three-dimensional islands (the precursors of NWs) are formed, due to the almost perfect lattice matching between AlN and Si (111). An alternative is the use of the substrate SiO_2/Si (100), that facilitates the formation of three dimensional islands, by the Volmer-Weber growth mode.[3] The control of the structural and optical properties of this kind of NWs is a challenge for the the MBE-based techniques. In Fig. 1.13 we show the AlN NWs obtained by MBE. The NW diameter are in the range of 80-100 nanometers. Again nitrogen-rich conditions are necessary for the growth process, and the substrate temperature is in the range of 900-950 ^{o}C, higher than in the case of InN and GaN NWs. This is

[3]In the Volmer-Weber mode the formation of three dimensional islands takes place without the formation of the wetting layer, characteristic of the SK mode. For a detailed exposition, see Ref. [81].

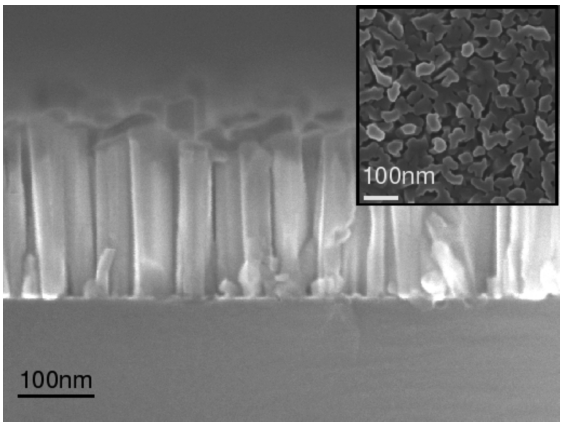

Figure 1.13: Scanning electron microscopy image of AlN NWs on SiO_2/Si (100) extracted from Ref. [69].

because the lower diffusion of aluminium atoms compared with indium or gallium atoms. The NWs are aligned parallel along the *c*-axis of the wurtzite structure and they are found to be free of dislocations and mostly relaxed, as confirmed by Raman spectroscopy. Other alternatives, such as the synthesis of the NWs from aluminium powder do not seem to obtain the crystalline quality achieved by MBE [82]. Other effort in the growth of AlN NWs has achieved, with a relative success, the fabrication of one-dimensional nanostructures, founded in the nitridation of aluminium powder, but with a large amount of staking faults [83].

1.2.4 Applications of III-N nanowires

Nanowires are interesting as a platform for fundamental physics research. For instance, studies concerned with the quantum confinement can be performed if the NWs have a diameter below ∼20 nm. In Fig. 1.14 we can see the photoluminescence spectra of single NWs with diameter below 20 nm. The NWs were grown by laser-assisted catalytic growth using gold catalyst, and dispersed on oxidized silicon substrate. In this case, the confinement leads a substantial increase in the emission energy [84]. This reported two-dimensional confinement endows NWs with unique properties which stray from those of their corresponding bulk materials [85]. The NWs have also demonstrated to be a suitable platform for the growing of the zinc-blende phase of materials, which are thermodynamically unstable when grown in bulk form. This is the case, for instance, of GaN and InP [15, 86]. In this sense, it is noticeable the absence of theoretical studies concerning the electronic structure of these wurtzite/zinc-blende semiconductors heterostructures. Moreover, NW heterostructures are currently being grown within the NWs

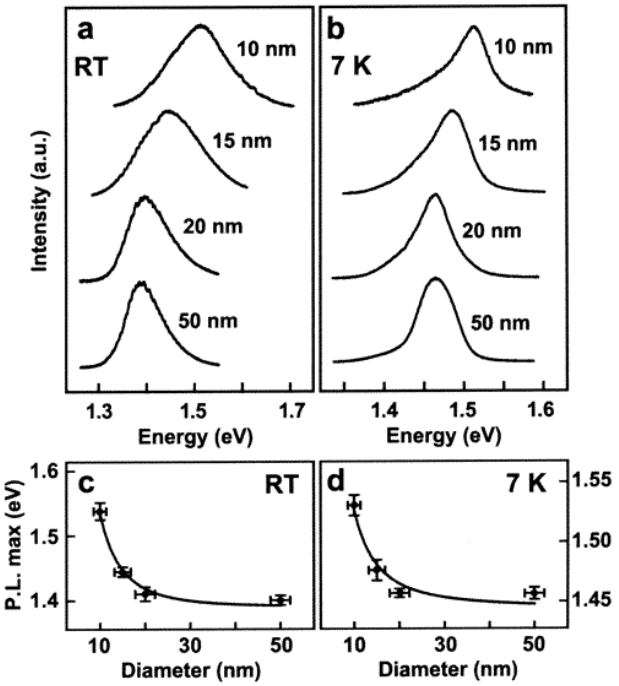

Figure 1.14: Photoluminescence spectra taken at (a) room temperature and (b) 7 K, for single InP NWs with nominal diameters of 50, 20, 15, and 10 nm. In (c) and (d), energy of the photoluminescence peak versus diameter. Extracted from Ref. [7].

themselves, as either nanodisks along the NW axis, or as radial nanowires (core-shell), where the composition varies with the radius [87]. In addition, the large aspect ratio of NWs makes them a convenient structure for studies related with transport phenomena [88].

The constant improvement of the technology for the fabrication of NWs, has made possible the design of novel devices and applications. In the field of the energy conversion, NWs has been received an increasing attention, proposing them as novel solar cells [6]. For instance, in solar cells, the efficient charge separation of electrons and holes after photoexcitation is desired. In this way, coaxial nanowires can in principle provide this feature [89]. Moreover, the possibility of separating NWs from the ensemble were they are grown, can allow the fabrication of single-nanowire solar cell, that can be useful in the design of future macroscopic solar cells based in arrays of such nanostructures [90]. In addition, the superlattice nanowires can lead the building of more efficient light-emitting diodes (LEDs), where the light emission is achieved in an active region of precisely controlled dimensions, by growing a section of an appropriate material inside a NW p-n junction [91].

1.3 Theoretical modeling of III-N nanowires

In this thesis, we have studied theoretically the electronic and optical properties of III-N NWs with several approaches, depending on the size of the NW. In a preliminary step, *ab initio* methods based on the density functional theory, have been used to obtain the bulk electronic structure of III-N semiconductors. On the other hand, the posterior study of the III-N NWs has been performed with semi-empirical methods, whose parameters have been derived from the bulk *ab initio* results. The term *semi-empirical* is used in this work to emphasize that the parameters are deduced from a well founded theoretical model, and are not just the result of an arbitrary fitting procedure. For the latter kind of procedures we reserve here the term empirical. The semi-empirical methods used in this thesis can be further divided into atomistic-like (the pseudopotential and tight-binding methods) and continuum-like (effective-mass approximation). An schematic guide of the calculations performed in this thesis is shown in Fig. 1.15. The pseudopotential model is used for the study of free-standing GaN NWs, with diameters ranging from 1 to 10 nm approximately. The tight-binding method, which is able to deal with larger NWs, until a diameter of 20 nm, is applied in a comprehensive study extended to all types of III-N NWs. It is worth to mention that our findings cannot be compared with experimental results since the current growth methods have not produced narrow III-N NWs, although as seen in Fig. 1.14, such capability has been demonstrated for InP nanowires. Therefore, the value of our atomistic calculations of our NWs lies on one hand in the methodological level and as predictions to be checked when sufficiently narrow NWs are available. On the other side, the study of the electron accumulation layer in InN NWs, and its influence on the optical properties needs a self-consistent solution of the Schrödinger-Poisson system of equations, that would be very computationally demanding for both the atomistic methodologies commented above. Fortunately, the size of the InN NWs is above 20 nm in the samples in which the optical experiments were performed, and for these dimensions, an atomistic treatment is unnecessary, and the effective-mass approximation (EMA) is a suitable method.

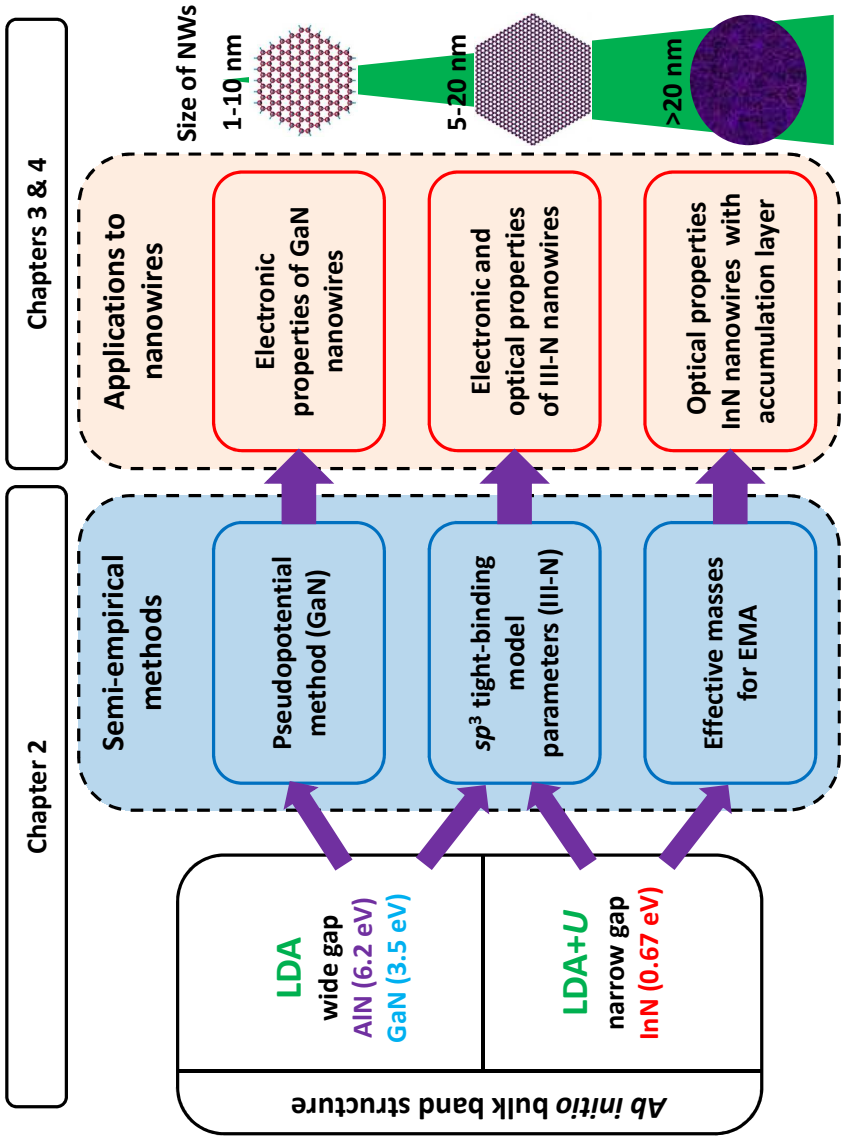

Figure 1.15: Flowchart of the calculations presented in this thesis.

In the following, we enumerate the main characteristic of the theoretical models employed in this thesis:

- *First principles or ab initio methods*: These approaches apply the laws of quantum mechanics, avoiding if possible the introduction of parameters. The atoms of the system are explicitly included, and an optimization process is applied until the system reaches the minimum of the total energy. The *ab initio* methods provide a very accurate information about the properties of bulk materials, such as the lattice constants, band structure, or elastic constant [92]. Thus, the obtained information from the *ab initio* methods is invaluable for a precise knowledge of the bulk band structure, and it is also useful for the deduction of parameters for the empirical methods. In Chapter 2, we present calculations performed by *ab initio* methods, based on the density functional theory, of the band structure of III-N semiconductors.

  The use of such *ab initio* methods in nanostructures, composed by many atoms (thousands of atoms), is strongly limited due to the computational resources required. The advance in the computational capabilities has made possible the application of the *ab initio* methods to small nanostructures [93]. Thus, in the field of III-N NWs, one can find *ab initio* calculations of the electronic structure of small NWs of AlN [94], GaN [95, 96] and InN [97, 98]. Such studies are very useful to confront their results with those obtained from empirical methods. However, the studies of trends in the physical properties with varying nanostructure sizes or shapes, that require efficient repetition of calculations, are still impractical and more simplified methods are demanded for such tasks.

  Another advantage of performing calculations with the *ab initio* methods is the availability of extensively developed software for those purpose. A large community of researchers is involved in the implementation of the theory in efficient and easy-to-use environments for the users. It is worth to mention that most of the *ab initio* codes are open-source, which certainly has contributed to their expansion. In this thesis, we have used the codes AB INIT [99] and QUANTUM ESPRESSO [100] codes, as explained in Chapter 2. Other popular codes that implement calculations based on the density functional theory are SIESTA [101], developed mainly in Spain, or WIEN2k, created at the University of Vienna, Austria [102].

- *Semi-empirical atomistic methods*: In these approaches the electronic structure of the material is also obtained by solving the one-particle Schrödinger equation with the explicit consideration of the atomic positions. However,

contrary to the *ab initio* methods, the interactions between the atoms are now simulated by a set of judiciously chosen parameters, thus avoiding the need of self-consistent calculations. The computation time for the calculations is now much shorter than in the case of *ab initio* methods and this means, their use has become very common in the study of the physical properties of all kinds of nanostructures. The most important semi-empirical atomistic methods are the empirical pseudopotential and the tight-binding approaches [103–105].

In the pseudopotential method, the electron-ion and electron-electron interaction is embedded in the use of atomic pseudopotentials, which are chosen in such a way that the band structures of the bulk materials reproduce to the largest possible extent the available experimental data and/or *ab initio* bulk results. This method has been widely used in the field of nanostructures to model the electronic structure and the optical properties of quantum dots [106, 107]. In the field of NWs, most of the theoretical effort has been addressed to the study of zinc-blende NWs grown in the [111] direction [108], and more recently, also in wurtzite NWs [109, 110]. In Chapter 3 of this thesis, we will study the electronic structure of wurtzite GaN nanowires, grown along the c-axis, by the semi-empirical pseudopotential method [111]. In Chapter 2 we present such formalism, together with our own calculations in GaN and AlN bulk of the band structure.

On the other side, the tight-binding method, which is also an atomistic approach, codes all the information about the interatomic interactions into a set of parameters interpreted as overlap integrals between atomic-like orbitals [112].[4] The tight-binding method offers an intuitive picture of the electronic states in terms of the mentioned atomic-like orbitals. The general formulation for the III-N bulk is given in Chapter 2. Analogously to the pseudopotential method, the tight-binding approach is also a suitable and broadly used methodology for the predictions of the electronic and optical properties of nanostructures [105, 113–115]. In the last years, the tight-binding method has also been applied to the calculation of the optical properties of zinc-blende [116] and wurtzite NWs [98, 117–119]. In this thesis, we apply the tight-binding method to study the electronic structure and the anisotropy in the optical response of the III-N nanowires, as presented in Chapter 3.

- *Effective-mass approximation*: In this approximation, the crystal microscopic potential is replaced by a constant potential. The electron is assumed to move

[4] This method is also called the linear combination of atomic orbitals (LCAO).

in vacuum with a renormalized mass (known as effective mass, m^*), that depends on the material [120]. The electron wave function is expressed as the product of a periodic function and an envelope function. In this thesis, the effective-mass approximation (EMA) is applied in its simplest version, assuming the single-band model (particle-in-a-box). In the treatment of large nanostructures, with 10^4-10^9 atoms, EMA is an appealing methodology since the computational requirements are essentially independent of the nanostructure size. Besides, the introduction of external fields is performed in a very intuitive way. Thus, for example, the problem of the electron accumulation layer in InN surfaces commented briefly in Section 1.2 is hardly affordable by means of an *ab initio* approach. The empirical atomistic approaches can give valuable information for large NW sizes, but parametric studies as a function of size or impurity concentration are impractical due to the large number of repetitive calculations required. It is here where the use of theoretical tools, based on the solid as a continuum, in which the electron moves as in vacuum but with a renormalized kinetic energy are especially suitable for the simulation of large nanostructures. Thus, although the EMA has been strongly criticized [121], it has demonstrated to be a valid method in an appropriate range of nanostructures sizes [122, 123], usually for dimensions above 10 nm. Besides, the required computational effort is minimal in comparison with the atomistic methods, being possible the performance of calculations in desktop computers [124]. In Chapter 4 of this thesis, the electron accumulation layer of large InN NWs (diameter above 20 nm) is calculated within the self-consistent (Schrödinger-Poisson) effective-mass approximation. This approach allows us to study the influence of the electron distribution on the optical properties, by varying the NW size and the impurity concentration, and to perform a successful comparison with available experimental measurements of photoluminescence excitation.

Chapter 2

Electronic structure of III-N semiconductors

The aim of this Chapter is to summarize the theoretical methods used in the calculation of the electronic structure of III-N nanowires. Besides the general formulation of each method, we also show our calculations of the band structure of bulk III-N semiconductors, in order to introduce concepts that help in the exposition of subsequent Chapters.

This Chapter is organized as follows:

- Section 2.1 gives an outline of the density functional theory and introduces the Kohn-Sham (KS) equations. The local-density approximation (LDA) and the variant constructed by adding the Hubbard-like term in the Hamiltonian (LDA+U) are exposed afterwards. Then, the pseudopotential concept and the plane-wave representation, used in practice to solve the KS equations, are explained. It follows a discussion of the results that we have obtained for the band structure of III-N semiconductors, InN, GaN, and AlN.

- Section 2.2 deals with the semi-empirical pseudopotential method as applied to wurtzite semiconductors. Unlike the standard procedure, we derive the pseudopotentials directly from the *ab initio* calculations. This procedure to obtain these screened pseudopotentials as well as the strategy to reduce the computation time and correct the *ab initio* band gap problem arex explained in detail. The set of obtained pseudopotentials are suitable to perform calculations in nanostructures, and in particular, we will use then to compute the electronic structure of GaN nanowires in Chapter 3.

- Section 2.3 is concerned with the introduction of the semi-empirical tight-binding method. The tight-binding parameters have been obtained by fitting the *ab initio* band structures calculated in Section 2.1. We have taken special care in obtaining the true symmetry of the wave functions at the center of the Brillouin zone. The set of tight-binding parameters obtained here will then be used in the electronic structure calculations of various III-N nanowires in Chapter 3. The treatment of the optical absorption within the tight-binding formulation is explained in Section 2.4.

2.1 Density functional theory

Many of the physical properties of solids are related to total energies or to total energy differences. For instance, the equilibrium lattice constant of a crystal is given by the atomic spacing that minimizes the total energy. Surfaces and defects of solids adopt the structure that minimizes their corresponding total energies. If total energies can be calculated, any of those physical properties, can be determined computationally, in principle. The methods that obtain the total energy of the system, and then by applying the laws of the quantum mechanics, starting exclusively with the atomic information of the constituents of the system (in the case of solids, the number of positively charged nucleus and the number of electrons), are termed as *ab initio* or *first principles* methods. Among the variety of *ab initio* methods proposed, the density functional theory (DFT) has demonstrated to be an extremely successful approach for the description of the ground state properties of solids. The main idea behind the DFT is the possibility to describe the system by its electronic density, instead of using its complete many-body wave function [125]. The Kohn-Sham (KS) equations provide the way to convert the DFT a practical methodology [126]. The approximation within the DFT most used often is the local-density approximation (LDA), which locally substitutes the exchange-correlation energy on an inhomogeneous system by that of the homogeneous electron gas. Next, we recall the main ideas concerning the DFT, KS equations, and LDA. At the end of the Section, we present our *ab initio* calculations of the electronic structure of III-N semiconductors. Readers familiarized to the fundamentals of DFT are suggested to go directly to Subsection 2.1.3.

2.1.1 General formulation

The problem of solving the Schrödinger equation of a solid, where there are numerous nuclei and electrons (of the order of 10^{23}), is computationally intractable

without some simplifications. The first one the Born-Oppenheimer approximation, which justifies the decoupling of the electronic and nuclear dynamics. In the next step one usually applies one of the various forms of mean field approximations, leading to the substitution of the N-electron problem by N single-electron problems. It is not our aim here to analyze in detail the implications of these fundamental approaches, and we therefore refer the reader to Ref. [127] for a detailed explanation.

As mentioned above, one of the most successful mean-field approaches is the density functional theory (DFT) formulated in the 60's of the past century by Hohenberg, Kohn and Sham [128, 129], that it has become the standard method in the calculation of the electronic structure of solids. For this work, W. Kohn received the Chemistry Nobel Prize in 1998, together with J. Pople [130].

Hohenberg-Kohn theorems: The starting point of DFT is a system of N interacting electrons under the influence of an external potential $V_{\text{ext}}(\boldsymbol{r})$. In most situations $V_{\text{ext}}(\boldsymbol{r})$ is the total coulombic potential created by the nuclei of the solid, assumed to be at fixed positions. The ground state many-body wave function of the system is denoted as Ψ and the corresponding density is $n(\boldsymbol{r})$. The ground state energy can be written as follows:

$$E = T + V_{ee} + V, \tag{2.1}$$

where $T = \langle\Psi|\hat{T}|\Psi\rangle$ is the kinetic energy term and $V_{ee} = \langle\Psi|\hat{V_{ee}}|\Psi\rangle$ is the Coulomb electron-electron interaction energy. The functional that relates the external potential with the density is then:[1]

$$V[n] = \int V_{\text{ext}}(\boldsymbol{r})n(\boldsymbol{r})d^3\boldsymbol{r}. \tag{2.2}$$

The first Hohenberg-Kohn theorem establishes that the ground state density $n(\boldsymbol{r})$ uniquely determines the external potential $V_{\text{ext}}(\boldsymbol{r})$, up to an additive constant. The second Hohenberg-Kohn theorem demonstrates that the functional $F[n]$, defined as follows:

$$F[n] = \langle\Psi|\hat{T} + \hat{V_{ee}}|\Psi\rangle = T[n] + V_{ee}[n], \tag{2.3}$$

is the same for all electronic structure problems, because in its definition no mention has been done to the external potential. Therefore, the total energy functional can be written as follows:

[1] A functional is a mapping that assigns a number to a function.

$$E[n] = F[n] + \int V_{\text{ext}}(\boldsymbol{r}) n(\boldsymbol{r}) d^3\boldsymbol{r}, \tag{2.4}$$

As the functional $F[n]$ takes its minimum value for the ground state density, and the first theorem establishes a univocal relation between the density and the external potential, the total energy potential has its minimum value for the ground state density [131].[2] Unfortunately, the Hohenberg-Kohn theorems do not provide the exact functional $F[n]$, and the problem of determining the ground state energy and density is subordinate to the discovery of sufficiently accurate estimations of such functional.

Kohn-Sham equations: These equations establish the methodology for the practical use of the Hohenberg-Kohn theorems [126]. In these equations, the interacting electron system under the influence of the external potential is represented (or screened) by a system of non-interacting electrons under the influence of a mean-field potential. This potential, called as KS potential $V_{\text{KS}}(\boldsymbol{r})$, is chosen in such a way that its ground state density is the same as for the interacting electron system. The one-electron KS wave functions are then the solutions of the single-particle Schrödinger equation[3]

$$\left\{ -\frac{1}{2}\nabla^2 + V_{\text{KS}}(\boldsymbol{r}) \right\} \psi_i(\boldsymbol{r}) = \varepsilon_i \psi_i(\boldsymbol{r}), \tag{2.5}$$

where ε_i are the energy eigenvalues. The potential $V_{\text{KS}}(\boldsymbol{r})$ includes the external potential and the electron-electron interaction, and will be explicited later. The density $n(\boldsymbol{r})$ is written as follows:

$$n(\boldsymbol{r}) = \sum_{i=1}^{N} |\psi_i(\boldsymbol{r})|^2, \tag{2.6}$$

where only the N occupied (lowest energy) states participate in the construction of $n(\boldsymbol{r})$.

Now we define the mean-field kinetic energy of the non-interacting electrons as follows:

[2] We assume here that electrons are non-spin-polarized. The extension to spin-polarized systems is straightforward; the total energy becomes a functional of the spin density, which in the general case is given as a four component spinor [132].

[3] Except where noted, we use here atomic units, so that: $e^2 = \hbar = m = 1$, the unit of energy is Hartree, and length is in Bohr.

$$T_s[n] = \sum_{i=1}^{N} \langle \psi_i | -\frac{1}{2}\nabla^2 | \psi_i \rangle, \tag{2.7}$$

that it is slightly different from the kinetic energy T of the interacting electron system [126]. The functional $F[n]$ is now conveniently rewritten in terms of T_s as follows:

$$F[n] = T_s[n] + V_H[n] + E_{XC}[n], \tag{2.8}$$

the Hartree energy

$$V_H[n] = \int \frac{n(\boldsymbol{r})n(\boldsymbol{r}')}{|\boldsymbol{r} - \boldsymbol{r}'|} d^3\boldsymbol{r} d^3\boldsymbol{r}', \tag{2.9}$$

and the term E_{XC} is the exchange-correlation energy. The exchange energy is due to the antisymmetry of the many-electron wave function, that produces a spatial separation between electrons with the same spin, thus reducing the Coulomb energy of the system [131]. On the other side, the correlation energy comes from the difference between the many-body energy of an electronic system and the energy of the system calculated in the Hartree-Fock approximation [133].

Therefore, the potential $V_{\mathrm{KS}}(\boldsymbol{r})$ of Eq. (2.5) is given by

$$V_{\mathrm{KS}}(\boldsymbol{r}) = V_{\mathrm{ext}}(\boldsymbol{r}) + \int \frac{n(\boldsymbol{r})}{|\boldsymbol{r} - \boldsymbol{r}'|} d^3\boldsymbol{r}' + V_{XC}, \tag{2.10}$$

where

$$V_{XC}[n] = \frac{\delta E_{XC}}{\delta n(\boldsymbol{r})}. \tag{2.11}$$

The system of equations (2.5), (2.6) and (2.10) are known as Kohn-Sham equations. By solving them self-consistently, the ground state density and the total energy of the system can be subsequently found [129]. In the following, the interaction of the electrons with the nuclei is introduced by means of the external potential. The Kohn-Sham equations are exact, and provide the exact ground state density. Moreover, the KS equations provide reliable solutions in reasonable computational times. However, all the benefits promised by this theoretical framework depend on the ability to deal with the exchange-correlation functional, in an exact rigorous manner (that nobody has succeeded to this date) or by means of finding accurate approximations.

Local-density approximation and the band gap problem: The simplest approximation, and also the most widely used to the exchange-correlation energy E_{XC}, is the local density approximation (LDA). The E_{XC} is obtained from

$$E_{XC} = \int \varepsilon_{XC}(\boldsymbol{r}) n(\boldsymbol{r}) d^3\boldsymbol{r}, \tag{2.12}$$

where $\varepsilon_{XC}(\boldsymbol{r})$ is a local functional of the density at every point $\boldsymbol{r}$, obtained by assuming the value it could take for the density of a homogeneous electron gas in its ground state [125]. Thus, the LDA assumes that the exchange-correlation energy of a non-uniform system can be obtained by using the information obtained from the uniform electron gas. Therefore, effects of the inhomogeneities in the density on E_{XC} are ignored. Despite this gross oversimplification, it is remarkable the good results that the LDA has provided over the years [131]. This is so to such an extent that DFT-LDA can be considered the cornerstone of most of the electronic structure calculations.

However, one of the major problems of LDA is that it systematically underestimates the band gap of semiconductors and insulators with respect to the experimental value. As we have illustrated in Fig. 2.1, the band gap of a semiconductor is the difference between the ionization potential ($I = -(E[N] - E[N-1])$) and electron affinity ($A = -(E[N+1] - E[N])$), with $E[M]$, indicating here the ground state total energy of the M-electron system, written as follows [134]:

$$E_g = A - I = E[N+1] + E[N-1] - 2E[N]. \tag{2.13}$$

Thus, the *exact* band gap can be expressed by

$$E_{\mathrm{g}} = E_{\mathrm{g,KS}} + \Delta_{XC}, \tag{2.14}$$

where the DFT-KS band gap is:

$$E_{\mathrm{g,KS}} = \varepsilon_{KS,N+1}(N) - \varepsilon_{KS,N}(N), \tag{2.15}$$

where $\varepsilon_{KS,i}(M)$ is the energy of the ith single particle eigenvalue of Eq. (2.5) for the M-electron system. The term Δ_{XC} is the difference between the $(N+1)-$th eigenvalues in the $(N+1)-$ and $N-$electron systems

$$\Delta_{XC} = \varepsilon_{KS,N+1}(N+1) - \varepsilon_{KS,N+1}(N). \tag{2.16}$$

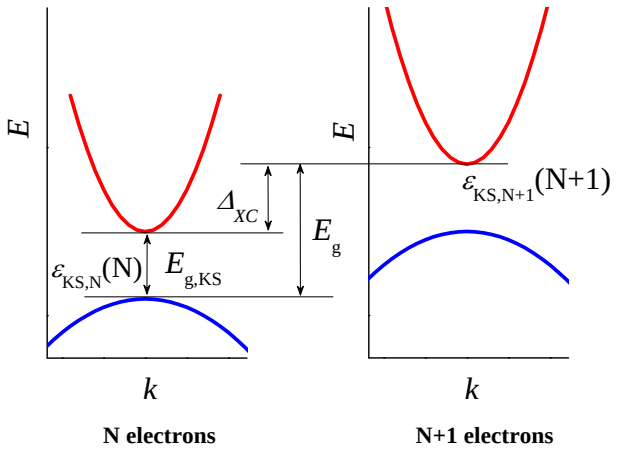

Figure 2.1: Illustration of the DFT Kohn-Sham one-electron energies, shown in the form of a band structure, for the N and $(N+1)$-particle systems, and their relation with the exact band gap of the solid. Extracted from Ref. [139].

This difference arises from the discontinuity in the exchange-correlation potential under adding and subtracting an infinitesimal fraction γ of the integer particle number N [135]

$$\Delta_{XC} = \lim_{\gamma \to 0} \left(\left. \frac{\delta E_{XC}[n]}{\delta n} \right|_{N+\gamma} - \left. \frac{\delta E_{XC}[n]}{\delta n} \right|_{N-\gamma} \right). \tag{2.17}$$

As the exchange-correlation functional is continuous in LDA , the discontinuity of Eq. (2.17) cannot be reproduced. In any case, the question if some other approximation to the functional $E_{XC}[n]$ can allow to DFT to estimate accurately the band gap is controversial and under debate [136]. In principle, for the wide band gap nitrides, GaN and AlN, the underestimation of the band gap given by LDA is not a pivotal problem, because it does not affect significatively to the quality of the calculated valence bands. Besides, the experimental band gap and upper unoccupied (conduction) bands can be forced upon by a rigid shift of the LDA conduction band. However, in InN, because of its narrow band gap, the LDA produces a zero or even negative band gap, altering substantially the valence bands, and making the whole band structure unreliable. For the correction of this underestimation of the band gap, a wealth of alternative approaches to LDA have been proposed, the most relevant ones being the application of exact-exchange potentials [137] and the LDA+U method [138].

Other approaches beyond DFT, that are based in many-body perturbation theory and in the Green-function formalism, e. g., the GW approximation, have

demonstrated the capability to improve the LDA results [52, 140]. However, these methods are much difficult of implementing and add a substantial increment in the computational time.

The LDA+U method: Among all the approaches applied to palliate the LDA band gap problem, the LDA+U method requires less computation time and it is simpler to apply. We explain briefly this approach, since it will be later applied to the narrow gap semiconductor InN. Although this method was initially introduced to make possible the description of strong electronic correlations, such as those found in transition metal or rare-earth metal ions, where partially filled d and f orbitals are of importance [138], it has been recently demonstrated its utility in the description of the electronic structure of ZnO and InN [51]. In the LDA+U approach, the Coulomb interactions between d electrons are taken into account via a mean-field Hubbard-like correction to the standard exchange-correlation functional [141]. While the s and p electrons could be excluded from this approximation, being dealt only within the LDA approach, the interactions between d electrons are supposed to be expressible as a function of the generalized orbital occupations, $n^I_{mm'}$ of atomic sites I, defined as:

$$n^I_{mm'} = \sum_i f_i \langle \psi_i | P^I_{mm'} | \psi_i \rangle, \tag{2.18}$$

where ψ_i are the wave functions of the KS eigenvalue $\varepsilon_{KS,i}$ (see Eq. (2.5)), f_i is the occupation number of the i-th state, and $P^I_{mm'}$ are the generalized projection operators

$$P^I_{mm'} = |\varphi^I_{l,m}\rangle\langle\varphi^I_{l,m'}|, \tag{2.19}$$

being $\varphi^I_{l,m}$ the valence orbital of atom at site I with angular momentum (l, m). The total occupation of the atomic site I is then $n^I = \sum_m n^I_m \equiv \sum_m n^I_{mm}$. The correction to the total energy considering the occupation of the d-states (here $l = 2$ and $-2 \leq m \leq +2$), is written in a simplified scheme as (a more detailed exposition on Ref. [142]):

$$E_{LDA+U}[n] = E_{\mathrm{LDA}}[n] + \sum_I \left[\frac{U}{2} \sum_{m,m'} n^I_m n^I_{m'} - \frac{U}{2} n^I (n^I - 1) \right], \tag{2.20}$$

where the first term represents the correct on-site correction to the correlation functional. As LDA is supposed to contain this contribution in an averaged manner, a

negative term is added to avoid such duplicity. U represents the screened on-site Coulomb parameter. Finally, the new potential to be included in the Kohn-Sham equation (2.5) ($V_{\mathrm{KS}} \rightarrow V_{LDA+U}$) is defined by

$$V_{LDA+U}|\psi_i\rangle = V_{\mathrm{LDA}}|\psi_i\rangle + \sum_I \sum_m U \left(\frac{1}{2} - n_m^I\right) P_{mm}^I |\psi_i\rangle. \tag{2.21}$$

To give an idea of how the LDA+U method works, let us take a simple example by considering the last occupied state ϵ_v (occupation $n_m \approx 1$) and the first unoccupied state ϵ_c (occupation $n_m \approx 0$). For simplicity we consider only one atomic site. If we differentiate the energy with respect to the occupation number n_m, we get

$$\varepsilon_m = \frac{\partial E_{LDA+U}}{\partial n_m} = \varepsilon_m^0 + U\left(\frac{1}{2} - n_m\right), \tag{2.22}$$

where ε_m^0 is the corresponding LDA result. The difference between ε_c and ε_v gives the corrected LDA+U band gap

$$\varepsilon_{LDA+U} = \varepsilon_c^0 - \varepsilon_v^0 + U = \varepsilon_{\mathrm{LDA}} + U. \tag{2.23}$$

Therefore, the gap between the last occupied orbital ($n_i \sim 1$) and the first unoccupied orbital ($n_i \sim 0$) would be opened a width U. As we will show later, LDA+U provides an optimal solution for the band gap problem in InN. For a more detailed account of LDA+U, we remit the interested reader to the Ref. [143].

2.1.2 Plane wave representation and pseudopotentials

In solid state physics, due to the periodicity of crystals, the Bloch's theorem establishes that the wave function of an electron with wave vector $\boldsymbol{k}$ in band j, $\psi_{j,\boldsymbol{k}}(\boldsymbol{r})$, can be written as the product of a plane wave and a periodic function, $u_{j,\boldsymbol{k}}(\boldsymbol{r})$:

$$\psi_{j,\boldsymbol{k}}(\boldsymbol{r}) = e^{i\boldsymbol{k}\cdot\boldsymbol{r}} u_{j,\boldsymbol{k}}(\boldsymbol{r}), \tag{2.24}$$

where $\boldsymbol{k}$ can be restricted without loss of generality to the first Brillouin zone (BZ) [144]. As $u_{j,\boldsymbol{k}}(\boldsymbol{r})$ has the periodicity of the crystal lattice, it can be expanded in a Fourier series of plane waves with wave vectors $\boldsymbol{G}$ belonging to the reciprocal lattice:[4]

[4]The reciprocal lattice is formed by those vectors $\boldsymbol{G}$ that satisfy $e^{i\boldsymbol{G}\cdot\boldsymbol{R}} = 1$ for any vector of the crystal lattice $\boldsymbol{R}$.

$$u_{j,\boldsymbol{k}}(\boldsymbol{r}) = \sum_{\boldsymbol{G}} A_{j,\boldsymbol{k}}(\boldsymbol{G}) e^{i\boldsymbol{G}\cdot\boldsymbol{r}}, \tag{2.25}$$

and the Bloch wave function of the electron can be expressed as follows:

$$\psi_{j,\boldsymbol{k}}(\boldsymbol{r}) = \sum_{\boldsymbol{G}} A_{j,\boldsymbol{k}}(\boldsymbol{G}) e^{i(\boldsymbol{k}+\boldsymbol{G})\cdot\boldsymbol{r}} = \sum_{\boldsymbol{G}} A_{j,\boldsymbol{k}}(\boldsymbol{G}) \langle \boldsymbol{r}|\boldsymbol{k}+\boldsymbol{G}\rangle, \tag{2.26}$$

where the plane waves $\langle \boldsymbol{r}|\boldsymbol{k}+\boldsymbol{G}\rangle = \frac{1}{\sqrt{V}} e^{i(\boldsymbol{k}+\boldsymbol{G})\cdot\boldsymbol{r}}$ form an orthogonal basis:

$$\langle \boldsymbol{G}|\boldsymbol{G}'\rangle = \delta_{\boldsymbol{G},\boldsymbol{G}'}. \tag{2.27}$$

Therefore, the plane wave basis is specially suited for such periodic systems. In the plane wave representation, the KS equation (2.5) takes a very simple form, that can be obtained by multiplying by $\langle \boldsymbol{k}+\boldsymbol{G}|$ from the left, and integrating over $\boldsymbol{r}$, to give a matrix eigenvalue problem for every $\boldsymbol{k}$ within the BZ [145]:

$$\sum_{\boldsymbol{G}'} \left\{ \frac{1}{2}|\boldsymbol{k}+\boldsymbol{G}|^2 \delta_{\boldsymbol{G},\boldsymbol{G}'} + \hat{V}_{\mathrm{KS}}(\boldsymbol{G}-\boldsymbol{G}') \right\} A_{j,\boldsymbol{k}}(\boldsymbol{G}') = \varepsilon_j A_{j,\boldsymbol{k}}(\boldsymbol{G}), \tag{2.28}$$

where $\hat{V}_{\mathrm{KS}}(\boldsymbol{G}-\boldsymbol{G}')$ is the Fourier transform of the K-S potential combining external and Coulomb (Hartree and exchange-correlation terms) terms. As we see, in the plane wave representation the eigenvalue problem expressed by the KS differential equations transforms into a matrix diagonalization problem where the kinetic energy only contributes to the diagonal matrix elements. Usually, to calculate the potential contribution, each part, external, Hartree and exchange-correlation, is considered separately (see Ref. [146] for details). Moreover, in practical calculations the plane wave basis must be truncated. This can be done by fixing the cutoff energy, E_{cut}, that determines the number of plane waves used by imposing:

$$\frac{1}{2}|\boldsymbol{G}|^2 \leq E_{\mathrm{cut}}, \tag{2.29}$$

the value of this energy cutoff is set by testing the convergence of the total energy with the increase of E_{cut}. Proceeding by this way we make the basis size to depend on only one parameter, E_{cut}.

However, the important disadvantage of the plane wave basis must also be commented. Since the plane waves are non-localized functions, it is required to use large basis sizes to deal with strongly oscillating functions (as the case of the

atomic orbitals) or very localized functions. This problem can be overcome by introducing the concept of pseudopotential [147], that it will be explained below. In addition, the plane wave basis is in principle not suitable to deal with finite system. Therefore, in these cases, the use of a plane wave basis cannot take advantage of the interface to vacuum to reduce the basis size. In those cases, a large supercell is defined to enforce the periodicity of the system, but the supercell must be large enough to prevent coupling between different replica of the system. This same problem arises in systems with relevant inhomogeneities. We will come back to this point in Chapter 3.

Before introducing the pseudopotentials, it is useful to split the electrons into core and valence electrons. This makes sense since most of the physical and chemical properties of crystals depend to a very good approximation only on the distribution of the valence electrons. Thus, the core electrons are strongly localized around the nucleus, interacting minimally with electrons from other atoms. It is therefore sensible to make the *frozen core* approximation that assumes the core electrons to be unperturbed by the environment. The contributions of the core electrons and nuclei are therefore combined into a single ionic pseudopotential. In this way, a great simplification is introduced into the KS equation, and the number of eigenvalues to be calculated now is substantially reduced. Note also that the external potential, mentioned in the exposition of the fundamentals of DFT, will be in the following this ionic potential ($V_{\text{ext}} \rightarrow V_{\text{ion}}$).

However, in spite of the frozen core approximation, the ionic potential still has a sharp oscillating profile near the core region, as a consequence of the orthogonality between the valence wave functions and the core electron wave functions [148]. Therefore, the number of plane waves necessary to describe such wave functions will still be huge. On the other hand, it is expected that for distances far enough from the core, the valence electrons feel only a smooth screened potential. Thus, it would be desirable to substitute the rippling ionic potential by a smoother function, that mimics the all electron wave function outside a selected ionic radius (cutoff radius r_c) as illustrated in Fig. 2.2 [149, 150]. This is the so-called pseudopotential approximation. Now, the pseudopotential and the pseudo wave functions have a nodeless profile, or in the pseudopotential terminology, they are *soft*. For soft pseudopotentials the number of plane waves necessary to expand the pseudo wave function should be as small as possible.

A formal justification of the pseudopotential approximation can be given following the formulation of Phillips and Kleinman [149], that we sketch here. Let $|\phi_i\rangle$ be the true valence wave function with energy ε_i, and $|\chi_n\rangle$ the true core wave functions with eigenvalues E_n. The aim is to achieve a smooth pseudo wave

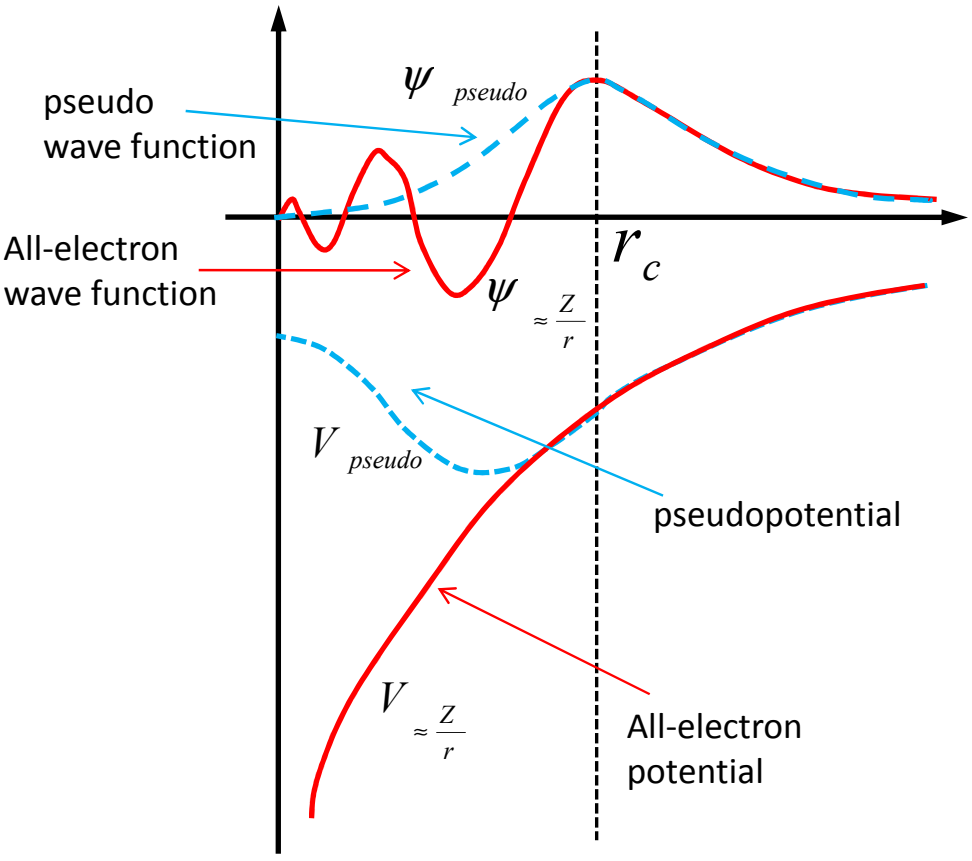

Figure 2.2: Illustration of the true wave function and electronic potential (solid lines) plotted against distance r from the atomic nucleus. The corresponding potential and pseudo wave function are drawn with dashed lines. The true wave function and the pseudo wave function are identical outside a certain radius, here denoted as r_c.

function ψ_i. We can write the valence wave function as:

$$|\phi_i\rangle = |\psi_i\rangle + \sum_n c_n |\chi_n\rangle. \tag{2.30}$$

Since the wave functions are orthogonal:

$$\langle\chi_n|\phi_i\rangle = 0 = \langle\chi_n|\psi_i\rangle + c_n \quad \rightarrow \quad c_n = -\langle\chi_n|\psi_i\rangle, \tag{2.31}$$

and the Eq.(2.30) is written now as:

$$|\phi_i\rangle = |\psi_i\rangle - \sum_n \langle\chi_n|\psi_i\rangle|\chi_n\rangle. \tag{2.32}$$

Now by introducing this expression into the Schrödinger equation, $\hat{H}|\phi_i\rangle = \varepsilon_i|\phi_i\rangle$, obtain an effective equation for $|\psi_i\rangle$ and ε_i:

$$\hat{H}|\psi_i\rangle + \sum_n (\varepsilon_i - E_n)|\chi_n\rangle\langle\chi_n|\psi_i\rangle = \varepsilon_i|\psi_i\rangle. \tag{2.33}$$

It can be shown that the second term is a strongly repulsive potential which almost cancels the strongly attractive core potential implicit in $\hat{H}$, leaving a weak soft effective potential. The smooth pseudo wave functions obey a Schrödinger equation with an additional energy dependent pseudopotential. The pseudopotential can be written as follows:

$$V_{\text{ps}} = V_{\text{ion}} + \sum_n (\varepsilon_i - E_n)|\chi_n\rangle\langle\chi_n|\psi_i\rangle. \tag{2.34}$$

Now we can write the KS equation (2.5), taking account this reformulation of the ionic potential:

$$-\frac{1}{2}\nabla^2|\psi_i\rangle + \left[V_H + V_{XC} + \left\{V_{\text{ion}} + \sum_n (\varepsilon_i - E_n)|\chi_n\rangle\langle\chi_n|\right\}\right]|\psi_i\rangle = \varepsilon_i|\psi_i\rangle. \tag{2.35}$$

Since the atomic core wave functions $|\chi_n\rangle$ depend on the angular momentum (l, m), the most general form of the ionic pseudopotential can be expressed as follows [151].

$$V_{\rm ps} = \sum_{l,m} V_{\rm ps,l} \hat{P}_{l,m}, \tag{2.36}$$

where $\hat{P}_{l,m} = |l,m\rangle\langle l,m|$ is the projector on the angular momentum state (spherical harmonic) (l,m). However, for computational tasks such expression is not convenient, and it is reformulated as follows. For large distances from the core, it is assumed that $V_{\rm ps,l}$ reduces to an screened Coulomb potential and gets independent of l. Thus, a good approximation would be to express the pseudopotential as a local part plus a sum over l-dependent nonlocal terms for $l < l_{max}$:

$$V_{\rm ps} = V_{\rm local} + V_{\rm nonloc} = V_{\rm local} + \sum_{l,m} |l,m\rangle v_{\rm nonloc,l} \langle l,m|, \tag{2.37}$$

In this expression the local term vanishes if $r < r_c$. In first approximation, the pseudopotential can be considered as local, though the nonlocal part is far from negligible. In Section 2.2 some further details will be given in the context of the calculations of the nonlocal part of the semi-empirical pseudopotential.

In summary, the pseudopotential formulation allows us to avoid the use of the true atomic potential, and simplifies enormously the resolution of the KS equations. However, the best pseudopotential is a priori unknown, and the problem of determining such pseudopotential is not a trivial task. Since the works where the use of pseudopotentials was first proposed [152], the sophistication of the methodology to generate accurate and efficient pseudopotential has grown notably. Usually, the construction of a pseudopotential starts from *ab initio* calculations for an isolated atom. However, it is also desirable a pseudopotential able to be used in other chemical environments, different from where it was generated. This property is the so-called transferability. The properties of softness and transferability are closely related to the cutoff radius r_c, and compete with each other. Thus, a low r_c gives pseudopotential very transferable, and on the other side, large r_c makes the the pseudopotential softer. Therefore, one must find a compromise between the two requirements. The main criteria to generate pseudopotentials, among others, are:

- Norm-conserving pseudopotentials: First, the pseudo wave function outside r_c must mimic the all electron wave function. Moreover, inside the sphere defined by the cutoff radius the pseudo wave function and the all electron wave function must have the same norm, in order to guarantee that both wave functions generate identical electron densities in the external region [153, 154].

- Ultra-soft pseudopotentials: Here the pseudo wave functions are required to be equal to the all electron wave functions for $r > r_c$ but the norm-conserving requirement is relaxed, and the pseudopotential for $r < r_c$ is allowed to be as soft as possible [155].

A more extended explanation of each kind of pseudopotential, and how to generate them can be found in Ref. [156].

2.1.3 Band structures of bulk III-N semiconductors

Once the theoretical background of the DFT and the description of the approximations LDA and LDA+U have been introduced, in this Subsection we illustrate the suitability of both approaches for the calculation of the band structure of III-N semiconductors. We have separated the discussion of our calculations for GaN and AlN (wide band gap nitrides) on one side, and InN on the other, because of the refinement of the LDA that it is required in the InN case on account of its narrow band gap. In the case of GaN and AlN, the code AB INIT has been used [99]. This open-source software is able to calculate the total energy, charge density and electronic structure of systems made of electrons and nuclei (molecules or periodic solids) within the DFT, using the plane wave representation and the pseudopotential method. The norm-conserving Troullier-Martins pseudopotentials have been used here [99]. On the other side, for the calculations of narrow band gap InN, the QUANTUM ESPRESSO software has been used [100, 157]. The QUANTUM ESPRESSO is an integrated suite of computer codes able to calculate the electronic structure of solids, within the DFT, as the mentioned AB INIT. In this case, Perdew-Zunger ultrasoft pseudopotentials were used [100]. Moreover, in all the *ab initio* calculations of III-N semiconductors, the spin-orbit interaction has not been included, with the intention of adding it a posteriori when implementing the semi-empirical approaches. The most important specifications of the calculations can be found in Table 2.1. Concerning the DFT calculations, we have performed the LDA calculations of the GaN and AlN band structure in collaboration with G. Bester, from the Max-Planck Institute, Stuttgart (Germany), and the LDA+U computation of the InN band structure has been carried out by A. Terentjevs and G. Cicero, from the Politecnico di Torino, Italy.

Wide-gap nitrides: GaN and AlN

For the LDA calculations[5] of the GaN and AlN band structure the lattice parametershave been fixed at the outset. The experimental values of the a lattice constant have been assumed, and c has been obtained under the condition of ideal wurtzite, in order to avoid artificial strain effects in the band structure, caused by the underestimation of the lattice parameters given by LDA, in the process of total energy minimization [39]. In Fig. 2.3 we show the calculated GaN and AlN LDA band structures, along the main high symmetry lines of the wurtzite Brillouin zone, as obtained with the code AB INIT. The zero of energy is placed at the top of the valence band. The valence band energies are similar to those computed in previous calculations [158]. In this Reference, the authors have calculated the band structure within the LDA, and then included a refinement by using the more sophisticated GW method. They have reported that the substantial changes as a consequence of improving LDA affect mainly to the conduction bands, and the valence bands are only slightly modified. Therefore, we can safely consider that our LDA description of the valence bands is accurate enough for our purposes. The calculated band gaps are listed in Table 2.2, in comparison with the experimental values and with the theoretical results obtained with the LDA+U approach of Ref. [51]. As it is expected, the band gap is underestimated in both materials. Although these values are still far from the experimental value, they are large enough to prevent a significatively coupling between the conduction and valence bands. In Fig. 2.3 we have drawn with red points some valence band energies, from *ab initio* data of Ref. [158], that show a reasonable agreement with our LDA band structures.

Therefore, it is expected that the improvements that one could achieve with LDA+U or other approaches, will yield a better estimation of the band gap in GaN and AlN but will leave the valence band unaltered. As we will see in Sections 2.2 and 2.3 in the semi-empirical models introduced in this work, the band gap is adjusted by hand to the experimental value. Therefore, for our purposes, the LDA is a suitable approximation in the case of GaN and AlN.

Narrow-gap nitride: InN

As explained above, in the case of InN, the use of LDA completely fails in describing correctly the band structure. Moreover, the consideration of the $4d$ electron

[5]For brevity, we refer throughout this thesis the DFT+LDA calculations simply as LDA calculations.

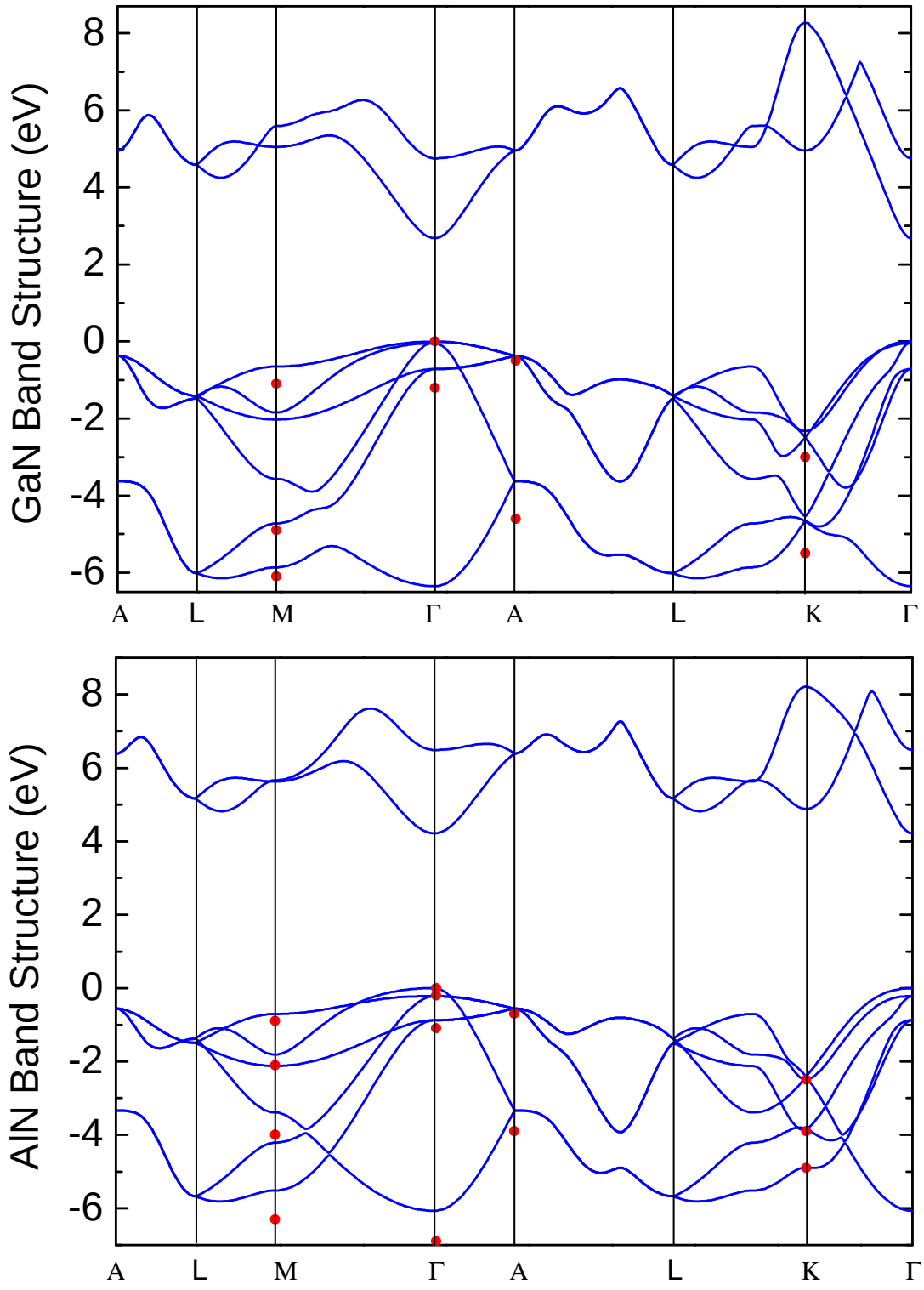

Figure 2.3: *Ab initio* GaN and AlN band structures, calculated within the LDA scheme by means of the AB INIT software. The calculation parameters have been summarized in Table 2.1. The red points are the data from Ref. [158].

Parameters of the calculation			
[1pt]	E_{cut}(Ha)	U (eV)	Mesh in $\boldsymbol{k}$-points
GaN	30.0	-	$6 \times 6 \times 6$
AlN	30.0	-	$6 \times 6 \times 6$
InN	60.0	6.0 (In), 1.5 (N)	$8 \times 8 \times 8$

Table 2.1: Parameters of the *ab initio* calculations of the bulk band structure of III-N compounds.

of indium atoms as valence electrons provides no significant improvement. This deficiency comes from an incorrect description of the Coulomb interaction between the localized d electrons of indium. As a consequence, the semicore $4d$ bands are too high in energy, and the Coulomb repulsion with the nitrogen p-like bands (located at the valence band maximum) is overestimated. This pushes up the valence band maximum, reducing the calculating band gap. In the particular case of InN, the LDA gives null or negative band gap. Some other approaches make use of the fact that d orbitals are strongly localized, and use a hybridized basis of plane waves (in the interstitial distances) and atomic orbitals (in the core region), with the aim of improving the description of such orbitals. This linear augmented plane wave (LAPW) method has been used with some success in In-based wurtzite semiconductors. In the case of InP the *ab initio* band gap is 0.432 eV [159] to be compared with the experimental gap of 1.488 eV [160]. Our choice to overcome the LDA band gap problem, the LDA+U method, that adds to the LDA functional a term, corresponding to the mean-field approximation of the Coulomb interaction, as described above.

The application of the on-site Hubbard U correction, presented in Section 2.1, to the $4d$ indium and $2p$ nitrogen electrons, palliates the problem of the null-band gap [142]. The selected U parameters for indium and nitrogen are listed in Table 2.1. The procedure to determine the U parameter can be consulted in Ref. [161]. Within this computational scheme, the calculated lattice parameters are $a = 3.505$ Å and $c = 5.664$ Å, deviated by only 0.9 % with respect to the experimental values. In Fig. 2.4(a) we have represented the InN band structure as calculated with the LDA+U approach, with the origin of energy placed at the top of the valence band. The red lines highlight the lower conduction band and highest valence band. The calculated band gap value is now 0.34 eV, which improves substantially the value achieved by other LDA+U approaches (0.03 eV in Ref. [51]). Another relevant feature is the valence band width, of value 6.3 eV, very close to the one of 6.4 eV predicted by experiments and by many-body corrections in Ref. [162]. Moreover, we can appreciate the existence of bands with a flat dispersion located around -16 eV. These bands correspond to the d orbitals

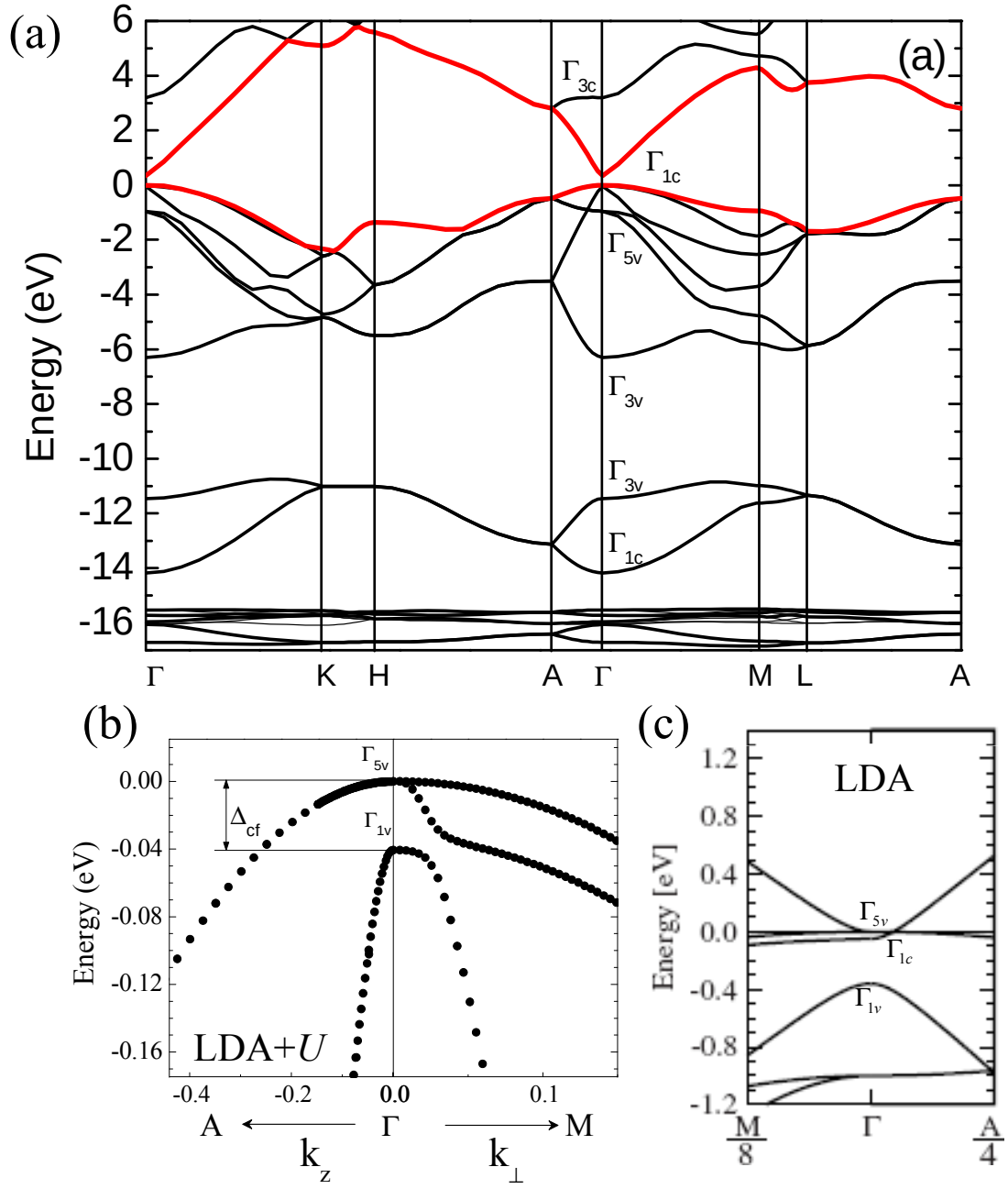

Figure 2.4: (a) InN band structure calculated within the LDA+U scheme. (b) Detail of the valence band structure near the Γ point. (c) InN band structure near the Γ point as calculated with LDA Ref. [39].

Lattice Parameters (Å)			
	Our	Van de Walle [51]	Experimental [20]
a-InN	3.505	3.488	3.548
a-GaN	3.189*	3.152	3.189
a-AlN	3.110*	3.090	3.110
c/a-InN	1.616	1.617	1.612
Bangap (eV)			
	Our	Van de Walle [51]	Experimental [39]
InN	0.34	0.03	0.67
GaN	2.68	2.87	3.5
AlN	4.22	4.41	6.2

Table 2.2: Equilibrium lattice parameters used in the band structure calculations and band gaps of III-N obtained, and compared with other theoretical and experimental data. The asterisk recalls that we have used the experimental a lattice parameters and assumed ideal wurtzite for GaN and AlN.

of the indium, strongly localized in the core. Therefore, the plane wave basis can still reproduce those localized states, although this is at the cost of increase in the energy cutoff (60 Hartree for InN).

From the LDA+U calculation one can confirm that the LDA not only has problems to reproduce a positive band gap, but also that the LDA results for the top of the valence band are not reliable. To illustrate this fact, in Figs. 2.4(b) and (c) we have represented our LDA+U valence bands and the LDA bands calculated in Ref. [39], in the vicinity of the Γ point. The bands are here labeled according to the irreducible representation to which the $\boldsymbol{k} = 0$ states belong. As we have established in Section 1.1, the conduction band and the crystal-field split-off band belong to the representation Γ_1. When the valence band is closer to the conduction band as happens in LDA, both states, that share group symmetry, repel each other, and the valence band is pushed down to lower energies. Therefore, due to null band gap obtained in LDA, Fig. 2.4(c) shows that the crystal-field splitting is largely overestimated, taking a value of around 300 meV, one order of magnitude larger than the experimental measurements, that give the value in the energy range of 15-80 meV [38]. Figure 2.4(b) shows the improvement achieved by our LDA+U scheme in the top of the valence band with respect to the LDA calculation. The separation of the conduction band from the valence band (0.34 eV) leads a reduction of the crystal-field splitting Δ_{cf}, having now a value of 40 meV, within the range of the reported experimental values. In addition, we can see the existence of an anti-crossing between the second and third valence bands, which is absent in the LDA calculations.

As we have seen, the LDA and LDA+U approaches offer a valuable framework to obtain the bulk electronic structure of III-N semiconductors. In the next Sections, the *ab initio* band structures combined with various semi-empirical strategies to obtain the corresponding parameters of each model. We will focus in achieving agreement in the energies and also in the symmetry of the wave functions at the Γ point, which is a crucial requirement for a reliable study of the electronic and optical properties.

2.2 Semi-empirical pseudopotential method in wurtzite semiconductors

In the previous Section, the band structures of III-N semiconductors were derived *ab initio*, by using a plane wave basis within the pseudopotential formulation. Whereas the ionic pseudopotentials (local and nonlocal terms) were chosen by us, the Hartree and exchange-correlation terms must be found self-consistently, within an approach of our choice, such as LDA (for GaN and AlN) or LDA+U (for InN). In order to avoid the self-consistent procedure to determine the contribution of the electron-electron interaction to the potential, V_{KS}, one could try to define a screened ionic pseudopotential, sum of the ionic potential and a contribution combining as much as possible of the electron-electron interactions. This screened pseudopotential could be tried to be written as a function of a set of parameters to be determined by fitting the corresponding band structure to experimental or accurate theoretical data. Once obtained, the screened pseudopotential can be used in further calculations without needing to resort to self-consistent solutions of the KS equations. This methodology is known as the empirical pseudopotential method (EPM) [163]. In this approach, there is no self-consistency and most of the difficulties that arise from the calculations that involve the exchange-correlation terms are avoided. The pseudopotentials are expressed in terms of analytical functions, such as a sum of Gaussian or exponential functions, which reduces significantly the complexity. The elimination of the self-consistent procedure, together with the parametrization of the empirical pseudopotentials, allows the use of a much lower energy cutoff (typically less than 5 Hartree), which decreases substantially the number of required plane waves. In contrast to the DFT-based methods, the computational time is much lower now, and the EPM is therefore apt for calculations of the electronic structure of systems with hundred thousand atoms. This is a non self-consistent approach, and the energy cutoff can be conveniently reduced in order to reduce the basis dimensions. This reduction implies a better applicability

in the calculation of the electronic states of nanostructures [164]. For all these reasons, the EPM has become enormously popular in the calculation of physical properties of nanostructures such as quantum wells, wires and dots [165].

However, a discretional fit of the pseudopotential with respect to the experimental data, as the band gap or the effective masses, is not exempt of problems. For instance, even if the eigenvalues are correctly reproduced, the wave functions may differ from the *exact* ones.[6] Moreover, as the empirical pseudopotentials are obtained for a given crystal configuration, serious doubts about their transferability arise. Thus, the use of empirical pseudopotentials in different environments from those where they were obtained does not guarantee reliable results. For instance, when empirical pseudopotentials generated from a bulk semiconductor *ab initio* calculations, are used in a strained nanostructure, as a self-assembled quantum dot, new parameters are needed to take into account the effects of the strain on the band structure. The same occurs when the crystal structure changes. Thus, if the potential was generated to reproduce the band structure of a wurtzite GaN crystal, it will probably be not useful in a GaN zinc-blende environment [166, 167]. Therefore, it would be desirable to generate transferable empirical pseudopotentials in a manner more consistent and robust, so that the potentials can be used in different environments, such as alloys, or with modified interatomic distances, such as in strained nanostructures without the inclusion of arbitrary additional parameters [168].

L. W. Wang and A. Zunger proposed a methodology to derive such high-quality pseudopotentials from the self-consistent KS potential V_{KS}, and applied it to zinc-blende (Si) and wurtzite (CdSe) structures [169]. In principle, the so-derived pseudopotentials retain to a great degree the information of the Coulomb and exchange-correlation interactions obtained by the DFT calculations. Once determined, these pseudopotentials are used in the same way as in the EPM and with the same advantages. Nevertheless, given the different procedure followed to obtain the pseudopotential, we will use in this case the name semi-empirical pseudopotential method (SEPM), as opposed to the EPM, that purely fits predetermined analytical forms of the pseudopotentials [111]. It is also important to clarify what the term semi-empirical means. We denominate as semi-empirical only the pseudopotential obtained directly from the DFT pseudopotential, considering empirical the pseudopotentials obtained from fitting of the band structure, even if such pseudopotentials include the nonlocal term.

In this thesis we will apply the methodology proposed by Wang and Zunger

[6] The use of the terms *exact* or *true* refers here and in the following to the *ab initio* solutions obtained in Section 2.1.

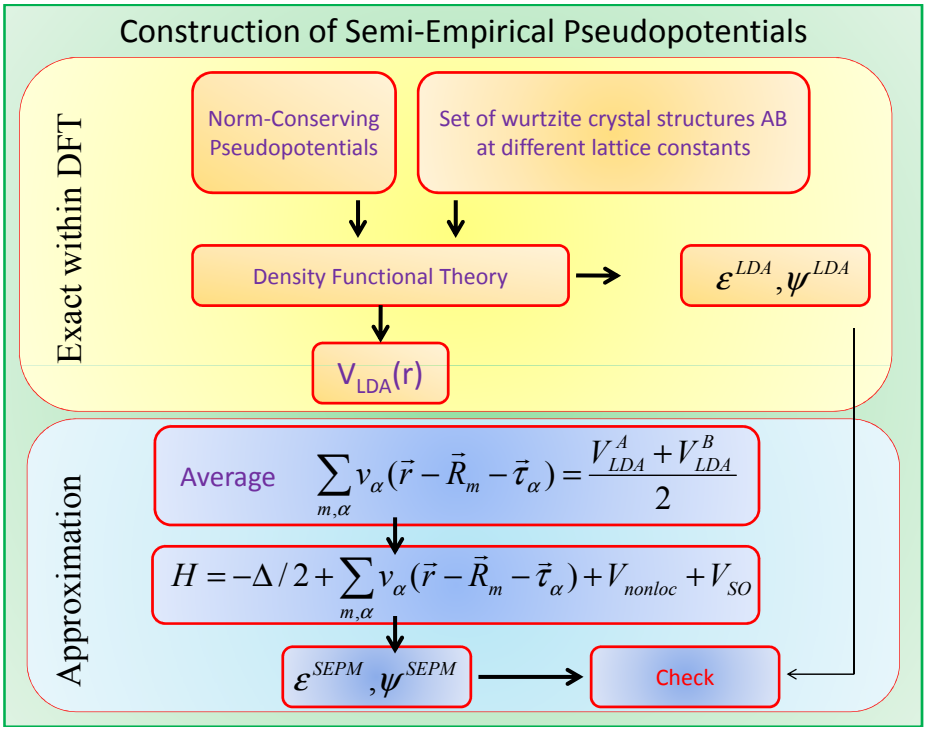

Figure 2.5: Flowchart describing the steps necessary to generate the semi-empirical pseudopotential for two crystal structures A and B at different lattice constants.

[169] to derive suitable semi-empirical pseudopotentials for GaN and AlN semiconductors, focusing on an accurate description of the valence band states in the vicinity of the Γ point. We will also show that with slight modifications in the pseudopotential, the calculated (underestimated by LDA) band gap can be corrected in order to set the experimental band gap. It is worth to mention that this methodology is completely general, and it could be in principle used to obtain semi-empirical pseudopotentials from more sophisticated *ab initio* approaches such as the GW method. In the next Subsections the methodology to obtain the semi-empirical pseudopotentials in wurtzite semiconductors is formulated, and applied to the particular case of GaN and AlN, whose LDA band structures have been reported in Section 2.1. The work presented in this Section has been performed during a research stay in the group of Theory of Semiconductor Nanostructures, lead by Dr. G. Bester, in the Max-Planck-Institut für Festkörperforschung, Stuttgart.

2.2.1 Methodology

In Fig. 2.5 we have composed a flowchart with the necessary steps to obtain the semi-empirical pseudopotentials from the LDA results. The first block is to obtain the band structure of the bulk system at different lattice constants by means of DFT calculations. These calculations were performed in Section 2.1 within the LDA for GaN and AlN, obtaining the eigenvalues and eigenvectors, ε^{LDA} and ψ^{LDA}. The total self-consistent potential is written as follows:

$$V_{\mathrm{KS}}(\boldsymbol{r}) = V_{\mathrm{ps}}(\boldsymbol{r}) + V_{\mathrm{HXC}}(\boldsymbol{r}) = V_{\mathrm{local}}(\boldsymbol{r}) + V_{\mathrm{nonloc}}(\boldsymbol{r}) + V_{\mathrm{HXC}}(\boldsymbol{r}), \tag{2.38}$$

where the V_{ps} is the input non-screened ionic pseudopotential, that we have separated into its local V_{local} and nonlocal V_{nonloc} terms, and the term V_{HXC} includes the Coulomb (Hartree) and exchange-correlation contributions, detailed in Section 2.1. We define the self-consistent local potential

$$V_{\mathrm{LDA}}(\boldsymbol{r}) = V_{\mathrm{local}}(\boldsymbol{r}) + V_{\mathrm{HXC}}(\boldsymbol{r}). \tag{2.39}$$

It has the lattice periodicity and needs therefore to be specified only in a unit cell. The first task of the second block of Fig. 2.5 is to express V_{LDA} in such way that it can be used as if it were an empirical potential, *i. e.*, as a sum of atomic-centered pseudopotentials (not necessarily spherical), to be determined[7]

$$V_{\mathrm{LDA}}(\boldsymbol{r}) = \sum_{m,\alpha} v_\alpha(\boldsymbol{r} - (\boldsymbol{R}_m + \boldsymbol{\tau}_\alpha)), \tag{2.40}$$

where $\boldsymbol{R}_m$ are vectors of the crystal lattice and $\boldsymbol{\tau}_\alpha$ are the basis vectors within the unit cell (see Eqs. (1.2) and (1.4)). These *screened* pseudopotentials v_α contain, additionally to the ionic part, in an average way, the contribution related to the electron-electron interaction, expressed by V_{HXC}. The goal now is to obtain an expression for v_α that we could use them in other environments, as in nanostructures. However, the procedure of obtaining these atomic potentials from the total local potential must be clearly specified and checked for consistency. In the following, we explain how the construction of the screened atomic pseudopotential is carried out.

[7] We use the capital letter V for crystal potentials and the small cap letter v for atomic potentials.

Since the total local potential $V_{\mathrm{LDA}}(\boldsymbol{r})$ is a periodic function, it can be written as a Fourier series in terms of reciprocal lattice vectors

$$V_{\mathrm{LDA}}(\boldsymbol{r}) = \sum_{\boldsymbol{G}} V_{\mathrm{LDA}}(\boldsymbol{G}) e^{i\boldsymbol{G}\cdot\boldsymbol{r}}, \tag{2.41}$$

where

$$\begin{aligned} V_{\mathrm{LDA}}(\boldsymbol{G}) &= \frac{1}{\Omega_c}\int_{\Omega_c} V_{\mathrm{LDA}}(\boldsymbol{r}) e^{-i\boldsymbol{G}\cdot\boldsymbol{r}} d^3\boldsymbol{r} \\ &= \frac{1}{\Omega_c}\int_{\Omega_c} \sum_{m,\alpha} v_\alpha(\boldsymbol{r} - (\boldsymbol{R}_m + \boldsymbol{\tau}_\alpha)) e^{-i\boldsymbol{G}\cdot\boldsymbol{r}} d^3\boldsymbol{r}, \end{aligned} \tag{2.42}$$

Ω_c being the unit cell volume. After some manipulations we obtain the final result

$$V_{\mathrm{LDA}}(\boldsymbol{G}) = \frac{1}{\Omega_c}\sum_{\alpha} e^{-i\boldsymbol{G}\cdot\boldsymbol{\tau}_\alpha} v_\alpha(\boldsymbol{G}), \tag{2.43}$$

with

$$v_\alpha(\boldsymbol{G}) = \int_{\Omega_0} v_\alpha(\boldsymbol{r}') e^{-i\boldsymbol{G}\cdot\boldsymbol{r}'} d^3\boldsymbol{r}', \tag{2.44}$$

where the integral is defined in the atomic volume Ω_0, as consequence of Eq. (2.40) and after Ref. [111].

This general expression can be expressed in a more compact form, in the particular case of the wurtzite structure. In this case there are only two different atomic centered pseudopotentials (although the number of atoms in the unit cell is $n = 4$), corresponding to cation (Ga or Al) and anion (N), labeled as $v_c(\boldsymbol{r})$ and $v_a(\boldsymbol{r})$, respectively. We also define the lattice vectors given by Eq. (1.4) in a more convenient way as a function of the primitive vectors (see Eq. (1.2))

$$\begin{aligned} \boldsymbol{\tau}_{a_1} &= -\frac{1}{6}\boldsymbol{a}_1 + \frac{1}{6}\boldsymbol{a}_2 - \frac{7}{16}\boldsymbol{a}_3 \longrightarrow \boldsymbol{\tau}_a \quad ; \quad \boldsymbol{\tau}_{a_2} = +\frac{1}{6}\boldsymbol{a}_1 - \frac{1}{6}\boldsymbol{a}_2 + \frac{1}{16}\boldsymbol{a}_3 \longrightarrow -\boldsymbol{\tau}_c, \\ \boldsymbol{\tau}_{c_1} &= -\frac{1}{6}\boldsymbol{a}_1 + \frac{1}{6}\boldsymbol{a}_2 - \frac{1}{16}\boldsymbol{a}_3 \longrightarrow \boldsymbol{\tau}_c \quad ; \quad \boldsymbol{\tau}_{c_2} = +\frac{1}{6}\boldsymbol{a}_1 - \frac{1}{6}\boldsymbol{a}_2 + \frac{7}{16}\boldsymbol{a}_3 \longrightarrow -\boldsymbol{\tau}_a. \end{aligned} \tag{2.45}$$

so that $V_{LDA}(\boldsymbol{G})$ can be written as:

$$V_{\mathrm{LDA}}(\boldsymbol{G}) = \frac{1}{\Omega_c}\left(e^{-i\boldsymbol{G}\cdot\boldsymbol{\tau}_a} v_a(\boldsymbol{G}) + e^{-i\boldsymbol{G}\cdot\boldsymbol{\tau}_c} v_c(\boldsymbol{G}) + e^{i\boldsymbol{G}\cdot\boldsymbol{\tau}_c} v_a(\boldsymbol{G}) + e^{i\boldsymbol{G}\cdot\boldsymbol{\tau}_a} v_c(\boldsymbol{G})\right). \tag{2.46}$$

We define now the symmetric (v_+) and antisymmetric (v_-) pseudopotentials as:

$$v_+(\boldsymbol{G}) = v_a(\boldsymbol{G}) + v_c(\boldsymbol{G}) \quad ; \quad v_-(\boldsymbol{G}) = v_a(\boldsymbol{G}) - v_c(\boldsymbol{G}), \tag{2.47}$$

and $V_{LDA}(\boldsymbol{G})$ can be finally expressed as:

$$\begin{aligned} V_{\mathrm{LDA}}(\boldsymbol{G}) = & \quad \frac{1}{\Omega_c} v_+(\boldsymbol{G}) \left[\cos\left(\boldsymbol{\tau}_a \cdot \boldsymbol{G}\right) + \cos\left(\boldsymbol{\tau}_c \cdot \boldsymbol{G}\right)\right] \\ & + \quad i\frac{1}{\Omega_c} v_-(\boldsymbol{G}) \left[\sin\left(\boldsymbol{\tau}_c \cdot \boldsymbol{G}\right) - \sin\left(\boldsymbol{\tau}_a \cdot \boldsymbol{G}\right)\right]. \end{aligned} \tag{2.48}$$

Since $v_{a/c}$ have inversion symmetry, $v_{+/-}$ are real, and they can be written in terms of the real and imaginary parts of $V_{\mathrm{LDA}}(\boldsymbol{G})$

$$\begin{aligned} v_+(\boldsymbol{G}) = & \quad \frac{\Omega_c}{\cos\left(\boldsymbol{\tau}_a \cdot \boldsymbol{G}\right) + \cos\left(\boldsymbol{\tau}_c \cdot \boldsymbol{G}\right)} \Re\{V_{\mathrm{LDA}}(\boldsymbol{G})\}, \\ v_-(\boldsymbol{G}) = & \quad \frac{\Omega_c}{\sin\left(\boldsymbol{\tau}_c \cdot \boldsymbol{G}\right) - \sin\left(\boldsymbol{\tau}_a \cdot \boldsymbol{G}\right)} \Im\{V_{\mathrm{LDA}}(\boldsymbol{G})\}. \end{aligned} \tag{2.49}$$

Once $v_{+/-}$ are obtained, the reciprocal-space atomic pseudopotentials $v_{a/c}$ are obtained by inverting Eq. (2.47).

So far, the procedure to obtain $v_{a/c}(\boldsymbol{G})$ is exact. However, we assume now that $v_a(\boldsymbol{G})$ and $v_c(\boldsymbol{G})$ are well represented by their spherically averaged counterparts $v_a(q)$ and $v_c(q)$, with $q = |\boldsymbol{G}|$. This approximation allows us to write the pseudopotentials as a manageable simple one-dimensional function.

Figures 2.6(a) and 2.6(b) show the LDA results (symbols) for v_+ and v_-, respectively, corresponding to GaN. Figure 2.6(c) shows the corresponding v_+ and v_- results for AlN. In order to have a better definition of the pseudopotential, we have done LDA calculations for several lattice constants, obtaining a large number of $\boldsymbol{G}$ points. In the case of GaN, we have obtained the five structures by changing the a lattice constant. In the case of AlN, we have reduced the number of computed structures to two, observing the same features as in the case of GaN. Observe that the pseudopotentials v_+ and v_- from different unit cell volume fall over the same line, and only there is only some slight dispersion in the data around $q = 2\ \mathrm{Bohr}^{-1}$ in v_+ of GaN. In principle, this proves that the spherical pseudopotentials are independent of the atom stacking, and justifies their atomic origin. Concerning

the pseudopotentials at $\boldsymbol{G} = 0$, $v_{+/-}(\boldsymbol{G} = 0)$, their values are arbitrary, and the variation of $v_+(\boldsymbol{G} = 0)$ produces a overall shift of the band structure. The value of $v_+(\boldsymbol{G} = 0)$ can be fixed to the electron affinity (see Section 2.1) deduced from experimental data [170] or obtained from *ab initio*. Neither the value $v_-(\boldsymbol{G} = 0)$ has relevant effects in the band structure as long as one fixes correctly the rest of the points. Moreover, in regions of small q ($\lesssim 2.5$ Bohr^{-1}), the changes in the pseudopotentials v_+ and v_- do not affect substantially the band structure, which also happens for the pseudopotentials v_a and v_c. In all the cases we have performed a fitting with spline functions, represented with lines. In regions of large q (> 12 Bohr^{-1}), small oscillations persist, requiring a careful fitting. Both curves prove that $v_{+/-}(q)$ seem to fall on a nearly unique curve.

The fact that the pseudopotentials follow a single curve suggests that an hypothetical strain of the system could be taken into account by just rescaling the interatomic distances without modifying the pseudopotentials. In the purely empirical pseudopotential method [163], the strain effects on the electronic states are usually introduced by adding a Gaussian potential. The parameters of the Gaussian are deduced from the deformation potentials [171]. Therefore, the semi-empirical pseudopotentials obtained here introduce an improvement to the method, by relieving it of further fitting parameters [172].

By inverting Eq. (2.47), the screened atomic pseudopotentials v_a and v_c can be derived. We have represented them in Fig. 2.7 for gallium, aluminium and nitrogen. Concerning the general behavior of the pseudopotential curves, the oscillations persist until large range ($q \approx 10$ Bohr^{-1}), which determines the energy cutoff in the subsequent calculations. Note that we have calculated the nitrogen pseudopotentials in the environments of GaN and AlN (the difference among them is the black dotted line). For $q > 1$ Bohr^{-1}, they are almost identical with the exception of a slight deviation around $q \sim 3$ Bohr^{-1}. Their disagreement ofr $q < 1$ Bohr^{-1} is due to the different electron affinity of GaN and AlN. However, those differences near $q = 0$ only affects the origin of the energies, but not the band structure. This is a another proof of the atomic nature of the obtained pseudopotentials, as we have indicated before. Even after adding the Coulomb interaction and the exchange-correlation information, that are supposed to be different in both semiconductors, the derived pseudopotentials keep the atomic flavor. This is important in connection with the *tranferability* of the pseudopotentials for their use in other systems.

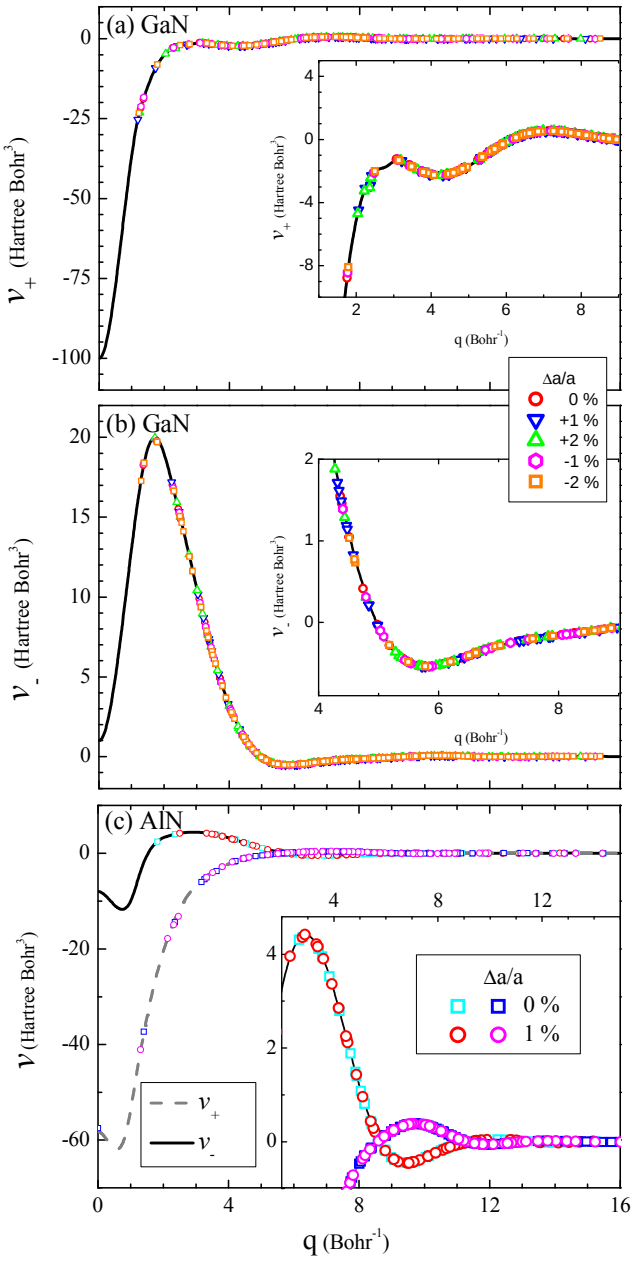

Figure 2.6: The LDA-derived contributions v_+ and v_- for GaN, (a) and (b), and AlN, (c), as defined in Eq. (2.49). We have calculated five structures in the case of GaN, and two structures for AlN, varying the lattice constant a as indicated in the legends. The ratio of the lattice constants c/a is kept the same (equal to the ideal value) in all the cases. The lines represent the fitting with splines functions.

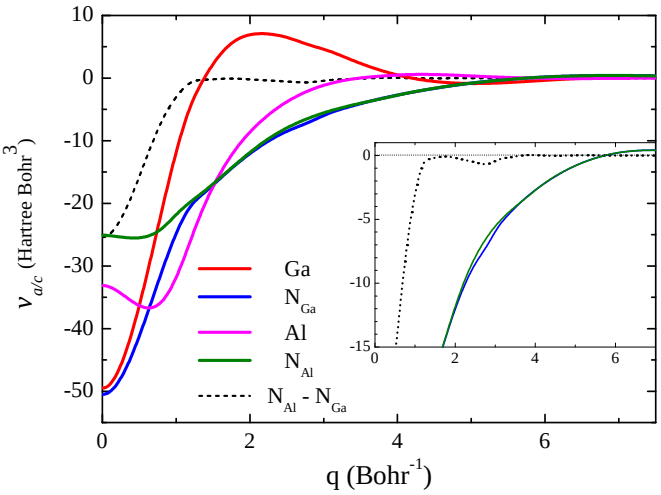

Figure 2.7: Screened atomic pseudopotentials v_a(N) and v_c(Ga or Al) obtained from the DFT-LDA calculations of the self-consistent crystal potential of GaN and AlN: Ga (red), N_{Ga} (blue), Al (magenta), and N_{Al} (green). The dashed black line is $v_{N(Al)} - v_{N(Ga)}$.

2.2.2 Calculations of the nonlocal potentials and spin-orbit interaction

Once the local part of the atomic pseudopotentials has been derived, it remains to recalculate the associated nonlocal part following the steps sketched in the flowchart of Fig. 2.5. We rewrite the nonlocal term of Eq. (2.37), given elsewhere [173, 174]:

$$V_{\text{nonloc}}(\boldsymbol{r}) = \sum_{\alpha} \sum_{l,m} |P_{l,m}(\boldsymbol{\tau}_\alpha)\rangle v_{\text{nonloc,l}}(|\boldsymbol{r} - \boldsymbol{\tau}_\alpha|)\langle P_{l,m}(\boldsymbol{\tau}_\alpha)|. \tag{2.50}$$

Here (l, m) denotes angular momentum, $v_{\text{nonloc,l}}$ is the lth angular momentum pseudopotential, and $|P_{lm}(\boldsymbol{\tau}_\alpha)\rangle$ is a projection function centered at the atomic site $\boldsymbol{\tau}_\alpha$. The nonlocal term is commonly calculated by the Kleinman-Bylander method [151], that scales as $\sim M^2$, where M is the size of the system. Another approach is the real-space implementation proposed by King-Smith *et. al.* [175]. We use here a method known as the *small box* implementation, that scales linearly with the system size, and has a simpler formulation. The interested reader can find a more detailed explanation in Ref. [169].

Furthermore, the nonlocal part of the pseudopotentials can be redefined in order to achieve a rigid shift of the conduction band with respect to the valence, which gives a mechanism to open the band gap up to the experimental value [176].

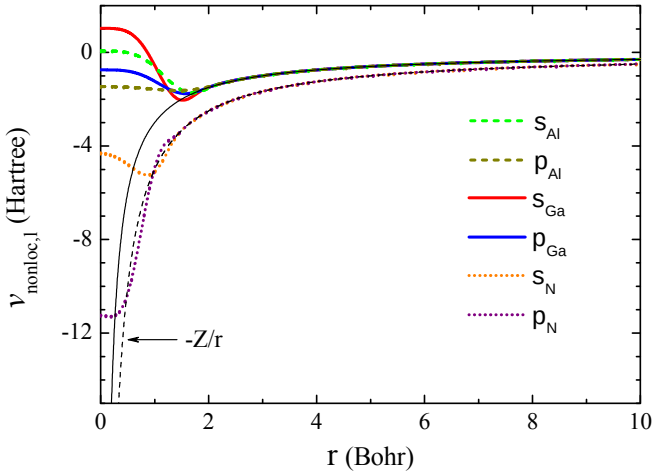

Figure 2.8: Nonlocal contributions to the atomic pseudopotential of: Ga (solid lines), Al (dashed lines) and N(dotted lines); in all the cases the s and p-orbital contribution are represented.

In Subsection 2.2.3, we apply such a slight modification to some selected nonlocal potentials, so as to force the SEPM calculation of the GaN bulk band structure to reproduce the experimental band gap. In Fig. 2.8 we present the nonlocal potentials, $v_{\mathrm{nonloc,l}}$, employed in this work, of Ga, Al and N. The bare Coulomb potentials are represented with the thin black lines, with $Z = 3$ for gallium and aluminium, and $Z = 5$ for nitrogen.

It is straightforward to incorporate at this level the spin-orbit interaction by means of the following potential:

$$V_{SO}(\boldsymbol{r}) = \sum_{\alpha} \sum_{l,m} V_l^{SO}(|\boldsymbol{r} - \boldsymbol{\tau}_\alpha|)|P_{l,m}(\boldsymbol{\tau}_\alpha)\rangle \boldsymbol{L} \cdot \boldsymbol{S} \langle P_{l,m}(\boldsymbol{\tau}_\alpha)|. \tag{2.51}$$

The notation for the angular momentum and projectors is the same as in Eq. (2.50), but now with the introduction of the spin operator $\boldsymbol{S}$ whose components are given by Pauli matrices, and $V_l^{SO}(r)$ is a potential describing the spin-orbit interaction. We have set its functional form to a Gaussian and only the effect on p states (with $l = 1$) has been included. In this way, we reduce the spin-orbit interaction to one parameter for every type of atom [177]. As the spin-orbit interaction is a relativistic effect, we apply it only to gallium and aluminium, much heavier than nitrogen.

The next step of the flowchart in Fig. 2.5 is the resolution of the KS equation 2.5, where the Kohn-Sham potential V_{KS} (eq. (2.10)) is replaced by the screened pseudopotentials calculated above and the nonlocal term:

$$V_{\mathrm{KS}}(\boldsymbol{r}) \quad \longrightarrow \quad \sum_{m,\alpha} v_\alpha(\boldsymbol{r} - \mathrm{R_m} - \tau_\alpha) + \mathrm{V_{nonloc}(r)}. \tag{2.52}$$

The Schrödinger equation in the semi-empirical method, taking into account the spin-orbit interaction, is written as follows:

$$\left\{ -\frac{1}{2}\nabla^2 + \sum_{m,\alpha} v_\alpha(\boldsymbol{r} - \mathrm{R_m} - \tau_\alpha) + \mathrm{V_{nonloc}(r)} + \mathrm{V_{SO}(r)} \right\} \tilde{\psi}_i(\boldsymbol{r}) = \tilde{\varepsilon}_i \tilde{\psi}_i(\boldsymbol{r}). \tag{2.53}$$

This Hamiltonian matrix requires to be solved only once for each given problem, as there is no need to achieve self-consistency, which reduces considerably the computation times. The eigenvalues and eigenvectors obtained by the SEPM Schrödinger equation, $\tilde{\varepsilon}$ and $\tilde{\psi}$, should be compared with their LDA counterparts, in order to verify the accuracy of our method. This is the last step of the flowchart of Fig. 2.5. We devote the next subsections to test the validity of our semi-empirical pseudopotentials and to correct the LDA underestimation of the band gap in bulk GaN and AlN. Also we define an optimal energy cutoff, that will be used in nanostructures calculations.

2.2.3 Band structure of GaN without spin-orbit interaction

Once the methodology is well established, we proceed to the comparison of the SEPM band structure with the LDA calculations. As the spin-orbit interaction only produces small splittings in GaN, we have neglected this interaction for the overall band structure comparison, but it will be introduced later on, once the validity of the SEPM has been demonstrated. The effects on the band structures caused by a reduction of the energy cutoff will also be analyzed. In Fig. 2.9 we have represented together the following GaN band structures: the same LDA results already shown in Fig. 2.3 (black solid lines), the SEPM band structure with E_{cut} = 90 Ry, 90-SEPM (red points), and the SEPM band structure with E_{cut} = 30 Ry, 30-SEPM (green dashed lines). In order to help in the discussion,

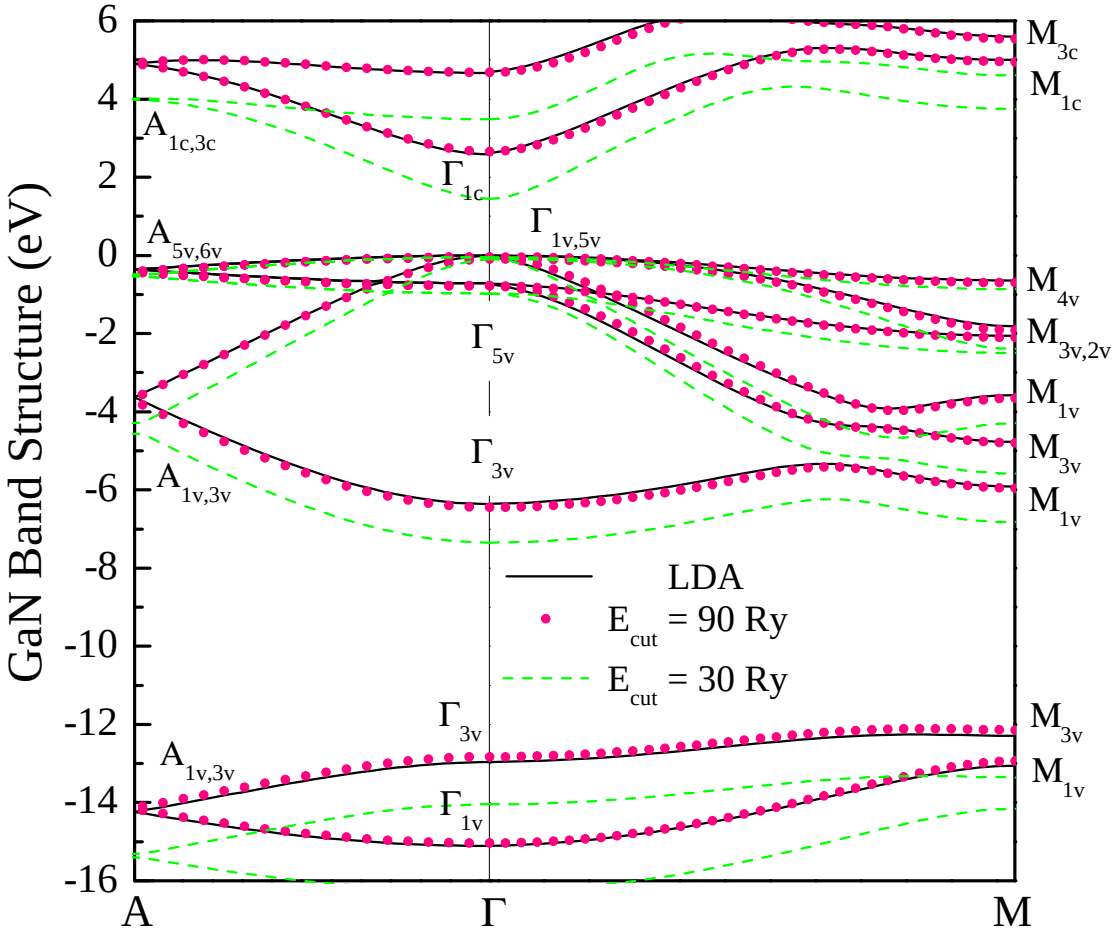

Figure 2.9: GaN band structure calculated with LDA (solid lines), and with the SEPM for two different cutoffs: $E_{\text{cut}} = 90$ Ry (points) and $E_{\text{cut}} = 30$ Ry (dashed lines).

the group represenation labels at the Brillouin zone points Γ, A, and M have been added [158].

The first conclusion is that the LDA and the 90-SEPM band structures have a nearly perfect coincidence for all bands and throughout the Brillouin zone. This definitely proves the validity of the spherical average assumed for $v_a(q)$ and $v_c(q)$ explained above. Usually, the EPM needs many parameters to obtain such a good agreement with *ab initio* band structures through whole Brillouin zone. This discretional addition of parameters makes those models less transferable to other environments. Hereby, only careful fitting the screened pseudopotential curves of Fig. 2.6, a perfect matching between LDA and SEPM method has been achieved.

However, the high cutoff implies a larger number of plane waves. Thinking in the applications to nanostructures, where thousands of atoms are involved,

it is desirable to set this cutoff as small as possible. The 30-SEPM GaN band structure shows the effects of fixing smaller energy cutoff. The main effect is a rigid displacement of the conduction bands towards the valence bands, reducing the band gap approximately by 1 eV. The same shift is appreciated for the states $A_{1c,3c}$ and $M_{1c,3c}$. The valence band states more affected by the reduction of E_{cut} are those belonging to the representations $\Gamma_1, \Gamma_3, A_1, A_3, M_1, M_3$, being less affected the states belonging to Γ_5, A_5, A_6, M_4. The topmost valence band states remain almost unaltered, and in both cases the topmost valence band state belongs to the representation Γ_5, in agreement with the *ab initio* band structure. It is also important that the curvature of the bands is not substantially changed.

The underestimation of the band gap is therefore enhanced if the energy cutoff is reduced. In the SEPM one can correct this problem easily, since the multiplication of the local potentials by a Gaussian function, can serve to open the band gap up to the experimental value. An alternative is an adequate renormalization of the nonlocal pseudopotentials [169]. In this work, always with the aim of using the smaller possible number of parameters, we have chosen this last possibility.

In Fig. 2.10 the 30-SEPM band structure of Fig. 2.9 has been represented again (here labeled as unshifted), together with the shifted 30-SEPM band structure resulting from a slight re-normalization of nonlocal potentials of momentum $l = 0$. For comparison, the reference LDA band structure is also shown. The band gap opening does not influence significatively the valence band curvatures, although a slight modification is appreciated in the vicinity of the Γ point, which produces an even better agreement with the LDA bands.

The conduction band is rigidly moved to higher energies. Its curvature varies as expected beyond the LDA results, so as to obtain the experimental band gap due to the decreased coupling with the valence bands. Energy cutoffs lower than 30 Ry have also been checked, but the changes in the band structure exceed the admissible margin.

As important as the agreement of the energies is the reproduction of the correct symmetry of the wave functions. On the right hand of Fig. 2.10 we show the projections of the charge density on the plane (0001).[8] As required by group theory (see Table 1.2), the states Γ_5 must have a charge density reminiscent of the p_x-p_y orbitals, and this is confirmed by our calculations in Fig. 2.10. On the other hand, the state Γ_1 has the charge density distributed with p_z symmetry. We conclude

[8] This projection is defined as: For a position vector written in terms of the primitive vectors, $\boldsymbol{r} = x\boldsymbol{a}_1 + y\boldsymbol{a}_2 + z\boldsymbol{a}_3$, $\rho(x,y) = \frac{1}{c}\int_0^1 |\psi(\boldsymbol{r})|^2 dz$. Analogously, the projection on the plane $(1\bar{1}00)$ is: $\rho(y,z) = \frac{1}{a}\int_0^1 |\psi(\boldsymbol{r})|^2 dx$.

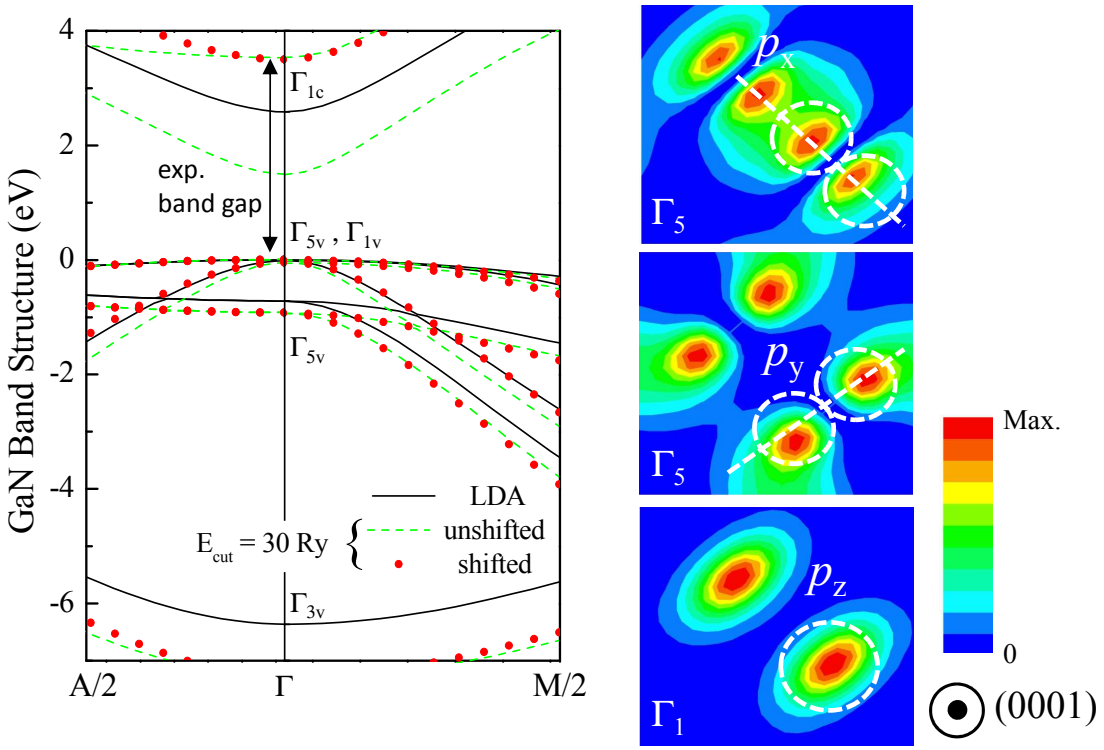

Figure 2.10: Left: SEP GaN band structure calculated with E_{cut} = 30 Ry versus LDA band structure. Right: Charge density of the states Γ_{5v} (4-fold degenerate) and Γ_{1v} (2-fold degenerate) projected on the (0001) plane.

that the action of reducing the cutoff energy, together with the correction of the band gap does not alter essentially the valence band structure, and in particular, conserves the symmetry of the states as required by group theory and obtained by the LDA calculations.

2.2.4 GaN and AlN band structure with spin-orbit interaction

Once the energy cutoff has been set and the band gap has been opened, the spin-orbit interaction can be added to our calculations [111], as explained in Subsection 2.2.2.

The corresponding valence bands in the vicinity of the Γ point of GaN and AlN have been represented in Fig. 2.11. Concerning the band dispersion, a zero-field Dresselhaus spin splitting is also observed for increasing values of the momentum vector $\boldsymbol{k}$ toward M point [178, 179]. This effect is too small to be observed in

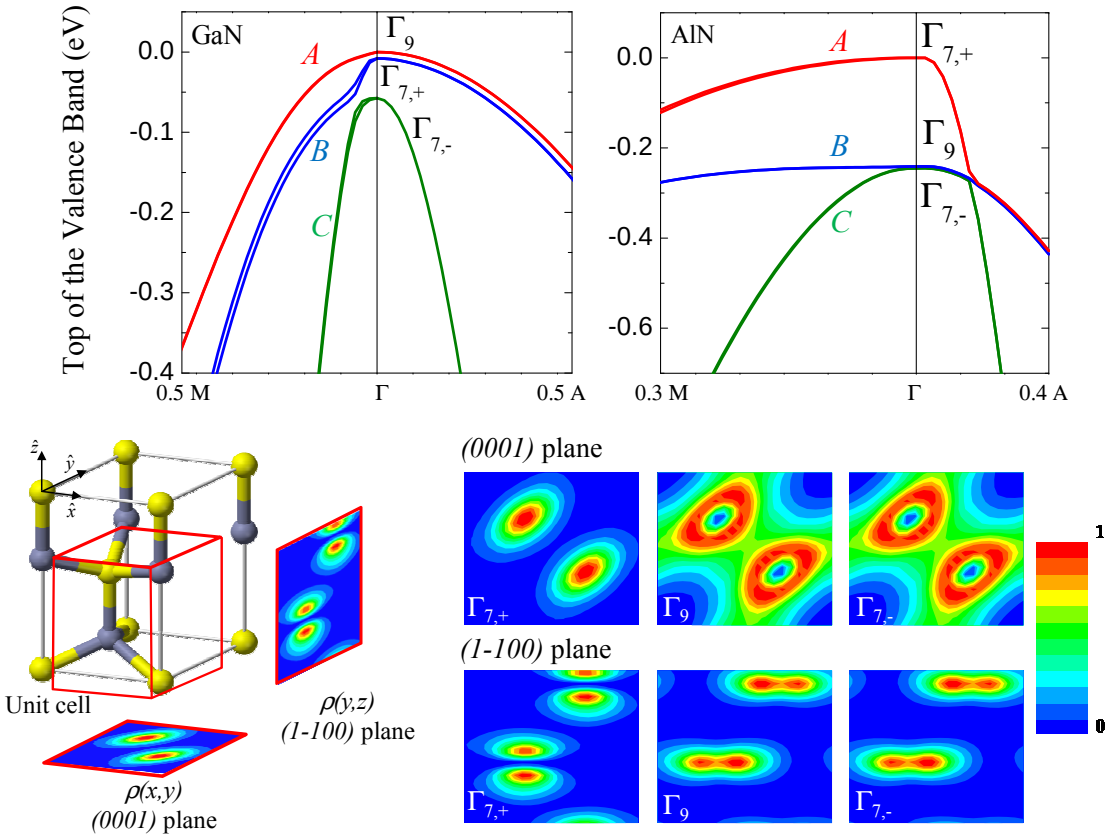

Figure 2.11: Valence band structure of GaN and AlN as calculated with the shifted 30-SEPM including the spin-orbit interaction. The lower part displays the projections of the charge density of the states Γ_7 and Γ_9 of AlN.

the bands of AlN. As it is sketched in Fig. 1.5 of Chapter 1, the states Γ_5 and Γ_1 split under spin-orbit interaction into Γ_9, $\Gamma_{7,+}$ and $\Gamma_{7,-}$. The ordering of these new valence band states is different in GaN and AlN. In the case of GaN, the sequence is Γ_9-$\Gamma_{7,+}$-$\Gamma_{7,-}$, and for AlN, $\Gamma_{7,+}$-Γ_9-$\Gamma_{7,-}$, as a consequence of its negative crystal-field parameter ($\Delta_{cf}(\mathrm{AlN}) < 0$). This change in the ordering is illustrated with the charge density of the wave functions drawn in Fig. 2.11, with the charge density of the states $\Gamma_{7,+}$-Γ_9-$\Gamma_{7,-}$ of AlN, projected on the planes (0001) and $(1\bar{1}00)$. The topmost state, $\Gamma_{7,+}$, separated 245 meV from the next states, Γ_9 and $\Gamma_{7,-}$, has p_z symmetry.

The splittings of the top of the valence band, the band gap, and the conduction and valence band effective masses are reported in Table 2.3, together with other available data. Although the band gaps and the conduction effective masses have a rather well established value, it is important to note the dispersion of the experimental values for the splitting parameters Δ_{cf} and Δ_{so}. These values are difficult

to access experimentally, and even the *ab initio* calculations are still uncertain, so that these values a provisional status even within an accepted range of energies.

In conclusion, we have demonstrated in this Section the quality of the LDA-derived semi-empirical pseudopotentials, and have compared the corresponding results with LDA calculations and experimental data for bulk GaN and AlN. The SEPM will be used in Chapter 3 for the calculation of the electronic structure of GaN nanowires.

	Parameter	SEPM	*Ab initio*	EPM	Experimental
AlN	Δ_{cf} (meV)	-245	-295^a	-199^c, -128^d	-230^e
	Δ_{so} (meV)	5	-	-	5-20^e
	E_g (eV)	6.2	6.47^a	6.2^c	6.2^e
	m_z^c	0.435	0.32^a, 0.427^b	0.232^d	0.29-0.45^f
	$m_\perp^c$	0.484	0.30^a, 0.465^b	0.242^d	0.29-0.45^f
	m_z^A	0.264	-	-	-
	$m_\perp^A$	8.876	-	-	-
	m_z^B	2.511	-	-	-
	$m_\perp^B$	1.143	-	-	-
	m_z^C	2.465	-	-	-
	$m_\perp^C$	1.143	-	-	-
GaN	Δ_{cf} (meV)	49	34^a	42^c,43^d	9-38^e
	Δ_{so} (meV)	8	-	-	8-20^e
	E_g (eV)	3.5	3.24^a	3.5^d	3.5^e
	m_z^c	0.210	0.190^a, 0.189^b	0.138^d	0.20^e
	$m_\perp^c$	0.239	0.210^a, 0.221^b	0.150^d	0.20^e
	m_z^A	2.110	-	-	-
	$m_\perp^A$	0.598	-	-	-
	m_z^B	1.640	-	-	-
	$m_\perp^B$	0.526	-	-	-
	m_z^C	0.025	-	-	-
	$m_\perp^C$	3.890	-	-	-

Table 2.3: Band parameters of AlN and GaN, as calculated with the SEPM, and compared with other available data of: (a) Ref. [39], (b) Ref. [180], (c) Ref. [167], (d) Ref. [181], (e) Ref. [19, 36, 37], and (f) Ref. [182].

2.3 The tight-binding method

In the previous Sections we have explained in detail the use of the plane wave pseudopotential method. The tight-binding (TB) method implies a radical change in the philosophy of the electronic structure calculations as exposed so far. Contrary to the plane wave pseudopotential method, where the electrons are modeled as nearly free particles, with their wave function expanded as a linear combination of plane waves, the tight-binding method is founded on the opposite. In the first place, the tight-binding method assumes that the valence electrons are tightly bound to their nuclei. It is then reasonable to approximate the electron wave function in the solid as a linear combination of atomic-like wave functions (atomic orbitals) [104]. In covalent materials, there are two kinds of electron states, the conduction band and the valence band states. The valence band states are concentrated in the covalent bonds and retain more of the atomic character than the delocalized conduction band states. In principle, the tight-binding method should give a very accurate description of the valence bands. Moreover, the interaction is now coded into the Hamiltonian matrix elements between neighboring atomic-like states. Thus, the band structure is represented in terms of a small set of overlap parameters. In the following we illustrate the formulation of the tight-binding approach for the wurtzite bulk crystal.

2.3.1 The tight-binding method in wurtzite crystals

Let us consider the atomic orbitals $\varphi_l(\boldsymbol{r} - \boldsymbol{r}_{m,\alpha})$ centered at the atomic site

$$\boldsymbol{r}_{m,\alpha} = \boldsymbol{R}_m + \boldsymbol{\tau}_\alpha, \tag{2.54}$$

where $\boldsymbol{R}_m$ is the lattice vector, and $\boldsymbol{\tau}_\alpha$ is the position of the atom α within the unit cell. For such orbital, a Bloch-like function can be constructed, as follows:

$$\Phi_{\boldsymbol{k}}^{\alpha,l}(\boldsymbol{r}) = \frac{1}{\sqrt{N}} \sum_m e^{i\boldsymbol{k}\cdot\boldsymbol{r}_{m,\alpha}} \varphi_l(\boldsymbol{r} - \boldsymbol{r}_{m,\alpha}), \tag{2.55}$$

where N is the number of unit cells in the crystal, and $\boldsymbol{k}$ the wave vector. The sought wave function Ψ is written as a linear combination of the Bloch functions

$$\Psi_{\boldsymbol{k}}(\boldsymbol{r}) = \sum_{\alpha,l} A_{\alpha,l}(\boldsymbol{k}) \Phi_{\boldsymbol{k}}^{\alpha,l}(\boldsymbol{r}). \tag{2.56}$$

In order to obtain the eigenvalues and eigenvectors of the system, we let the crystal Hamiltonian $\mathcal{H}$ to act on $\Psi_{\boldsymbol{k}}(\boldsymbol{r})$, and multiply by the left with a Bloch function

$$\langle \Phi_{\boldsymbol{k}}^{\alpha',l'} | \mathcal{H} | \Psi_{\boldsymbol{k}} \rangle = E(\boldsymbol{k}) \langle \Phi_{\boldsymbol{k}}^{\alpha',l'} | \Psi_{\boldsymbol{k}} \rangle. \tag{2.57}$$

At this point we assume the orthogonality of the Bloch functions for different orbitals and/or different atoms is desirable. Instead of the usual atomic orbitals, we use here the Löwdin basis, constructed formally to guarantee that the orbitals centered on different atoms are orthogonal to each other [183]. The eigenvalue equation in the Löwdin basis is written as follows:

$$\sum_{\alpha,l} H(\alpha',l';\alpha,l) A_{\alpha,l}(\boldsymbol{k}) = E(\boldsymbol{k}) A_{\alpha',l'}(\boldsymbol{k}). \tag{2.58}$$

The Hamiltonian matrix elements are:

$$\begin{aligned} H(\alpha',l';\alpha,l) &= \frac{1}{N} \sum_{m',m} e^{i\boldsymbol{k}\cdot(\boldsymbol{r}_{m,\alpha} - \boldsymbol{r}_{m',\alpha'})} \langle \varphi_{l'}(\boldsymbol{r} - \boldsymbol{r}_{m',\alpha'}) | H | \varphi_l(\boldsymbol{r} - \boldsymbol{r}_{m,\alpha}) \rangle \\ &= \sum_{m} e^{i\boldsymbol{k}\cdot(\boldsymbol{R}_m + \boldsymbol{\tau}_\alpha - \boldsymbol{\tau}_{\alpha'})} \langle \varphi_{l'}(\boldsymbol{r} - \boldsymbol{r}_{m',\alpha'}) | H | \varphi_l(\boldsymbol{r} - \boldsymbol{r}_{m,\alpha}) \rangle \end{aligned} \tag{2.59}$$

The problem is completely determined at this stage, with the exception of the value of the integrals $\langle \varphi_{l',\alpha'} | H | \varphi_{l,\alpha} \rangle$.[9] These integrals represent the overlap, mediated by the Hamiltonian, between the atomic orbitals. The tight-binding method convert these integrals into empirical parameters, and assumes that the relevant electron-electron and electron-ion interactions are included in the parameters. How to determine such parameters will be discussed later. However, some fundamental approximations can be introduced beforehand to reduce the number of independent matrix elements. We enumerate these approximations in the following:

1. The crystal Hamiltonian can be expressed, to a good approximation, as a sum of centered atomic potentials, V_β. The integral discussed above is then

$$\langle \varphi_{l',\alpha'} | H | \varphi_{l,\alpha} \rangle = \langle \varphi_{l',\alpha'} | \sum_{\beta} V_\beta | \varphi_{l,\alpha} \rangle, \tag{2.60}$$

[9] In the following, we adopt this abbreviated notation for the orbitals: $\varphi_{l,\alpha} \equiv \varphi_l(\boldsymbol{r} - \boldsymbol{r}_{m,\alpha})$.

the sum $\sum_\beta$ run over all the atoms. The first approximation is to keep only two-center integrals, that only involve potentials due to atoms $\beta = \alpha$ and $\beta = \alpha'$ [112].

The two-center approximation allows to classify the overlap integrals into two classes; on-site elements, $E_{\alpha,l}$, and overlap parameters, $V_{\alpha,l,\alpha',l'}$. The on-site elements are the energies of the orbital l of the atom α. These energies should in principle be related to the atomic energies of the isolated atom. However, the crystal environment modifies these values. The other terms, $V_{\alpha,l,\alpha',l'}$, take account of the overlap between two orbitals, l and l', of the atoms α and α'.

2. The overlap parameters $V_{\alpha,l,\alpha',l'}$ are considered only up to nearest neighbors (nn), and the Hamiltonian matrix elements are

$$H(\alpha', l'; \alpha, l) = \sum_m^{\text{nn}} \langle \varphi_{l',\alpha'} | H | \varphi_{l,\alpha} \rangle e^{i\boldsymbol{k}\cdot(\boldsymbol{R}_m + \boldsymbol{\tau}_\alpha - \boldsymbol{\tau}_{\alpha'})}. \tag{2.61}$$

Considering the approximations proposed here, the matrix elements can be of two types:

$$\begin{aligned} H(\alpha, l; \alpha, l) =& E_{\alpha,l}, \\ H(\alpha', l'; \alpha, l) =& \sum_m^{nn} V_{\alpha',l',\alpha,l} e^{i\boldsymbol{k}\cdot(\boldsymbol{R}_m + \boldsymbol{\tau}_\alpha - \boldsymbol{\tau}_{\alpha'})}. \end{aligned} \tag{2.62}$$

Although the applied approximations have reduced the problem enormously, one can make a further reduction by using symmetry considerations, and express the overlap terms as a function of a minimal set of parameters, depending on the choice of the basis (number and type of atomic orbitals per atom).

The choice of the basis deserves a careful discussion to justify the adequacy of our selection. In principle, a larger basis may offer more accurate results for the same system than a smaller basis. However, it also implies the addition of more and more parameters, which makes difficult the interpretation of the results, and it does not always imply an improvement of the band structure [184–186]. Moreover, the increase of the basis requires more computational effort when the method is applied to nanostructures. In the literature, one can find tight-binding models that use a minimal basis that only takes account a s orbital of the cation (group III element, in our case) and three p orbitals of the nitrogen (anion), also

called $s_c p_a^3$ basis (four parameters). This model seems to give reliable results for the confined states of GaN/AlN zinc-blende quantum dots [187]. However, a small size basis could be insufficient to reproduce accurately the band structure far from the Γ point. In the other extreme, there is a parametrization by J. M. Jancu *et. al.* [188], with a large basis of 20 orbitals $sp^3d^5s^\star$ considering the $3d$ orbitals of gallium and spin-orbit interaction, and applied to solve the band structure of wurtzite bulk GaN and AlN. This basis assures a precise result for the band structure along the whole Brillouin zone, but it needs a lot of information for the parametrization. A more refined parametrization, extending the interaction to second neighbors, as in Ref. [189], has been used for calculations of bulk GaN, InN and their alloys, considering also the $4d$ orbitals of the indium atoms. The disadvantage of these large bases is additionally the large number of parameters (more than 40) that involves, and the prohibitive increase in the computational requirements when applied in nanostructure calculations. Although an accurate description of the whole band structure is always desired, in nanostructure applications, there must be a compromise between the accuracy and the computational cost. Furthermore, the optical properties of direct band gap semiconductors as measured in the majority of the experiments, are related only to the bands in the vicinity of the Γ point.

Considering all these arguments, we have decided to use an sp^3 basis, including spin-orbit interaction [190]. This basis gives a good description of the band structure near the Γ point, and reproduces reasonably well the other bands. On the other hand, the number of parameters (10) is much smaller than in the $sp^3d^5s^\star$ method, providing an intuitive physical picture. We omit the addition of the excited orbital $s^\star$, proposed by P. Vogl *et. al.* [191], that would be nevertheless necessary for indirect semiconductors or for an accurate description of the bands near the L or K edges.

The minimal set parameters needed to define the Hamiltonian matrix elements is obtained, as commented before, by symmetry considerations. We have illustrated in Fig. 2.12 how the overlap between orbitals of adjacent atoms can be decomposed in terms of the director cosines $\hat{\boldsymbol{u}}_d = (p, q, r)$. A detailed and general guide can be found in the book of R. Enderlein and H. Höring (Ref. [127]). The exact expressions are as follows:

$$
\begin{aligned}
\langle s_{\alpha'}|H|s_{\alpha'}\rangle &= V_{ss\sigma}, \\
\\
\langle s_{\alpha',c}|H|p^x_{\alpha,a}\rangle &= pV_{s_cp_a\sigma}, \\
\langle s_{\alpha',c}|H|p^y_{\alpha,a}\rangle &= qV_{s_cp_a\sigma}, \\
\langle s_{\alpha',c}|H|p^z_{\alpha,a}\rangle &= rV_{s_cp_a\sigma}, \\
\\
\langle p^x_{\alpha'}|H|p^x_{\alpha}\rangle &= (1-p^2)V_{pp\pi} + p^2V_{pp\sigma}, \\
\langle p^y_{\alpha'}|H|p^y_{\alpha}\rangle &= (1-q^2)V_{pp\pi} + q^2V_{pp\sigma}, \\
\langle p^z_{\alpha'}|H|p^z_{\alpha}\rangle &= (1-r^2)V_{pp\pi} + r^2V_{pp\sigma}, \\
\\
\langle p^x_{\alpha'}|H|p^y_{\alpha}\rangle &= pq(V_{pp\sigma} - V_{pp\pi}), \\
\langle p^x_{\alpha'}|H|p^z_{\alpha}\rangle &= pr(V_{pp\sigma} - V_{pp\pi}), \\
\langle p^y_{\alpha'}|H|p^z_{\alpha}\rangle &= qr(V_{pp\sigma} - V_{pp\pi}).
\end{aligned}
\tag{2.63}
$$

The case of the integral $\langle s_{\alpha,a}|H|p^x_{\alpha',c}\rangle$ is analogous to $\langle s_{\alpha',c}|H|p^x_{\alpha',a}\rangle$. After these symmetry considerations, the independent overlap parameters are just five: $V_{ss\sigma}$, $V_{s_cp_a\sigma}$, $V_{s_ap_c\sigma}$, $V_{pp\pi}$, and $V_{pp\sigma}$. In Appendix A, we have written the final tight-binding Hamiltonian matrix within the sp^3 model for a crystal with the wurtzite structure (with respect to the unit cell given in Section 1.1). The determination of the optimal values of the parameters can be done in several ways. The most common one fits the parameters to reference band structures (as given by *ab initio* calculations). Alternatively they can be fitted to experimental information such as the band gap, effective masses, etc. In the next Subsection we will combine both theoretical and experimental information to deduce the tight-binding parameters of the III-N semiconductors.

The Hamiltonian matrix as defined in Appendix A is ready for calculating the band structure of any wurtzite semiconductor or nanostructure. However, the sp^3 basis in the first neighbor approximations cannot reproduce the crystal-field splitting, and gives in the absence of spin-orbit interaction a six-fold degeneracy at the top of the valence band [190]. This is because at the nearest neighbors level the wurtzite structure is indistinguishable from the cubic zinc-blende. The introduction of second and farther neighbors would palliate this deficiency [115]. Notice that in the pseudopotential method, the crystal-field splitting is well reproduced since we have not introduced any approximation concerning the neighbors. An alternative to the addition of farther neighbors, is to distinguish by hand between the $p_x - p_y$ and p_z orbitals. This *ad hoc* modification is performed on the on-site energy $E_{a,p_z} \neq E_{a,p_x} = E_{a,p_y}$. The major impact on the valence band will be the splitting into the states Γ_5 and Γ_1. These changes have been taken into account

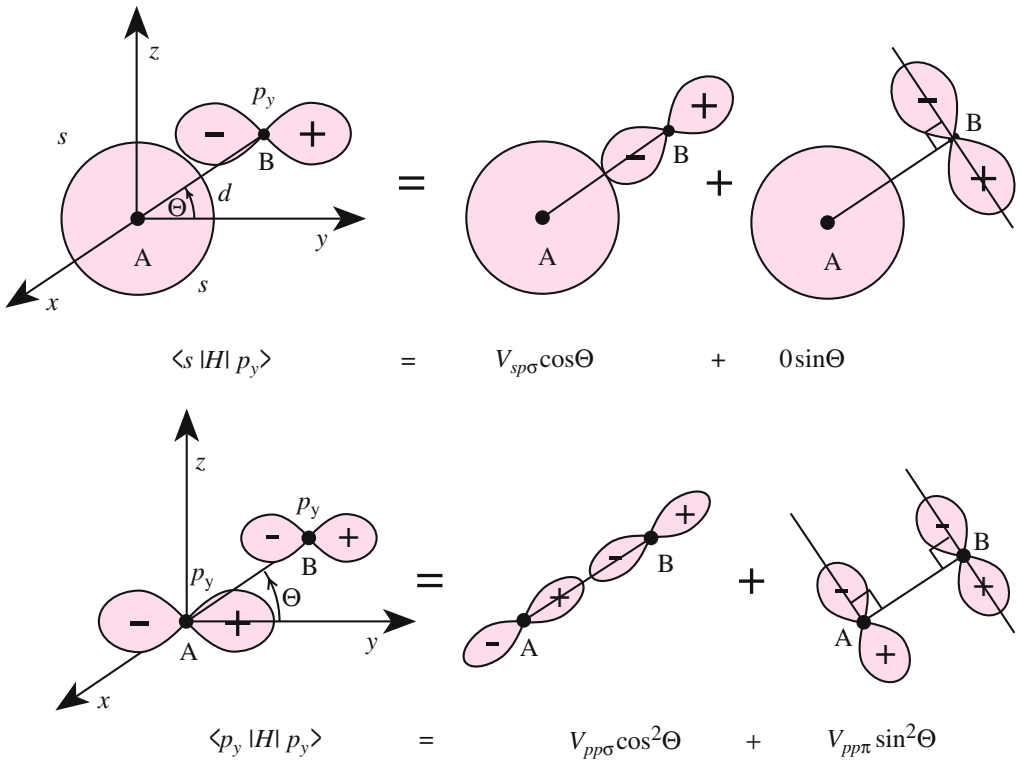

Figure 2.12: Projection of the overlap parameter between an s and a p_y orbital, and between p_y orbitals, along the vector $\boldsymbol{d}$ joining the two atoms and perpendicular to it (Extracted from Ref. [192]).

in the tight-binding Hamiltonian matrix shown in Appendix A,

In addition to the crystal-field splitting, the non-ideality of the wurtzite unit cell can also be included by means of the Harrison's rule [193]. In its original this rule establishes version that the overlap parameters depend quadratically on the inverse of the distance between the adjacent atoms

$$V_{\alpha',l',\alpha,l} = \left(\frac{d^{(0)}_{\alpha',\alpha}}{d_{\alpha',\alpha}}\right)^2 V^{(0)}_{\alpha',l',\alpha,l}, \tag{2.64}$$

where $V^{(0)}_{\alpha',l',\alpha,l}$ is the overlap parameter at the equilibrium bond distance. The exponent of 2 has being modified in subsequent works, in order to have a better agreement between theory and experiments. It has also been proposed a dependence on the orbital. In this work, we will take the exponent in the Harrison's rule as an additional fitting parameter $\eta_{l,l'}$ [194]:

$$V_{\alpha',l',\alpha,l} = \left(\frac{d^{(0)}_{\alpha',\alpha}}{d_{\alpha',\alpha}}\right)^{\eta_{l,l'}} V^{(0)}_{\alpha',l',\alpha,l}. \tag{2.65}$$

The fitted exponent can be found in Appendix A. We have followed the criteria of keeping the exponent in values close to two, in order to keep the physical meaning of the Harrison's rule [195].

The last point of this exposition of the tight-binding method concerns the spin-orbit interaction. In the approximation assumed in this work, this interaction only couples p orbitals of the same atom. This assumption for the III-N semiconductors is already sufficient to reproduce the three-edge valence band structure at the Brillouin zone center. We add the spin-orbit energy to the tight-binding Hamiltonian as follows [196]:

$$H = H_0 + H_{\mathrm{SO}}, \tag{2.66}$$

where:

$$H_{\mathrm{SO}} = \frac{\hbar}{2m^2c^2}\frac{1}{r}[\nabla V \times \boldsymbol{p}] \cdot \sigma. \tag{2.67}$$

V is the total crystal potential and σ de Pauli matrices. After some algebraic manipulations, the spin-orbit interaction can be described by a single parameter:

$$\lambda = \langle p_x, \uparrow | \frac{\hbar}{4m^2c^2}[\nabla V \times \boldsymbol{p}] | p_y, \downarrow \rangle. \tag{2.68}$$

In Appendix A we give the explicit form of the tight-binding Hamiltonian matrix with the spin-orbit interaction. In the rest of the work, the notation for the orbital including the spin is: $|\varphi_{\alpha,l,\sigma}\rangle$ with $l = s, p_x, p_y, p_z$ and $\sigma = \uparrow, \downarrow$.

The results of the tight-binding band structures are presented in the next Subsection, with special attention to the Brillouin zone center. In order to facilitate the interpretation of the electronic structure, it is convenient to have a method to characterize the symmetry of the wave functions. By taking advantage of the atomistic nature of the tight-binding method, we can define the symmetry character of each calculated wave function n, as its projection over the atomic orbital l $(= s, p_x, p_y, p_z)$:

$$\phi_l^n = \sum_{\alpha,\sigma} |\langle \Phi_{\boldsymbol{k}}^{\alpha,l,\sigma} | \Psi_{\boldsymbol{k}}^n \rangle|^2 = \sum_{\alpha,\sigma} |A_{\alpha,l,\sigma}^n|^2. \tag{2.69}$$

The set of numbers $\{\phi_l^n\}_{l=s,p_x,p_y,p_z}$ for a given state n summarizes the relevant information about the symmetry of the state and satisfies $\sum_l \phi_l^n = 1$. Usually one of these numbers is dominant (say > 0.5). In this situation we say that the state has dominant l-character. Given the isotropy in the basal plane (in-plane isotropy) of the wurtzite structure, it is convenient to introduce in further analysis the quantity $\phi_\perp = \phi_{p_x} + \phi_{p_y}$.

2.3.2 Tight-binding band structure of III-N semiconductors

The formulation presented above will be applied here to obtain the band structures of III-N semiconductors. The set of parameters have been deduced by fitting the *ab initio* calculations presented in Section 2.1, except for the case of AlN, where we have used those provided by A. Kobayashi *et. al.* [190]. In the cases of GaN and InN, the parameters have been adjusted to obtain the experimental value of the band gap. The emphasis in the fitting procedure has been put in obtaining a precise agreement at the top of the valence band, with a special care in reproducing the symmetry of the wave functions. These requirements provide a set of tight-binding (TB) parameters suitable for predictions of the optical properties of nanostructures.

In Fig. 2.13 we present the InN band structure as calculated with the TB method (solid lines) and the LDA+U method (dotted lines). The topmost valence and the lowest conduction bands are drawn with red lines. In both cases, the spin-orbit interaction has not been included. First, we highlight the good matching in the valence bands, in the energy range between -7 and 0 eV. This demonstrates

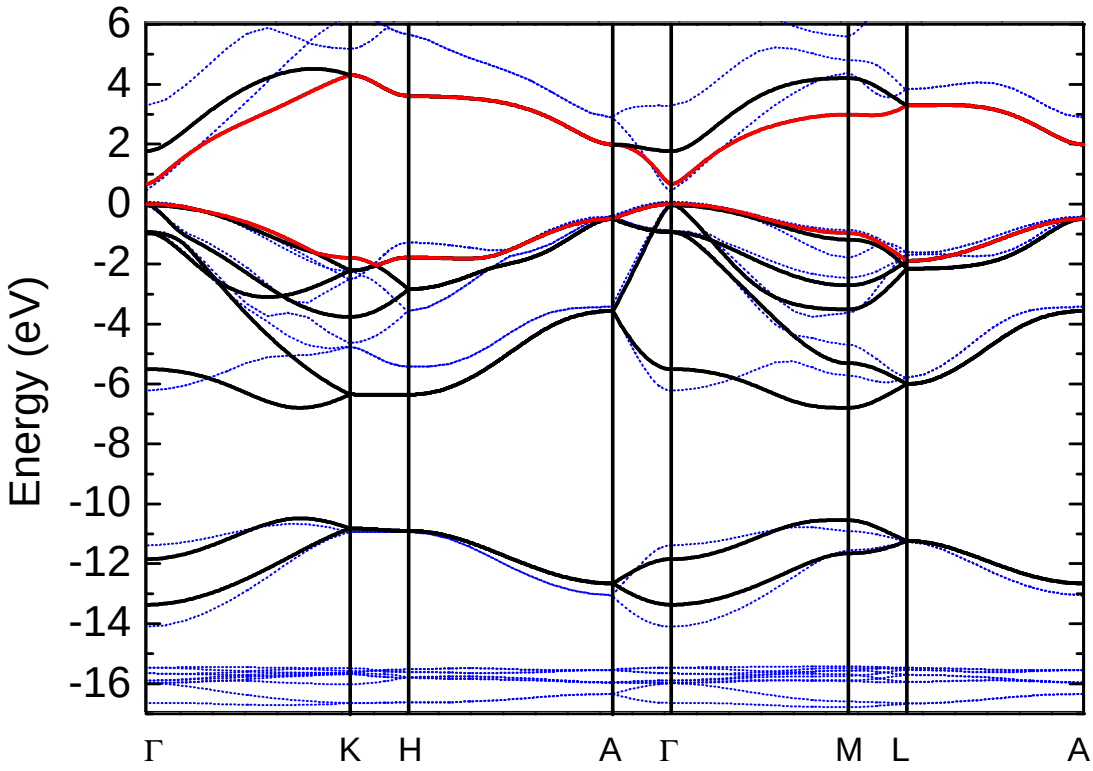

Figure 2.13: Band Structure of InN as calculated with the sp^3 tight-binding model (solid lines) and with LDA+U (dotted lines).

that the sp^3 basis is sufficient to give a reasonable agreement also at points in the Brillouin zone other than Γ. For instance, the coincide is surprising by good at the A, M and L points (shown in Fig. 2.13), and the larger deviations are located at K and H. The exception is the conduction band. The conduction bands obtained by DFT with energies above 3 eV, are not at all reliable and therefore we have renounced to fit them with our tight-binding model. Note that there are no d bands in the tight-binding results due to the absence of d states in the TB basis. In Table 3.12 we have compared the energies of TB and LDA+U approaches at some points of the Brillouin zone.

We depict in Fig. 2.14 a zoom of the valence band structure. We observe a very accurate fitting for the A and C bands whereas the B-band shows a slight deviation for $k > 0.1$ in the M direction. Along the ΓA direction, A and B bands are degenerate and both calculations match perfectly. The anti-crossing between B and C bands is also well captured by the TB method.

Therefore, the numerical results for InN confirm that the TB method based on the sp^3 basis is an optimal solution between the small basis ($s_c p_a^3$) and the

Energy (eV)					
	LDA+U	TB		LDA+U	TB
$A^c_{1,3}$	2.812	1.993	$L^c_{1,3}$	3.750	3.292
$A^v_{5,6}$	-0.485	-0.474	$L^v_{1,3}$	-1.687	-1.894
$A^v_{1,3}$	-3.506	-3.566	$L^v_{1,3}$	-5.871	-6.002
M^c_1	4.297	2.990	$L^v_{1,3}$	-11.333	-11.133
M^v_4	-0.938	-0.964	Γ^c_3	3.2064	1.7783
M^v_3	-1.864	-1.181	Γ^c_1	0.34	0.67
M^v_2	-2.532	-2.711	Γ^v_6	0.0	0.0
M^v_1	-3.708	-3.515	Γ^v_1	-0.040	0.040
M^v_3	-4.761	-5.306	Γ^v_5	-0.9561	-0.93599
M^v_1	-5.785	-6.794	Γ^v_3	-6.2955	-5.504601
InN valence band effective masses					
$m^A_\perp$	2.80			m^A_z	1.86
$m^B_\perp$	0.07			m^B_z	1.86
$m^C_\perp$	0.57			m^C_z	0.07

Table 2.4: Comparison between *ab initio* reference values obtained by LDA+U (Section 2.1) and corresponding optimized TB method values for high symmetry points in InN (eV).

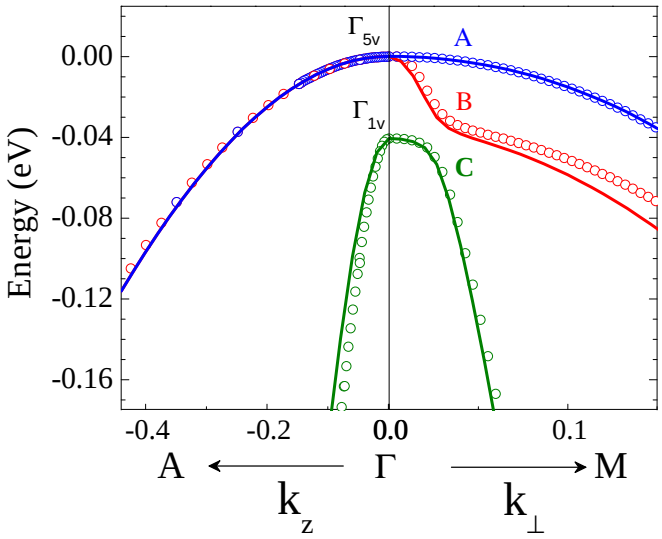

Figure 2.14: Top of the InN valence band. The empty circles correspond to the LDA+U bands, and the lines represent the TB bands. The component k_z of the wave vector $\boldsymbol{k}$ is normalized to $\frac{\pi}{c}$, such that $k_z = 1$ corresponds to A. The wave vector in the M direction is expressed as $\frac{\pi}{a}(\xi, \frac{1}{3}\xi, 0)$, where $0 \leq \xi \leq 1$. The symmetry group of the states at Γ are indicated and the bands are denoted as A, B, and C.

large basis ($sp^3d^5s^\star$) models. The addition of the $s^\star$ orbital could be performed straightforwardly without affecting the obtained parametrization, if one desire to make corrections of the conduction band far from Γ. However, new experimental results should be available in the literature to make these corrections necessary. The effective masses of the topmost valence band states are also given. The same procedure has been followed to fit GaN to LDA results of Section 2.1. Figure 2.15 reproduces a more detailed picture of the top the valence bands of InN, GaN and AlN. The spin-orbit interaction is included as explained before and in Appendix A. Therefore, the corresponding group representations are now Γ_9 and Γ_7, as labeled in Figure 1.5. The alternative labeling of the bands A, B and C, in decreasing order of energy, is also used. Although the parameters were obtained by fitting *ab initio* band structures where the spin-orbit interaction was absent, when this is introduced, due to its small contribution the splittings Δ_{so} are not larger than 10 meV and no modification of the TB parameters is required. The main effect concerns the topmost valence band state. For the InN and GaN semiconductors, this valence band state belongs to the representation Γ_9, having a character $\phi_\perp = 1$. On the contrary, the AlN topmost state belongs to the representation Γ_7, and the character is now purely ϕ_{p_z}, due to the negative and large crystal field splitting [197]. The spin-orbit interaction, that depends on the atomic number, is larger in InN (10 meV) (indium has an atomic number of 49), and minimum in AlN (5

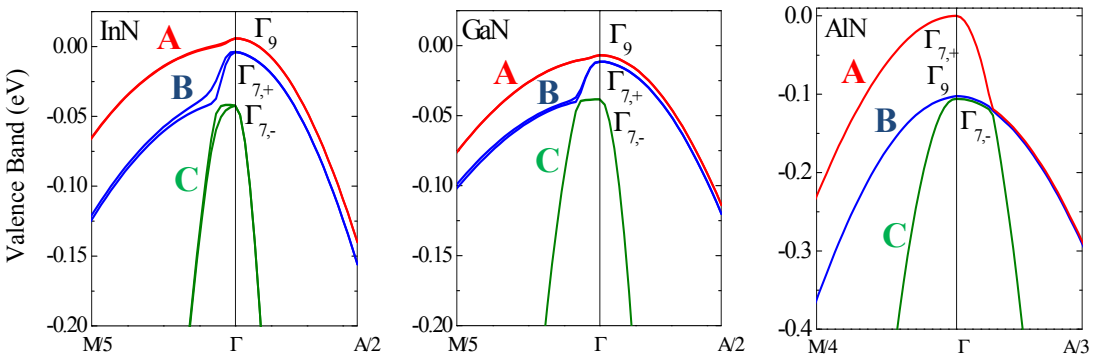

Figure 2.15: Detail around the Γ point of the bulk band structures calculated with the tight-binding method, for InN, GaN, and, AlN. All the tight-binding parameters are given in Appendix A.

meV).

The tight-binding approach presented in this Section is ready to be used for any kind of nanostructures, as will be shown for the case of nanowires in Chapter 3. In the next Section, the formulation to find the optical absorption in terms of the tight-binding wave functions is explained.

2.4 Optical properties

2.4.1 Calculation of the absorption coefficient within the tight-binding method

We describe the light-matter interaction by a semi-classical formulation, where the electronic structure is modeled by means of quantum mechanics, as shown in previous Sections, and the electromagnetic field is introduced by the classic theory of the electromagnetism [198]. For the description of the electromagnetic field we use the vector potential, $\boldsymbol{A}(\boldsymbol{r},t)$. The Hamiltonian for an electron with charge $-e$ in such electromagnetic field

$$H = \frac{1}{2m_0}[\boldsymbol{p} + (e\boldsymbol{A})]^2 + V(\boldsymbol{r}). \tag{2.70}$$

Here the vector potential is supposed to have an harmonic temporal evolution

$$\boldsymbol{A}(\boldsymbol{r},t) = A_0\boldsymbol{e}\left\{e^{i(\boldsymbol{q}\cdot\boldsymbol{r}-\omega t)} + \text{c.c.}\right\}. \tag{2.71}$$

where $\boldsymbol{e}$ is the light polarization vector and $\boldsymbol{q}$ the light wave vector. In this thesis, we assume the dipole approximation, where the wave vector is negligible, *i. e.*, $\boldsymbol{q} \approx 0$. The Hamiltonian of Eq. (2.70) can be written, by using the fact of $\nabla \cdot \boldsymbol{A} = 0$ (Coulomb gauge), and neglecting terms proportional to $\boldsymbol{A}^2$

$$H = \frac{\boldsymbol{p}^2}{2m_0} + V(\boldsymbol{r}) + \frac{e}{m_0}\boldsymbol{A} \cdot \boldsymbol{p}. \tag{2.72}$$

Therefore, the effect of the electromagnetic field is a perturbation to the problem of an electron in a periodic crystal. This additional term is called the light-matter interaction Hamiltonian, and in the following, we refer it as H_I. If we apply the Fermi's golden rule, the probability of transition from an initial state, $|\Psi_v\rangle$, to a final state, $|\Psi_c\rangle$, can be calculated as [199]:

$$W_{v\to c} = \frac{2\pi}{\hbar}|\langle\Psi_c|H_I|\Psi_v\rangle|^2\delta(\varepsilon_c - \varepsilon_v - \hbar\omega), \tag{2.73}$$

and

$$\boldsymbol{p}^{\boldsymbol{e}}_{v,c} = |\langle\Psi_c|H_I|\Psi_v\rangle|^2 = \left(\frac{eA_0}{m_0}\right)^2 |\langle\Psi_c|\boldsymbol{e}\cdot\boldsymbol{p}|\Psi_v\rangle|^2. \tag{2.74}$$

where we have considered only transitions from the valence to the conduction band accompanied by the absorption of a photon with energy $\hbar\omega = \varepsilon_c - \varepsilon_v$.

The absorption coefficient is then defined as the sum over all the possible processes [200]:

$$\alpha(\hbar\omega) \sim \sum_{c,v} W_{v\to c}. \tag{2.75}$$

We describe below how to calculate the momentum matrix element $\boldsymbol{p}^{\boldsymbol{e}}_{v,c}$ within the tight-binding formulation.

In the tight-binding method, the exact form of the wave functions is not known. In Section 2.3 we have explained how the wave functions are expanded in terms of an orthogonal basis composed ofthe atomic orbitals. In principle, by means of *ab initio* calculations one could obtain the exact atomic functions and then calculate exactly the momentum matrix elements of Eq.(2.74). However, this procedure would increase the difficulty of the tight-binding method. An alternative solution is the proposed in Refs. [201], [202], and [203]. In these works, the authors propose, by algebraic manipulation and using basic quantum mechanics, to write the momentum matrix element as a product of the tight-binding parameters and the coefficients of the corresponding wave functions. Therefore, there is no need

of additional parameters to calculate the optical absorption. Thus, for the wave functions μ $(= v, c)$

$$|\Psi_\mu\rangle = \sum_{\alpha,l} A_{\mu,\alpha,l}(\boldsymbol{k})|\varphi_l(\boldsymbol{r} - \boldsymbol{\tau}_\alpha)\rangle, \tag{2.76}$$

we can write $\boldsymbol{p}^{\boldsymbol{e}}_{v,c}$ as [203]:

$$\boldsymbol{p}^{\boldsymbol{e}}_{v,c} = \frac{m_0}{\hbar} \sum_{\alpha',l',\alpha,l} A^\dagger_{c,\alpha',l'}(\boldsymbol{k}) i(\boldsymbol{\tau}_{\alpha'} - \boldsymbol{\tau}_\alpha) \cdot \boldsymbol{e} H_{\alpha',l',\alpha,l} e^{i\boldsymbol{k}\cdot(\boldsymbol{\tau}_{\alpha'} - \boldsymbol{\tau}_\alpha)} A_{v,\alpha,l}(\boldsymbol{k}). \tag{2.77}$$

The indices α and α' runs over atoms and the indices l and l' over orbitals.

Taking advantage of the definition of the Brillouin zone and the fact of that our states are grouped in bands, we can rewrite the absorption coefficient

$$\alpha(\hbar\omega) \sim \int_{\mathrm{BZ}} f^{\boldsymbol{e}}_{v,c}(\boldsymbol{k}) \delta(\varepsilon_{c,\boldsymbol{k}} - \varepsilon_{v,\boldsymbol{k}} - \hbar\omega) d\boldsymbol{k}, \tag{2.78}$$

where $f^{\boldsymbol{e}}_{v,c}(\boldsymbol{k}) = \frac{|\boldsymbol{p}^{\boldsymbol{e}}_{v,c}|^2}{\varepsilon_c - \varepsilon_v}$ is the oscillator strength. The optical transitions between two energy levels are characterized by a radiative recombination time that introduces an inhomogeneous broadening of the spectral line. In such circumstances, the spectra line can be described by a Lorentz function instead of the Dirac's delta. As we have mentioned in Chapter 1, nanowires are not placed in an ideal environment, and many factors contribute to further increase the broadening of the optical transitions. A typical value of this broadening is in the range of several meV. The parameter Γ represents along this work such broadening. Hence, the absorption takes the form:

$$\alpha(\hbar\omega) \sim \int_{\mathrm{BZ}} f^{\boldsymbol{e}}_{v,c}(\boldsymbol{k}) \frac{1}{\pi} \frac{\Gamma/2}{(\varepsilon_{c,\boldsymbol{k}} - \varepsilon_{v,\boldsymbol{k}} - \hbar\omega)^2 + (\Gamma/2)^2} d\boldsymbol{k}. \tag{2.79}$$

The absorption coefficient $\alpha(\hbar\omega)$ depends on the light polarization $\boldsymbol{e}$. In this work, we study the following two polarizations:

$$\begin{aligned} \boldsymbol{e}_\perp &= \tfrac{1}{\sqrt{2}}(\hat{x} + i\hat{y}), \\ \boldsymbol{e}_{\boldsymbol{z}} &= \hat{z}, \end{aligned} \tag{2.80}$$

where $\hat{x}$, $\hat{y}$ and $\hat{z}$ are the unitary vectors parallel to the cartesian axis. These two configurations of a possible experiment of absorption or photoluminescence

are specially important in wurtzite, due to the anisotropy between the c-axis and the basal plane [204].

2.4.2 Group theoretical analysis of the optical transitions in wurtzite semiconductors

The application of the group theory can give valuable information about the allowed and forbidden transitions from the valence to the conduction band, as a function of the light polarization [192]. The point symmetry of the wurtzite is C_{6v}, and the possible symmetries of Γ-point states are compiled in Table 1.2. The information given by the character table and the multiplication table is enough to establish the selection rules for the optical transitions from the valence to the conduction band. The Hamiltonian term H_I, for the light polarizations of Eq. (2.80), belong tos the following representations [30]:

$$\boldsymbol{e} \in \begin{cases} \Gamma_5 & \text{if } \boldsymbol{e} = \boldsymbol{e}_\perp \\ \Gamma_1 & \text{if } \boldsymbol{e} = \boldsymbol{e}_z \end{cases} \tag{2.81}$$

Therefore, if the initial state has a symmetry Γ_v, the final state is Γ_c, and the perturbation operator transform like Γ_I, the following rule indicates whether the momentum matrix element is zero or non-zero:

$$\boldsymbol{p}^{\boldsymbol{e}}_{v,c} = \begin{cases} \neq 0 & \text{if } \Gamma_v \otimes \Gamma_I \supseteq \Gamma_c; \\ 0 & \text{otherwise} \end{cases} \tag{2.82}$$

The selection rules for wurtzite semiconductors, without spin-orbit interaction, are written as follows ($\Gamma_v = \Gamma_1$ or Γ_5 and $\Gamma_c = \Gamma_1$):

$$\begin{aligned} \boldsymbol{e}_\perp & \begin{cases} \Gamma_5 \otimes \Gamma_5 \twoheadrightarrow \Gamma_1 + \Gamma_2 + \Gamma_6 & \supseteq \Gamma_1 \Longrightarrow \boldsymbol{p}^{\perp}_{\Gamma_{5,v},\Gamma_{1,c}} \neq 0, \\ \Gamma_1 \otimes \Gamma_5 \twoheadrightarrow \Gamma_5 & \not\supseteq \Gamma_1 \Longrightarrow \boldsymbol{p}^{\perp}_{\Gamma_{1,v},\Gamma_{1,c}} = 0, \end{cases} \\ \boldsymbol{e}_z & \begin{cases} \Gamma_5 \otimes \Gamma_1 \twoheadrightarrow \Gamma_5 & \not\supseteq \Gamma_1 \Longrightarrow \boldsymbol{p}^{z}_{\Gamma_{5,v},\Gamma_{1,c}} = 0, \\ \Gamma_1 \otimes \Gamma_1 \twoheadrightarrow \Gamma_1 & \supseteq \Gamma_1 \Longrightarrow \boldsymbol{p}^{z}_{\Gamma_{1,v},\Gamma_{1,c}} \neq 0. \end{cases} \end{aligned} \tag{2.83}$$

In Fig. 2.16(a) we have represented with arrows the allowed and forbidden transitions deduced from Eq. (2.83). As we can see, p_x-p_y orbitals are related to $\boldsymbol{e}_\perp$ light polarization and p_z orbitals to $\boldsymbol{e_z}$ polarization. If the spin-orbit interaction is considered, the relations are quite different [30]

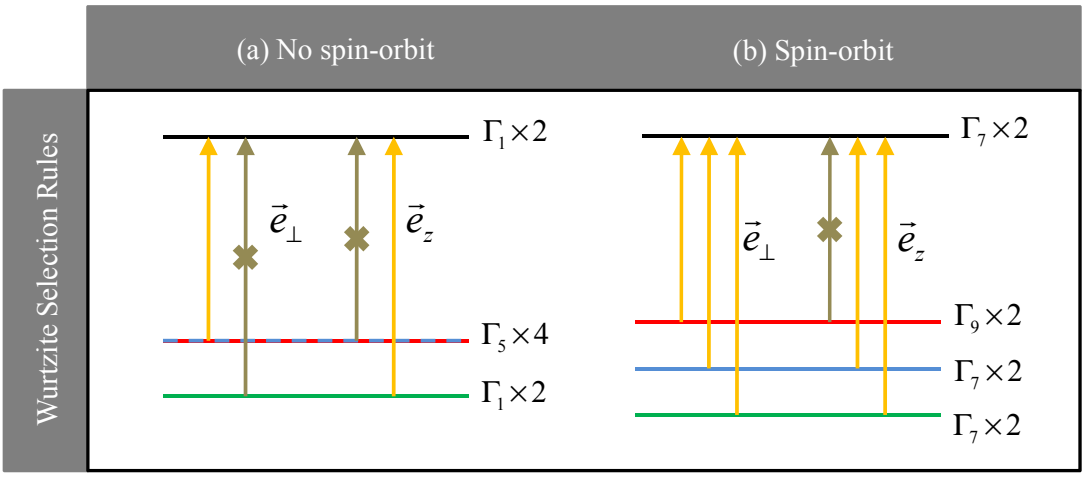

Figure 2.16: Scheme of the optical transitions between the valence and conduction bands for the wurtzite bulk considering the different polarizations. The degeneration of each state is also indicated.

$$
\begin{aligned}
\boldsymbol{e}_{\perp} &\begin{cases} \Gamma_9 \otimes \Gamma_5 \twoheadrightarrow \Gamma_7 + \Gamma_8 & \supseteq \Gamma_7 \Longrightarrow \boldsymbol{p}^{\perp}_{\Gamma_{9,v},\Gamma_{7,c}} \neq 0, \\ \Gamma_7 \otimes \Gamma_5 \twoheadrightarrow \Gamma_7 + \Gamma_9 & \supseteq \Gamma_7 \Longrightarrow \boldsymbol{p}^{\perp}_{\Gamma_{7,v},\Gamma_{7,c}} \neq 0, \end{cases} \\
\boldsymbol{e}_{z} &\begin{cases} \Gamma_9 \otimes \Gamma_1 \twoheadrightarrow \Gamma_9 & \not\supseteq \Gamma_7 \Longrightarrow \boldsymbol{p}^{z}_{\Gamma_{9,v},\Gamma_{7,c}} = 0, \\ \Gamma_7 \otimes \Gamma_1 \twoheadrightarrow \Gamma_2 + \Gamma_7 + \Gamma_9 & \supseteq \Gamma_7 \Longrightarrow \boldsymbol{p}^{z}_{\Gamma_{7,v},\Gamma_{7,c}} \neq 0. \end{cases}
\end{aligned}
\tag{2.84}
$$

Now, only one transition $\Gamma_9 \nrightarrow \Gamma_{7c}$ for $\boldsymbol{e}_z$-polarized light is strictly forbidden. In Fig. 2.16(b) we have also indicated the transitions in the case of including the spin-orbit interaction. Notice that all the transitions from valence states Γ_7 to the conduction state Γ_7 are allowed and only the calculation of $\boldsymbol{p}^{\boldsymbol{e}}_{c,v}$ will tell us information about the intensity of such transitions. While in the case of InN and GaN the lowest valence band-conduction band transition ($\Gamma_{9v} \rightarrow \Gamma_{7c}$) is allowed for $\boldsymbol{e}_{\perp}$-polarized light, in the case of AlN the intensity of this transition depends on the $p_{\perp}$-orbital composition. The opposite occurs for $\boldsymbol{e}_z$-polarized light, for which the band gap transition $\Gamma_{9v} \nrightarrow \Gamma_{7c}$ is forbidden for InN and GaN. In the case of AlN, this transition is allowed ($\Gamma_{7v,+} \rightarrow \Gamma_{7c}$). Therefore, the group theory can result useful for the analysis of the electronic structure in nanowires, as shown in Chapter 3.

Chapter 3

Atomistic modeling of free-standing nanowires

In this Chapter we present atomistic calculations of the electronic structure and optical absorption for III-N nanowires. The calculation have been made by using both the semi-empirical pseudopotential method (SEPM) described in Section 2.2, and the tight-binding (TB) method, formulated in Section 2.3. Although both sets of calculations have a very different nature, it is convenient to highlight first some of the aspects they have in common.

Concerning the geometry, the NWs are assumed to be infinite in the c-axis, with hexagonal cross-section, and lateral faces parallel to the planes $(1\bar{1}00)$. This geometry is compatible with the observations made by microscopy, and with the theoretical *ab initio* calculations performed in nonpolar slabs, as discussed in Section 1.2. In real systems, the NW surface are free and therefore this implies a surface reconstruction, *i. e.*, the near surface atoms modify their interatomic distances in order to minimize the total energy. For simplicity, in our calculations, we will assume the atomic arrangement corresponding to the perfect wurtzite everywhere. This approximation is reasonable since the surface reconstruction structure takes place only in a few outer atoms, affecting only slightly the electronic states of thick enough NWs [193]. In the following, the term NW diameter is used to mean the lateral size of the NW as defined in Fig. 3.1.

Not only is the atomic arrangement modified close to the NWs free surfaces. In addition, the atoms at those surfaces will have dangling bonds, where no atom is attached [193]. The existence of these dangling bonds generates electronic states localized at the surfaces, whose energies are within the band gap of the semiconductor and are eventually hybridized with the conduction and valence states. A

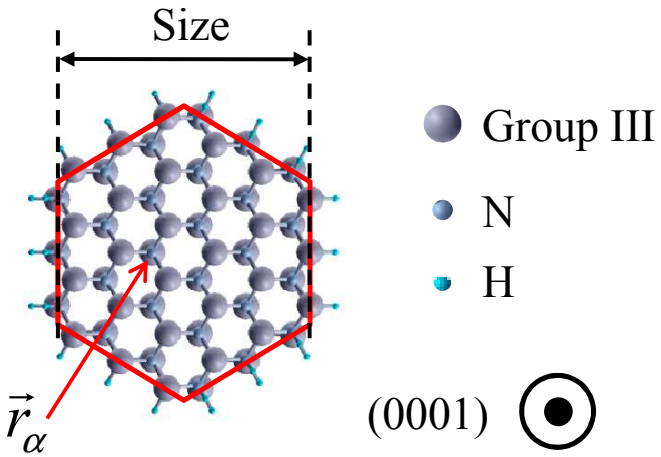

Figure 3.1: Ball-and-stick representation of the nanowire cross-section, with the arrow indicating the size. The hydrogen atoms are also shown.

detailed and careful analysis of what happens at the surface must be carried out for studies about surface properties. In our case, we are only interested in the confined states related with the small size of the crystal, disregarding the study of the surface states. However, as these states have energies close to the conduction and valence band edges, they can induce an artificial modification of the conduction and valence states, and they have to be eliminated. Moreover, the appearance of more states in the energy range of interest impoverishes the efficiency of the calculations, increasing unnecessarily the computation time. Therefore, there are multiple reasons for developing a method for their elimination. One possibility is to surround the nanostructure by a virtual material with a larger gap, in order to achieve quantum confinement for the inner atoms [165]. The disadvantages of using this virtual material is the increasing of the number of atoms, which requires much more computation time, and also that it could add artificial effects due to the interaction of the barrier atoms with the nanostructure atoms. Another way to remove this annoyance consists of attaching an atom, usually of hydrogen, to the dangling bonds (the so-called passivation), which displaces the energies of the surfaces states far from the band gap [205]. In this thesis we use the passivation with hydrogen-atoms to saturate the dangling bonds of the surface atoms and thus get rise of the surface states.

The atomic positions $\boldsymbol{r}_\alpha$ are denoted by:

$$\boldsymbol{r}_1, \boldsymbol{r}_2, \ldots, \boldsymbol{r}_{n_{atom}}, ..., \boldsymbol{r}_{h_1}, ..., \boldsymbol{r}_{h_p}, \tag{3.1}$$

where n_{atom} is the number of group III element and nitrogen atoms, and h_p is the number of hydrogen atoms, used to *passivate* the dangling bonds at the NW surface.

In both methods, the single-particle Schrödinger equation to be solved to obtain the electronic structure has translational symmetry along the NW axis. Therefore, the electronic states are organized in an one-dimensional band structure $\varepsilon(k)$, depending only on the wave vector $\boldsymbol{k} = k\boldsymbol{n}$, $\boldsymbol{n}$ being a unit vector along the NW axis. The eigenvalue problem is written in any case as:

$$H(\boldsymbol{k})\Psi_{\boldsymbol{k}}(\boldsymbol{r}) \equiv H(k)\Psi_k(\boldsymbol{r}) = \varepsilon(k)\Psi_k(\boldsymbol{r}). \tag{3.2}$$

The Brillouin zone is here one-dimensional, with length $2\pi/c$. All the calculations are performed including the spin-orbit interaction, but all the obtained NW electronic states are still doubly degenerate, due to Kramer's degeneracy.

The Chapter is divided in two parts, briefly described as follows:

- In Section 3.1, the semi-empirical pseudopotential method (SEPM) is applied to find the electronic states of GaN NWs up to a diameter of 6 nm. As a previous step, an *ab initio* methodology has been developed to obtain a local-density derived pseudopotential for the hydrogens attached to the surface atoms. We also analyze the NW energy spectrum, determining the allowed and forbidden optical transitions using the concepts of group theory explained in Section 2.4.

- In Section 3.2, the tight-binding (TB) method is used to determine the NW band structure. The atomistic nature of the TB method allows us to compare the TB results with the *ab initio* results obtained for a thin NW. With this test, we can confirm the suitability of the TB bulk parameters derived in Section 2.3. We have therefore studied the electronic structure and the optical absorption as a function of the NW size and the light polarization, for the whole set of III-N semiconductor NWs.

3.1 Semi-empirical pseudopotential method applied to free-standing GaN nanowires

In this Section we present the calculation of the electronic structure of GaN NWs with the semi-empirical pseudopotential method. First, in order to benefit from

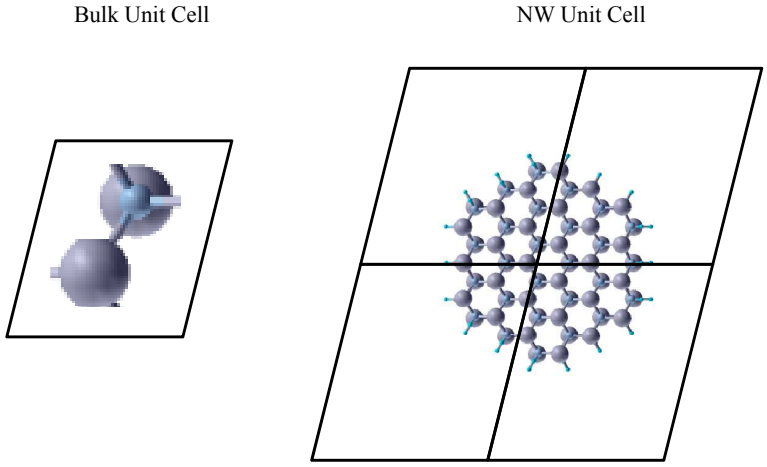

Figure 3.2: Ball-and-stick representation of the bulk and nanowire supercell. Notice that the representation does not respect the scale.

the plane wave representation in which the SEPM is formulated, it is mandatory to embed the NW in a periodic system. We proceed by defining the NW supercell as shown in Fig. 3.2. A vacuum space of several angstrom must be left to prevent the coupling between adjacent NWs. We construct the NW supercell by reproducing the wurtzite bulk, and defining the NW lattice vectors:

$$\begin{aligned} \boldsymbol{A}_1 = &\quad N_1\boldsymbol{a}_1 = N_1\left(\frac{a}{2}, \frac{\sqrt{3}a}{2}, 0\right), \\ \boldsymbol{A}_2 = &\quad N_2\boldsymbol{a}_2 = N_2\left(-\frac{a}{2}, \frac{\sqrt{3}a}{2}, 0\right), \\ \boldsymbol{A}_3 = &\quad N_3\boldsymbol{a}_3 = N_3\left(0, 0, c\right), \end{aligned} \tag{3.3}$$

where bulk lattice vectors $\boldsymbol{a_1}$, $\boldsymbol{a_2}$ and $\boldsymbol{a_3}$ are those of Eq. (1.4) and N_1, N_2, and N_3 integers.[1]

Related to the Hamiltonian matrix obtained after Eqs. (2.53) and (3.2), due to its large size, we only calculate how the Hamiltonian matrix acts on a vector, and such matrix is never explicitly computed. We calculate the kinetic energy part in Fourier space, where it is diagonal, and the potential energy part in real space where the number of operations for the matrix-vector product is smaller than in the reciprocal space. Then, we move between the real and reciprocal spaces by means of Fourier transforms. The diagonalization is performed by the conjugate gradient algorithm applied with the folded spectrum method [206, 207]. The states

[1] For the case of an infinite NW in the (0001) direction $N_3 = 1$.

obtained from the solution of the Schrödinger Eq. (3.2) will be indexed in ascending order according to their separation in energy from the respective band edge, as calculated at $k = 0$. The Kramer's double degeneracy is omitted from the indexing and the NW energies are written as follows:

$$\begin{array}{rcll} \text{Valence Band edge:} & E_v & \Rightarrow & v_1(s), v_2(s), v_3(p), \ldots \\ \text{Conduction Band edge:} & E_c = E_v + E_g & \Rightarrow & c_1(s), c_2(p), c_3(p), \ldots \end{array} \tag{3.4}$$

In all the calculations presented in this Section, the bulk valence band edge is set as the zero of energy, $E_v = 0$. The letters $s, p, \ldots$, indicate the envelope shape of the wave function, according with the Bessel functions. The s-type envelope corresponds to $J_0(x)$, p-type envelope to $J_1(x)$, etc.

Another practical way to characterize the NW wave functions is the projections of a NW state onto given bulk states:

$$P_n(i) = \langle \Psi_{\boldsymbol{k},i} | \Psi_{k,n} \rangle, \tag{3.5}$$

where $\Psi_{k,n}$ is the NW n state, and $\Psi_{\boldsymbol{k},i}$ is the bulk state, being i the bulk band. If the wave functions are normalized, the projections $P_n(i)$, obey:

$$\sum_{i=1}^{\infty} P_n(i) = 1. \tag{3.6}$$

The projections tell us the composition of the NW states in terms of the bulk states, and give a valuable information about their. Moreover, predictions concerning the allowed and forbidden optical transitions can be attempted with the help of this information. In the analysis presented below, only $k = 0$ NW states have been considered by projecting them onto Γ ($\boldsymbol{k} = 0$) bulk state.

3.1.1 Surface states and passivation

Before calculating the electronic states of GaN NWs, it is necessary to design a methodology to deal with the free surfaces. An efficient passivation is a crucial prerequisite for obtaining reliable results of the electronic structure.

More specifically, the application of the passivation in the pseudopotential method requires to find the adequate passivant pseudopotential. The simplest way is to assume that the dangling bonds are saturated by hydrogen atoms and to

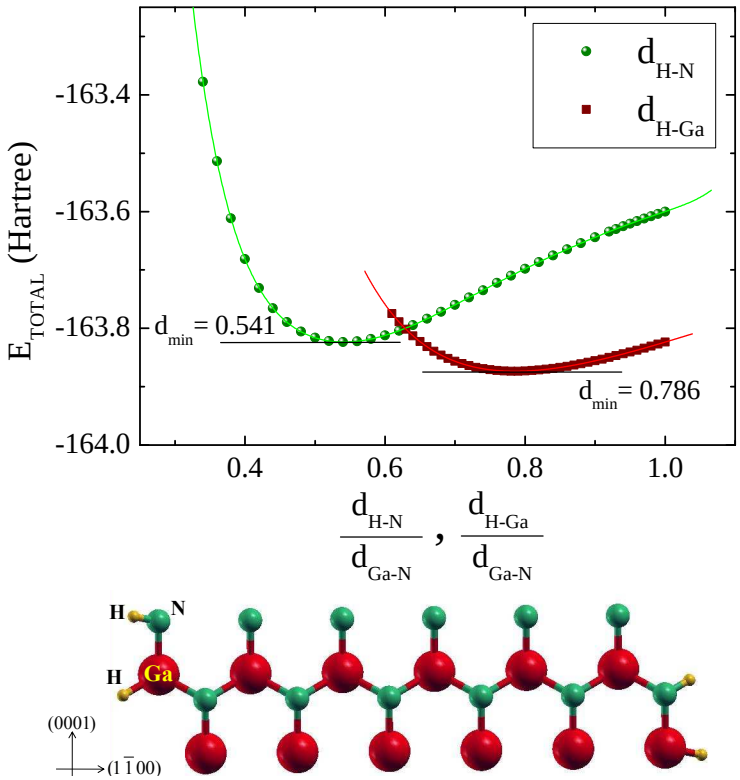

Figure 3.3: Total energy as a function of the distance between the hydrogen atoms attached to gallium and nitrogen atoms of the surface. In the lower part a ball-stick representation of the passivated layer is drawn.

model the hydrogen pseudopotential by an analytical function, such as a Gaussian profile with two parameters (height and width). In principle, this function must be different for each atom (gallium, nitrogen, aluminium, etc.) and one has to search the Gaussian parameters for each case. The method to optimize the form of the Gaussian function can be a simple trial and error procedure, or a more sophisticated approach. For instance, one can define a target function, such as the charge density inside the crystal, and search with a genetic algorithm the Gaussian function that maximizes this target [208]. However, the empirical parametrized Gaussian pseudopotentials involve iterative calculations of the electronic structure, which complicates the computational task, and this does not always guarantee to achieve an adequate passivation.

The SEPM presented in Section 2.2 to obtain *ab initio*-quality semi-empirical pseudopotentials of gallium, aluminium and nitrogen atoms, suggests the following question: Why do not adapt the methodology to obtain local-density derived passivating hydrogen pseudopotential? We propose to derive the hydrogen pseudopotential from LDA calculations on a very small free-standing structure, such

as a thin nonpolar layer, and then introduce this pseudopotential in the hydrogen placed in the lateral nonpolar surfaces of the nanowires.[2] In principle, as we have argued before, the atomic nature of this screened pseudopotential, and its good *transferability* properties, should allow its application also to the nanowire surface. In the next paragraphs we explain the steps followed to perform a proper passivation:

Step 1: Ab initio calculation of the self-consistent potential. We calculate within DFT-LDA the self-consistent potential of a free-standing $(1\bar{1}00)$ GaN layer, terminated by hydrogen atoms. The calculation is performed by arranging a periodic system, whose supercell is formed by the layer under study plus some portion of vacuum. The vacuum layer is thick enough as to prevent the coupling between neighbors GaN layers. Specifically, in each supercell, the GaN layer is approximately 15 Ångstrom thick, and the vacuum 10 angstrom in both sides. The dimensions of the GaN layer should be large enough to prevent the coupling between the two free surfaces, and thin enough to reduce as much as possible the computation time. In addition, these planes coincide with those of the GaN nanowires. Two different layers have to be calculated. The first one with unsaturated dangling bonds. The second one with the dangling bonds passivated by hydrogen atoms. The input hydrogen potential is taken to be the same for hydrogen atoms bound to gallium and nitrogen, being a Troullier-Martins pseudopotential with one electron [99]. For the atomic arrangement we assume the bulk lattice constants, and perfect wurtzite structure everywhere. However, the distance between the hydrogen and the corresponding gallium and nitrogen atoms must be determined by minimizing the total energy (E_{TOTAL}) of the passivated layer. Figure 3.3 shows two sets of points, corresponding to the dependence of E_{TOTAL} on the distance between the hydrogen and the gallium and nitrogen atoms, denoted as d_{H-Ga} and d_{H-N}, respectively. The polynomial fittings are represented with lines. From these results we determine the equilibrium and its electronic properties. After structure relaxation, we will in step 2 obtain the screened hydrogen potential. It is worth to mention that a correct passivation, in the sense of moving the surface states away from the band gap, could not be achieved without minimizing the total energy, as shown in Fig. 3.3.

The band structures of the bare and relaxed passivated $(1\bar{1}00)$-layers can be now examined. In Fig. 3.4 both LDA band structures have been represented. The conduction bands are plotted with red lines, the valence bands with blue lines and the surface state bands with green lines. First, the flatness of all bands

[2]Note that for calculations performed in polar layer, one should take care of the polarization fields of wurtzite semiconductor [209].

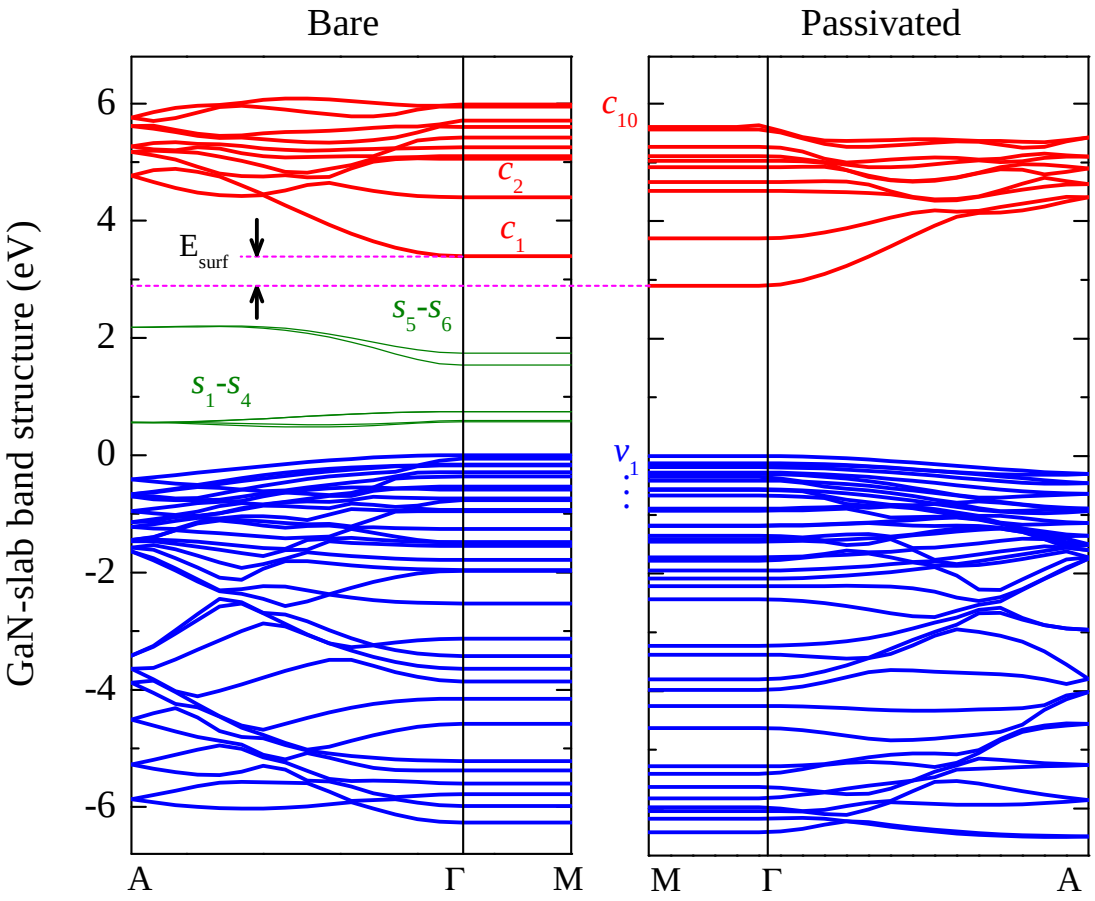

Figure 3.4: Band structure of a bare and passivated $(1\bar{1}00)$ GaN layers calculated with LDA.

along the Γ-M direction confirms the decoupling between adjacent layers, and therefore indicates that our results are representative of an isolated layer. The energy dispersion along the Γ-A line of the Brillouin zone is shown, exhibiting the same behavior as in the case of a quantum well [210]. The curvature of the conduction and valence bands is the same for both cases. We can appreciate that the bare layer has a larger band gap, with a difference of 0.370 eV. The main difference is obviously the presence of surfaces states, located within the band gap, in the case of the bare layer. These states are grouped in two energy ranges. The states $s_1 - s_4$ (the index assigned in increasing order of energy), are closer to the valence band edge and have a flatter dispersion . The other group, formed by the states s_5 and s_6, located in the middle of the band gap, have a more pronounced dispersion. On the contrary, the band structure of the passivated layer has no state within the band gap.

This analysis is further clarified by examining the charge density in real space.

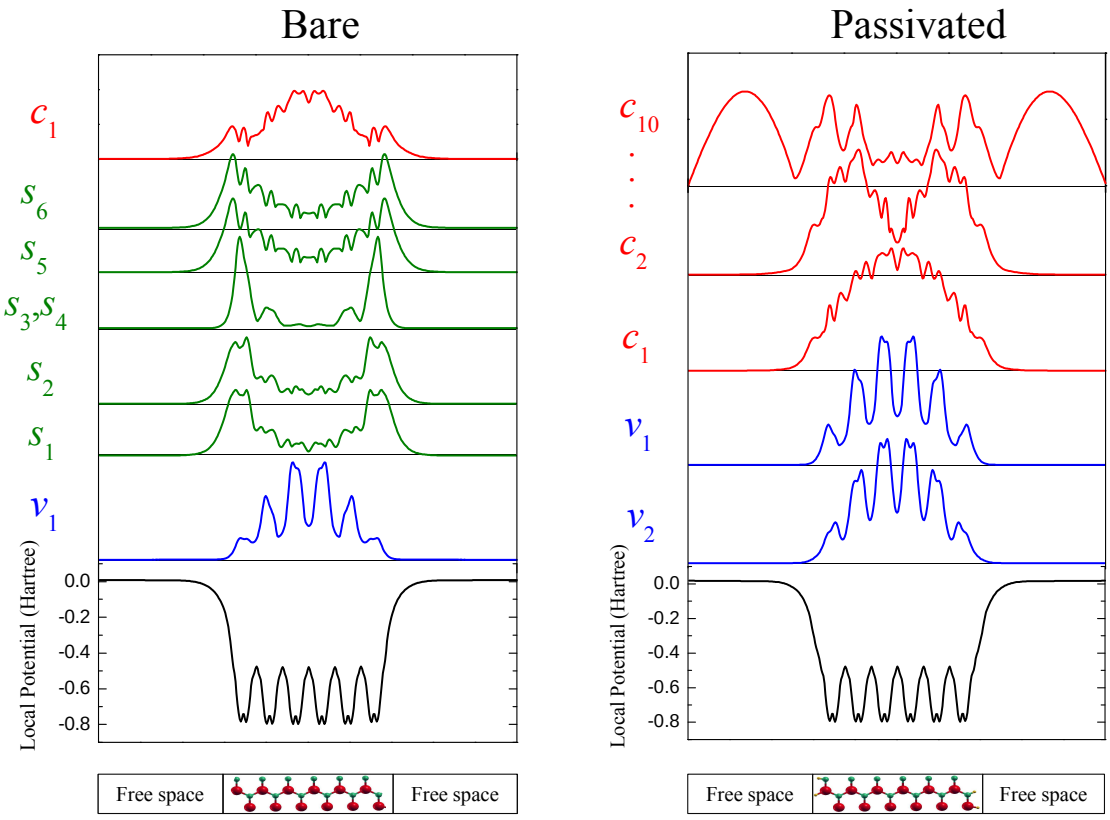

Figure 3.5: Selected Γ-point states, corresponding to the band structures of Fig. 3.4.

Figure 3.5 shows the plane-averaged self-consistent potential profile, along the $[1\bar{1}00]$ direction (lower panel), together with the plane-averaged density corresponding to some relevant states of the bare and passivated $(1\bar{1}00)$-layers (upper panel). The surfaces states $s_1, \ldots, s_6$ present different profiles. For instance, we can see that the mid-gap states s_5 and s_6 have a strong hybridization with the layer atoms, penetrating appreciably inside the layer. Correspondingly, the state c_1 in the bare layer shows a non negligible contribution near the surface. The charge density of the valence states seems to vanish at the surface. On the other side, the passivated layer shows all the conduction and valence states totally embedded in the crystal, without localization at the surfaces. In particular, note that the two surface peaks of the state c_1 in the bare layer have disappeared here. The valence states exhibit the same profile as in the bare slab. We can therefore conclude that the dangling bonds affect mainly the states of the conduction band. The conduction band state c_2 has a p-type envelope at $\boldsymbol{k} = 0$, as expected. The state c_{10} is the first one (2.70 eV above ϵ_{c_1}) showing coupling effects with neighbors GaN layers. In conclusion, we have illustrated by means of DFT-LDA calculations to which extent the passivation via hydrogen atoms is able to eliminate the surface states.

Step 2: Determination of the screened hydrogen pseudopotential. As we have demonstrated in Section 2.2 for the bulk system, we are able to determine the screened pseudopotential of an atom, from the self-consistent potential of the whole system. In this step, we read the self-consistent potential of each layer as calculated in the Step 1. If there are many interior atoms, and the vacuum space is large enough to prevent the coupling between adjacent layers, both potentials are expected to be very similar, except at the surface (see Fig. 3.4). Thus, it is reasonable to assume that the screened hydrogen pseudopotential can be obtained by subtracting from the passivated layer potential the one from the bare layer. By this simple operation, we can obtain a self-consistent potential around the hydrogen sites. Although the procedure is basically the same that for the bulk, the presence of vacuum and the existence of free surfaces introduces some difficulties in comparison with the bulk case, and some additionally approximations have to be applied in order to successfully obtain an efficient passivant pseudopotential. Such considerations have been discussed in Appendix B. Figure 3.6 shows the obtained hydrogen screened potentials that must be attached to the dangling bonds of gallium and nitrogen. Since only one electron is involved, the profile of both pseudopotentials is much simpler than in the case of gallium or nitrogen (see Fig. 2.7). A slight difference is observed when $q \to 0$, resulting from the distinct interaction between hydrogen and gallium or nitrogen atoms.

Step 3: Check the wave functions of the passivated layer obtained by the SEPM

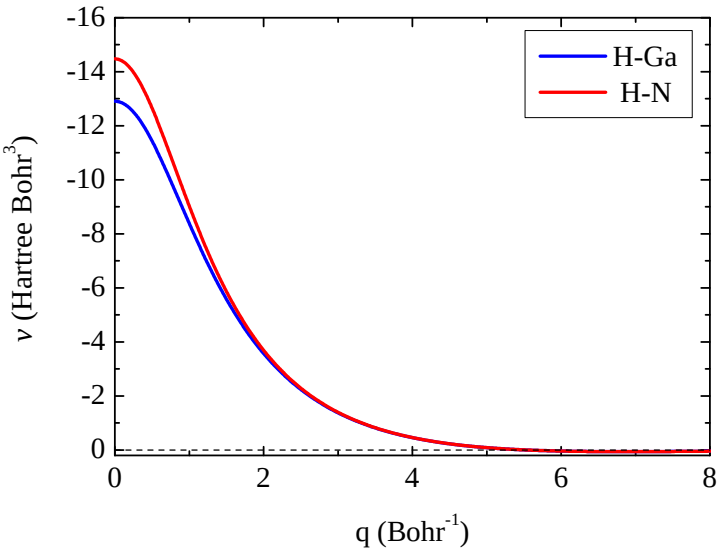

Figure 3.6: Hydrogen screened pseudopotentials, represented in the reciprocal space, as calculated following the procedure summarized in Appendix B.

with the hydrogen screened potentials. The correctness of the passivation procedure has been checked by applying the SEPM to the same slab used for the LDA calculations. Figure 3.7 shows (a) the energy spectrum and (b) the charge density of some conduction and valence band states. In these calculations the same cutoff energy of 30 Ry as in the case of GaN bulk has been used, and the nonlocal part of the Ga and N pseudopotentials is already adjusted to obtain the experimental bulk band gap. We have obtained a band gap cleared up of spurious states, with the state c_1 having a reasonable density profile, well embedded within the layer. The valence states v_1 and v_2 have the same s-type envelope that their counterparts LDA states. The discrepancies can be attributed to the small dimensions of the layer, and are expected to gradually disappear for larger nanostructures. To summarize, we have demonstrated a suitable passivation strategy in $(1\bar{1}00)$ GaN surfaces, based on the use of semi-empirical passivating hydrogen pseudopotentials. This procedure can be straightforward generalized to other surfaces and/or materials, such as $(11\bar{2}0)$ and (0001) surfaces. For every crystallographic orientation the distance between the hydrogens and the crystal atoms may change, and the potential will be slightly different. The hydrogen pseudopotentials obtained here are used in the next Subsection to calculate the electronic structure of GaN nanowires with $(1\bar{1}00)$ facets.

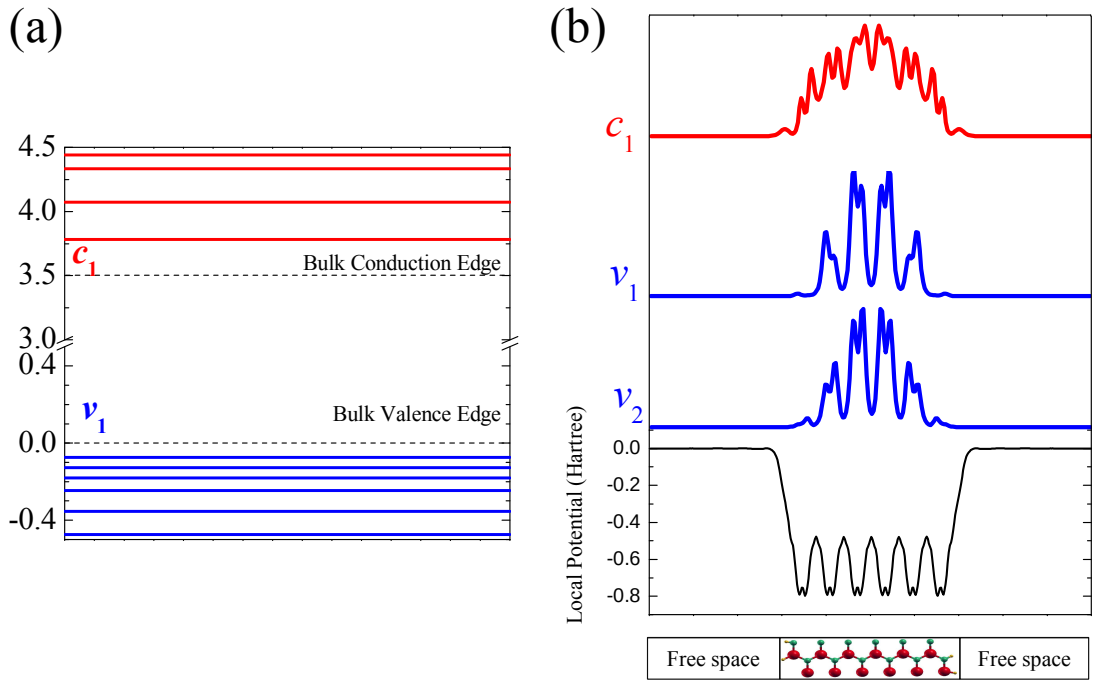

Figure 3.7: Energies and charge densities of selected states of a passivated slab, as calculated with the SEPM.

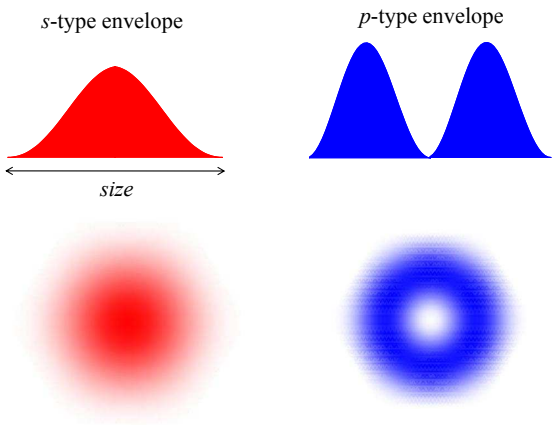

Figure 3.8: Schematic representation of the s-type and p-type envelopes of two nanowire states.

3.1.2 Electronic states of GaN nanowires

The GaN NWs studied here have hexagonal cross-section with lateral size ranging from 1 to 6.5 nm. The number of atoms in the supercell varies from 100 to 1500 approximately, and the computation time is significantly shorter here than in the corresponding *ab initio* calculations (that we have not tried), since we do not perform energy minimization. In the following results, there will be no surface states within the NW band gap or in the conduction or valence bands, as a result of the passivation procedure employed. In Fig. 3.8 we show the notation used here to characterize the envelope of the NW states, where the s-type corresponds to the Bessel function $J_0(x)$ and the p-type to the Bessel function $J_1(x)$. States related to Bessel functions of higher order do not appear in our study.

We begin our study with the analysis of the dependence of the electronic structure with the NW size. Figure 3.9 shows the confinement energy of the NW conduction band (CB) states, calculated at the Γ point, as a function of the NW size.[3] As we have highlighted during Chapter 2, the wide band gap of GaN bulk (see Fig. 2.3) decouples almost totally the conduction and the valence bands, and the first conduction band exhibits a parabolic profile in the vicinity of Γ. Moreover, the lowest conduction band is far away from the other conduction bands. Therefore, the confinement effects for the first NW CB states could be in principle similar to those predicted by a single-band model within the effective mass ap-

[3] We define the confinement energy as the difference between the energy of a confined electron in a NW and the band edge of the bulk material.

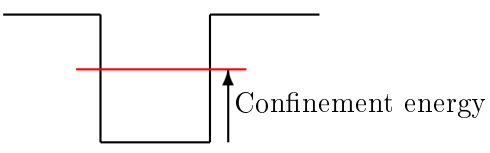

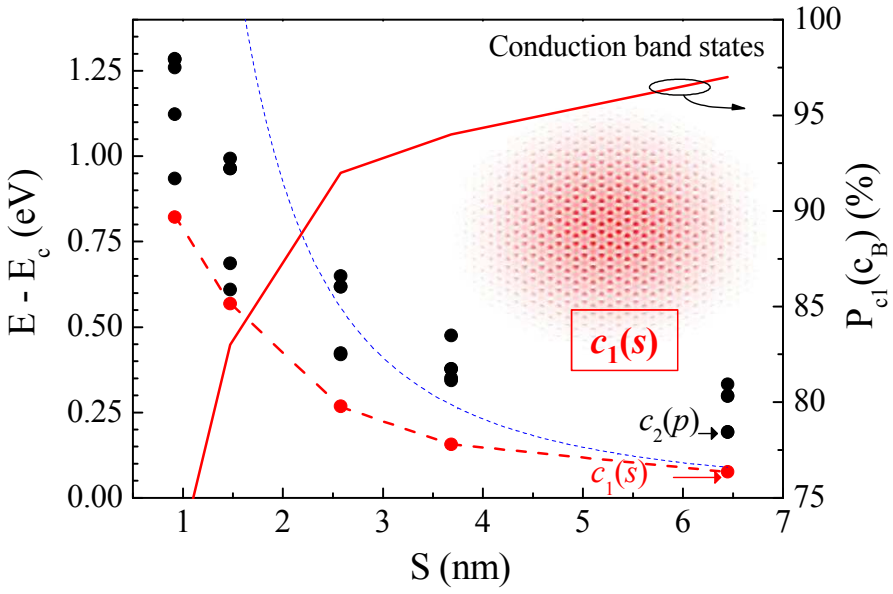

Figure 3.9: Confinement energy of the CB states as a function of the nanowire size (as defined in Fig. 3.1). The dashed line is the confinement energy of the CB state $c_1(s)$ given by the effective-mass approximation. The projection onto the bottom conduction state of the bulk is given by the red solid line. The charge density of the CB state c_1 for nanowire size of 6.5 nm is shown as an inset.

proximation (EMA). Under this assumption, it is expected a direct relationship of the NW CB states with the bulk CB edge state. Thus, the projection of CB state c_1, highlighted with red circles, is associated to the lowest bulk conduction band. The projection of c_1 onto the first conduction bulk state c_B, $P_{c_1}(c_B) = \langle \Psi c_1 | \Psi_{c_B} \rangle$, (which is represented by a red line in Fig. 3.9), tends towards $P_{c_1}(c_B) \sim 100\%$, for the largest size explored here, and stays above 75 % for the smallest radius. Therefore, the state c_1 comes mostly from the first bulk conduction band. Additionally, the c_1 charge density exhibits a clear s-type envelope for all the sizes explored here (see the case of 6.5 nm in the inset of Fig. 3.9). In order to know how much the confinement energy of the CB state c_1 deviates from the prediction of the single-band EMA energy, we have fitted its energy to the function

$$\varepsilon_{c_1}(S) = E_c + a\frac{1}{S^b}, \tag{3.7}$$

with S representing the NW size. We have found the values $a = 1.28 \pm 0.01$ and $b = 1.62 \pm 0.02$, with E_c fixed at 3.5 eV. This value of b differs from the prediction of the effective-mass approximation for a single-band

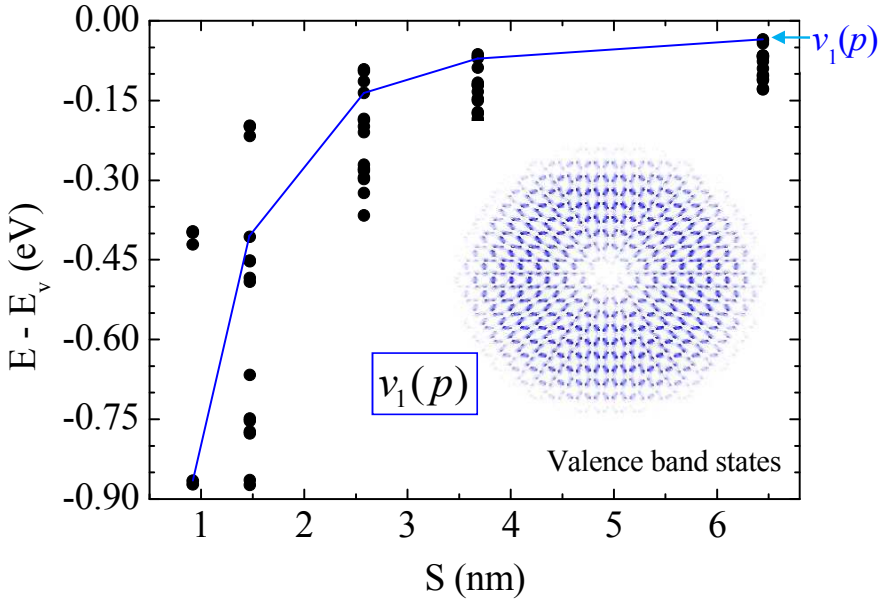

Figure 3.10: Size dependence of the confinement energy of the first VB states. The charge density of state v_1 is represented as an inset.

$$\varepsilon_{c_1}^{EMA}(R) = \frac{\hbar^2}{2m_{\perp}^{c}} \left(\frac{k_1^0}{R}\right)^2 \tag{3.8}$$

where we assume $R = S/2$ as the NW radius and $k_1^0 = 2.4048$ is the first zero of the Bessel function $J_0(x)$. We have also represented $\varepsilon_{c_1}^{EMA}$ in Fig. 3.9 by a dashed line (the electron effective mass of Table 2.3 was used). In spite of coming mainly from the CB bulk state, the CB state c_1 has a subtle mixing with other bands, which makes the single-band EMA results to overestimate the confinement energy, this discrepancy being more pronounced as the size is reduced.

For the NW CB states of higher energy, a stronger mixing is expected. Thus, by examining the CB state c_2 for the largest NW size, we have found a p-type envelope of the charge density, and a main contribution to the projection of the bulk state c_B. However, as the NW size is decreased the difference of energies $\varepsilon_{c_2} - \varepsilon_{c_1}$ does not follow a monotonous trend, having a maximum around $S \sim 3.6$ nm. We have also seen sudden changes in the charge density profile. The higher confinement energy of c_2 probably enhances the mixing with higher conduction bands. Nevertheless, these CB states have energies much higher than the NW band gap and would not be relevant in the study of optical transitions near the band edges.

We now turn to the analysis of the valence band (VB) electronic structure.

As opposed to what happens in the conduction band electronic structure, the symmetry mixing and spin-orbit coupling within the bulk valence (see Fig. 2.11) together with the weaker confinement effects (due to larger effective masses, presented in Table 2.3) will cause a complicated size dispersion of the valence band energy level structure of the GaN NW, as will be shown below. It is worth to mention that in the absence of the spin-orbit interaction there would be an exact degeneracy between orbitally symmetric (equivalent) states. This degeneracy is broken in our calculations including the spin-orbit interaction. Nevertheless, due to the symmetry mixing, it becomes impossible to identify quasi-degenerate pairs of states. Therefore, we have represented in Fig. 3.10 the energy levels of a set of representative $k = 0$ VB states. Specifically, we show the 15 highest-energy levels (labeled v_1 to v_{15}) for every NW size, irrespective of their symmetry properties. Thus, Fig. 3.10 gives an overall view of the confinement effects. For the largest NW explored (size of 6.5 nm), the set of 15 levels spans an energy range of around 120 meV, with the highest one showing a confinement energy of around 30 meV. On the other hand, for a small radius NW, say 1.5 nm in size, the levels span a range of 700 meV, and the highest one VB state being 200 meV below the bulk valence band edge. We have also studied the envelope of the wave functions. For the largest NW, the first confined state shows a p-type envelope, as shows its charge density, represented in Fig. 3.10. However, as the NW size is decreased, the envelope of the VB state v_1 becomes s-type.

From this first analysis we appreciate a complex interplay between the valence band mixing and the confinement mentioned above. The interpolation of the energy levels to represent the energy spectrum in Fig. 3.10 as a series of continuous size dispersion curves cannot be done without an exhaustive group theoretical analysis of the eigenvalue problem, that would allow to assign the exact symmetry (the group representation) of every state. Not having done this analysis, which is outside the scope of this work, we must content ourselves with an individual state-by-state analysis of the eigenstates obtained numerically.

A visualization of the charge density of the topmost valence band states for different sizes can help to understand the complex evolution of the energy depicted in Fig. 3.10, and to perform a state-by-state analysis. Figure 3.11 shows the charge densities of the first four VB states as a function of the NW size (lower panel). The corresponding energies are also drawn in the upper panel. A first examination reveals that the wave functions are well confined inside the NWs, and only for some states of the smallest NW there is a slight spreading beyond the surface atoms. In particular, the analysis of the charge density of the VB state v_1 shows that its envelope changes suddenly from p-type for the largest NW to s-type for smaller

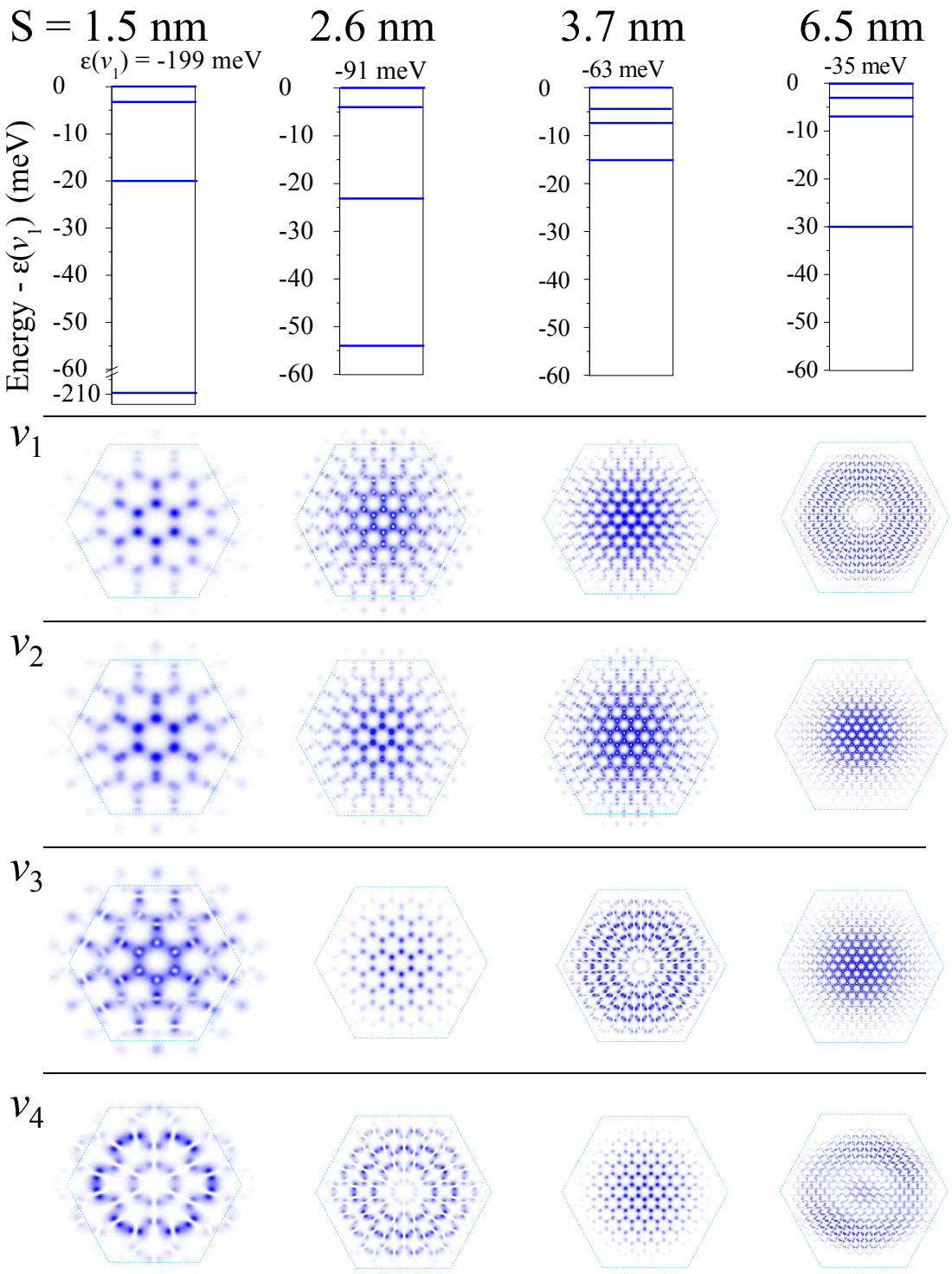

Figure 3.11: Energy (upper panel) and charge density (lower panel) of the first four valence states, v_1, v_2, v_3, v_4, for NWs of varying radius.

NWs. We can also appreciate that for size 2.6 nm and below, the first three VB states show a s-type envelope, and the VB state with p-type envelope is moved to the fourth place in the energy spectrum. Therefore, after a careful examination of the wave functions, we have traced a line connecting the state with p-type envelope, as depicted in Fig. 3.10. This shows a nontrivial evolution of such state. In particular, it crosses with the state of s-like envelope that turns out to be the first state for some size between 4 and 6 nm.

Having seen the evolution of the overall charge densities it would be necessary to complete the study by obtaining the projections of the NW valence band states onto the bulk states $A(\Gamma_9)$, $B(\Gamma_{7,+})$ and $C(\Gamma_{7,-})$, at the Γ point. This projection will give us additional information about the symmetry of the states. In Fig. 3.12 we have made a pie chart representation, wherein each piece includes the value of the corresponding projection ($P_{v_i}(A)$, $P_{v_i}(B)$ and $P_{v_i}(C)$), for the same set of NWs size of Fig. 3.11. We have tuned the degree of transparency to be proportional to the value of the projection. The violet portion contains the sum $P_{v_i}(A) + P_{v_i}(B) + P_{v_i}(C)$. We start the analysis with the largest nanowire shown here. The composition of the topmost state is almost equally divided between the bulk states A and B, which confirms the mixed nature of the VB state v_1 inferred above. The next two VB states, v_2 and v_3, clearly show a dominant contribution from states A and B, respectively ($P_{v_2}(A) = 82\%$ and $P_{v_3}(B) = 76\%$). Neither of these two states has a significant contribution from the C-band. When the nanowire size is reduced we observe that the mixed state A-B is not the topmost state anymore, becoming v_3 with energy -35 meV for $S = 6.5$ nm and v_4 with energy -135 meV for $S = 2.6$ nm. For these two sizes, the two topmost states exhibit an almost pure composition of A and B bands, and a state with main contribution from the C band has appeared between the first four valence states. In addition, the impossibility of identifying quasi-degenerate pairs of states is clearer from the analysis of Fig. 3.11 and Fig. 3.12. Thus, the states v_1, v_2 and v_3 for NW sizes of 1.5 and 2.6 nm, where they show a mix composition A-B-C, having the same s-type envelope and being ambiguous the identification of two equivalent states.

Therefore, the detailed analysis of the NW wave functions as a function of size, allows us to define the state with p-type envelope function as a mixture of bands A and B. This is possible due to the interplay of different factors that enhance the mixing. The first is a weak spin-orbit interaction, and the second is the large valence band effective masses, which prevent an excessive separation of the energy levels due to the quantum confinement. This unconventional trend of the nanowire electronic structure has also been reported by calculations using the tight-binding method [117]. Moreover, studies in other wurtzite systems, as the one made in

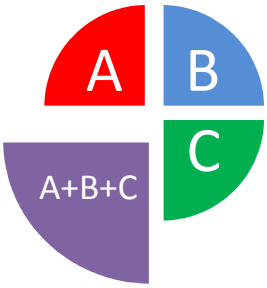

$A \equiv \Gamma_9$

$B \equiv \Gamma_{7,+}$

$C \equiv \Gamma_{7,-}$

S (nm)	1.5	2.6	3.7	6.5
v_1	3 40 89 46	76 8 90 6	79 9 93 5	50 47 97 0
v_2	69 7 81 5	7 68 92 17	9 75 95 11	82 12 97 3
v_3	4 29 86 53	3 8 96 85	48 45 94 1	18 76 97 3
v_4	41 42 83 0	45 45 90 0	3 6 98 89	38 42 96 16

Figure 3.12: Scheme of the projection of the NW states onto the bulk valence band states (at Γ), A (red),B (blue), and C (green). The bulk bands are defined in Fig. 2.11. Inside each portion we have written the corresponding percentage. The violet portions are $A+B+C$. Transparency of colors is proportional to the projection value.

ZnO nanocrystals by S. Baskoutas and G. Bester [211] shows also that the highest state of the valence band is characterized by a p-type envelope.

To conclude this Section we will discuss qualitatively the possible optical transitions between the valence band and the conduction band states for a fixed nanowire size. As discussed in Chapter 2, each $\boldsymbol{k} = 0$ state from the bulk valence bands belongs to a specific representation, which can be Γ_9 or Γ_7. Due to the inclusion of spin-orbit interaction, the states Γ_9, $\Gamma_{7,+}$ and $\Gamma_{7,-}$ at the Γ point can no longer be classified according to their atomic symmetry (p_x-p_y or p_z) due to the mixing induced by the spin-orbit interaction. This makes difficult the application of selection rules (see Fig. 2.16). However, in GaN, the spin-orbit interaction is much smaller than the crystal field interaction, and we can assume as a reasonable approximation to consider the states A and B belonging to the representation Γ_5 and the state C to Γ_1 of the space group C_{6v} (without spin). This approximation is useful for a qualitative understanding without explicitly calculating the oscillator strength. Figure 3.13 illustrates the charge density of the conduction ($c_1(s)$ and $c_2(p)$) and valence states ($v_1(p)$, $v_2(p)$ and $v_3(p)$) for a nanowire with size 6.5 nm, together with an scheme of the relevant optical transitions. We explain through an example how to determine if one transition is allowed or forbidden and which probability it has. In general, transitions that involve s and p-type envelope are considered as forbidden due to the small spatial overlap. Thus, if we take the states $v_1(s)$ and $c_1(p)$, we can appreciate the small spatial overlapping due to the distinct envelope function. Alternatively, the transition $v_2(s)$-$c_1(s)$ has a large spatial overlap, and the main contribution to the state $v_2(s)$ comes from the state A (symmetry Γ_5). Therefore, this transition is almost totally in-plane polarized ($\boldsymbol{e}_\perp$ light polarization, see Fig. 2.16). Thus, the oscillator strength of a transition from a VB state to a CB state will vanish if their envelopes are different. On the contrary, its value is one their envelopes are the same. The oscillator strength value for each light polarization is estimated with the projection value, where $P_v(A) + P_v(B)$ is related to $\boldsymbol{e}_\perp$ and $P_v(C)$ to $\boldsymbol{e}_z$.

In Figure 3.14 we have summarized the relevant optical transitions in the energy range close to the nanowire band gap. We have represented the oscillator strength (at $k = 0$) versus the transition energy. As we can see, there is a larger number of allowed transitions for $\boldsymbol{e}_\perp$ light than for $\boldsymbol{e}_z$ light. In addition, the energy difference between the first transition for each polarization is 32 meV, being the lowest one corresponding to in-plane polarization. It is also noticeable the fact that for this NW size the lowest transition (NW band gap), namely $v_1(p)$-$c_1(s)$, is not optically (dark) allowed. Nevertheless, this will be a hardly observable effect since the first allowed transitions, v_2-c_1 and v_3-c_1 are shifted only 3 meV with re-

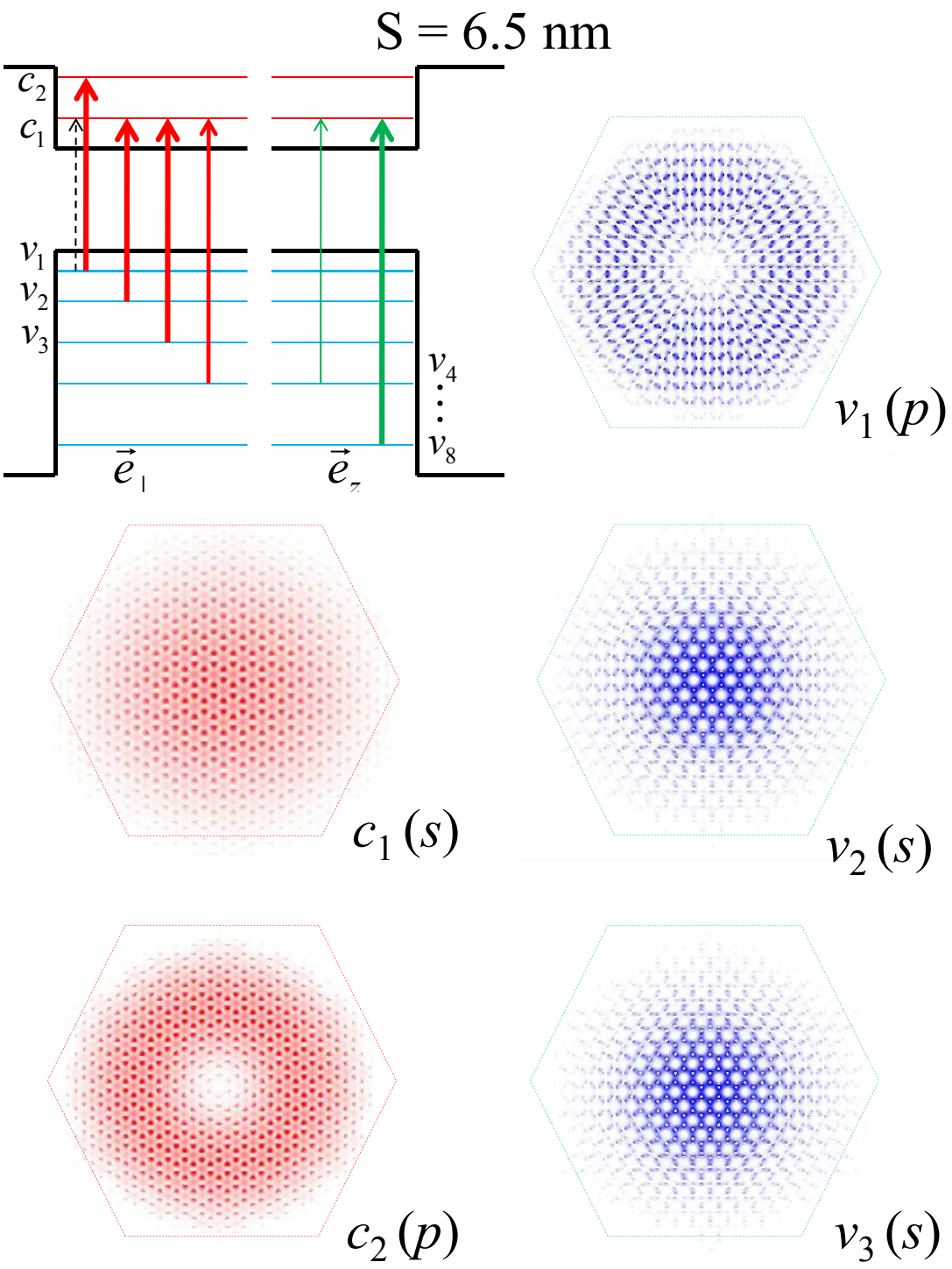

Figure 3.13: Squared wave functions of the first two conduction band states c_1, c_2, and the first three valence states v_1, v_2, v_3 of the NW with $S = 6.5$ nm.

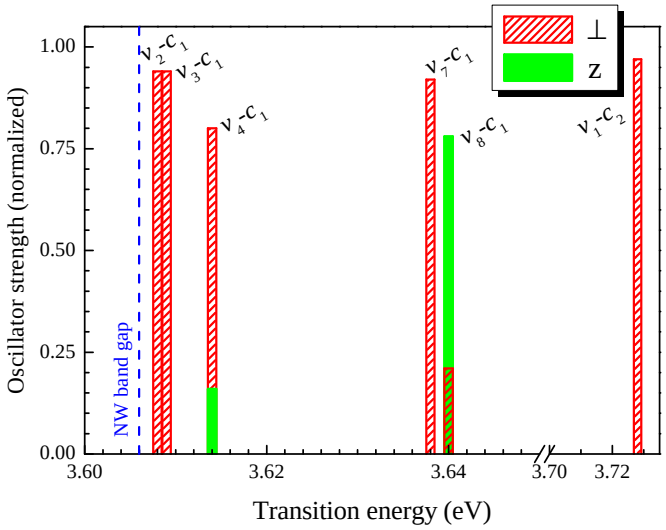

Figure 3.14: Oscillator strength versus transition energy. Red striped bars are transitions observable for in-plane light polarization and green filled columns are transitions for on-axis light polarization.

spect to the nanowire band gap. Moreover, a more complete study must include the calculations of the oscillator strength for every k, as we present in the next Section, in the framework of the tight-binding method.

In summary, we have demonstrated the applicability of the SEPM by performing a study of relatively large GaN nanowires that would have been extremely costly to perform directly by *ab initio* methods. The strategy designed to passivate the surface dangling bonds has been successfully applied to the nanowires surfaces. The main electronic properties of GaN nanowires, extracted from our study can be summarized as follows: (i) The complex interplay between valence band mixing and quantum confinement leads to a non-trivial valence band electronic structure. (ii) The anisotropy of the wurtzite structure is translated to the optical response of the GaN nanowires. (iii) Regarding the conduction band, although its behavior is simpler to interpret, it shows deviations with respect to the predictions of the single-band effective-mass approximation. The SEPM that we have implemented can be improved in order to achieve a still better computation efficiency. One possibility is to try to reduce the cutoff energy, by smoothing the screened pseudopotentials (a reduction of the energy cutoff), while keeping their *ab initio* quality.

3.2 Tight-binding method in III-N nanowires

In the previous Section, we have demonstrated the capability of the semi-empirical pseudopotential method to deal with small NWs, up to a size of 6 nm. However, in its present state, the SEPM is still prohibitive in terms of computational time for the exploration of sizes up to 15-20 nm. Alternatively, the tight-binding (TB) method has demonstrated its capability of performing calculations in structures with thousands of atoms in much shorter times, and presumably can give also reliable results [94, 118]. One of the reasons of its computational efficiency lies in the small sp^3 basis used here, which represents each atom by a small matrix 8×8 (including spin). Besides, the nearest neighbors approximation gives a Hamiltonian matrix (Eq. (3.2)) composed mainly by zeros (less than the 0.5 % of the Hamiltonian matrix elements are non-zero). This kind of matrix is called *sparse* matrix, and its eigenvalues and eigenvectors can be efficiently calculated by computational methods such as the Arnoldi algorithm (see Appendix C for details). Figure 3.15 illustrates the computation time versus the number of atoms required to obtain the energy spectrum of an InN nanowire of varying size, as calculated in a single processor (IBM AIX Power 5), with our implementation of the TB method. We can observe a nearly linear relation. This allows us to extrapolate that, *e. g.*, the time employed in the calculation for a nanostructure of one million of atoms, if performed in parallel with eight processors, would take 3-4 days.

On the other hand, the TB parameters used here have been adjusted to the III-N bulk band structures, and in principle lack the consistency of the semi-empirical pseudopotentials obtained by the robust procedure explained in Section 2.2. Therefore, it would be desirable to examine the reliability of the TB method to deal with nanostructures. It would also be interesting to establish the smallest NW size that the method can treat accurately. In this sense, the atomistic nature of the tight-binding method allows us to make a relatively unambiguous comparison with the *ab initio* approaches as we will shown later.

Before analyzing the results of our calculation about the electronic structure of III-N nanowires, it is convenient to present some definitions. As commented in the introduction of this Chapter, the states are labeled in increasing order of energy. Moreover, it is also interesting to analyze the shape of the charge density, defined as $n(\boldsymbol{r}) = |\Psi(\boldsymbol{r})|^2$. The $k = 0$ nanowire wave functions are written as follows:

$$\Psi_\Gamma(\boldsymbol{r}) = \sum_{\alpha,l} A_{\alpha,l} \varphi_l(\boldsymbol{r} - \boldsymbol{r}_\alpha), \tag{3.9}$$

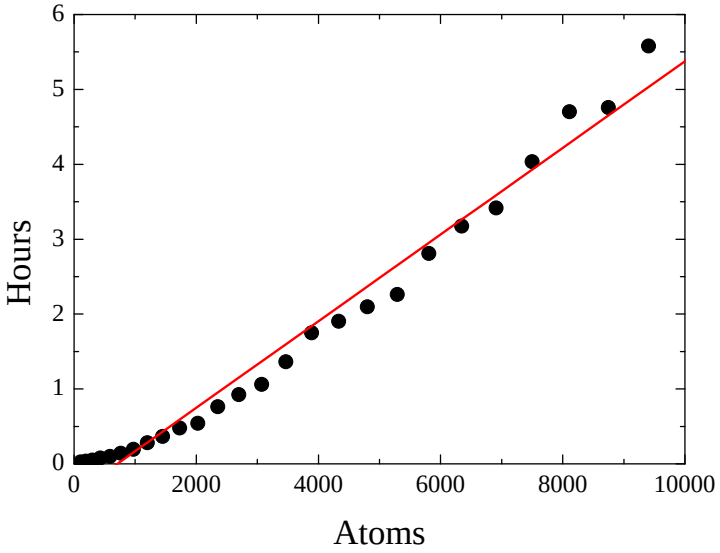

Figure 3.15: Band structure computation time versus the number of atoms of the NW. The approximate linear fit is $T(\text{hours}) \approx 6 \times 10^{-4}\text{N(atoms)}$.

where the index α runs over atoms and l over orbitals. In order to identify the orbital composition of the nanowires states when analyzing the TB results we denominate each state by its predominant character ($\phi_i > 50\%$), as defined in Section 2.3. As we know from Section 2.3, the functional dependence of the orbitals φ_l is unknown. To overcome this ambiguity we have chosen two ways of representing the wave function. (i) If we are interested in representing explicitly the orbital symmetry, we can substitute each orbital φ_l by the spherical harmonic that shares the same symmetry [212], and then averaging over the z variable in order to obtain a map of the density in the c-plane. Such representation gives a detailed picture of the charge distribution around the atomic sites, similar to those obtained in the SEPM (for instance, Fig. 3.11), and it results also very useful for the analysis of small nanowires. (ii) The other representation sums the coefficients $A_{\alpha,l}$ of atoms with identical coordinates in the c-plane, without differentiating between orbital symmetry, and gives a crude average of the charge density. However, this representation is clearer for larger nanowires, where the atomic detail can be misleading.

The optical absorption of III-N nanowires, calculated as explained in Section 2.4, is also investigated for light polarization $\boldsymbol{e}_\perp$ (in-plane) and $\boldsymbol{e}_z$ (on-axis). The broadening Γ introduced to represent the delta function in the absorption spectrum is 10 meV in all the cases.

We have organized this Section as follows: First, the passivation of the free

surfaces is formulated in the framework of the tight-binding model. Next, an assessment of the TB parameters fitted to bulk InN is performed by comparing the band structure and wave functions obtained by the TB method and the LDA+U approach for small nanowires. The subsequent Subsections are devoted to a comparative study of the electronic structure and the optical properties of InN, GaN and AlN nanowires.

3.2.1 Treatment of free surfaces in the tight-binding model

In Subsection 3.1.1 we have defined the procedure used for the passivation within the SEPM of dangling bonds at the free surfaces. Here we will give the procedure followed within the tight-binding method.

The use of the TB method in systems with free surfaces has been traditionally related to the theoretical study of the porous silicon. This was motivated by the measurement of intense photoluminescence from porous silicon, attributed to quantum confinement effects in the existing holes inside the material [213–215]. In this context, the TB method is an ideal tool because given its atomistic nature it can model any structure shape. Moreover, it could be implemented in large supercell calculations, thus gaining tremendous popularity in the study of nanocrystals or nanoparticles of silicon, germanium, among others materials [216, 217]. These advantages have made the TB method a broadly used tool to study the optical properties of nanostructures, and in particular, of nanowires [116–118].

Within the TB model, the passivation is carried out in essentially the same way that in the SEPM, *i. e.*, by attaching a hydrogen atom at each dangling bond. However, instead of defining a passivant pseudopotential, an s orbital is assigned to each hydrogen atom, according to the TB formulation [218]. The interaction between the hydrogen and the orbitals of the wurtzite atoms is modeled by writing the interaction parameter according to the Harrison's rule:

$$V_{H-\lambda}(d) = \left(\frac{d_0}{d_{H-\lambda}}\right)^{\eta_{H-\lambda}} V_0, \tag{3.10}$$

where the parameter V_0 is a concise notation for any of the overlap integrals $V_{ss\sigma}$, $V_{s_c p_a \sigma}$, and $V_{s_a p_c \sigma}$ described in Section 2.3. The interatomic distances d_0 and $d_{H-\lambda}$ correspond to the bulk wurtzite structure (d_0), and to the distances between the hydrogen atom and atom of the III-N compound, $\lambda = c, a$, for cation and anion, respectively. For the sake of simplicity we assume the same distance $d_{H-\lambda} = \frac{1}{2}d_0$ for all the dangling bonds, independently of the atomic species. This is in concordance with the *ab initio* results for the GaN shown in Fig. 3.3, where $d_{H-\lambda} <$

d_0. The exponent $\eta_{H-\lambda}$ enters here as a fitting parameter. Also for simplicity, the value of $\eta_{H-\lambda}$ is imposed to be the same for every atom and every orbital, denoted in the following as η_H. The interaction between different hydrogen atoms is disregarded. Here, the limiting case of an unpassivated nanowire would be represented by $d_{H-\lambda} \to \infty$.

The influence of the parameter η_H on the nanowire band structure is illustrated in Fig. 3.16 through an example for InN NWs. Figure 3.16 shows the energy of the first conduction band state, c_1, as a function of the NW size, for several values of the exponent η_H. It is important to note that for all the η_H shown here, there are no surface states within the band gap at all. However, smaller values of η_H, or distances $d_{H-\lambda}$ too large, could lead to the presence of states within the band gap. In Fig. 3.16, we see that the sensitivity of the c_1 energy to the parameter η_H is reduced as the NW size increases, the change in the energy being negligible for $S > 6$ nm. This is consistent with the fact that for larger NW cross sections, the surface effects are less important. Moreover, there is no hybridization between the conduction states and the surface states. In the inset of Fig. 3.16 we have fixed the nanowire radius to $S = 1.6$ nm, and plotted the energy of the state c_1 versus η_H. For $\eta_H \gtrsim 3.5$, a saturation of the energy is observed, reminiscent of the *hard-wall* condition (infinite barrier), often used in the effective-mass approximation. Concerning the valence band states, they do not show significant changes in their energy in the range of the parameter η_H studied here. This is again understandable since the interaction of the hydrogen atoms with p orbitals takes place only through the parameters $V_{s_c p_a}$ and $V_{s_a p_c}$. It also agrees with the results of the pseudopotential method for the GaN $(1\bar{1}00)$-layer presented in Section 3.1, where the valence band wave functions remained almost identical in the cases of unpassivated and passivated surfaces. The passivation procedure in the TB model is much simpler than in the SEPM (see Section 3.1), since it only requires one parameter η_H to be fixed. We have determined η_H for InN NWs by adjusting the band gap of a small NW to the value obtained by LDA+U calculations, as shown below. The parameters η_H for GaN and AlN NWs have been adjusted to the available *ab initio* or semi-empirical approaches data for small NWs.

Now we examine the electronic structure and optical absorption of III-N nanowires obtained by means of the TB method.

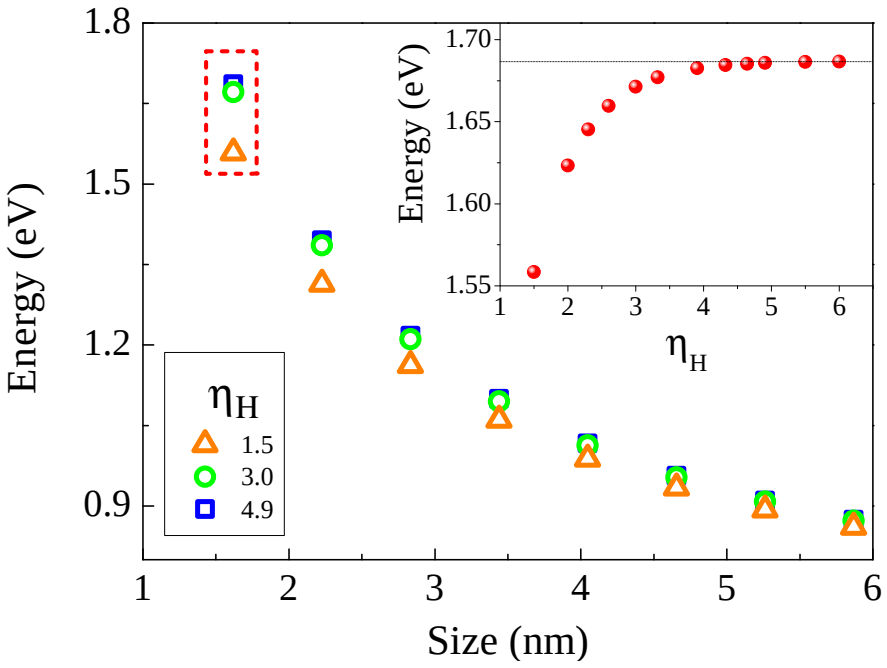

Figure 3.16: Energy of the first CB state, c_1, as a function of the InN NW size, for different values of η_H. In the inset, variation of the energy with the parameter η_H for fixed size, $S = 1.6$ nm.

3.2.2 Assessment of the tight-binding parameters: Comparison with LDA+U results

The tight-binding parameters are usually deduced from a bulk band structure, as we have shown in Section 2.3. Its use is justified when the nanostructures are large enough. However, it is somewhat uncertain the minimum nanostructure size for which their use is reasonable. In addition, there is some controversy about whether an increase in the number of the atomic orbital used would be needed for the electronic structure calculations of small nanostructures [184–186]. A robust test would be to compare the tight-binding results with those obtained from *ab initio* calculations for a small nanostructure. In this Section we make such a study by comparing the electronic structure of a small InN nanowire ($S = 1.6$ nm) as obtained with the LDA+U and the tight-binding methods. To make the comparison we can neglect the spin-orbit interaction, because it only affects slightly the band structure. The LDA+U calculations shown here have been performed by A. Terentjevs and G. Cicero, from the Politecnico di Torino (Italy) [161].

The electronic structure of an InN nanowire of $S = 1.6$ nm has been calculated first with the LDA+U, by passivating the dangling bonds at the surface with

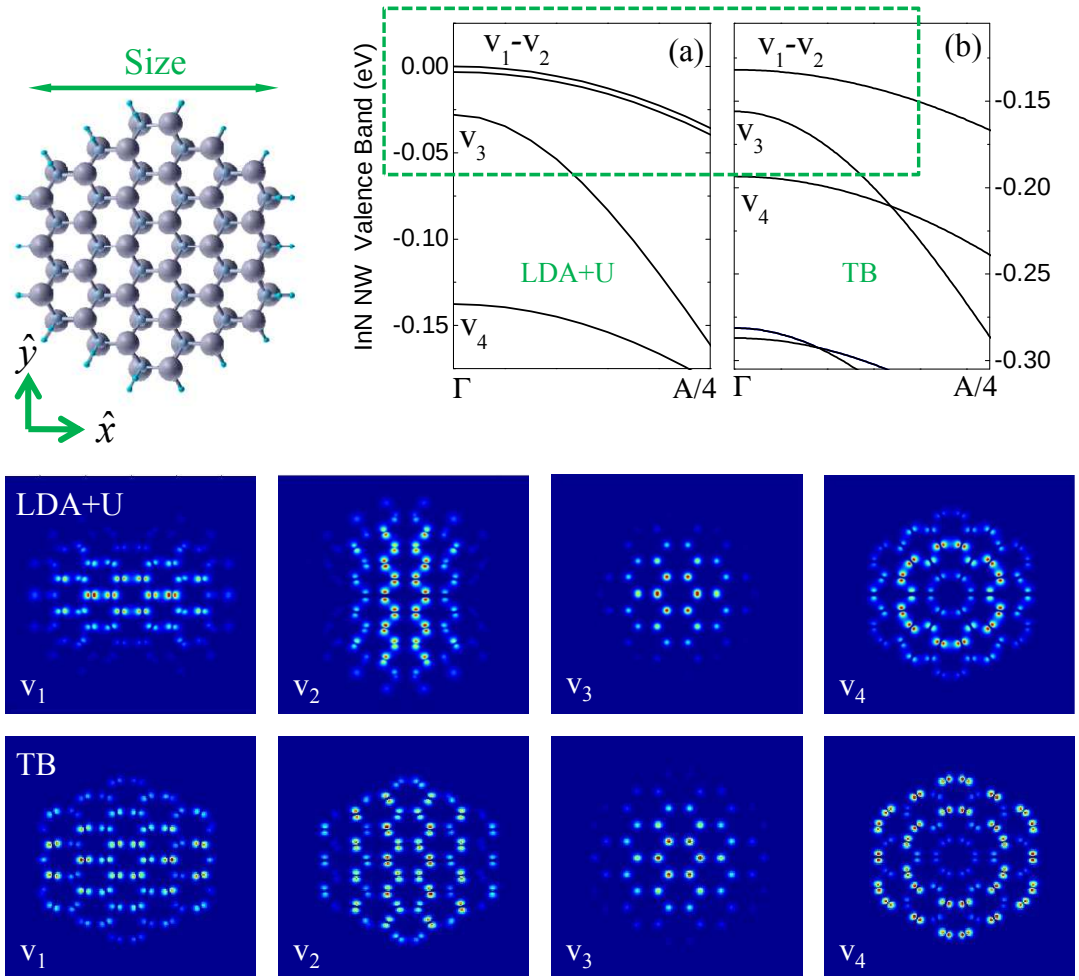

Figure 3.17: In the left upper part, ball-and-stick picture of a nanowire of size 16.2 Å. In the right upper part, top of the valence band as calculated with (a) LDA+U (b) and TB method. In the lower part, we represent the square of the wave function for the valence band states v_1, v_2, v_3, and v_4 as calculated with both approaches.

hydrogen atoms, as usual. The nanowire atomic arrangement has been fully optimized until forces are less than 0.001 Ry/Bohr per atom. A Monkhorst-Pack mesh of 6 points for the one dimensional nanowire Brillouin zone has been used. It is found that the indium and nitrogen atoms placed at the surface, have their tetragonal bonds slightly distorted due to the presence of the passivant hydrogen atoms [219]. This surface reconstruction is not taken into account in our tight-binding calculations, which assume a perfect wurtzite everywhere [117].

A ball-and-stick representation of the nanowire used in our calculations is given in Fig. 3.17 (upper part), together with the topmost valence band states, as obtained by the (a) LDA+U and (b) TB methods. The states v_1 to v_4 are within a

range of 150 meV in both calculations. The TB result yields in addition the value of -130 meV for the confinement energy of the states v_1 and v_2 with respect to the top of bulk valence band. In the case of the LDA+U calculation, the degeneracy between v_1 and v_2 is broken (the splitting being around 3 meV) due to the exact consideration of the atomic distances when the structure is relaxed, an effect that the TB method ignores. In any case, the portion of the band structure framed by a dashed green line, that contains the v_1, v_2, and v_3 sub-bands, exhibits a remarkable similarity in both calculations. In particular, the curvature of the bands is identical and only a slight difference in the energy splitting of the states v_1 and v_3 (26 meV and 18 meV for LDA+U and TB calculation, respectively) is observed. On the other hand, the v_4 state is closer in energy to v_3 in the TB calculations than in the LDA+U approximation. Despite that its confinement energy is underestimated by the TB calculation, v_4 has the same curvature in both approaches. Another difference is the appearance of more states (v_5, v_6,...) in the range of -150 meV from the state v_1, in the case of TB calculation than in the LDA+U one. In order to exclude the relaxation performed in the LDA+U calculation as a source of these discrepancies, calculations with LDA+U in a nanowire with perfect wurtzite structure arrangements everywhere were also performed, without finding any substantial difference with those for a relaxed NW.

Once the overall agreement of the valence band structure has been confirmed, we can go further in the test of the TB method, by comparing the squared wave functions, *i. e.*, the charge density, of the four valence band states, from v_1 to v_4. The lower part of Fig. 3.17 shows the charge density maps calculated by both methods. To plot the TB charge densities we have used Eq. (3.9). We can see the charge density localized on the indium and nitrogen atoms, without significative spreading towards the hydrogen atoms. Concerning the first two degenerate valence band states (v_1 and v_2), they exhibit an electron density elongated along two perpendicular directions (x and y). By looking closely to the density near each atom, it is evident that it is dominated by the p_x and p_y orbitals, for the x-elongated (v_1) and y-elongated (v_2) states, respectively. In the next valence band state, v_3, the wave function is notably confined at the center of the NW, being the p_z-orbital component predominant. In the case of the v_4 state, we find that the wave function has a node at the nanowire center, and a mixed composition of p_x and p_y orbitals. One can appreciate that TB charge densities are more delocalized toward the nanowire surface as compared to the LDA+U ones. However, the TB method reproduces exactly the qualitative behavior of the charge density in terms of symmetry and orbital composition. Concerning the charge density of the first conduction band state, both models give an identical picture (not shown here),

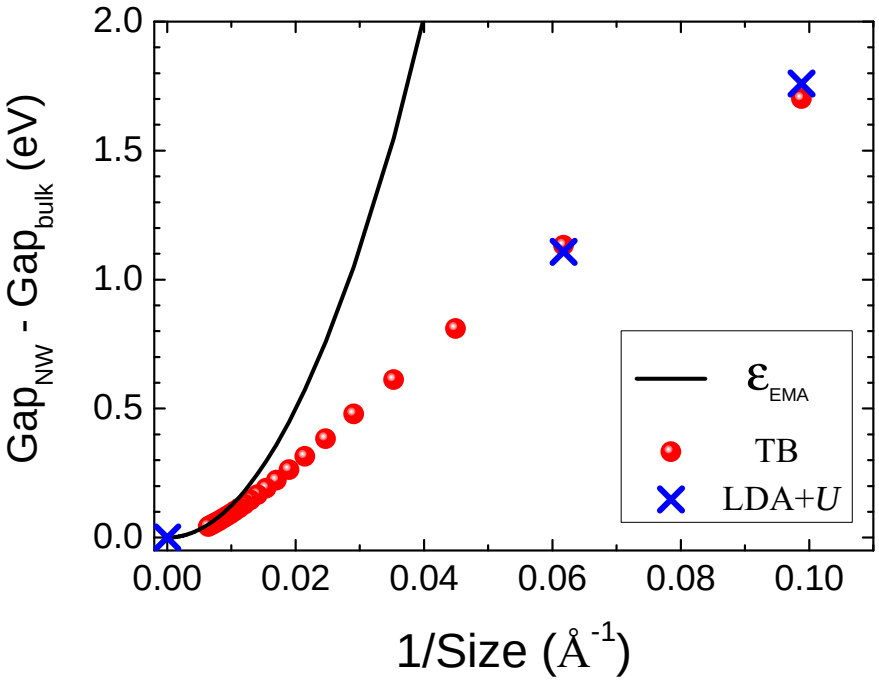

Figure 3.18: Dependence of the confinement energy on the nanowire size. The limit of $1/S \to 0$ corresponds to the bulk material.

with the density concentrated at the NW core. Overall, we consider the comparison between both sets of results are very satisfactory given the small size of the TB basis and the tiny NW size. For larger NWs, the small differences between the TB method and the LDA+U approximation are expected to be reduced, but that kind of comparison is difficult due to the computation time limitations.

Regarding the conduction band, a direct comparison of the TB method with the *ab initio* results cannot be done, since the band gap was set to the experimental value (0.67 eV) in the current set of tight-binding parameters, and LDA+U underestimates this value (0.34 eV). Alternatively, we can compare the calculated confinement transition energies for both approaches.[4] Figure 3.18 shows the confinement transition energy, versus $1/S$, being S the NW size. The red spheres correspond to the TB results and blue crosses to the energies calculated with LDA+U. In addition, it is also shown (solid line) the confinement energy calculated within the effective-mass approximation (EMA), by assuming parabolic valence and conduction bands

[4]The confinement transition energy is $E_{\mathrm{g,NW}} - E_{\mathrm{g,bulk}}$

$$\varepsilon_{\mathrm{EMA}} = \left(\frac{\hbar^2}{2m_{\perp}^{c}} + \frac{\hbar^2}{2m_{\perp}^{A}}\right)\left(\frac{k_1^0}{R}\right)^2, \tag{3.11}$$

where $k_1^0 = 2.4048$ is the first zero of the Bessel function $J_0(x)$, and the effective masses are reported in Sec. 2.3 (we approximate the radius as $R = S/2$). The TB and EMA predictions almost coincide for large sizes, $S > 30$ Å, the difference being related to the non-parabolic conduction band of InN, typical of narrow band gap semiconductors. For decreasing size ($S < 5$ Å), the EMA overestimates the confinement energy as compared with the TB results, that changes in this range the behavior from $\sim 1/S^2$ to $\sim 1/S$. Moreover, the TB results connect perfectly with the *ab initio* computed values, for sizes of 16 Å and 10 Å. This smooth interpolation confirms the suitability of the TB method to link the NWs size ranges of ~ 10 Å, where *ab initio* calculations are feasible and ~ 100 Å, where the EMA starts to be applicable. For this intermediate size range, the TB approach has the advantages of keeping the atomistic nature of the system and be efficient in terms of computational effort.

We can conclude that the TB parameters obtained and tested here are suitable to be used in the calculation of optical properties of InN-based nanostructures. The sets of TB parameters obtained for GaN and AlN by an identical procedure, should be as good as the InN parameters for the simulation purposes. In the next Subsections we will study in detail the band structure and the optical absorption of the III-N nanowires, InN, GaN and AlN.

3.2.3 Electronic structure and optical properties of InN nanowires

The reliability of the TB approach demonstrated above allows us to extend the use of the model to large structures. The spin-orbit interaction, omitted for the comparison with the LDA+U results, is now included in all the subsequent calculations.

Band structure

We start with the analysis of the band structure. As we have seen in Fig. 3.18, the NW band gap does not follow the $1/S^2$ behavior, as a consequence of the strong coupling between the conduction and valence bands. We add to our study the information given by the state character, which helps us in the understanding of the NW band states behavior when the NW size changes.

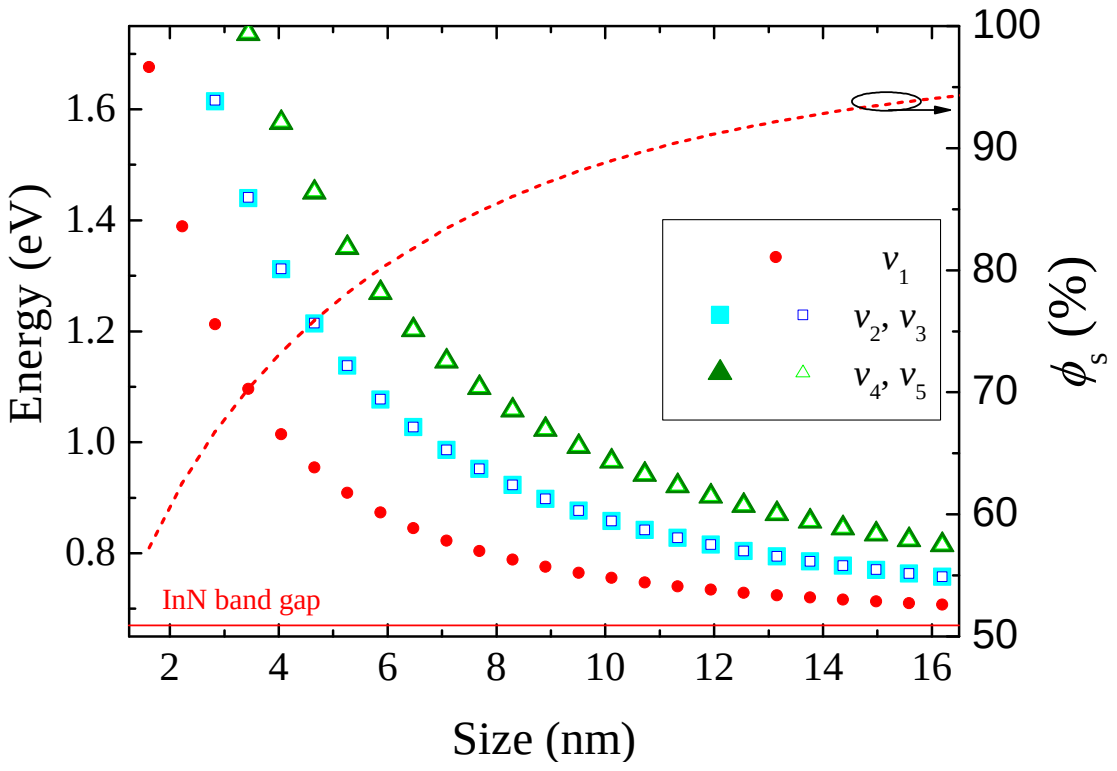

Figure 3.19: Energy of the InN NW conduction states versus nanowire size. The energy of InN bulk band gap is also indicated. The *s*-orbital contribution is represented with a dashed line.

Figure 3.19 shows the variation with the NW size of the energy of the first five conduction band (CB) states at Γ point. In the absence of the spin-orbit interaction, there would be an exact degeneracy between orbitally symmetric (equivalent) states. This degeneracy is broken in our calculations including the spin-orbit interaction, and the CB states labeled (c_2, c_3) and (c_4, c_5) are no longer degenerate. Nevertheless, the corresponding splittings $\epsilon_3^{(c)} - \epsilon_2^{(c)}$ and $\epsilon_5^{(c)} - \epsilon_4^{(c)}$ are so small (< 5 meV) that they cannot be appreciated in Fig. 3.19. The small band gap of InN leads a strong coupling between the conduction and the valence bands, and the conduction band cannot be considered parabolic around Γ point. Moreover, the small effective mass of the conduction band produces a large quantum confinement of the CB states, which still remains for large sizes ($\epsilon_{c_1} - E_c \sim 35$ meV at $S = 15$ nm). On the other side, the lowest CB energies exhibit a monotonous decreasing evolution with the NW diameter, without any crossing or anti-crossing effects. This is related to the single lowest conduction band of the InN bulk band structure, shown in Fig.2.13, that prevents of the mixing between different conduction bands. It is also interesting to quantify the deviation of the first CB state energy with respect to the prediction made by the EMA. Thus, the energy ϵ_{c_1} has been fitted to the function:

$$\epsilon_{c_1}(S) = E_c + \frac{a}{S^b} \quad , \tag{3.12}$$

and obtained the values: $a = 1.94 \pm 0.05$ and $b = 1.28 \pm 0.02$, being $E_c = 0.67$ eV. This function deviates significantly from the $\sim 1/S^2$ function of the EMA for a single-band. Further proof of the inadequacy of the single-band approximation applied to the case of InN NWs is revealed by the c_1 state character. Figure 3.19 also shows the s-orbital contribution of the CB state c_1 (dashed line). Notice that ϕ_s decreases below 85 % for NW sizes below 9 nm. The remaining contribution is provided by p_z orbitals.

In spite of the trend observed for the CB states, the analysis of the confinement effects in the valence band (VB) states reveals more complicate tendencies, as shown in Section 3.1. Thus, as presented in Fig. 2.15 and discussed in the case of GaN NWs in Section 3.1, we recall here the impossibility of identify exactly the quasi-degenerate pair of states as those shown in Fig. 3.19. Analogously to the exploration performed in Section 3.1, Figure 3.20(a) shows the energy at $k = 0$ of the first 20 valence band states as a function of the NW size (labeled from v_1 to v_{20}), irrespective of their symmetry properties. Two vertical lines highlight the nanowires sizes, which band structures will be shown later.

For the largest NW analyzed (of size 16 nm), the set of the 20 levels spans an

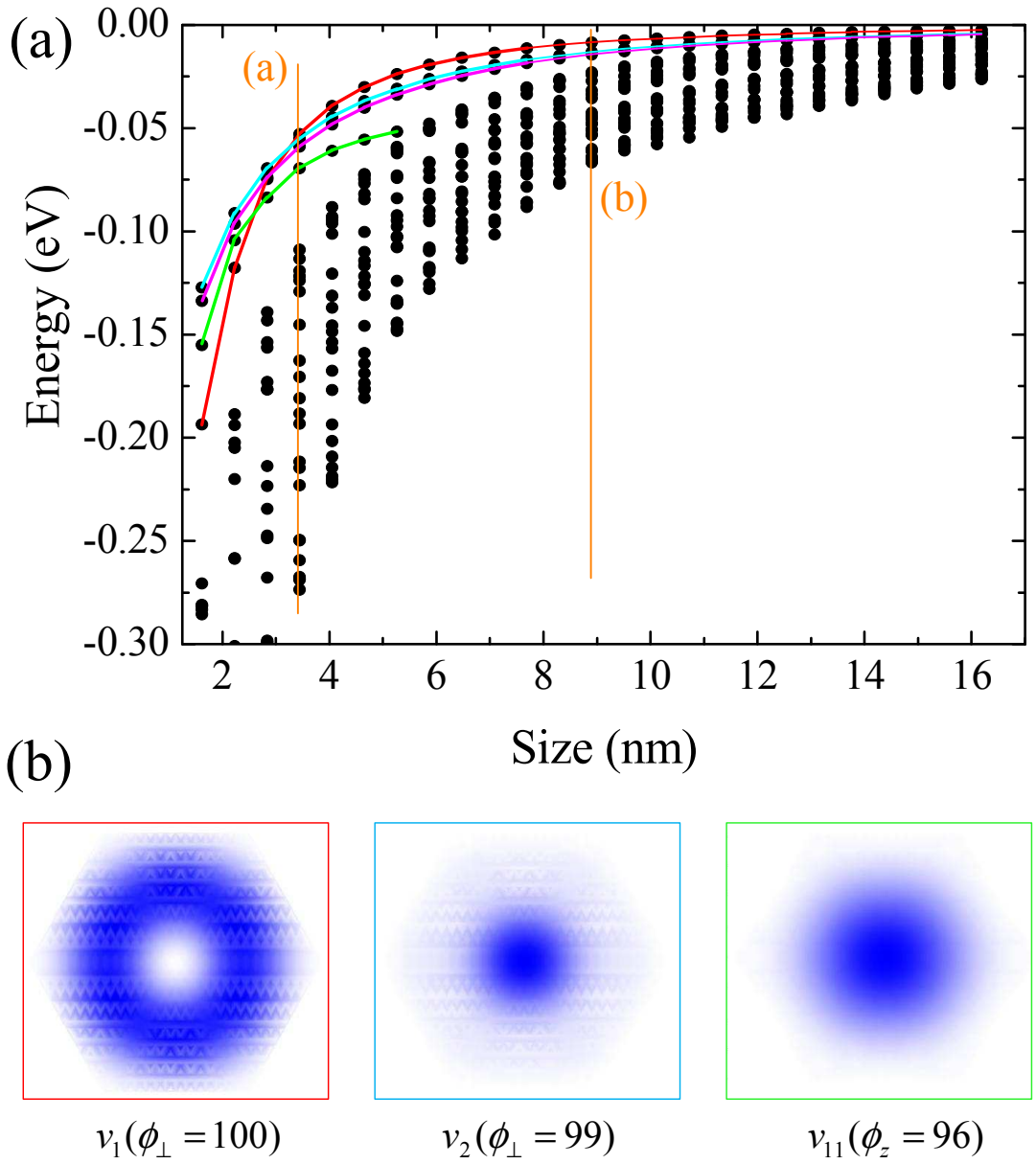

Figure 3.20: (a) Confinement energy of the first 20 valence band states versus the InN nanowire size. (b) Wave function of the states v_1, v_2, v_{11} with the main orbital contribution between parenthesis, for a InN nanowire of size 8.9 nm.

energy range around 30 meV, with the highest one showing a confinement energy of around 3 meV. On the other hand, for a small radius NW, say 5 nm in size, the levels span a range of 175 meV, and the highest one being 40 meV below the bulk valence band edge, showing a similar range from that calculated for GaN NWs. Concerning the spin-orbit interaction, it affects the electronic structure slightly, with a splitting not larger than 2 meV in the VB states explored here. The energy spectrum of Fig. 3.20(a) cannot be represented as a set of continuous size dispersion curves, due to the complex interplay between valence band mixing and confinement mentioned above. Alternatively, by examining the character of the topmost valence band states, and their corresponding charge densities, we have been able to trace various interpolating lines connecting states with the same global symmetry. We have traced interpolated lines for the VB states v_1, v_2 and v_3 (all of them with $p_\perp$-character) along the full range of sizes. For the VB state v_4 (with p_z-character) we have drawn the curve until 5 nm. This simple exercise already shows the existence of both crossing (between states of different symmetry) and anti-crossing effects (between states of equal symmetry). This results in a non-trivial and non monotonous evolution of such curves. In particular, a rather noticeable behavior arises as a consequence of this level interaction: The two quasi-degenerate VB states (cyan and pink lines), that occupy the topmost position in the valence band (see also Fig. 3.17) at $S = 1.6$ nm, become the second and third states for sizes above 4 nm. For a NW size above 4 nm, the first VB state v_1 (red line) has a node in the center. On the other hand, the green line symbolizes the first VB state with p_z-character, which has only one maximum at the NW center. Figure 3.20(b) shows the charge densities for a NW size 8.9 nm, of the first VB states v_1 and v_2, with $p_\perp$-character, with the first VB state with p_z-character, that occupies the 11-th position in the valence band energy spectrum.

We have here similar results for the valence band of the InN NW as the obtained for the GaN NW calculated within the SEP approach. This is reasonable due to the similarity between valence bands of both semiconductors. However, the larger InN crystal-field splitting can lead to some differences, as we analyze later.

The results concerning the evolution of the electronic structure with the size of the nanowire can be analyzed more widely by representing the band structure for two representative sizes. Figure 3.21 shows the band structures for sizes (a) 3.4 and (b) 8.9 nm, highlighted also in Fig. 3.20(a) with the orange vertical lines. We have chosen these sizes due to the difference in the confinement energy between each other. The conduction and valence bands are represented by red and blue lines, respectively.

The conduction bands for both sizes show a quasi-parabolic line shape. In

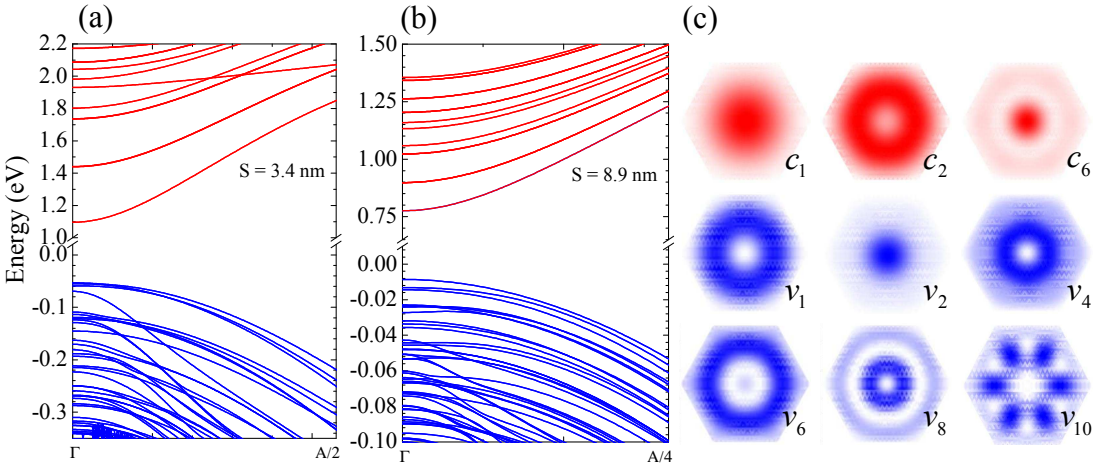

Figure 3.21: Band structure of the InN NWs of size (a) $S = 3.4$ and (b) $S = 8.9$ nm. (c) Some selected wave functions of the nanowire of size 8.9 nm.

general, as the coupling with the valence band decreases with the increasing of NW band gap, the conduction bands are better suited to a parabolic function for smaller NWs. Moreover, for $S = 3.4$ nm, shown in Fig. 3.21(a), the conduction sub-bands all exhibit a similar curvature, because they come from the same bulk conduction band. The only exception is the band whose energy at $k = 0$ is 1.93 eV, recognizable by its curvature flatter than the rest of the bands. This band comes from a bulk conduction band of higher energy, and its crossing with the other bands implies that belongs to a different representation, *i. e.*, has a different global symmetry. In the case of $S = 8.9$ nm, the weaker confinement results in a larger number of sub-bands even in a lower energy range, as Fig. 3.21(b) shows. Now, all the bands belong to the same family of curves.

On the other side, the valence bands show a distinct picture. The participation of bands with different curvatures complicates their profiles. At first glance we can appreciate multiple crossing and anti-crossing in the energy dispersion. By analyzing the band structure of the smaller NW, we can see that the topmost VB state, with $\phi_{p_\perp} = 100\%$, has an energy of -53 meV, and a almost flat band. The first VB state with p_z-character is placed at -70 meV (state v_4), having a band of more pronounced curvature. After analyzing the character of each VB state at the Γ point, we can assign in most cases, a $p_\perp$-character to the flatter bands, and a p_z-character to the bands with stronger curvature. The exceptions are VB states with same global symmetry and close in energy, whose characters may be difficult to be defined. This correspondence between character and curvature evokes the bulk band structure, where the C-band, of p_z-character, has the most

pronounced curvature of all. The valence band dispersion for the larger NW (shown in Fig. 3.21(b)) is more complicated as the result of the weaker confinement. Now, we find a larger number of flatter bands, all with $p_\perp$-character. The first VB state with p_z-character is found in the 11th band. In addition to the band structures, the charge densities of some relevant states of the nanowire of size 8.9 nm has also been represented in Fig. 3.21(c). Although the NW states seem to have a circular symmetry, the NW hexagonal cross-section determines the envelope of the wave function. This is evident in the VB state v_{10}, with six maximum related to the cross-section corners. Moreover, from this picture, a qualitative idea of the magnitude of the oscillator strength can be inferred. Thus, the states v_1 and c_1 will have a small spatial overlap, which means a low transition probability. We complete below the information given by the NW energy spectrum with the calculation of the absorption spectra.

Optical absorption

According to the discussion about the NWs electronic structure we can infer that the NW optical properties can be strongly determined by the spatial overlapping of the VB and CB states. Moreover, the optical response will also depends on the light polarization as a consequence of the anisotropy of the wurtzite crystalline structure, exhibited also in the electronic states. To complete the information given by the band structures of Fig. 3.21, we calculate here the absorption for the InN NWs of the same size.

Figure 3.22 shows the absorption spectra, for the same NWs size of Fig. 3.21 (sizes 3.4 and 8.9 nm), for $\boldsymbol{e}_\perp$-polarized light (in-plane) and $\boldsymbol{e}_z$-polarized light (on-axis). Concerning the general behaviors presented by the absorption, both spectra exhibit the characteristic one-dimensional density of states (modulated by the oscillator strength). While the spectra of $\boldsymbol{e}_\perp$-polarized light present a more complex profile, the spectra $\boldsymbol{e}_z$-polarized light are composed by single peaks well separated from each other. This is explained by the large number of states with $p_\perp$-character than states with p_z-character, as we have appreciated before in the band structures (Fig. 3.21). Thus, for both NW sizes, in the in-plane spectra we recognize a structure composed by group of peaks of similar energies, where several transitions participate. In the case of the on-axis spectra, the structure is simpler, and exhibits the mentioned single-peak profile. The average separations between consecutive on-axis absorption peaks and groups of in-plane absorption peaks are approximately the same, being 0.4 eV for size of 3.4 nm, and 0.1 eV in the case of 8.9 nm.

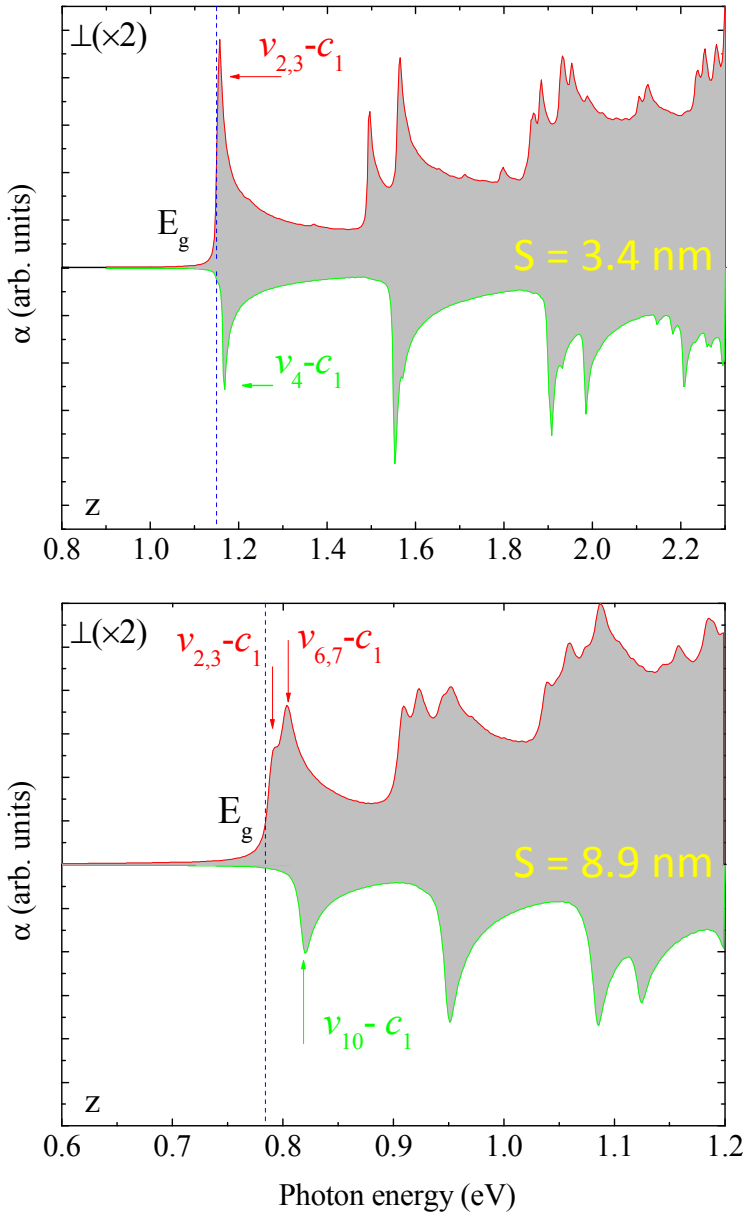

Figure 3.22: Optical absorption spectra for in-plane ($\boldsymbol{e}_\perp$) and on-axis ($\boldsymbol{e}_z$) light polarization, for the NW sizes $S = 3.4$ and $S = 8.9$ nm.

In spite of the oscillator strength of the transition v_1-c_1 is practically zero, the absorption edge energy of the spectra of $\boldsymbol{e}_\perp$-polarized light coincides with the NW energy gap in the spectra of both NW sizes. This is due to the small separation between the energies of the state v_1 and states $v_2 - v_3$ (3 meV). In the case of the on-axis spectra, the first VB state with p_z-character has a large spatial overlap with the CB state c_1. Therefore, the absorption edge energy is exactly placed at the transition energy from this VB state to the CB state c_1. Moreover, the absorption edge energy of the on-axis spectra is blue-shifted with respect to the in-plane spectra. This shift is 10 meV for the NW size of 3.4 nm and 38 meV for a NW size of 8.9 nm. We can also observe that the difference between the absorption edge energies of in-plane and on-axis spectra can be lower than the value of the bulk crystal-field splitting, due to the different level of confinement of states with $p_\perp$ or p_z-character, motivated by the complex interplay between the valence band mixing and the quantum confinement. Nevertheless, this blue-shift will tends asymptotically to the crystal-field splitting value as the NW size increases.

In conclusion, the absorption of wurtzite InN NWs exhibits a relevant anisotropy depending on the light polarization, which also leads a different absorption edge energy. Moreover, the interplay between the quantum confinement and the valence band mixing produces non-trivial trends in the optical properties when the NW size changes. Thus, the complete study of the absorption of InN NWs of sizes below 20 nm, where the quantum confinement effects are important, should be performed within a precise description of the valence bands dispersion.

3.2.4 Electronic structure and optical properties of GaN nanowires

In Section 3.1 the SEPM was able to establish the relevant electronic properties of GaN NWs with sizes below 6.5 nm. However, a more detailed studied was lack due to the required computational time. On the other hand, in previous Subsections, the tight-binding method has handled with InN NWs (size up to $\sim$ 16 nm), and also the absorption spectra were obtained. It would be interesting to complement the SEPM results with more calculations of the electronic structure for larger GaN nanowires.

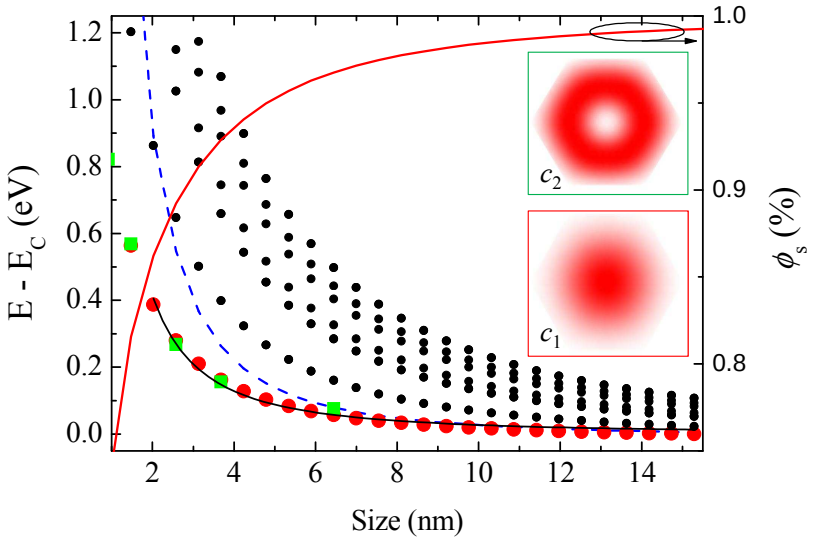

Figure 3.23: Confinement energy of the conduction band states versus nanowire size. Squares represent the data of SEPM calculations of Section 3.1. The dashed lines is a single-band EMA calculation for the first state. The square of the wave functions, c_1 and c_2, are also depicted.

Band structure

We start by analyzing the influence of the NW size on the conduction band (CB) energy spectrum. In Fig. 3.23 we present the variation with the NW size of the confinement energy of the first ten CB states at $k = 0$ (circles). We have highlighted the first CB state, c_1, with red circles. As we have mentioned above, the absence of spin-orbit interaction there would be an exact degeneracy between orbitally symmetric (equivalent) states. Analogously to the situation of InN NWs, this degeneracy is broken also in these calculations including the spin-orbit interaction. Nevertheless, the corresponding splittings between the quasi-degenerate CB states are as small (< 5 meV) as in InN NWs, and cannot be distinguished in Fig. 3.23. Analogously to the case of InN NWs, the CB energies exhibit a monotonous decreasing evolution with the NW size, without any crossing or anticrossing effects. This is related to the rather simple nature of the bulk conduction band, and the wide band gap of GaN. This wide band gap also prevents a strong coupling between the conduction and valence bands, being the dispersion of the conduction bands around the Γ point nearly parabolic. The differences with the InN NWs arise as a result of the larger effective mass of the GaN conduction band. This results in a lower confinement energy. In Fig. 3.23 we can see that the state c_1 confinement energy is smaller than 5 meV for large NW sizes, while for the same CB state was around 35 meV in InN NWs. Another difference among InN

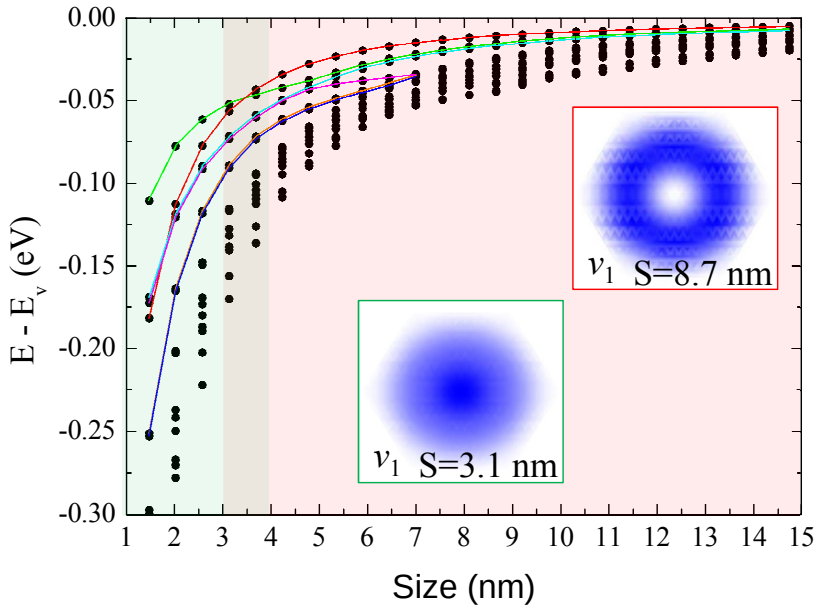

Figure 3.24: Confinement energy of the VB states versus nanowire size. The charge density of the topmost VB state is represented for two relevant sizes.

and GaN NWs is the dependence of the confinement energy with the NW size. We have fitted the confinement energy ϵ_{c_1} to the function:

$$\epsilon_{c_1}(S) = E_c + \frac{a}{S^b} \quad , \tag{3.13}$$

and obtained: $a = 1.34 \pm 0.07$ and $b = 1.69 \pm 0.02$, being $E_c = 3.5$ eV. Now, the exponent b is larger to the value obtained in InN NWs, and closer to the value of 2 established by the effective-mass approximation (EMA). For comparison, we have represented the EMA result for ϵ_{c_1} with a dashed blue line in Fig. 3.23. In addition, the representation of the ϕ_s corresponding to the CB state c_1, explains in part this deviation with respect to the EMA result. As we can see in Fig. 3.23, the decreasing of the NW size entails a decreasing of ϕ_s, that falls below 95 % for $S < 5$ nm. This reveals a slight multi-orbital composition, to a lesser degree than in InN NWs. Finally, we have also shown $\epsilon_{c_1}^{\text{SEPM}}$ as calculated with the SEPM (green rectangles). We can appreciate a good agreement with the current TB results. However, a comparison with higher CB states is misleading due to differences in the bulk band structure for the higher conduction bands. Nevertheless, such states are not of much interest in the optical properties.

In the case of the valence band (VB) states, as opposed to what happens in the conduction electronic structure, a complex size dispersion of the VB energy

is expected. As in the case of InN NWs, it becomes impossible to identify quasi-degenerate pairs of states as shown in Fig. 3.23 for the CB state c_1. Therefore, we have represented in Fig. 3.24 the energy levels as done in Fig. 3.20, for a set of representative $k = 0$ VB states. More precisely, we show the 15 highest-energy levels (labeled v_1 to v_{15}) for every NW size, as obtained from the numerical diagonalization, irrespective of their symmetry properties.

Figure 3.24 shows an overall view of the confinement effects. For the largest NW analyzed ($S = 15$ nm), the set of 15 levels spans an energy range of around 20 meV, with the highest one showing a confinement energy of around 5 meV. On the other hand, for a small radius NW, say 5 nm in size, the levels span a range of 100 meV, the highest one being 30 meV below the bulk VB band edge. We have also studied the symmetry of the wave functions. For the largest NW, the confined states exhibit all definite character $p_\perp$, with no state in this energy range with character p_z, that allows to identify such confined states as originating from the GaN bulk band edges Γ_9 and $\Gamma_{7,+}$ of Fig. 2.15.

Nevertheless, as the NW size decreases, the complex interplay between VB mixing and confinement precludes a systematic identification of the origin of each VB state. Analogously to the case of InN NWs, the representation of the energy levels as a series of continuous size dispersion curves, can be only achieved after an exhaustive group theoretical analysis. Not having done this analysis, we have proceeded as in Fig. 3.20, tracing interpolating lines connecting states with the same global symmetry. As in the InN NWs, this exercise shows several crossing and anti-crossing effects, with the known nontrivial evolution of the size dispersion curves. However, a difference can be appreciated with respect to the VB behavior studied for InN NWs. Here, the two highest energy size dispersion curves cross at around 4 nm, so that the highest energy valence band state exhibits a change in its properties at that critical size. For NWs with diameter larger than 4 nm, the highest-energy state has dominant $p_\perp$-character ($\phi_\perp$ larger than 98 %), as the bulk band edge. However, when the diameter decreases below 4 nm, the dominant character of the highest state becomes p_z. Moreover, this change in the orbital composition is accompanied by a change in the envelope of the VB state. We illustrate this in Fig. 3.24 by representing the charge density of the VB state v_1 for NW sizes 3.1 and 8.7 nm. We recognize a charge density with one maximum at the NW center, for the VB state of p_z-character ($S \lesssim 4$ nm). The envelope of v_1 changes to have a node at the NW center, exhibiting an overall annular form when $S \gtrsim 4$ nm. Therefore, we can identify clearly two regions with different ground state of the valence band, illustrated in Fig. 3.24 by shaded areas (green and red). This difference behavior between the VB ground states of GaN and InN NWs is

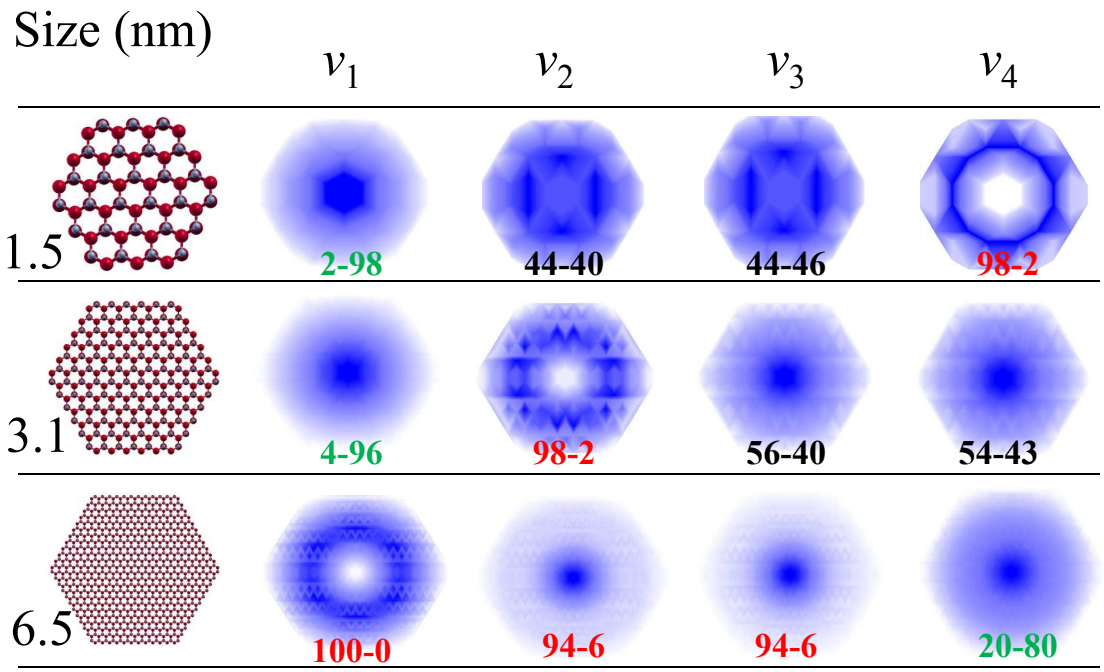

Figure 3.25: Charge density of the four NW valence band states for varying sizes. A ball-and-sticks representation of every NW is given for clarity. Numbers indicate the contribution from p orbitals to the character state, $\phi_{p_\perp} - \phi_{p_z}$.

a consequence of the smaller crystal-field splitting of GaN. For larger NW sizes, where the confinement effects are weaker, the VB state v_1 has the same properties of character and envelope in GaN and InN NWs. This result is interesting because demonstrates differences in the electronic structure of GaN and InN NWs caused by the quantum confinement. Concerning the other dispersion curves, various crossings and anticrossings are observed, as for instance, at $S = 6$ nm, among the green and pink curves.

The changes in the global symmetry of the topmost VB states of the GaN NWs can be examined more carefully. In order to illustrate how this changes take places, we have represented in Fig. 3.25 the charge densities of the VB states from v_1 to v_4 for several representative sizes, $S = 1.5$,3.1, and 6.5 nm. The $p_\perp$ and p_z-character of every VB state is also shown as a number in the format $\phi_{p_\perp} - \phi_{p_z}$. We indicate as well with the number color if it has a preponderant orbital contribution, corresponding red to $p_\perp$-character, green to p_z-character, and black when it is undefined.

First, the VB state v_1 has p_z-character for the sizes 1.5 and 3.1 nm. The consecutive VB states (v_2 and v_3) for the size 1.5 nm have a strong mixing in their orbital compositions (44-46), being impossible to assign an univocal character.

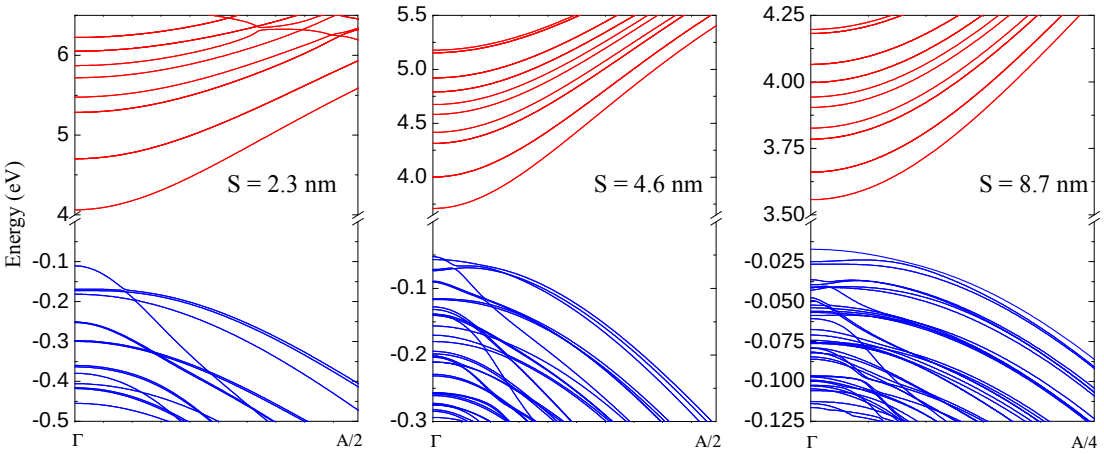

Figure 3.26: Band structure for GaN nanowires of $S = 1.5, 3.1$ and 6.5 nm.

The VB state v_4 for this NW size has the aforementioned node in the center and a clearly $p_\perp$-character. As the size of the NW increases, the VB state with p_z-character occupies lower positions in the energy spectrum, until the largest NW presented here ($S = 6.5$ nm), where it is the state v_4, and has a mixture composition (20-80). Precisely for this NW size, the topmost VB state has a $p_\perp$-character and the annular envelope described above. The two following VB states have now their own fully defined $p_\perp$-character with a $\phi_{p_\perp} = 94\%$. This result agrees to some extent with those obtained by the SEPM in Section 3.1.

The study of the electronic states can be enriched by checking the band dispersion for several NW sizes. Figure 3.26 shows the band structures of the GaN NWs studied in Fig. 3.25. The conduction and valence bands have been highlighted in red and blue, respectively. The conduction bands are decoupled of the valence bands due to the wide band gap of GaN and they can be considered parabolic for $k < |A|/4$. We can appreciate a family of curves not intersecting, because they come exclusively from the confinement of a single band. Concerning the valence bands, they show a much more complicated profiles than the conduction ones, similar to the behavior of their counterparts valence bands of the InN nanowires (see Fig. 3.21). However, a distinct feature is observed here. The band structure of the smallest NW shown here has a topomost band with a narrower curvature than the topmost valence band of larger NW sizes. This is consistent with that shown in Fig. 3.25, where the state v_1 has a p_z-character and comes from the bulk C-band. Thus, the increasing of the NW size changes the curvature of the topmost VB, adopting a profile similar to those of the bulk A- and B-bands.

Complementing the information of the band structure, we can investigate the influence of varying the wave vector k instead of changing the NW size. As studied

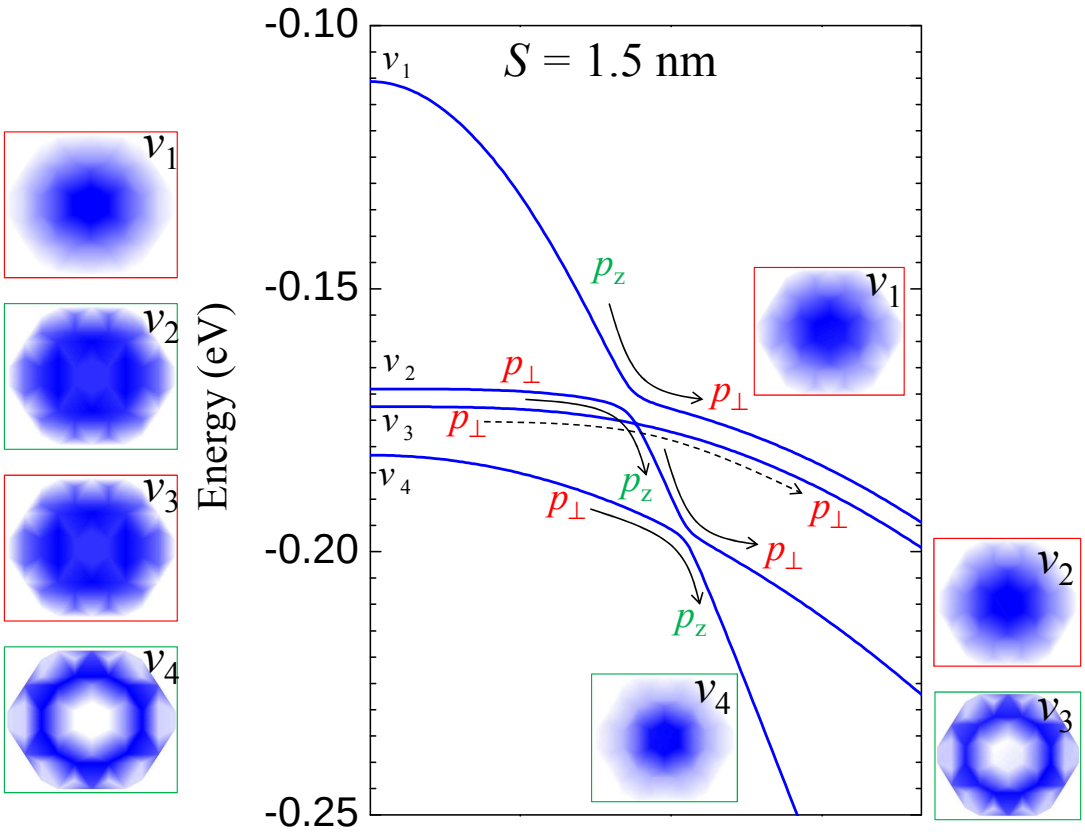

Figure 3.27: Detail of the valence band structure of the NW with $R = 2.3$ nm. The four topmost wave functions at the Brillouin points Γ and $A/10$ has been also drawn. The rectangle colors indicate the character, being red for character $p_\perp$ and green for character p_z.

in Fig. 3.24, the global symmetry of the wave functions determines the behavior of the band dispersion. For clarity, we have analyzed the dispersion of a thin NW, of size 1.5 nm, where the bands are sufficiently separated due to the confinement. Figure 3.27 shows a zoom of the four topmost valence bands near the Γ point. On the left hand we also represented the corresponding charge densities at the Γ point. The arrows highlight the crossings (dashed lines) and the anticrossing (solid lines) of the bands. In addition, the character of the VB states before and after the crossing is also indicated. We can now examine some VB states by way of illustration. Thus, a look at the evolution of v_3 with k, shows how its dispersion crosses the second band, becoming the VB state v_2 at $k = A/10$, and keeping the same character and charge density envelope. On the other hand, the VB states v_1 and v_2 while differing in the character, share the same global symmetry. Therefore, they exchange the character, in the anticrossing located at -170 meV (red solid arrows). Thus, the topmost VB state at $k = A/10$ has now a $p_\perp$-character. Next, another anticrossing takes place at -200 meV (green solid arros). Here, the VB state v_4, exchanges with the old VB state v_1 character and evelope. We can see that the VB state v_3 has now a node at the NW center.

We can conclude the study of the electronic properties of the GaN NWs with the summary of the main results. First, the topmost VB state, for sizes larger than 4 nm, has an unconventional node in the NW center, as exhibited also in InN NWs. A plausible explanation of such atypical envelope is the proximity of the bulk bands A and B. Besides, the curvature of such bands is very similar, and therefore, the resulting confined states are close in the energy spectrum, which enhances the mixing between the VB states. In contrast, in a hypothetical case where the spin-orbit and crystal-field interactions were large enough to separate the three valence bands of wurtzite bulk, we would expect a topmost VB state similar to the topmost CB state, *i. e.*, with a maximum of the charge density in the NW core. This hypothetical result was obtained numerically by using tight-binding parameters of a virtual material with large Δ_{so} and Δ_{cf}. This trend was also obtained in a similar work of M. P. Persson and A. Di Carlo for GaN nanowires and nanotubes [117], and also in calculations with the empirical pseudopotential method in ZnO nanoparticles, performed by S. Baskoutas and G. Bester [211]. Moreover, a difference with the electronic structure of InN NWs is the p_z-character of the topmost VB state for NW sizes below 4 nm, as a consequence of the smaller Δ_{cf} of GaN. Concerning the CB states, as the conduction band effective mass is much larger, being ~ 0.24 for GaN and ~ 0.07 for InN, the confinement is here much lower. Also the deviation respect the EMA prediction is less pronounced here.

Optical absorption

Figure 3.28 shows the absorption spectra for the same nanowire size of Fig. 3.25 for light polarizations $\boldsymbol{e}_\perp$ (in-plane) $\boldsymbol{e}_z$ and (on-axis). The transitions close to the absorption edge has been highlighted. First, for the thinnest NW explored here ($S = 1.5$ nm), we observe the absorption edge of $\boldsymbol{e}_z$-polarized light at lower energy than for $\boldsymbol{e}_\perp$-polarized light. Besides, the absorption edge energy coincides with the NW band gap (E_g) energy (4.17 eV). The absorption edge of $\boldsymbol{e}_\perp$-polarized light is blue-shifted 60 meV with respect to the NW E_g. For this spectrum, the first allowed transitions correspond to $v_{2,3} - c_1$, practically at the same energy. The next transition of similar peaks high is found at 4.88 eV (v_4-c_2). Concerning the general attributes of both spectra, we recognize the one dimensional profile of the NW density of states (modulated by the oscillator strength), being the spaces between peaks layer for $\boldsymbol{e}_z$-polarized light than for $\boldsymbol{e}_\perp$, due to the smaller number of VB states with p_z-character.

The absorption spectra of larger NWs (size 3.1 and 6.5 nm) present an increasing number of peaks as a result of the weaker confinement, being still recognizable the one-dimensional density of states. For the NW size of 3.1 nm, the lowest absorption edge energy is still for $\boldsymbol{e}_z$-polarized light, as a result of the allowed transition between states v_1 (p_z character) and c_1. The blue-shift of the absorption edge of $\boldsymbol{e}_\perp$-polarized light with respect to the NW E_g is now 23 meV. In the case of the nanowire of size 6.5 nm, the absorption edge for in-plane polarization is now at lower energy for the case of on-axis polarization, being the energy shift of the latter 10 meV. Since the topmost VB state has a node at the NW center for this size, the transition $v_1 - c_1$ is now forbidden. However, due to the small difference in energy between the state v_1 and the v_2 and v_3 pair, the changes in the absorption edge are minimal. We note also that the blue-shift energy difference between the spectra of $\boldsymbol{e}_\perp$ and $\boldsymbol{e}_z$-polarized light is lower than the GaN bulk Δ_{cf}. For larger NWs, the energy difference between the absorption edges of distinct polarization will tends asymptotically to the GaN crystal-field splitting.

In addition to the information provided by the absorption spectra, we can study how the oscillator strength of several selected transitions varies with the NW size. From the experimental point of view, this information can be more practical, because most of the optical experiments concerns to the measurements of the photoluminescence spectra, where the radiative efficiency of the transitions of lower energy is accessed. Therefore, the value of the oscillator strength of the two transitions of lower energy has been calculated at $k = 0$ and shown in Fig. 3.29. The oscillator strength, denoted as $f_{v,c}(\boldsymbol{e})$ (between parenthesis the light

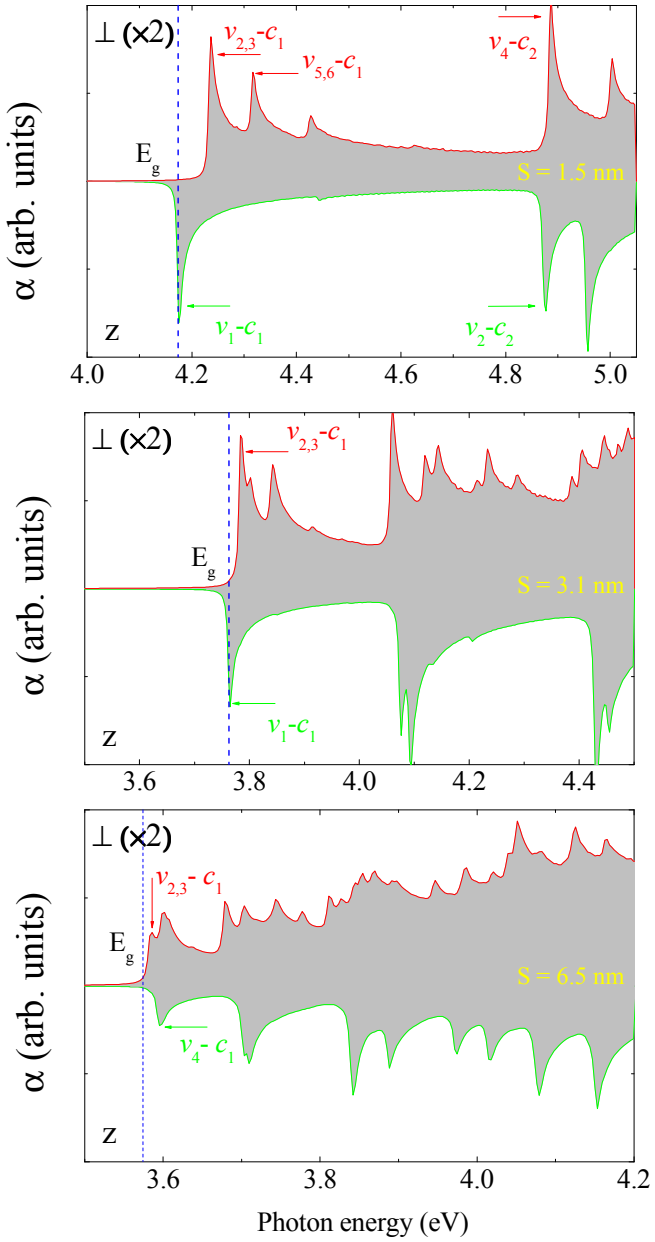

Figure 3.28: Absorption spectra for the nanowires ranging their sizes in $1.5, 3.1, 6.5$ nm, for the polarizations in-plane ($\boldsymbol{e}_\perp$) and on-axis ($\boldsymbol{e}_z$). The transitions related with the absorption edges has been labeled. E_g is the NW band gap.

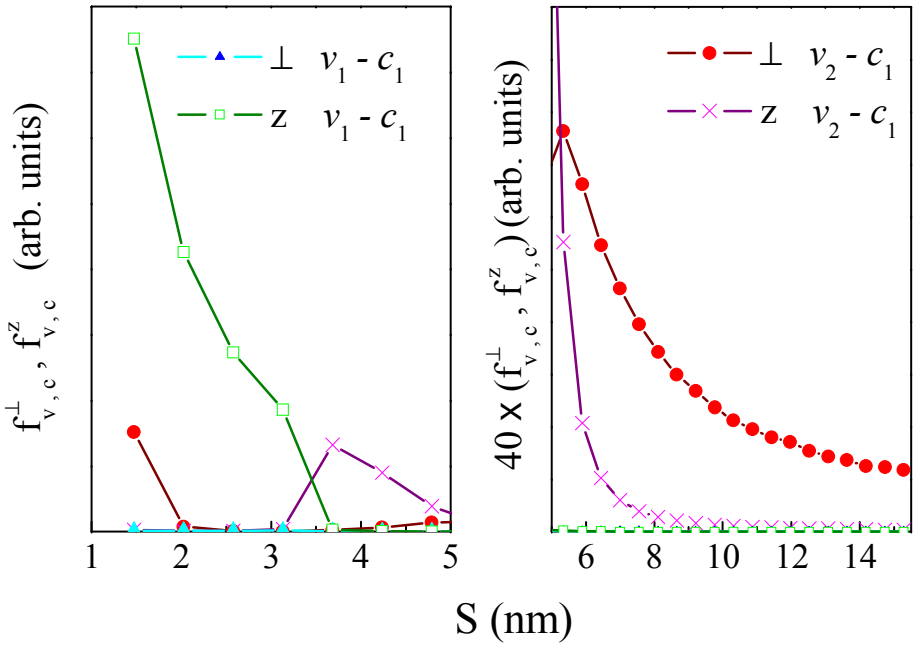

Figure 3.29: Optical matrix element as a function of the NW radius. The transitions represented are from the VB states v_1 and v_2 to the CB state c_1, for the in-plane and on-axis polarizations. For clarity, for $S > 5$ the scale has been augmented 40 times.

polarization), has been represented versus the NW size, calculated for the in-plane and on-axis polarizations. For clarity, at the right side we have augmented 40 times $f_{v,c}$ for sizes above 5 nm. In general, the value of $f_{v,c}$ decreases asymptotically as the NW size increases toward a constant value. We can also observe that $f_{v_1,c_1}(z)$ has the largest value for the smallest NW sizes until it intersects with $f_{v_2,c_1}(z)$, at $S \approx 3.5$ nm. Then, $f_{v_2,c_1}(\perp)$ passes $f_{v_2,c_1}(z)$, taking the largest value. Note that $f_{v_1,c_1}(\perp)$ is zero for all the NW sizes explored here.

In conclusion, GaN NWs show a strong anisotropy in their optical spectra, as a result of the anisotropy of wurtzite crystalline structure, with similar trends to those observed for InN NWs. The absorption edge is found to be in lower energy for $\boldsymbol{e}_{\perp}$ light polarization than for $\boldsymbol{e}_z$ light polarization, with the exception of NW sizes below 4 nm, where the absorption edge is at lower energy for $\boldsymbol{e}_z$-light. As far we know, the current NWs have diameters over 20 nm. However, the recent advances in the deposition of a single NWs in surfaces, that allow the performance of experiments in one NW, open the possibility of testing the theoretical results proposed here. Accordingly, our results are offered as prediction of the optical properties, and also to propose theoretical tools to model nanostructures.

3.2.5 AlN nanowires: polarized absorption along the c-axis

In Subsections 3.2.3 and 3.2.4 we have explored the optical absorption of the InN and GaN NWs, and also investigated the symmetry of the NW band states. Moreover, we have related the optical properties of the NWs with the bulk band structure. Therefore, most of the analysis performed above can be used in understanding the optical properties of AlN NWs.

First, we have seen in Section 2.3 that the AlN bulk valence band is substantially different than those of InN and GaN. We recall that the order of the VB states is $\Gamma_{7,+}$-Γ_9-$\Gamma_{7,-}$, having the topmost VB state a p_z-character ($\phi_{p_z} = 100\%$). The splitting between the topmost VB state and the other VB states ranges roughly from 100 to 300 meV (in our TB parameter is set in $\sim$ 120 meV). On the other hand, the spin-orbit splittings takes a small value, as seen in Fig. 2.15. Concerning the conduction band, the large band gap of AlN, $\sim$ 6.2 eV, decouples almost totally the conduction and topmost valence band would have a behavior similar to those of a single-band, as we will see.

Regarding the CB states behavior when the NW size varies, we found that CB states energy at $k = 0$ decreases in a similar way that in the case of GaN NWs. However, in this case, this behavior is closer to the EMA prediction, and the energy of the CB state c_1, can be fitted to the following function:

$$\epsilon_{c_1} = E_c + \frac{a}{S^2} - \frac{b}{S^3} \qquad \text{(in eV)}, \tag{3.14}$$

where $a = 1.84 \pm 0.02$, $b = 0.85 \pm 0.02$, and $E_c = 6.2$ eV. For small sizes, although the AlN band gap is very large, the strong quantum confinement deviates the energy dependence slightly from the EMA prediction for parabolic bands, *i. e.*, from $1/S^2$. We have corrected this overestimation by adding a cubic term, which it is only effective for sizes below 5 nm. For larger NWs, the expression given by EMA works reasonably well. On the other hand, the s-orbital contribution to the state c_1 has found to be $\phi_s > 95\%$ for all the cases, which confirms a single-band for the CB state c_1 of AlN NWs.

On the other hand, the analysis of the VB states is more interesting because their influence on the optical properties. Figure 3.30 shows the evolution of the VB states with the NW size. Due to the large splitting among the VB states with p_z-character and $p_\perp$-character in the bulk band structure (see Fig. 2.15), we can now label the states as $v_{z,n}$ (n in increasing order of energy) until the first VB state with $p_\perp$-character. In Fig. 3.30 the VB states $v_{z,1}$, $v_{z,2}$ and $v_{z,3}$ have been represented with black circles and the two VB states $v_{\perp,1}$ and $v_{\perp,2}$ with red circles.

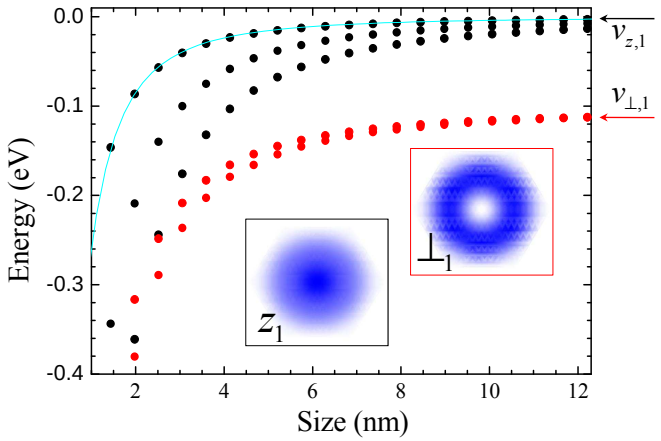

Figure 3.30: Valence band states as a function of the AlN nanowire radius. Black dots are the first three valence states with character $p_z > 95$. The red dots are the first two valence states with character $p_\perp > 95$. The wave functions of the first state of each class are given for a size of 8 nm. The solid line is a fitting with a function given in the main text.

With the aim of having a clear picture of the evolution, we have eliminated all the states between these two sets of energies. Contrary to the case of InN and GaN, we can observe the absence of the complex crossings and anti-crossings observed in the valence band of GaN NWs (see for instance Fig. 3.24). Now, we can fit the energy of the VB state $v_{z,1}$ by the same function of Eq. (3.14), obtaining the following results:

$$\epsilon_{v_1} = -\frac{417}{S^2} + \frac{159}{S^3} \qquad \text{(in meV)}, \tag{3.15}$$

where the error of the coefficients is 3 meV. The fitting is represented in Fig. 3.30 with a solid cyan line. Other differences with previous results come from the symmetry of the wave functions. In Fig. 3.30, we have plotted the charge density of the VB states $v_{z,1}$ and $v_{\perp,1}$. Here, the state $v_{z,1}$ has the density concentrated at the NW core, decaying smoothly until be zero at the border. This shape of the charge density amply matches with that of the first CB state (not shown here). This agrees with the expected EMA result for the first confined state in a NW when the Hamiltonian is solved in the single-band approximation. In addition, the state $v_{\perp,1}$ of $p_\perp$-character has the annular profile also exhibited by the topmost VB state of GaN and InN NWs, due to the mixing between contiguous states, as we have explained above.

After the analysis of the electronic structure of the AlN NWs, we do not expect radical changes in the optical absorption when the NWs size varies. For this reason, in Fig. 3.31 we have represented the absorption of a NW of $S = 5.3$ nm, for the

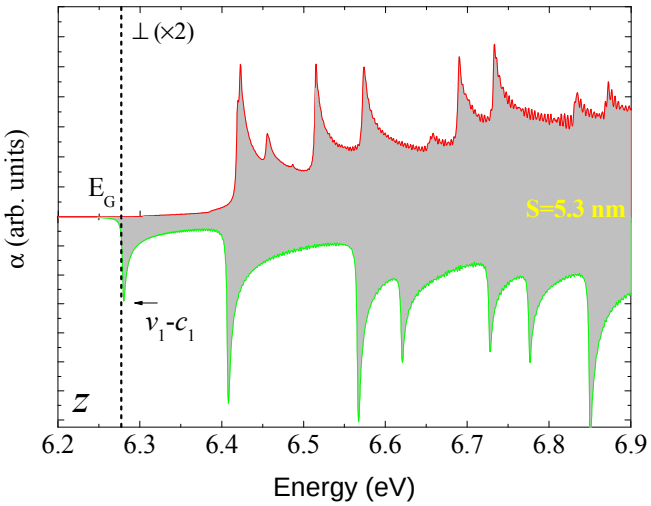

Figure 3.31: Absorption spectra of a AlN NW with $S = 5.3$ nm, for the light polarizations in-plane ($\boldsymbol{e}_\perp$) and on-axis ($\boldsymbol{e}_z$).

light polarizations in-plane and on-axis. The one-dimensional density of states is indubitably recognized, observing a larger number of transitions in the case of the $\boldsymbol{e}_\perp$-light, as usual. The difference with the other spectra (see Figs. 3.22 and 3.28) arises in the relative position of the absorption edges obtained for different light polarizations. Hence, the absorption edge for $\boldsymbol{e}_z$-light is clearly located at an energy much lower than its counterpart in the case of $\boldsymbol{e}_\perp$-light, being separated by 143 meV for the NW size shown here. Still the second relevant transition for on-axis light takes places at lower energy than the absorption edge of the in-plane polarization (129 meV blue-shifted with respect to the first transition). Considering the evolution of the VB states shown in Fig. 3.30, we can argue that the optical spectra for thicker AlN NWs will be very similar to the one displayed here, with the only difference of a ripple profile. Also, the shift between absorption edge of the different polarizations will tend to the bulk AlN Δ_{cf}, as the NW size increases.

We can conclude this Chapter by summarizing the most relevant physical properties of III-N NWs calculated from our atomistic semi-empirical methods. First, the anisotropy of the crystal structure is transferred to the absorption spectra. The absorption edge energy depends on the light polarization, being determined by the crystal-field splitting and by the quantum confinement of the NWs states.

In the case of InN and GaN NWs, except in quantitative differences, they show a similar blue-shift of the absorption edge for on-axis polarization with respect to the in-plane polarization. On the opposite, the AlN NWs exhibit a large blue-shift for the in-plane polarization, as a consequence of the negative crystal-field splitting. It is worth to mention the weak impact of the spin-orbit splitting in the overall optical properties of free-standing III-N NWs. We recall the importance of the semi-empirical atomistic methods due to their capability to cover a wide range of sizes, being an accurate extension of the *ab initio* approaches [220].

Chapter 4

Inhomogeneous electron distribution in InN nanowires: Influence on the optical properties

In Chapter 1 we advanced a discussion about the existence of an electron accumulation layer near the surface of InN films and nanowires. Besides the accumulation layer, a high density of electrons inside the material has been evidenced by a significant Burstein-Moss shift observed in absorption and emission measurements in InN films [28, 45, 221]. Subsequent infrared reflection studies on InN films have estimated a free electron concentration of approximately $\sim 10^{18}$ cm^{-3} [28, 222]. Concerning the electron accumulation layer, X-ray photoemission spectroscopy experiments have confirmed the presence of such charge layer in surfaces of both polar and nonpolar InN films, which indicates an universality of such phenomena [223]. It also worth highlighting the angle resolved photoemission spectroscopy experiments, which can accurately measure the difference between the Fermi level and the valence band [1, 224]. There are only a few results of cross-sectional scanning photoelectron microscopy and spectroscopy performed on cleaved $(11\bar{2}0)$ InN surfaces, that claim the absence of the electron accumulation layer [225]. However, it cannot be excluded that the cleavage has an influence on the electronic properties measured in those experiments. On the theoretical side, *ab initio* calculations for films have delimited the origin of this unintentional doping, by proposing a mechanism in nonpolar InN layer related to the presence of nitrogen vacancies, that tend to segregate closer to the surface, and act as n-type defects [97]. Alternatively, another source of such doping could be the presence of hydrogen impurities [226, 227]. Some other theoretical studies have pointed to the absence of electron accumulation layer in stoichiometric surfaces because the band structure does not

have any surface states within the band gap, and attributed the electron accumulation in actual surfaces to the presence of an indium layer [53]. However, the tendency of indium to oxidize makes it unlikely the existence of such a bare indium layer. Instead, it seems more plausible the termination of the surface by some sort of indium-oxide layer, that could also be a possible source of free-electrons [97]. Therefore, more experiments and theoretical calculations investigating the exact origin of the electron accumulation layer are demanded before definite conclusions are agreed.

In relation to the InN NWs, most of the experimental results to date also indicate the presence of the electron accumulation layer in the NW lateral walls. Due to their elongated shape, *e.g.*, the length is much larger than the cross-section, the NWs are especially appropriate to implement in them carrier transport experiments. Such transport measurements have been performed on InN in various forms, such as the atomic force microscopy conductivity measurements [75], and the magneto-transport experiments [228]. The results of these experiments are compatible with the assumption that carrier transport takes place mainly in an electron shell, adjacent to the surface. Other electrical measurements performed by contacting the InN NW with metallic pads [229] or by means of a polymer electrolyte gating [230] coincide in that the electron accumulation layer makes a certain contribution to the measured carrier transport. Other experimental evidences based on spectroscopy confirm the existence of the electron accumulation layer in InN NWs, as we will explain below.

The causes of the accumulation layer in InN NWs are currently assumed to be the same as for InN films, on account of the dimensions of the existing NWs in the literature, with diameter larger than 20 nm (see also Table 1.10). However, it is not only of interest to determine the origin of the electron accumulation layer, but also to investigate the influence of such accumulation on the electronic and optical properties of InN NWs. Though several studies have addressed the effect of the electron accumulation layer in the electronic structure of InN films [74], a model taking into account the columnar morphology is still lacking. It is expected that the specific geometry of the NWs can lead to differences in the spatial distribution of the free electrons, which possibly has also impact on the optical properties. Concerning the choice of the theoretical framework, the application of atomistic methods seems inappropriate here due to the large size of the NWs. While it is clear that *ab initio* approaches are not suitable for problems which involve millions of atoms, the semi-empirical atomistic approaches, such as the pseudopotential and tight-binding methods used in Chapter 3 to investigate the electronic structure of moderate size free-standing NWs, could in principle deal with this

problem [113, 231]. However, the large computation times required, make prohibitive the repetitive calculation needed to implement a self-consistent procedure and to investigate trends as a function of the sizes, among other parameters. The alternative proposed here consists of the use of the effective-mass approximation (EMA), applied within a self-consistent procedure, to find the electron distribution. Moreover, as concluded in Chapter 3, for NW diameters larger than 20 nm, it is not expected a large discrepancy between the electronic structure predictions of the semi-empirical atomistic approaches and the EMA (see Figs. 3.18 and 3.23).

We have organized this Chapter as follows: first of all, in Section 4.1 we will present some relevant experiments connected with our theoretical model. Then, the formulation and approximations of the model are explained in detail in Section 4.2. The numerical results and the comparison with the experiments are summarized in Sections 4.3 and 4.4.

4.1 Experimental evidences of the electron accumulation in InN nanowires

Among the variety of experiments reported in the literature, we have chosen a work by A. Rizzi, of the University of Göttingen, concerning electrical measurements on InN nanowires [229], to illustrate the role of the electron accumulation layer in the carrier transport. Figure 4.1(a) shows an InN NW, deposited on a surface of oxidized silicon, and with four contact pads attached by electron beam lithography. The experiment measures the NW resistance, R_W, between the voltage probe contacts. In Fig. 4.1(b) the authors have represented a cylindrical NW, where two region are distinguished: the center of the NW, where a low density of electrons is assumed, and can be considered equivalent to a bulk (3D region), and shell of a few nanometers thick (2D region), where the electron density is assumed to be several orders of magnitude larger in comparison with the concentration in the 3D region. Consequently, the conductance (defined as $g = L_W/R_W$ where L_W is the NW length), has two distinct contributions:

$$g \sim \frac{1}{\rho_{3D}} r^2 + \frac{1}{\rho_{2D}} r. \tag{4.1}$$

The first term, with quadratic dependence on the NW radius, r, is due to electron transport through the NW core (3D region or bulk), with resistivity ρ_{3D}. The second term, with linear dependence on the NW radius, is the contribution of

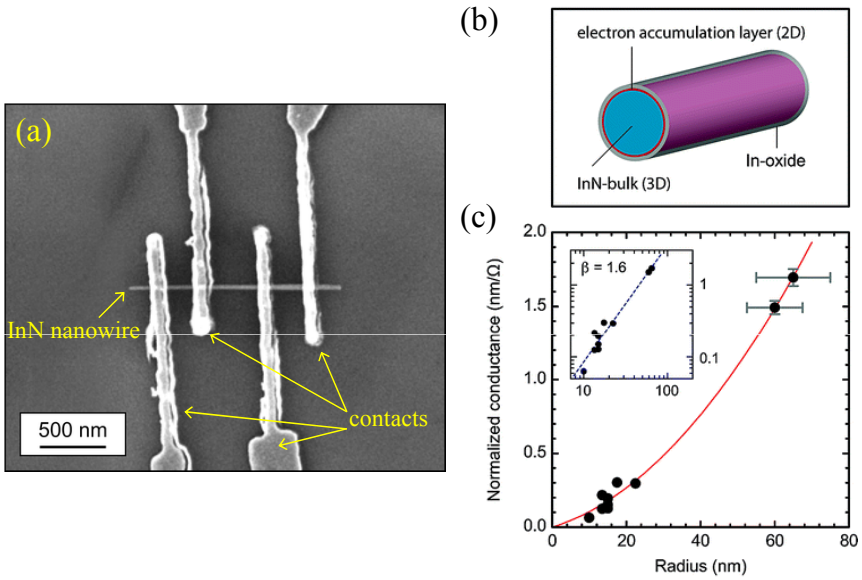

Figure 4.1: (a) Scanning electron microscopy image of a single InN nanowire contacted by electron beam lithography in a four-point probe geometry. (b) Sketch of the InN nanowire, where the different regions have been marked: bulk (3D), shell (2D), and the indium oxide at the surface. (c) Normalized conductance g versus the radius r of the nanowire, derived from the electrical measurements (see main text). In the inset, the same data points in logarithm scale, with a power law fit (dashed line) to determine the exponent $\beta = 1.6 \pm 0.2$ in the relation $g \sim r^{\beta}$. Extracted from Ref. [229].

the electron accumulation layer, close to the surface (2D region), with resistivity ρ_{2D}.

The results of the resistance measurements for ten nanowires have been plotted in Fig. 4.1(c). As we can see in the inset, the conductance follows the equation $g \sim r^{\beta}$, where $\beta = 1.6 \pm 0.2$. As $1 < \beta < 2$, the authors infer that the carrier transport takes place both through the core and the shell of the InN nanowire, which points out to a certain electron accumulation at the surface. Similar results of other transport measurements made by different groups agree with the work described here [75, 228, 230].

In addition to the transport experiments, the optical spectroscopy studies based in the Raman scattering, the photoluminescence (PL) and the photoluminescence excitation (PLE) have also shown evidences for the existence of the electron accumulation layer. At this point it is interesting to describe some relevant results, which have been obtained by these techniques and are closely related to our work. The PL and PLE experiments explained here have been performed by J. Segura-Ruiz for his Ph. D. thesis under the supervision of N. Garro and A. Cantarero [232],

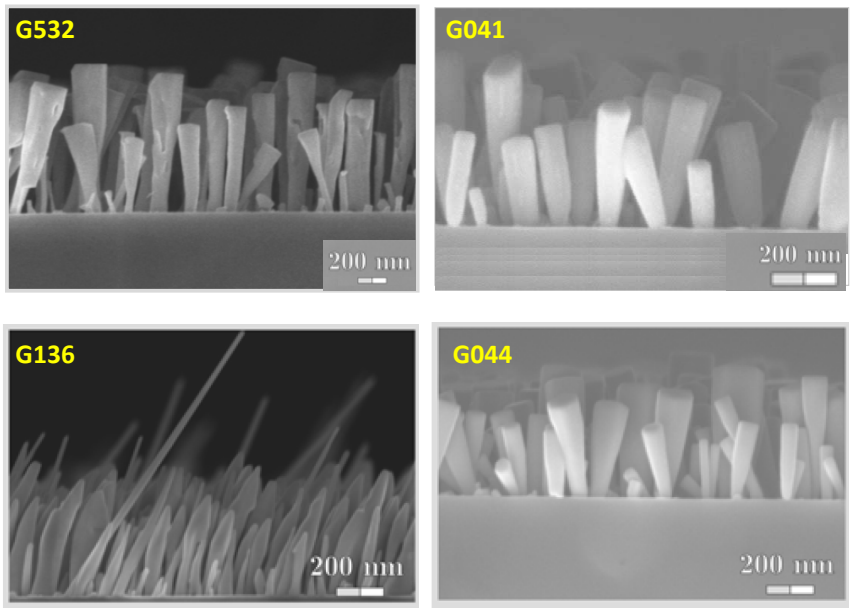

Figure 4.2: InN nanowire ensembles employed for the PLE measurements in Ref. [233].

and have motivated a great deal of our theoretical calculations. Figure 4.2 shows the InN nanowire ensembles used in the spectroscopy studies of Ref. [49, 233]. The samples were grown by C. Denker, J. Malindretos and A. Rizzi, from the University of Göttingen, by plasma-assisted molecular beam epitaxy on Si (111) substrates, under nitrogen-rich conditions. They are oriented along the c-axis, and the conditions of substrate temperature and nitrogen flux, among others, were slightly varied to obtain different morphologies. More details about the growth conditions can be found in Ref. [67]. We can recognize an hexagonal cross-section of the NWs from the samples G532, G041 and G044, while the sample G136 shows unfaceted wires. The samples show a dispersion in the NW diameter, varying from 40 to 100 nm, the sample G136 having the thinnest NWs. With this range of sizes the quantum confinement effects are excluded.

The Raman scattering spectra present very narrow E_2^h phonon peaks, with FWHM ranging from 3 to 5 cm^{-1}, thus revealing a high crystalline quality of the InN nanowires. It has also been observed the coexistence of the plasmon-coupled mode (PLP^- mode) and the uncoupled longitudinal optic mode in the Raman spectrum [49, 234]. Such coexistence indicates two regions with a substantial difference in the electron concentration. Hence, the plasmon-coupled mode is related with high electron densities, presumably localized near the NW surface, and the uncoupled longitudinal optic mode is associated with a low electron concentration region, located at the NW core. The measured frequencies for the PLP^- mode,

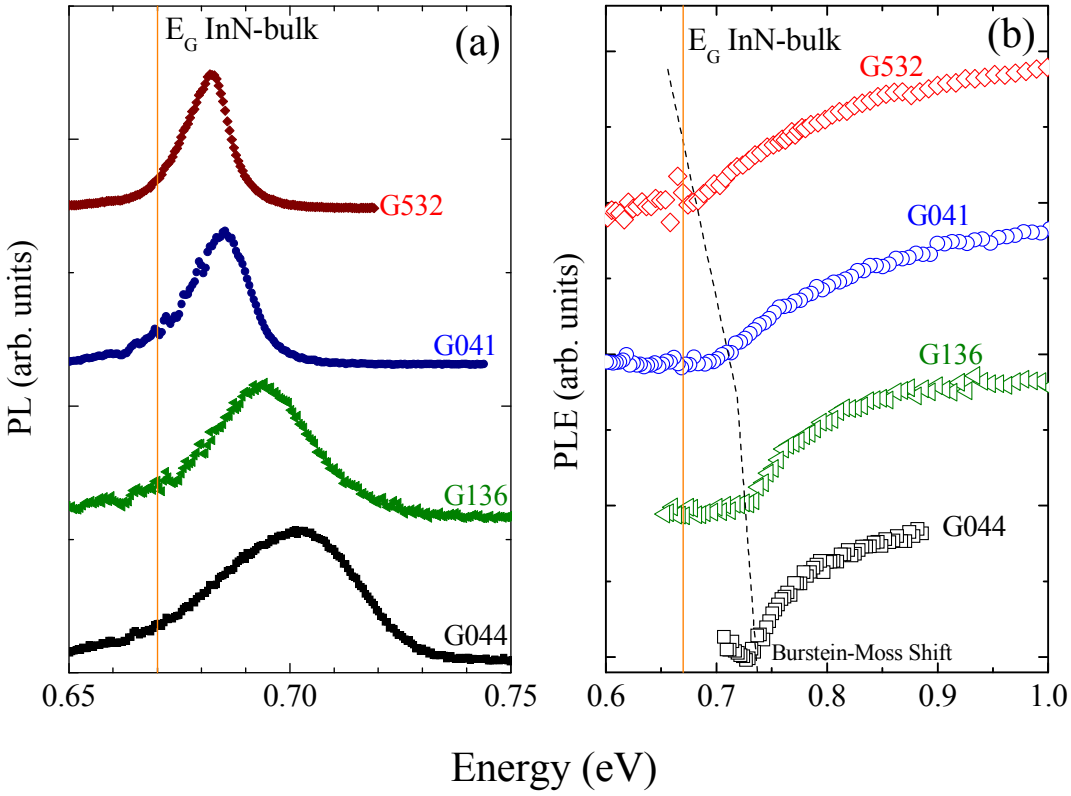

Figure 4.3: PL and PLE spectra of the InN nanowire ensembles shown in Fig. 4.2, measured at $T = 10$ K.

around 435 cm^{-1} corresponds to electron concentration of the order of 10^{-19} cm^{-3} close the NW surfaces [235].

The photoluminescence (PL) and photoluminescence excitation (PLE) experiments also add some relevant information complementary to the Raman scattering. Figure 4.3 shows the PL and PLE spectra of various samples, measured at $T = 10$ K (the details of the experimental setup can be found in Ref. [232]). First of all, the PL spectra show different emission energies, blue-shifted in all the cases with respect to the InN band gap (at 0.67 eV). The different blue-shift can be attributed to changes in the electron concentration from sample to sample. Also, it can be appreciated that the peak asymmetry and the broadening increase with the emission energy.

The large broadening observed in the PL spectra (from 40 to 100 meV) could be in principle attributed to the inhomogeneous distribution of sizes in the InN nanowire ensembles. However, by selectively exciting different sizes, no changes

were detected in the line width and in the peak position. This could indicate that this broadening is intrinsic to each nanowire. However, more sophisticated experiments, for instance, in micro PL, where only one nanowire is excited, should be carried out to confirm this hypothesis [160]. The experiments also show that the integrated PL intensity decreases with the energy of the PL peak. Overall the available data suggest differences in the electron accumulation layer for each sample, attributed to the different growth conditions.

Under certain conditions, which will be explained later, PLE and absorption spectra are equivalent [236]. Therefore, the PLE is an alternative to absorption when the samples have been grown on opaque substrates, where the standard absorption experiments are not possible. Figure 4.3(b) shows the PLE spectra of the InN NW ensembles shown in Fig. 4.2, measured in the same conditions as the PL spectra presented above. The following facts deserve to be highlighted. (i) The spectra are featureless and no exciton related peaks have been observed. (ii) There is a relevant blue-shift of the absorption edge in all the samples, up to 58 meV for the sample G044, but now the PLE edges are located at higher energies than the PL peaks. (iii) A careful look at the absorption edge reveals higher slopes for the samples with higher absorption edges. (iv) The energy of the PL peak and the Stokes shift between the PL and PLE increases with the PLE edge energy [232]. Therefore, the results of PLE spectroscopy also suggest changes in the electron accumulation layer dependent on the growth conditions [72]. These PLE experimental data will be discussed in the following Sections together with the theoretical results.

4.2 Electrostatic potential and charge density in InN nanowires

The available experimental data summarized above make desirable a theoretical model for investigating the influence of the electron accumulation layer on the optical properties of NWs, taking into account the columnar morphology of the NWs. In order to obtain the electrostatic potential and the electron distribution in the nanowire, we propose an iterative procedure for solving the Schrödinger-Poisson system of equations [237]. Before detailing the formulation, the main approximations assumed for our model are explained here.

Concerning the morphology of nanowires, although Figure 4.2 shows a wide variety of shapes, we assume the NWs as infinite cylinders of radius R, and associated cylindrical coordinates (r, φ, z) will be used throughout. This is consistent

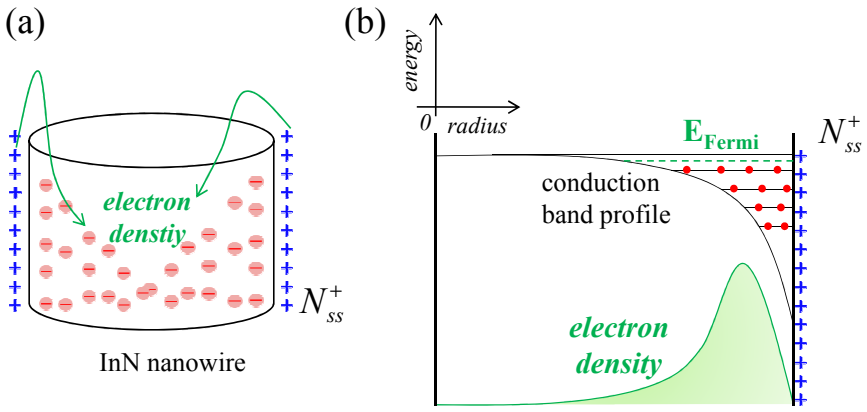

Figure 4.4: (a) Surface donors release their electrons inside the nanowire, remaining positively charged. (b) Electrons arrange in the energy levels until certain Fermi energy.

with our discussion in Chapter 3, where we have demonstrated that the NW states are not significatively affected by the cross-section shape above a diameter of 20 nm, smaller than the one of the NWs studied here.

The electronic states are found by solving the single-particle Schrödinger equation within the single-band in the effective-mass approximation. The conduction band is assumed to be isotropic and parabolic with the effective mass m_c^*. Despite the reported non-parabolicity of InN far from the Γ point [238], the parabolic approximation is valid in the range of energies where the model will be applied [239]. The contribution of the valence band to the electron accumulation has been disregarded, since there is no experimental evidence of the influence of the acceptor states in the formation of the electron accumulation layer. In order to determine the optical properties, the valence band is calculated *a posteriori*, once the self-consistent electrostatic potential and the electron density have been found.

The formation of the electron accumulation layer, which motivates the approach presented here, is explained in Fig. 4.4. Independently of their origin, there are donor-like surface states located above the Fermi level, which release their electrons to the InN conduction band. This results in a free-electron population inside the wire, and a positive charge density N_{ss}^+ at its surface ($r = R$), which provides an electric field that bends the conduction band near the surface. Figure 4.4(b) shows how these free-electrons occupy the energy levels, which are determined by the potential energy. The Fermi level indicated by the last energetic level occupied by free electrons, determined by applying the charge neutrality condition, *i. e.*, the number of free electrons is equal to the ionized impurities. Furthermore, since the presence of impurities within the nanostructure cannot be avoided [240], we

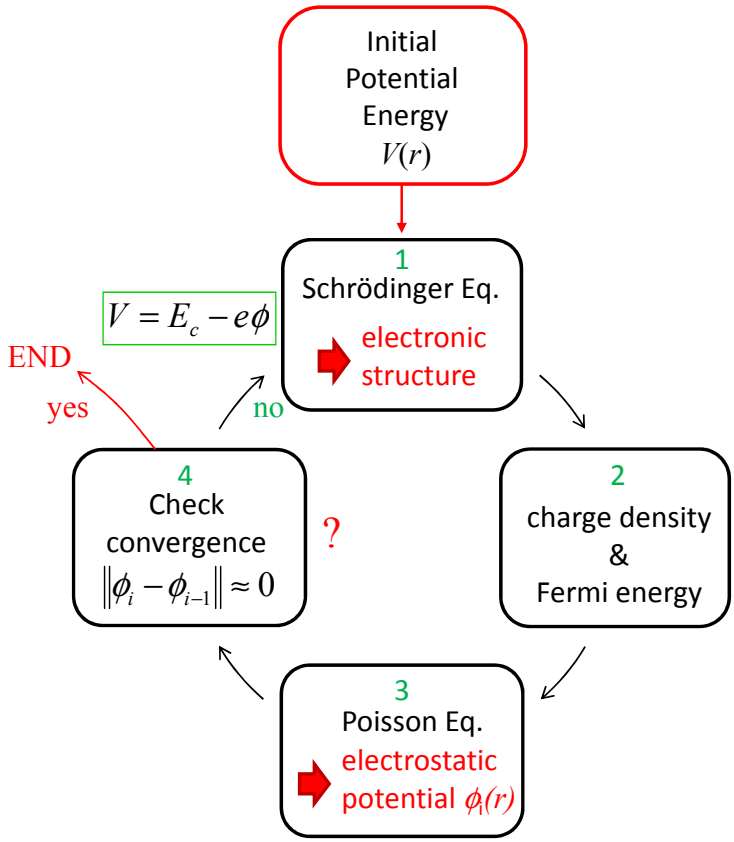

Figure 4.5: Flowchart of the self-consistent procedure designed to find the potential energy $V(r)$ and the charge density $n(r)$.

have assumed the presence of a uniform ionized donor bulk doping (concentration $N_D^+ \sim 10^{17} - 10^{18}$ cm^{-3}). These impurities also provide electrons, which must be taken into account when calculating the Fermi level [74].

In the next Subsections we present in detail the formulation of a self-consistent method for obtaining the electrostatic potential and the electron density, together with the derivation of the absorption spectrum.

4.2.1 Self-consistent procedure

The self-consistent procedure is divided in four steps, represented in Fig. 4.5, as explained in detail in the following paragraphs.

Step 1: Resolution of the Schrödinger equation. For a given potential energy, $V(\boldsymbol{r})$, the single-particle Schrödinger equation is written as follows:

$$\left[-\frac{\hbar^2}{2m_c^*}\vec{\nabla}^2 + V(\boldsymbol{r})\right]\Psi(\boldsymbol{r}) = \epsilon\Psi(\boldsymbol{r}). \tag{4.2}$$

In the effective-mass approximation, $V(\boldsymbol{r})$ is the conduction band profile, given by

$$V(\boldsymbol{r}) = \begin{cases} E_c - e\phi(\boldsymbol{r}) & r \leq R \\ \infty & r > R \end{cases}, \tag{4.3}$$

where $\phi(\boldsymbol{r})$ is the electrostatic potential and E_c the conduction band edge (hard-wall conditions outside the nanowire). Given the axial symmetry of our geometry, the potential energy, $V(\boldsymbol{r})$, only depends on the radius, and therefore the wave function is separable as follows:

$$\Psi_{n,l,k}(\boldsymbol{r}) = \psi_{n,l}(r)\frac{1}{\sqrt{2\pi}}e^{il\varphi}\frac{1}{\sqrt{L_z}}e^{ikz}, \tag{4.4}$$

where $n = 1, 2, \ldots$ is the radial quantum number and $l = 0, \pm 1, \ldots$ is the z-component of the angular momentum. The length L_z is the normalization length of the plane wave in the z-direction, with vector k. The eigenvalues of the Eq. (4.2) are

$$\epsilon_{n,l}(k) = E_{n,l} + \frac{\hbar^2 k^2}{2m_c^*}, \tag{4.5}$$

showing the parabolic one-dimensional dispersion in k. After some algebraic manipulations one can derive the equation for the radial part of the wave function, that determines the eigenvalues $E_{n,l}$

$$\left\{-\frac{\hbar}{2m_c^*}\left(\frac{\partial^2}{\partial r^2} + \frac{\partial}{r\partial r} - \frac{l^2}{r^2}\right) + V(r)\right\}\psi_{n,l}(r) = E_{n,l}\psi_{n,l}(r). \tag{4.6}$$

Initially the electrostatic potential is taken to be zero, $\phi(\boldsymbol{r}) = 0$.

Step 2: Calculation of the charge density and Fermi energy. Once the electronic states are determined, the electron density $-en(r)$ is deduced by summing the squared wave functions multiplied by the occupancy probabilities

$$n(r) = 2\sum_k\sum_{n,l} f_{n,l,k}|\Psi_{n,l,k}(r,\varphi,z)|^2 = 2\sum_{n,l}\frac{1}{L_z}\frac{1}{2\pi}|\psi_{n,l,k}(r)|^2\sum_k f_{n,l,k}, \tag{4.7}$$

where factor 2 counts for the spin degeneracy and $f_{n,l,k}$ is the occupancy probability given by the Fermi-Dirac distribution. Therefore

$$\sum_k f_{n,l,k} = \frac{L_z}{2\pi}\int_{-\infty}^{+\infty} dk \frac{1}{1+e^{\frac{\epsilon_{n,l}(k)-E_F}{k_BT}}} = \frac{1}{2}\sqrt{\frac{2m_c^*}{\hbar^2}\frac{k_BT}{\pi}}F_{-1/2}\left(\frac{E_F-E_{n,l}}{k_BT}\right), \quad (4.8)$$

where $F_{-\frac{1}{2}}$ is the semi-integer Fermi integral [241], and the final expression for the electron density is then

$$n(r) = \sum_{n,l}\sqrt{\frac{2m_c^*k_BT}{\hbar^2\pi}}F_{-\frac{1}{2}}\left(\frac{E_F-E_{n,l}}{k_BT}\right)|\psi_{n,l}(r)|^2. \quad (4.9)$$

The contribution of all the sub-bands to the electron density is explicitly calculated in the present approach [242], in contrast with other methods, such as the modified Thomas-Fermi approximation [74].

The Fermi level E_F in Eq. (4.9), which sets the conduction band occupancy, is determined by taking into account that the total electron charge must be equal to the charge provided by the densities of bulk donor impurities density, N_D^+, and surface states N_{ss}^+, *i. e.*,

$$\int_0^R n(r)rdr = 2\pi R N_{ss}^+ + \pi R^2 N_D^+. \quad (4.10)$$

This nonlinear equation for E_F is solved by the Newton-Raphson method [243].

Step 3: Resolution of the Poisson equation. The electrostatic potential $\phi(r)$ is obtained via the Poisson equation:

$$\frac{1}{r}\frac{d}{dr}\left(r\frac{d\phi(r)}{dr}\right) = -\frac{e}{\epsilon_0\epsilon_r}[N_D^+ - n(r)]. \quad (4.11)$$

The presence of ionized surface states with density N_{ss}^+ imposes the boundary condition for the potential:

$$\left.\frac{d\phi}{dr}\right|_{r=R} = \frac{N_{ss}^+}{\epsilon_0\epsilon_r}. \quad (4.12)$$

Step 4: Check of the convergence. The new potential energy is updated with the solution of Eq. (4.11), $V(r) = E_c - e\phi(r)$ and the Schrödinger equation (4.6)

is solved again. This procedure is iterated with the method of successive over-relaxation until convergence is achieved [243]. The Schrödinger and Poisson equations, (4.6) and (4.11), are numerically solved by finite difference methods, and the singularity at $r = 0$ is treated by following Refs. [244–246].

At this point, it should be mentioned that the Hamiltonian of Eq. (4.6) may not be hermitic unless an adequate transformation is used to discretize it. In the finite difference method applied here, the discretized Hamiltonian results in a real non-symmetric three-diagonal matrix. However, it would be desirable to operate with a symmetric Hamiltonian matrix to facilitate the computational task. Thus, the following symmetrization procedure has been used: Let H^S be a symmetric matrix, and H the Hamiltonian matrix, obtained after discretizing Eq. (4.6). We can find a matrix M that obeys

$$H^S_{i,i+1} = M_{i,i}H_{i,i+1} = M_{i+1,i+1}H_{i+1,i} = H^S_{i+1,i}, \tag{4.13}$$

we set $M_{1,1} = 1$, and therefore

$$M_{i+1,i+1} = M_{i,i}\frac{H_{i,i+1}}{H_{i+1,i}}, \tag{4.14}$$

if we apply this in the Schrödinger Eq. (4.6)

$$H^S\psi = MH\psi = \epsilon M\psi, \tag{4.15}$$

where ϵ are the energy eigenvalues. Let $M_{i,i'} = L_{i,i'}L_{i,i'}$, we obtain

$$\begin{gathered} L^{-1}H^S L_{-1}L\psi = L^{-1}LLH\psi = \epsilon L^{-1}LL\psi = \epsilon L\psi, \\ H_R\phi = \epsilon\phi_R. \end{gathered} \tag{4.16}$$

The Hamiltonian matrix $H_R = L^{-1}H^S L^{-1}$, is then symmetric and three-diagonal, with eigenvalues ϵ. The true wave functions are recovered via $\psi = L^{-1}\phi_R$. With this transformation, we save a noticeable computational time in storing and solving the eigenvalue problem [247].

The over-relaxation method guarantees the convergence of the self-consistent procedure. In each iteration, we must check the difference of two consecutive potentials (or electron densities). The Fermi level calculated from the iterated electron densities also reflects adequately the convergence. Figure 4.6(a) shows the Fermi level dependence on the iteration step of the self-consistent procedure, for several nanowire radius, 10, 20, 40 and 50 nm. In all the cases there is a fast convergence in less than 50 cycles (in terms of computation times, for a dense grid,

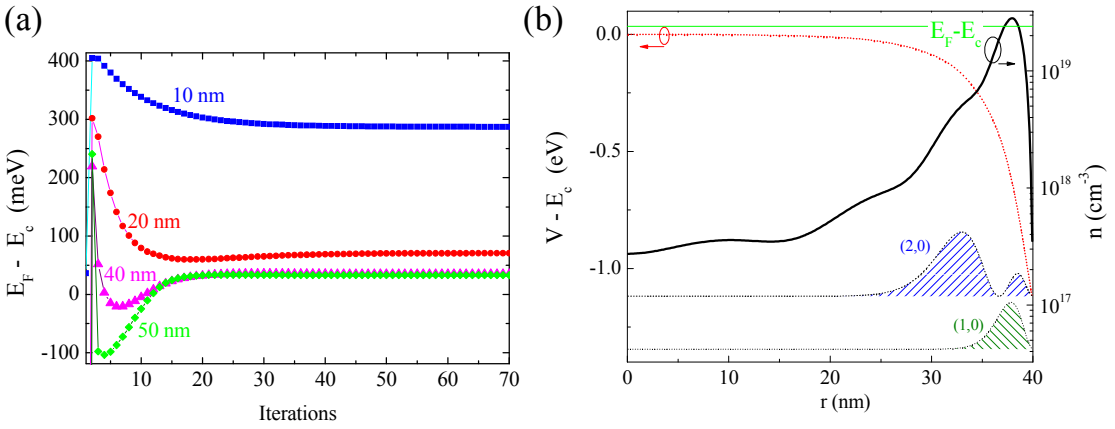

Figure 4.6: (a) Convergence of the Fermi energy versus the iteration step for different values of the nanowires radius. The donor concentration are $N_{ss}^{+} = 10^{12}$ cm^{-2} and $N_{D}^{+} = 10^{17}$ cm^{-3}. (b) Conduction band profile, $V(r)$, electron density, $n(r)$, and two first wave functions with $l = 0$, for a nanowire of $R = 40$ nm. The impurities concentration are $N_{ss}^{+} = 10^{13}$ cm^{-2} and $N_{D}^{+} = 3 \times 10^{17}$ cm^{-3}.

it means total converged times of less than 15 minutes in a standard processor). We also observe the decrease of the Fermi level as the NW radius increases until it stabilizes above a certain value ($R \approx 40$ nm). This value also depends on the density of N_{ss}^{+} and N_{D}^{+} impurities, as we explain in Section 4.3.

The self-consistent results for a specific nanowire of $R = 40$ nm are given in Fig. 4.6(b). First of all, the conduction band profile falls abruptly from zero to approximately -1 eV, in the range $R - r < 10$ nm. Therefore, the lowest electronic states are confined near the surface, as shown by the two states, with quantum numbers $(1, 0)$ and $(2, 0)$, represented with dashed lines in Fig. 4.6(b). In Fig. 4.6 we also show the electron density $n(\boldsymbol{r})$ and the obtained Fermi level which appears above the conduction band edge, E_c. The electron accumulation layer is observed at the surface in a notably higher electron concentration of ~ 10 nm thick. Besides, a careful look at the electron density reveals an oscillating profile, known as Friedel-type spatial oscillations [242]. The physical origin of such oscillations is related to the confined wave functions and the extent to which the associated sub-bands (of larger quantum number l) are populated. This behavior is absent in other approaches as the semi-classical Thomas-Fermi approximation [248]. We have checked that the spatial oscillations are less pronounced if the temperature increases, which is consistent with the results reported in [242].

4.2.2 Calculation of the valence band states and absorption spectra

The calculation of the optical absorption requires determining the nanowire valence band states. Although in Chapter 3 we have insisted in the importance of considering valence band mixing that leads to a nontrivial anisotropy in the optical properties of nanowires, the PLE experiments presented in Section 4.1 have not been performed for different light polarizations. Therefore, for the purpose of analyzing those experiments, we can assume a single-band effective-mass approximation (here associated to the band A) that leads to a Schrödinger equation for the valence states, where we have retained the anisotropy of the valence band effective-mass reported in Section 2.3. The LDA+U effective mass of the A valence band (see Table A.1) are used here and denoted as $m^*_{v,\perp}, m^*_{v,z}$. The potential energy is now $V(r) = E_v + e\phi(r)$, where $E_v = E_c - E_g$ is the valence band edge, associated to the band A, and therefore the Schrödinger equation is:

$$\left\{ -\frac{\hbar}{2m^*_{v,\perp}} \left(\frac{\partial^2}{\partial r^2} + \frac{\partial}{r\partial r} - \frac{l_v^2}{r^2} \right) + V(r) \right\} \psi_{n_v,l}(r) = E_{n_v,l_v} \psi_{n_v,l_v}(r). \tag{4.17}$$

Figure 4.7 shows (a), the energy potential, and (b), the valence band states obtained by solving the Schrödinger Eq. (4.17), imposing hard-wall conditions. The states, labeled according to their quantum numbers (n, l), are represented for $n = 1, \ldots, 5$ and angular momentum $l = 0$ (red line) and $l = 1$ (blue line), and $k = 0$. Contrary to the conduction band wave functions shown in Fig. 4.6(b), the valence states are now displaced toward the nanowire core, with a slight penetration in the potential barrier. We note that the valence band states are spread along the radius for increasing energies, although due to the high value of the potential energy ($E_v - 1$ eV at $r = R$), the localization is still remarkable even for the state (5,1). Hence, there is a spatial separation of the conduction and valence band states with the energy close to the respective band edges, which could eventually reduces the absorption efficiency.

The spectrum of optical absorption coefficient, $\alpha(\hbar\omega)$, is calculated as follows [124]:

$$\alpha(\hbar\omega) \propto \sum_{n_c,n_v,l,k} P^2_{n_c,n_v,l}(1 - f_{n_c,l,k})\delta(\hbar\omega - (\epsilon_{n_c,l}(k) - \epsilon_{n_v,l}(k))), \tag{4.18}$$

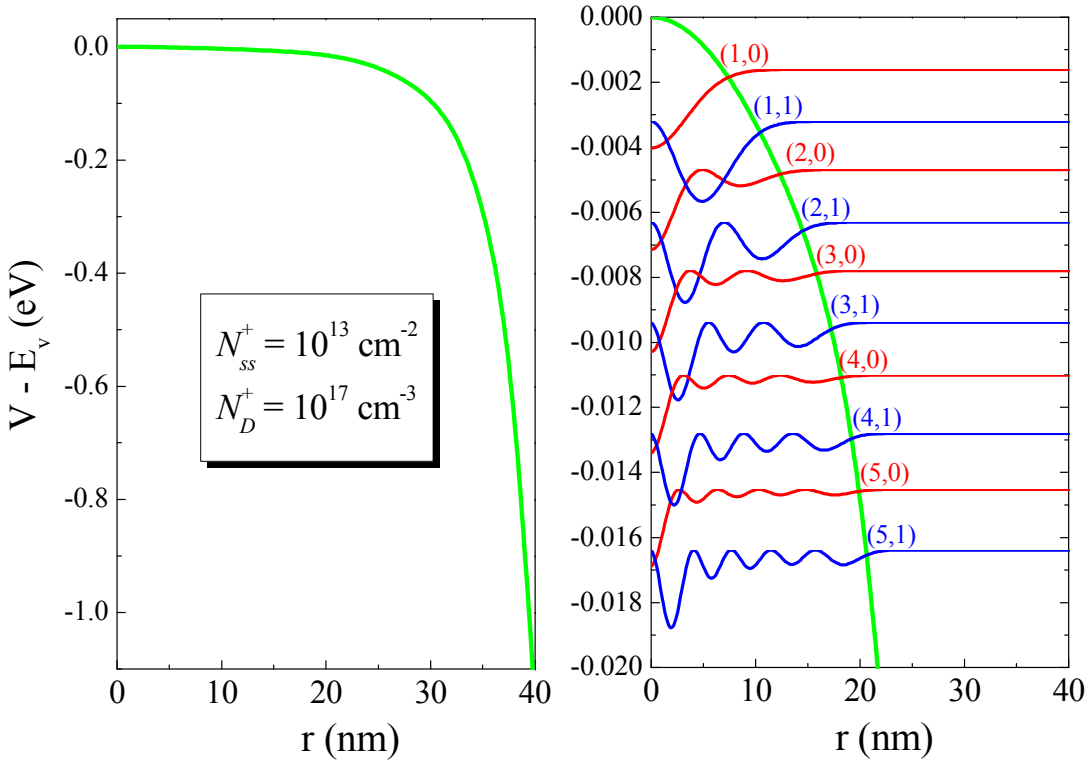

Figure 4.7: Radial function of some nanowire valence band states with $l = 0$ (blue lines) and $l = 1$ (red lines). The input of the calculation is: $R = 40$ nm, $N_{ss}^{+} = 10^{13}$ cm^{-2} and $N_D^{+} = 10^{17}$cm^{-3}. Note the change in the energy scale for panel (b).

where $P_{n_c,n_v,l}$ is the oscillator strength for the transition from the valence sub-band (n_v, l) to the conduction sub-band (n_c, l) (note the angular momentum conservation). The term $f_{n_c,l,k}$ is the Fermi-Dirac distribution of the conduction band states described above. The valence band is assumed to be completely occupied. The conservation of k in the absorption event has also been taken into account. The oscillator strength, which does not depend on k, is written as

$$P_{n_c,n_v,l} = \int_0^R \psi_{n_c,l}(r)\psi_{n_v,l}(r) r dr. \tag{4.19}$$

On the other hand, energies depend on k as: $\epsilon_{n_c,l}(k) = E_{n_c,l} + \frac{\hbar^2 k^2}{2m_c^*}$ and $\epsilon_{n_v,l}(k) = E_{n_v,l} - \frac{\hbar^2 k^2}{2m_{v,z}^*}$. Therefore

$$\sum_k (1 - f_{n_c,l,k}) = \sum_k \left(1 - \frac{1}{1 + e^{\frac{\epsilon_{n_c,l}(k) - E_F}{k_B T}}}\right) \delta(\hbar\omega - (\epsilon_{n_c,l}(k) - \epsilon_{n_v,l}(k))) =$$

$$= \frac{L_z}{2\pi} \int_{-\infty}^{+\infty} dk \left(1 - \frac{1}{1 + e^{\epsilon_{n_c,l}(k) - E_F} k_B T}\right) \delta(\hbar\omega - (\epsilon_{n_c,l}(k) - \epsilon_{n_v,l}(k))). \tag{4.20}$$

After some algebraic manipulations [249], this integral is

$$g(\epsilon) = \sqrt{\frac{\mu}{\pi\hbar^2\epsilon}} \left\{1 + \exp\left[-\frac{\frac{\mu}{m_c^*}\epsilon - (E_F - E_{n_c,l})}{k_B T}\right]\right\}^{-1}, \tag{4.21}$$

where μ is the electron-hole reduced mass $\mu = (m_c^* m_{v,z}^*)/(m_c^* + m_{v,z}^*)$ and $\epsilon = \hbar\omega - (E_{n_c,l} - E_{n_v,l})$. The absorption is therefore written now as

$$\alpha(\hbar\omega) \propto \sum_{n_c,n_v,l} P_{n_c,n_v,l}^2 g(\hbar\omega - (E_{n_c,l} - E_{n_v,l})), \tag{4.22}$$

where the factor $g(\hbar\omega - (E_{n_c,l} - E_{n_v,l}))$ takes care of the occupancy of the conduction band until the Fermi energy. Note that the integral in k has been eliminated from the absorption equation, and now there is a sum over the conduction and valence band states, only calculated at $k = 0$. This is an important simplification for the calculation of the absorption.

4.3 Influence of size and doping on the electron accumulation layer

The self-consistent method formulated above is applied here to study the changes in the electron accumulation layer when we vary the nanowire radius and the concentration of impurities in both the volume and surface. The donor concentration has been varied in the ranges proposed in the literature, being N_{ss}^{+} between $10^{12} - 10^{13}$ cm^{-2}, and N_D^{+} between $10^{17} - 10^{18}$ cm^{-3} [224, 250]. In order to give a better understanding of the experimental results described in Section 4.1, we have also studied the influence of such changes on the absorption.

All calculations were performed assuming a temperature of $T = 10$ K, although we have found that the electron accumulation layer does not change substantially with the temperature in the range from 295 to 595 K, in agreement with the experimental results reported for InN layers [251]. The fundamental band-gap of $E_g = 0.67$ eV reported for bulk InN was used (see Chapter 2). Also in the practical numerical results presented here, the function $1/\sqrt{\epsilon}$ in the absorption Eq. (4.22) is substituted by $\Re(1/\sqrt{\epsilon + i\gamma})$, with $\gamma = 10$ meV, to smooth the singularity around $\epsilon = 0$.

4.3.1 Influence of the nanowire radius

We have applied the self-consistent model for nanowires with different radius ($R =$ 10, 20, 40 and 50 nm), in order to match the average sizes reported for MBE-grown InN nanowires (see Table 1.10). The donors concentrations are $N_D^{+} = 3{\times}10^{17}$ cm^{-3} and $N_{ss}^{+} = 10^{13}$ cm^{-2}, in concordance with the values for high quality InN polar surfaces [224, 250].

Figure 4.8 shows (a) the conduction band profile $V(r) = E_c - e\phi(r)$, and (b) the electron density $n(r)$ for the selected NW sizes. The Fermi level is also indicated for each size. In all the nanowires, the conduction band profile falls from the inner part to $E_c - 1$ eV at the surface. This bend of the conduction band profile occurs abruptly near the surface (in the range $R - r \leq 10$ nm) of the nanowire for the thicker NWs ($R = 40, 50$ nm), and starts at the nanowire core for thinner nanowires, which thus presents a nearly parabolic profile. Thus, the electron accumulation is strongly localized at the surface of the NWs of $R = 40$ and 50 nm, with densities of the order of 10^{19} cm^{-3} in a range of 10 nm approximately, whereas in the case of thinner NWs, the difference in the concentration of electrons between the core and the surface is less pronounced.

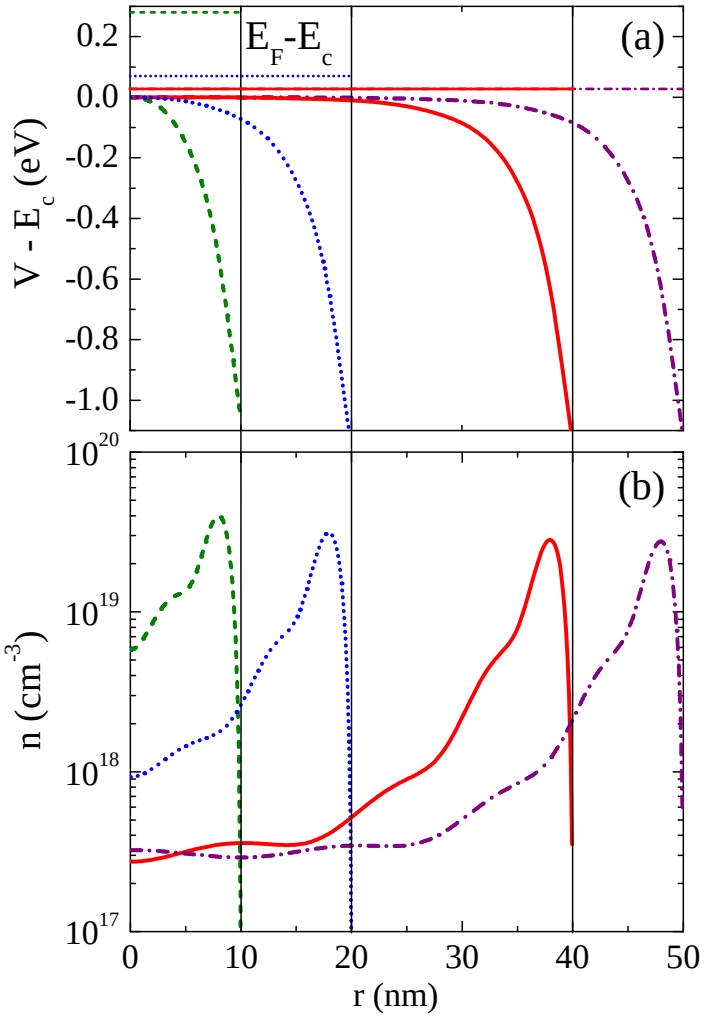

Figure 4.8: Conduction band profile, $V(r) = E_c - e\phi(r)$ and (b) electron density profiles for InN NWs with $N_D = 3 \times 10^{17}$ cm^{-3} and $N_{ss} = 1.0 \times 10^{13}$ cm^{-2}, and different radius ranging from 10 (dashed line) to 50 nm (dash-dotted line). The Fermi level of each NW is also indicated.

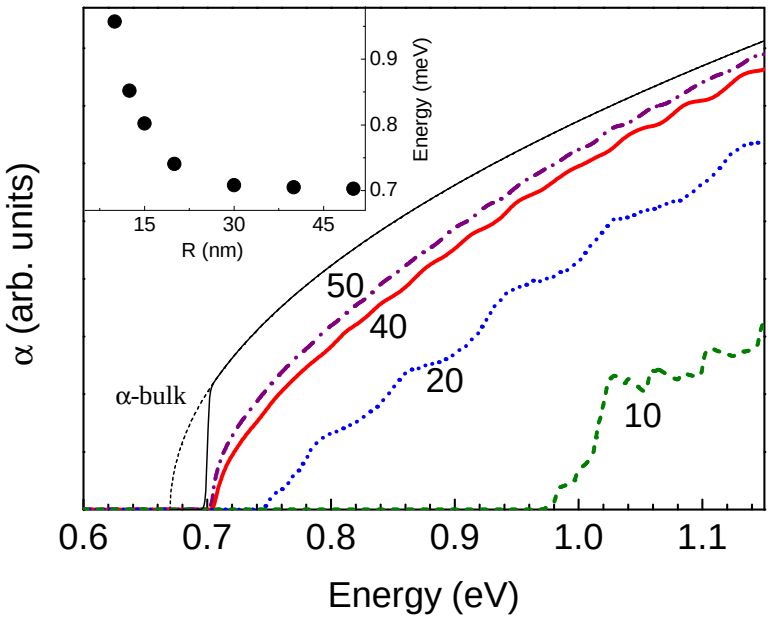

Figure 4.9: Optical absorption spectra for the same InN nanowires as Fig. 4.8. The number next to the curves indicates the radius. The $E^{1/2}$ ideal dependence of the absorption of bulk InN with a band-gap energy of 0.67 eV is also displayed in two cases; intrinsic bulk (black dashed line) and degenerate bulk $E_F - E_c = 30$ meV (black solid line). The inset shows the evolution of the absorption edge with the radius.

We can see how the density in core increases as the radius decreases and reaches a concentration in the core of the same order of magnitude than at the surface for the thinner NWs. The changes in the density profile can be best understood by looking at the variation of the Fermi level, $E_F - E_c$, with the NW radius. This has a value of 0.29 eV for $R = 10$ nm, and then decreases to an almost constant value of 0.03 eV for radius larger than 30 nm. Thus, the Fermi level will increase with decreasing radius because the sub-band energy separation is larger for smaller NW radius. Moreover, the Friedel-type oscillations are observed for all the density profiles, as explained before. As we have discussed in the example of Fig. 4.6(b), an increase of the temperature smoothes such undulations until they become imperceptible for $T > 200$ K.

In order to analyze how the size affects the optical properties, the absorption spectra for the nanowires calculated above are displayed in Fig. 4.9. The absorption spectra of intrinsic and degenerate bulk InN are also drawn with dashed and solid black lines, respectively. Since the Fermi level is above the conduction band edge, a Burstein-Moss shift is observed for all the nanowire considered here and this increases with decreasing radius. All the nanowire spectra differ from that of the

degenerate bulk InN. The blue-shift of the absorption edge is accompanied by a decrease in the intensity of the absorption, which is related to a smaller spatial overlapping between valence and conduction band states. Thus, for nanowires of radius 10 and 20 nm, the potential energy profile is not flat in any region and the valence band states are confined at the NW core. On the other side, the conduction band states displaced partially toward the surface. In the cases of $R =$ 40 and 50 nm, the potential energy profile have a larger flat region, and the spatial overlapping between valence and conduction band states increases, and therefore, the absorption in larger NWs converges to the intrinsic bulk spectrum before (about 1.1 eV) than in thinner NWs. Moreover, the spectrum corresponding to $R = 10$ nm shows certain structure in the profile related to the quantum confinement produced by large energy separation between the valence and conduction sub-bands. This is confirmed by the absorption edge energy, 25 meV over the Fermi level. The evolution of the absorption edge with the radius is shown in the inset of Fig. 4.9. On the other hand, we see that for NWs with $R > 30$ nm the absorption edge is not significantly affected by the NW size.

4.3.2 Influence of N_{ss}^{+} and N_{D}^{+} on the absorption

In addition to the influence of size on the absorption, we study the dependence of the electron accumulation layer on the changes in the donor concentration. As we have seen in Section 4.1, different growth conditions with slight variations in the substrate temperature or nitrogen-flux, result in InN nanowires of different morphology. Also, we can infer the presence of different concentrations of free-electrons in the samples of Fig. 4.2 from the PL and PLE spectra. It is therefore interesting to explore how the electron accumulation layer and the absorption spectrum change with varying concentrations of impurities, N_{D}^{+} and N_{ss}^{+}. In this Subsection we have considered a NW radius of $R = 40$ nm.

Figure 4.10(a) shows the conduction band profile for several values of the donor concentration. First of all, it is noteworthy to mention that the variation of the volume concentration of impurities N_{D}^{+} does not substantially affect the conduction band profile, and we have represented only two potential profiles, corresponding to the cases of $N_{ss}^{+} = 1.0 \times 10^{12}$ cm^{-2} and $N_{ss}^{+} = 1.0 \times 10^{13}$cm^{-2}. In any case, the consequence of incrementing the surface donors concentration, N_{ss}^{+}, is a more pronounced bending of the conduction band profile. On the other side, a deeper energy potential compensates the increasing of the electron population, and therefore, the Fermi level remains unaltered. It is worth to mention that for very thin nanowires, the increasing of N_{ss}^{+} will increment of the Fermi levels. In the inset

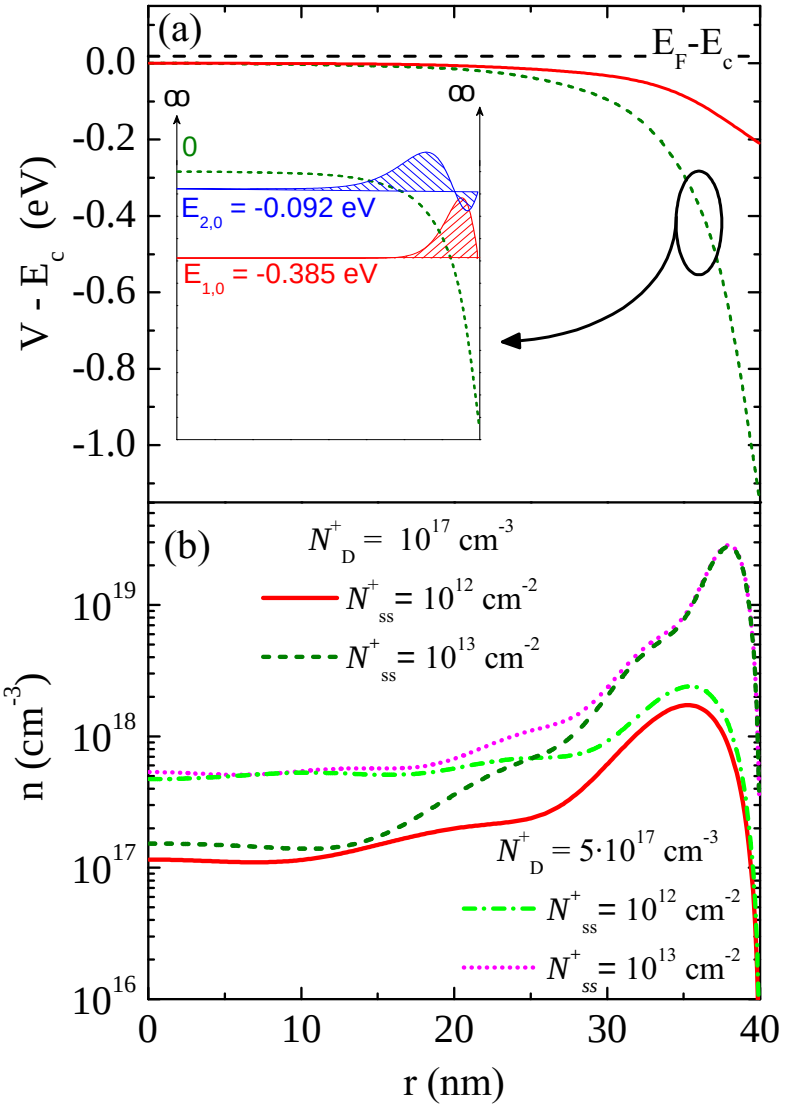

Figure 4.10: (a) Conduction band and (b) electron concentration profiles of a 40 nm radius InN nanowire. In panel (a) $N_D^+ = 1.0 \times 10^{17}$ cm^{-3} and two different values of N_{ss}^+: 1.0×10^{12} and 1.0×10^{13} cm^{-2}. The inset shows the conduction band profile for the higher N_{ss}^+ value and the first two conduction band states ($l = 0$). In panel (b) the electron density profiles are also plotted for $N_D^+ = 5.0 \times 10^{17}$ cm^{-3}.

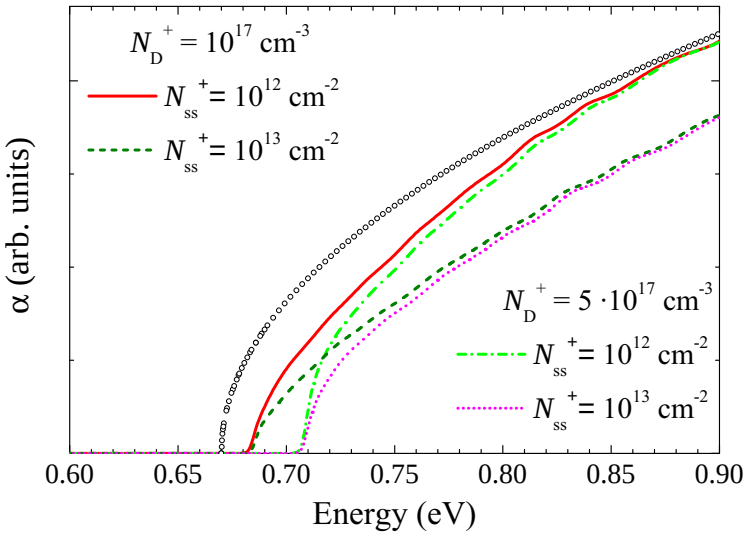

Figure 4.11: Calculated absorption spectra for InN nanowire with radius 40 nm and for two values of N_D^+; 1.0×10^{17} and 5.0×10^{17}, and two values of N_{ss}^+; 1.0×10^{12} and 1.0×10^{13} cm^{-2}. The $E^{1/2}$ ideal dependence of the absorption for intrinsic bulk InN (open circles) is also displayed.

of Fig. 4.10(a) we can see that the first two conduction band states of $l = 0$ are clearly localized near the nanowire surface.

Figure 4.10(b) displays the charge density. The increment in the surface donor concentration N_{ss}^+ induces a rise of the density $n(r)$, which is concentrated near the surfaces. However, the electron concentration in the core is not substantially modified. This is due to the increase in the potential energy at the surface. On the contrary, if we augment the contribution of the volume donors, N_D^+, keeping constant N_{ss}^+, the opposite effect is noticed in the density profile: Now, the increment of N_D^+ entails a rise of $n(r)$ at the NW core, without changing significatively in the region close to the surface. The corresponding Fermi levels for each concentration are 17 and 47 meV for $N_D^+ = 1 \times 10^{17}$ and $N_D^+ = 5 \times 10^{17}$ cm^{-3}, respectively. Basically, the increase of volume impurities N_D^+ results in a filling of the conduction band. These results indicate that the effects of volume and surface impurities on the nanowire charge density are approximately decoupled to some extent. This will also manifest in the absorption coefficient as we show below.

The above results suggest that the optical absorption would be also affected by changes in the donor concentrations. Figure 4.11 shows the optical absorption calculated for the same set of nanowires considered in Fig. 4.10. The $E^{1/2}$ ideal dependence of the absorption for intrinsic bulk InN is plotted with empty circles. Figure 4.11 shows that distinctive optical features can be associated to

variations in the bulk impurity concentration and surface charge density of the NWs. First, the increase in N_D^+ blue-shifts the absorption (see red solid line and dotted-dashed green line) 30 meV in this case and does not affect the overall efficiency (see at higher energies). On the other hand, the increase of the surface donor concentration N_{ss}^+ from 1.0×10^{12} to 1.0×10^{13} cm^{-2} quenches the overall value of the absorption, but does not influence in the absorption edge (see the spectra represented by red solid line and dashed green line). We can also appreciate that for energies beyond 0.9 eV the spectra of surface donor concentration $N_{ss}^+ = 1.0 \times 10^{12}$ tends to the $E^{1/2}$ curve, which indicates that the effects of the electron accumulation layer in the absorption are negligible in that energy range ($\sim$ 200 meV above the band gap). In the cases of $N_{ss}^+ = 1.0 \times 10^{13}$, the optical spectra does not converge to the $E^{1/2}$ curve in the energy range represented here. This negative influence on the absorption efficiency of increasing N_{ss}^+ is due to the larger potential drop. Therefore, while valence band states are more localized at the NW center, the conduction band states, even with energy above the Fermi level, will be perturbed by the energy potential well at the surface, which modulates its wave function, shifting toward the surface. This is evident in the case of $N_{ss}^+ = 1.0 \times 10^{12}$, where the potential falls to ~ -0.2 eV (see Fig. 4.10), and the corresponding absorption profiles (solid red and dashed dark green lines) approach the bulk absorption in energies above ~ 0.2 eV respect the band gap. On the other side, the influences of the surface and volume donors on the absorption spectra are practically decoupled.

In conclusion, the self-consistent procedure developed here is a suitable tool to study how the electrostatic potential and the electron density depend on such parameters as the nanowire radius and the doping density. In the next Section, we end this Chapter by comparing our theoretical absorption spectra with the photoluminescence excitation spectra presented in Section 4.1.

4.4 Comparison with photoluminescence excitation experiments

We will present here a comparison is carried out between the measured PLE spectra commented in Section 4.1 and the theoretical absorption spectra calculated by the self-consistent method in Section 4.3.

First of all, it must be recalled that only under certain conditions the PLE and absorption spectra are equivalent and can be compared. As opposed to the standard PL measurement, in a PLE experiment the detector is locked at a fixed

detection energy (usually coinciding with the maximum of the PL spectrum, generally assigned to the ground state energy of the system), whereas the excitation energy is varied over a wide range above the detection one. As a result, the PLE spectrum is believed to represent the ground state emission intensity as a function of the excess excitation energy. It would be helpful examine the relation between the emission intensity I_{em} and the excitation intensity, I_{ex}, which can be generally written as follows:

$$I_{em} = I_{ex} P_{abs} P_{rel} P_{em}, \tag{4.23}$$

where P_{abs} is the probability of absorbing an incident photon thereby creating an electron-hole pair, P_{rel} is the probability of the photoexcited electron-hole pairs to relax to the emitting state, and P_{em} is the probability of the radiative recombination from this emitting state, which can be assumed to be a constant (independent of the excitation energy) in a PLE experiment. In principle, the two other terms, P_{abs} and P_{rel}, depend strongly on the energy, among other parameters. In Fig. 4.12 we have displayed an scheme of the electron-hole pair recombination. In the case studied here the conduction band is already filled with electrons up to the Fermi level. Thus, the lowest energy emission takes place by the recombination of a hole that has relaxed to the emitting state (highest valence band states), with an electron that already occupies an emitting state. Therefore, P_{rel} depends almost exclusively on the hole relaxation. The dependence of the hole relaxation process on the energy determines the feasibility of correlating I_{em} with P_{abs} and therefore the comparison between the measured PLE and the theoretical absorption spectra. If P_{rel} can be considered as close to 1 (very efficient relaxation of the hole to the top of the valence band) and independent of the initial hole energy (for the energies relevant to the experiment), then the spectrum of I_{em} mimics that of P_{abs}, and therefore PLE and absorption measurements would yield essentially the same profile. In high quality samples, and at low temperature, the non-radiative processes can be neglected as compared to the relaxation induced by electron-phonon scattering, so that one can expects a good correspondence between the PLE and the absorption spectra at low excitation energies [192].

Therefore, we are going to attempt to fit the PLE experiments by means of our theoretical model for the absorption spectrum. As we have shown in Subsection 4.3.1, a change in the nanowire radius leads to changes in the distribution of free electrons and hence in the absorption spectrum. However, given the inhomogeneity in the size of the NWs (see Fig. 4.2), and knowing that most of the NWs investigated here have a large radius ($R > 30$ nm), we have assumed a fixed radius of $R = 40$ nm, for the calculations of the absorption presented here. On the other

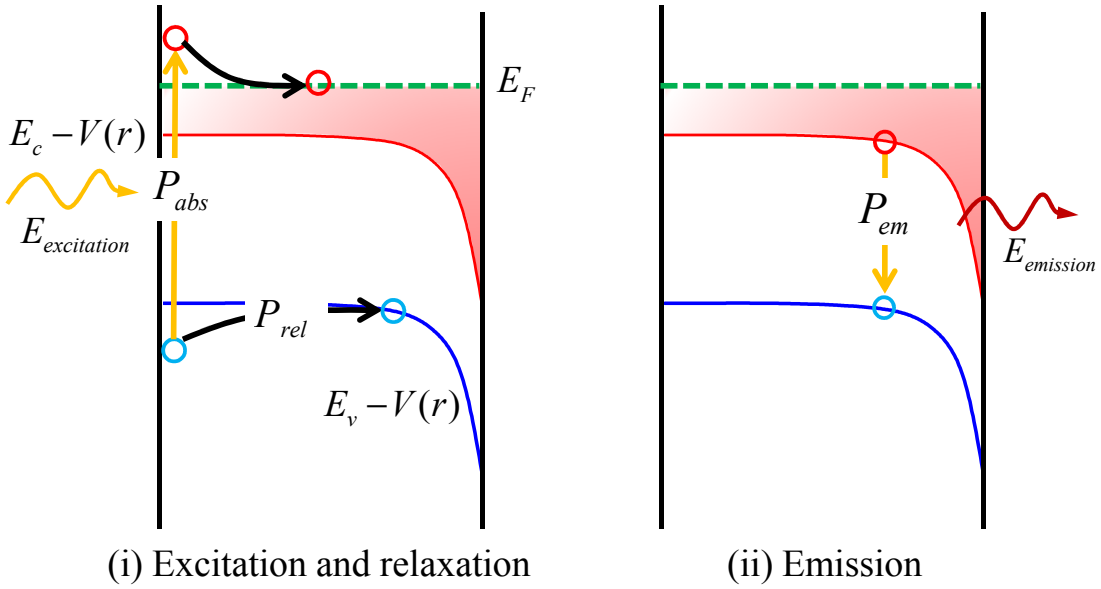

Figure 4.12: Scheme of the relevant process involved in a PLE experiment.

side, the N_D^+ and N_{ss}^+ values that allow the best fit of the theoretical spectra to the PLE experiments have been summarized in Table 4.1. As we have shown in the previous Section, the influence of N_D^+ and N_{ss}^+ on the absorption is decoupled, and they can be estimated independently to a great extent.

The PLE spectra (symbols) and the theoretical fits (solid lines) are shown in Fig. 4.13, together with the associated PL spectra (dashed lines). We can appreciate the good agreement of the theoretical spectra with the experimental data at energies close to the absorption onset. At higher values, the experimental PLE intensity decreases presumably due to the activation of non-radiative recombination channels and deviates considerably from the theoretical spectrum. The blue-shift of the absorption edge energy observed in the four spectra is accompanied by an increase in the fitted concentration of impurities in the volume, N_D^+, as it is reported in Table 4.1. The values found for N_D^+ are in good agreement with those cited in the literature and point out that InN NWs grown by plasma-assisted MBE contain a relatively low density of donor impurities. On the other side, in the previous Section we have established that the line shape of the absorption is controlled by the surface donor concentration N_{ss}^+. The variation of the fitted value from one sample to another suggests that this parameter is also affected by the specific growth conditions. Such a result is expected from the theoretical predictions of Van der Walle and coworkers for nonpolar InN surfaces [53].

Regarding the PL spectra, all of them show a clear Stokes shift, whose mag-

Sample	E_0 (eV)	N_D (cm^{-3})	N_{ss} (cm^{-2})
G532	0.687	0.8×10^{17}	2.5×10^{13}
G041	0.696	2.0×10^{17}	2.4×10^{13}
G136	0.711	5.0×10^{17}	1.7×10^{13}
G044	0.726	7.5×10^{17}	1.4×10^{13}

Table 4.1: Experimental absorption edge energy (E_0), and values of the donor concentrations N_D^+ and N_{ss}^+ that provide the best fit of the theoretical absorption spectra to the experimental PLE measurements of the samples studied in this work. All the calculations have been done for $R = 40$ nm, a band gap $E_g = 0.67$ eV, and with the isotropic electron mass $m_c^* = 0.05$ [233].

nitude increases with the absorption edge energy. The PL emission is broader for the samples G136 and G044, that also exhibit the largest PL peak blue-shifts with respect to the bulk band gap. A plausible explanation of this fact lies in the differences between the processes of absorption and emission. Indeed, the absorption is just the transition of an electron from the valence band to an unoccupied level of the conduction band (in the case of the InN NWs studied here, this level must be above the Fermi level). On the other hand, the emission takes place after the recombination of a free electron with a hole, which may be free or localized (if it is attached to an impurity) [252]. The existence of such localized holes has been determined by exploring the dependence on the temperature of the PL response [232]. The momentum conservation selection rule, followed in the absorption process, would break for the case of emission involving localized states, thus allowing recombination with all the free electrons in the conduction band, which would imply an increased broadening of the emission. If the Fermi level increases, the number of electrons available to recombine with the localized holes is notably increased. Such electrons have the energy ranging between E_c and $E_c + E_F$, and therefore, the range of energy from where it is possible a recombination increases with the Fermi energy, which also enlarges the PL broadening. The fact that optical transitions are less probable for larger values of the wave vector explains why the PL energy lies between the band gap and the absorption edge. This also explains why the Stokes shift increases with the increase in the absorption edge energy.

Not only the PL and PLE experiments can be interpreted on the basis of our theoretical model. Also the reported Raman scattering and transport measurements are compatible with the theoretical results. The measured frequency of the PLP^- mode suggests a charge near the surface of approximately 10^{-19} cm^{-3}. As we can see in Figs. 4.8 and 4.10 the electron density takes a value of this magnitude

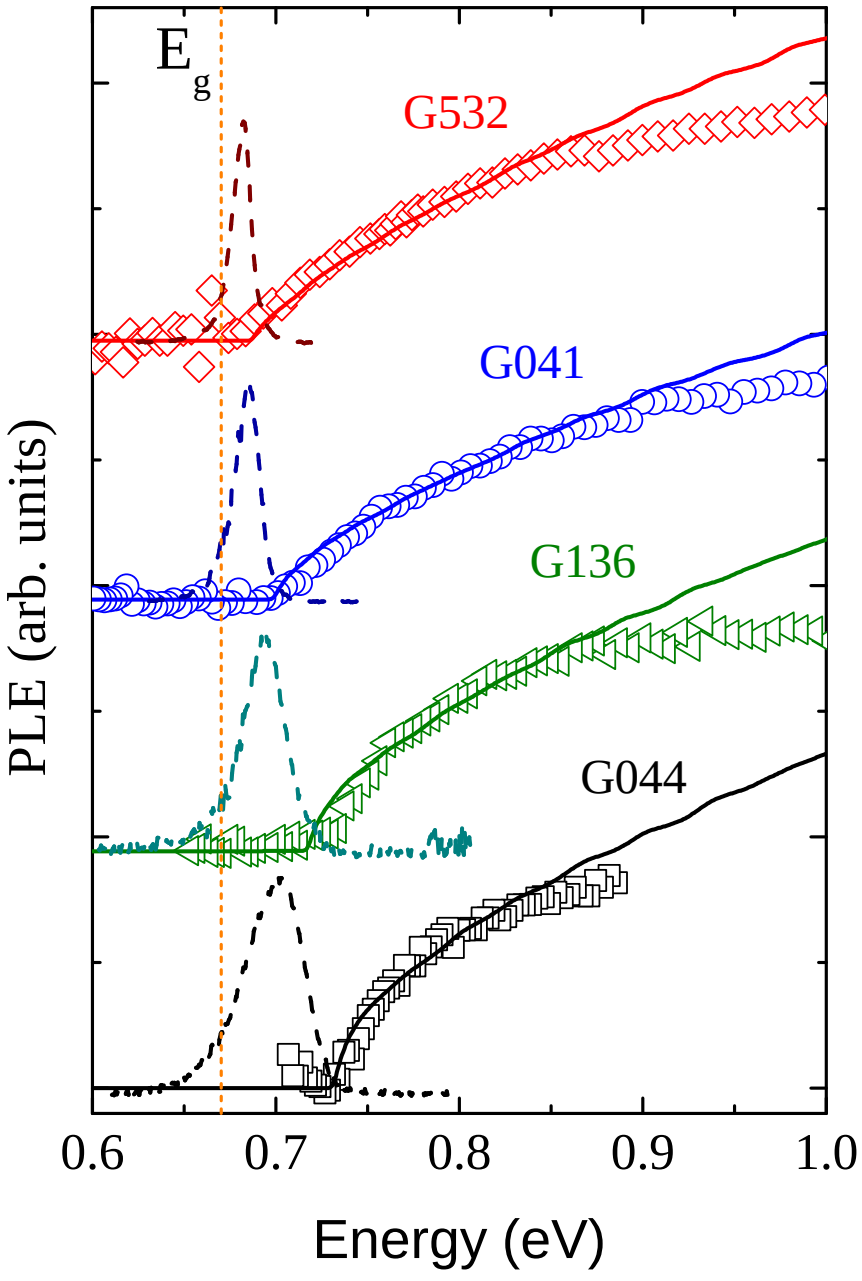

Figure 4.13: PL spectra (dashed-line) and PLE spectra detected at the PL peak energy (open symbols), for the different InN NW samples. Spectra are shifted along the vertical axis. Calculated absorption spectra (solid lines) showing the best agreement with the experimental ones are also included. For experimental details, see Ref. [233]

close to the surface. The depletion of electrons in the NW core is also compatible with the existence of the uncoupled longitudinal optic mode. In relation to the transport measurements, all the electron density profiles shown in this Section confirm the accumulation at the surface. However, the accumulation layer thickness varies with the NW radius, as shown in Fig. 4.8. A more sophisticated calculation of the resistivity for along-axis conduction, based on our self-consistent calculation of the electronic spectrum would give more conclusive results.

In conclusion, the self-consistent model formulated in this Chapter is suitable for the study of the optical absorption of InN NWs, and is favorably compared with the reported PLE spectra. Even with the simplifications implicit in our model, where the conduction band was considered parabolic, our approach has given convincing explanation to the experimental data concerning the electronic inhomogeneous distribution in InN NWs, and has also established the dependence of such electron density with external parameters as the NW radius and doping level. One major improvement of the model would be to consider realistically the non-parabolic dispersion of the conduction band within the effective-mass approximation. However, this would be accompanied by a substantial increase in the complexity of the problem, because many approximations taken to calculate the electron density or the absorption (see Eqs. (4.9) and (4.20)) would no longer be valid. Other extensions of the model can be done by performing a study of the recombination problem taking account the existence of localized holes, once the electrostatic potential inside the NW is known.

Chapter 5

Conclusions

In this thesis we have developed a theoretical methodology in order to study the electronic and optical properties of III-N nanowires, that applies different models depending on the size and complexity of the system. Below, we summarize the main conclusions and give a graphical scheme of the work performed in Fig 5.1.

- The *ab initio* methods based on the density functional theory, within the local density approximation (LDA) and the improved approach called LDA+U have been applied to obtain the bulk band structure of the III-N semiconductors. These results have been used to derive the parameters of the empirical methods. More specifically, for the wide band gap semiconductors GaN and AlN, the LDA gives reliable results for the band structure but underestimates band gap, that is subsequently corrected within the empirical pseudopotential and tight-binding methods. On the other side, in the case of the narrow gap semiconductor InN, it is necessary a refinement of LDA to get a reliable band structure. We have demonstrated that the LDA+U is a suitable approach to improve the LDA band structure of InN. This is possible because the LDA+U opens the LDA zero band gap, separating the valence band from the conduction band.

- We have derived screened pseudopotentials directly from the *ab initio* results, which are the sum of the ionic pseudopotential and the contribution of the electron-electron interaction, calculated by *ab initio* LDA. The good agreement between the band structures calculated by this semi-empirical pseudopotential method and LDA approach confirms the suitability of the derived pseudopotentials. Moreover, within the semi-empirical pseudopotential method the band gap, underestimated by the LDA, can be easily corrected without compromising the other virtues of the method. In order to

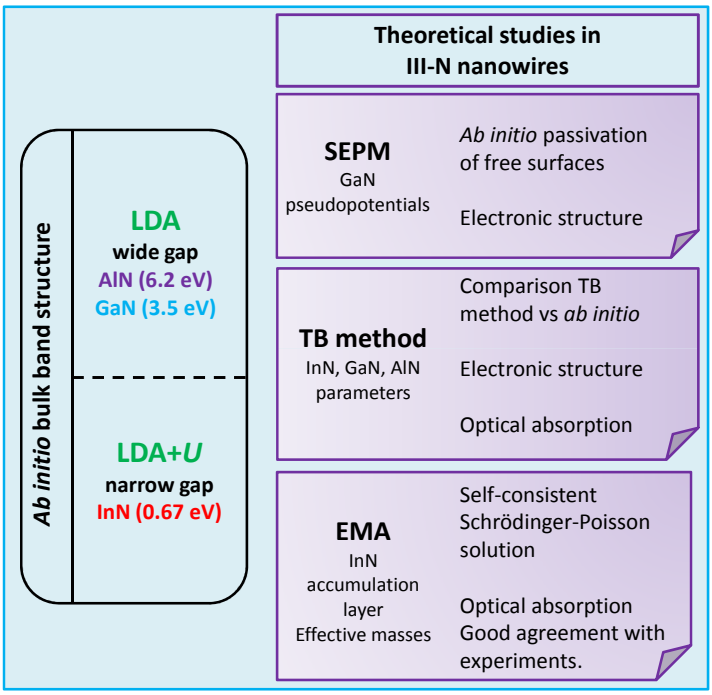

Figure 5.1: Summary of the main results.

use such pseudopotentials in the study of nanostructures with free surfaces, a passivation strategy has been formulated, which obtains the suitable passivant pseudopotentials also from the LDA method. This strategy removes the surface states from the nanostructure band gap, what has allowed us to apply successfully the semi-empirical pseudopotential method to nanowires. The electronic structure of GaN nanowires has been obtained for nanowire sizes varying from 1 to 6.5 nm. From the symmetry of the wave function we deduce an anisotropic optical absorption, much stronger for light polarization vector ($\boldsymbol{e}_\perp$) perpendicular than parallel ($\boldsymbol{e}_z$) to the NW axis. We have also demonstrated a non-trivial size dependence of the valence band states.

- In order to extend the study to larger nanowires, we have adapted the tight-binding method. The tight-binding parameters have been derived from the *ab initio* LDA and LDA+U band structures. In addition, they are also forced to fit the experimental band gap. A comparison between the LDA+U and tight-binding results for a thin InN nanowire shows an excellent agreement, which validates the use of tight-binding parameters fitted to bulk properties to study nanostructure systems. Based on these results, we have used the tight-binding method to study the band structure and the absorption spectra of III-N nanowires. The following conclusions have emerged from

that study: (i) Both InN and GaN nanowires show an absorption edge at lower energy for the $\boldsymbol{e}_\perp$ light polarization than for $\boldsymbol{e}_z$ polarization. (ii) The separation between these polarized absorption edges energy varies with the size and converges for large NWs to the crystal-field splitting value. (iii) An unconventional topmost valence band state with p-type envelope is found in both InN and GaN nanowires, as a consequence of the A-B bands mixing. (iv) A completely different picture of the optical properties has been found for AlN nanowires. The absorption edge is located at lower energy for $\boldsymbol{e}_z$ light polarization than for $\boldsymbol{e}_\perp$ polarization, as a consequence of the negative crystal-field splitting of AlN. Moreover, the evolution of the topmost valence band state almost follows the prediction given by the EMA in the single-band approximation, and the charge density of those valence band states shows an s-type envelope. In conclusion, the III-N nanowires present an important anisotropy in the optical response, enhanced by the quantum confinement for sizes below 20 nm. We have shown that the tight-binding approach acts as an ideal bridge between the *ab initio* methods suitable for small sizes (~ 1 nm) and the of effective-mass approximation, originally formulated for larger sizes (~ 20 nm).

- We have also studied the optical properties of InN nanowires with electron accumulation layer at the surface, as a function of the nanowire radius, the surface and volume impurity concentration. Due to the large size of the system, it is not amenable to treatment by means of *ab initio* or empirical atomistic models. Instead we have used the effective mass approximation, that furthermore allows a direct implementation of the Poisson equation need to take account of the electrostatic potential and summarize here the main results: (i) The absorption edge is determined mainly by the volume impurity concentration, and the absorption profile is related to the surface impurity concentration. (ii) A decrease in the nanowire radius entails a blue-shift of the absorption edge, together with changes in the electron distribution in the nanowire, with a tendency to a more homogeneous distribution. Finally, theoretical absorption spectra have been compared with those obtained from photoluminescence experiments, and a very good agreement has been found.

Appendix A

Tight-binding Hamiltonian matrix for wurtzite semiconductors

The tight-binding Hamiltonian matrix, H_{WZ}, for wurtzite semiconductor, without spin-orbit interaction, can be expressed in block from as

$$H_{\mathrm{WZ}} = \begin{pmatrix} E_c & \hat{V}_{1,2} & 0 & \hat{V}_{4,1}^{\dagger} \\ \hat{V}_{1,2}^{\dagger} & E_a & \hat{V}_{2,3} & 0 \\ 0 & \hat{V}_{2,3}^{\dagger} & E_c & \hat{V}_{3,4} \\ \hat{V}_{4,1} & 0 & \hat{V}_{3,4}^{\dagger} & E_a \end{pmatrix}. \tag{A.1}$$

Each block is a 4×4 matrix. The diagonal matrices E_β, $\beta = c, a$ contain the orbital energies. The matrices $\hat{V}$ represent the interaction up to nearest neighbors:

$$E_c = \begin{pmatrix} E_{c,s} & 0 & 0 & 0 \\ 0 & E_{c,p} & 0 & 0 \\ 0 & 0 & E_{c,p} & 0 \\ 0 & 0 & 0 & E_{c,p} \end{pmatrix}; \quad E_a = \begin{pmatrix} E_{a,s} & 0 & 0 & 0 \\ 0 & E_{a,p_x} & 0 & 0 \\ 0 & 0 & E_{a,p_x} & 0 \\ 0 & 0 & 0 & E_{a,p_z} \end{pmatrix}; \tag{A.2}$$

$$\hat{V}_{1,2} = \begin{pmatrix} V_{ss\sigma} f(\boldsymbol{k}) & 0 & 0 & V_{s_c p_a} f(\boldsymbol{k}) \\ 0 & V_{pp\pi} f(\boldsymbol{k}) & 0 & 0 \\ 0 & 0 & V_{pp\pi} f(\boldsymbol{k}) & 0 \\ -V_{s_a p_c} f(\boldsymbol{k}) & 0 & 0 & V_{pp\sigma} f(\boldsymbol{k}) \end{pmatrix}; \quad \hat{V}_{3,4} = \hat{V}_{1,2} \tag{A.3}$$

$$\hat{V}_{4,1} = \begin{pmatrix} V_{ss\sigma}h_1 & \sqrt{\frac{2}{3}}V_{s_ap_c}h_3 & V_{s_ap_c}(\frac{2}{\sqrt{3}}h_2 - \sqrt{\frac{8}{9}}h_4) & \frac{1}{3}V_{s_ap_c}h_1 \\ -\sqrt{\frac{2}{3}}V_{s_cp_a}h_3 & V_{pp\pi}h_4 + (\frac{2}{3}V_{pp\sigma} + \frac{1}{3}V_{pp\pi})h_2 & \frac{2}{3\sqrt{3}}(V_{pp\sigma} - V_{pp\pi})h_3 & \sqrt{\frac{2}{27}}(V_{pp\sigma} - V_{pp\pi})h_3 \\ -V_{s_cp_a}(\frac{\sqrt{2}}{3}h_2 - \sqrt{\frac{8}{9}}h_4) & \frac{2}{3\sqrt{3}}(V_{pp\sigma} - V_{pp\pi})h_3 & V_{pp\pi}h_4 + (\frac{2}{3}V_{pp\pi} + \frac{1}{3}V_{pp\sigma})h_2 & (V_{pp\sigma} - V_{pp\pi})(\frac{\sqrt{2}}{9}h_2 - \sqrt{\frac{8}{81}}h_4) \\ -\frac{1}{3}V_{s_cp_a}h_1 & \sqrt{\frac{2}{27}}(V_{pp\sigma} - V_{pp\pi})h_3 & (V_{pp\sigma} - V_{pp\pi})(\frac{\sqrt{2}}{9}h_2 - \sqrt{\frac{8}{81}}h_4) & (\frac{8}{9}V_{pp\pi} + \frac{1}{9}V_{pp\sigma})h_1 \end{pmatrix}; \tag{A.4}$$

$$\hat{V}_{2,3} = \begin{pmatrix} V_{ss\sigma}t_1 & \sqrt{\frac{2}{3}}V_{s_ap_c}t_3 & V_{s_ap_c}(\sqrt{\frac{8}{9}}t_4 + \frac{2}{\sqrt{3}}t_2) & \frac{1}{3}V_{s_ap_c}t_1 \\ -\sqrt{\frac{2}{3}}V_{s_cp_a}t_3 & V_{pp\pi}t_4 + (\frac{2}{3}V_{pp\sigma} + \frac{1}{3}V_{pp\pi})t_2 & -\frac{2}{3\sqrt{3}}(V_{pp\sigma} - V_{pp\pi})t_3 & \sqrt{\frac{2}{27}}(V_{pp\sigma} - V_{pp\pi})t_3 \\ -V_{s_cp_a}(\frac{\sqrt{2}}{3}t_2 - \sqrt{\frac{8}{9}}t_4) & -\frac{2}{3\sqrt{3}}(V_{pp\sigma} - V_{pp\pi})t_3 & V_{pp\pi}t_4 + (\frac{2}{3}V_{pp\sigma} + \frac{1}{3}V_{pp\pi})t_2 & (V_{pp\sigma} - V_{pp\pi})(\sqrt{\frac{8}{81}}t_4 - \frac{\sqrt{2}}{9}t_2) \\ -\frac{1}{3}V_{s_cp_a}t_1 & \sqrt{\frac{2}{27}}(V_{pp\sigma} - V_{pp\pi})t_3 & (V_{pp\sigma} - V_{pp\pi})(\sqrt{\frac{8}{81}}t_4 - \frac{\sqrt{2}}{9}t_2) & (\frac{8}{9}V_{pp\pi} + \frac{1}{9}V_{pp\sigma})t_1 \end{pmatrix}. \tag{A.5}$$

The coefficients f,h and t are

$$
\begin{aligned}
f(\boldsymbol{k}) = & \quad e^{ik_z uc}, \\
h_1(\boldsymbol{k}) = & \quad e^{i(-k_y \frac{a}{\sqrt{3}} + k_z(\frac{1}{2}-u)c)} \left[1 + 2\cos(k_x \frac{a}{2}) e^{ik_y \frac{\sqrt{3}a}{2}}\right] \\
h_2(\boldsymbol{k}) = & \quad 2e^{i(k_y \frac{a}{\sqrt{12}} + k_z(\frac{1}{2}-u)c)} \cos(k_x \frac{a}{2}) \\
h_3(\boldsymbol{k}) = & \quad 2ie^{i(k_y \frac{a}{\sqrt{12}} + k_z(\frac{1}{2}-u)c)} \sin(k_x \frac{a}{2}) \\
h_4(\boldsymbol{k}) = & \quad e^{i(-k_y \frac{a}{\sqrt{3}} + k_z(\frac{1}{2}-u)c)} \\
t_1(\boldsymbol{k}) = & \quad e^{i(k_y \frac{a}{\sqrt{3}} + k_z(\frac{1}{2}-u)c)} \left[1 + 2\cos(k_x \frac{a}{2}) e^{-ik_y \frac{\sqrt{3}a}{2}}\right] \\
t_2(\boldsymbol{k}) = & \quad 2e^{i(-k_y \frac{a}{\sqrt{12}} + k_z(\frac{1}{2}-u)c)} \cos(k_x \frac{a}{2}) \\
t_3(\boldsymbol{k}) = & \quad 2ie^{i(-k_y \frac{a}{\sqrt{12}} + k_z(\frac{1}{2}-u)c)} \sin(k_x \frac{a}{2}) \\
t_4(\boldsymbol{k}) = & \quad e^{i(k_y \frac{a}{\sqrt{3}} + k_z(\frac{1}{2}-u)c)}
\end{aligned}
\tag{A.6}
$$

The Hamiltonian matrix with the spin-orbit interaction can be constructed straightforward by adding to the orbital basis the spin of the electron

$$\hat{H}_{\mathrm{WZ,SO}} = \begin{array}{c} \\ \sigma=\uparrow \\ \\ \sigma=\downarrow \\ \\ \end{array} \begin{array}{c} \begin{array}{cccc} \sigma=\uparrow & & & \end{array} \\ \left(\begin{array}{cccc} & & & \\ & \hat{H}_{\mathrm{WZ}} & & \\ & & & \\ & & & \end{array}\right. \\ \left(\begin{array}{cccc} H^{\dagger}_{\mathrm{SO,c}} & 0 & 0 & 0 \\ 0 & H^{\dagger}_{\mathrm{SO,a}} & 0 & 0 \\ 0 & 0 & H^{\dagger}_{\mathrm{SO,c}} & 0 \\ 0 & 0 & 0 & H^{\dagger}_{\mathrm{SO,a}} \end{array}\right. \end{array} \begin{array}{c} \begin{array}{cccc} \sigma=\downarrow & & & \end{array} \\ \left(\begin{array}{cccc} H_{\mathrm{SO,c}} & 0 & 0 & 0 \\ 0 & H_{\mathrm{SO,a}} & 0 & 0 \\ 0 & 0 & H_{\mathrm{SO,c}} & 0 \\ 0 & 0 & 0 & H_{\mathrm{SO,a}} \end{array}\right. \\ \left(\begin{array}{cccc} & & & \\ & \hat{H}_{\mathrm{WZ}} & & \\ & & & \\ & & & \end{array}\right. \end{array} \tag{A.7}$$

The matrix $\hat{H}_{\mathrm{WZ}}$ is the same as H_{WZ} (dimension 16×16) with the addition of the following matrix element of the spin-orbit interaction V_{SO}, that couples states of the basis with the same spin

$$\begin{aligned} \langle p_x, \uparrow | V_{\mathrm{SO}} | p_y, \uparrow \rangle &= -i\lambda_\beta, \\ \langle p_x, \downarrow | V_{\mathrm{SO}} | p_y, \downarrow \rangle &= i\lambda_\beta. \end{aligned} \tag{A.8}$$

The matrix $H_{\mathrm{SO},\beta}$ couples states of the basis with different spin:

$$H_{\mathrm{SO},\beta}(\uparrow\downarrow) = \begin{pmatrix} 0 & 0 & 0 & 0 \\ 0 & 0 & 0 & \lambda_\beta \\ 0 & 0 & 0 & -i\lambda_\beta \\ 0 & -\lambda_\beta & i\lambda_\beta & 0 \end{pmatrix}. \tag{A.9}$$

Here $\lambda_\beta = \lambda_c, \lambda_a$ are the spin-orbit splitting of anion and cation p states. The fitted tight-binding parameters used in this work are listed in Table A.1.

	InN	GaN	AlN
$E_{c,s}$	-5.90550	-7.97000	-0.09600
$E_{c,p}$	9.61790	15.00000	9.41900
$E_{a,s}$	-6.79100	-13.00000	-12.10400
E_{a,p_x}	0.04470	0.37170	3.58100
E_{a,p_z}	-0.00222	0.32800	3.72500
$V_{s_c p_a}$	2.99810	4.70550	4.22400
$V_{s_a p_c}$	-0.10830	2.11700	3.50390
$V_{ss\sigma}$	-1.75000	-3.44280	-2.68375
$V_{pp\sigma}$	3.07000	3.55000	5.69500
$V_{pp\pi}$	-1.30000	-0.88175	-0.66950
λ_c	0.5	0.1	0.01
η	1.8	2.0	-
η_{s,p_z}	2.5	2.0	-

Table A.1: The notation follows the Ref. [190]. InN and GaN parameters have been derived from the *ab initio* calculations presented in Chapter 2. AlN parameters are extracted from Ref. [190]. Parameters are given in eV.

Appendix B

Determination of the hydrogen pseudopotentials

The details of how determine the screened hydrogen pseudopotentials are explained here. In principle, if we denote the self-consistent potentials as $V_{\text{bare}}(\boldsymbol{r})$ and $V_{\text{pass}}(\boldsymbol{r})$, it is reasonable to obtain the screened hydrogen potential $V_h(\boldsymbol{r})$ from the following operation:

$$V_h(\boldsymbol{r}) = V_{\text{pass}}(\boldsymbol{r}) - V_{\text{bare}}(\boldsymbol{r}). \tag{B.1}$$

We Note that there are actually two different hydrogen potentials, one attached to the cation and the another to the anion. By applying the same methodology as described in Section 2.2 one would obtain the screened hydrogen pseudopotentials, that together with the Ga and N semi-empirical pseudopotentials, would allow to construct a semi-empirical model for the passivated $(1\bar{1}00)$-layer, with the surface states removed from the band gap region. However, a problem arises when applying the above procedure. A careful look at the LDA potential profile, shown in Fig. B.1, reveals the potential decays smoothly toward the vacuum energy in both cases. This decay is obtained in LDA, calculating self-consistently the charge distribution. Thus, the charge density around the Ga and N atoms at the surface is different at the layer borders than in the interior of the film. Therefore, the simple adding of atomic semi-empirical pseudopotentials that underlie the SEPM, without any self-consistent procedure cannot reproduce this situation. Therefore, the direct application of the passivation with the screened hydrogen pseudopotentials as defined in equation (B.1) will ignore the smooth attenuation toward the vacuum, and possibly will not fulfill our goal of eliminating the surface states. It would be highly desirable to include such attenuation in some way into our calcu-

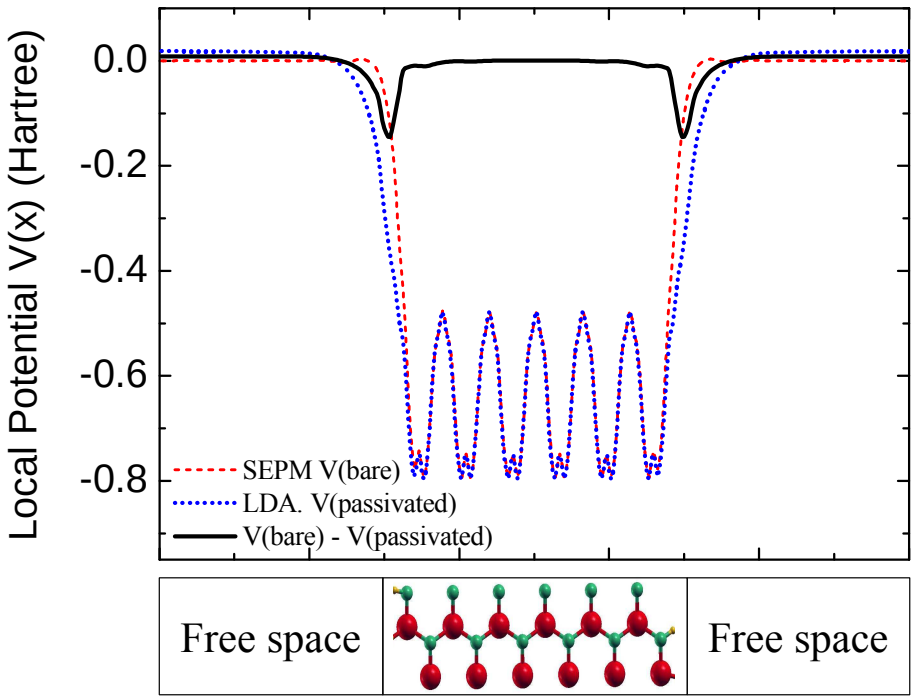

Figure B.1: The average potential in the $(1\bar{1}00)$ direction, passivated LDA (blue points), bare SEPM (red dashed), and the difference between both (black line).

lations. The most simple approach is to add as much as possible to the hydrogen pseudopotentials. Hence, we redefine the hydrogen potential as follows:

$$\tilde{V}_h(\boldsymbol{r}) = V_{\text{pass,LDA}}(\boldsymbol{r}) - V_{\text{bare,SEPM}}(\boldsymbol{r}), \tag{B.2}$$

where the passivated layer potential is taken from the LDA calculation, but the bare layer potential is the one calculated within the SEPM. Figure B.1 shows both potentials, together with $\tilde{V}_h(\boldsymbol{r})$. We note an abrupt drop in the surface of the semi-empirical potential for the bare layer. With the new definition of $\tilde{V}_h(\boldsymbol{r})$ this effect is partially corrected. Now, the same procedure of Section 2.2 is applied here to obtain the pseudopotentials of the hydrogen atoms bond to the nitrogen and gallium atoms, V_{NH} and V_{NGa}, respectively. We have represented the obtained potentials in Fig B.2, in real space. We observe that near the center, for $r < 1$ Bohr, both potentials show almost no dispersion of values for different directions, as in the case of the bulk potentials shown in Fig. 2.6. However, the dispersion is more important for larger radius, and an average must be applied to enforce an spherical approximation. In order to fit the pseudopotential to a simple function, we have applied the following criteria: (i) For radii smaller than a certain cutoff radius, where the points do not show dispersion, we will fit the potential with

a function of three splines. (ii) For $r > R_C$, we approximate the behavior by a function that simulates the screening of the pseudopotential at large distances. For this purpose, we have employed a Yukawa-like potential of the form:

$$V_Y(r) = -g^2 \frac{e^{-mr}}{r}, \tag{B.3}$$

where m and g^2 depend on the radius cutoff R_C, and are:

$$m = -\frac{V_Y'(R_C)R_C - V_Y(R_C)}{V_Y(R_C)R_C}; \quad g^2 = -V_Y(R_C)R_C e^{mR_C}. \tag{B.4}$$

The Yukawa-like fit function $V_Y(\boldsymbol{r})$ depends ultimately only on R_C: The parameters m and g^2 depend on the values of the pseudopotential and its derivative at R_C, and these values are determined by the splines fit function for the region $r < R_C$, in order to guarantee a smooth pseudopotential. Figure B.2 shows with lines the results of several fits obtained for different values of R_C (= 0.75, 0.80, 0.85 Bohr). All the derived pseudopotentials eliminate the surface states from the band gap.[1] The only difference between them is the hybridization of the conduction band states. For R_C 0.75 and 0.85 Bohr, the first conduction band state shows a slight localization near the surface, which is totally absent in the case $R_C = 0.80$ Bohr. Note that we have not tried to fit the shoulder around 1.2 Bohr. In calculations not shown here, where the whole potential range was fitted with splines, thus fitting more accurately the shoulder located at 1.2 Bohr, the surfaces states were not removed at all. This led us to think that the application of the spherical average is not very accurate for large radius, where the asymmetry around the hydrogen atoms is significant. Its enforcement and simultaneous fitting of the shoulder would give an artificial landscape in the pseudopotential profile, that is otherwise smoothed in the fitting procedure illustrated in Fig. B.2.

[1] The values for m and g^2 of the Yukawa potential for $R_C = 0.80$ Bohr, are $m = 1.408226$ and $g^2 = 2.583077$.

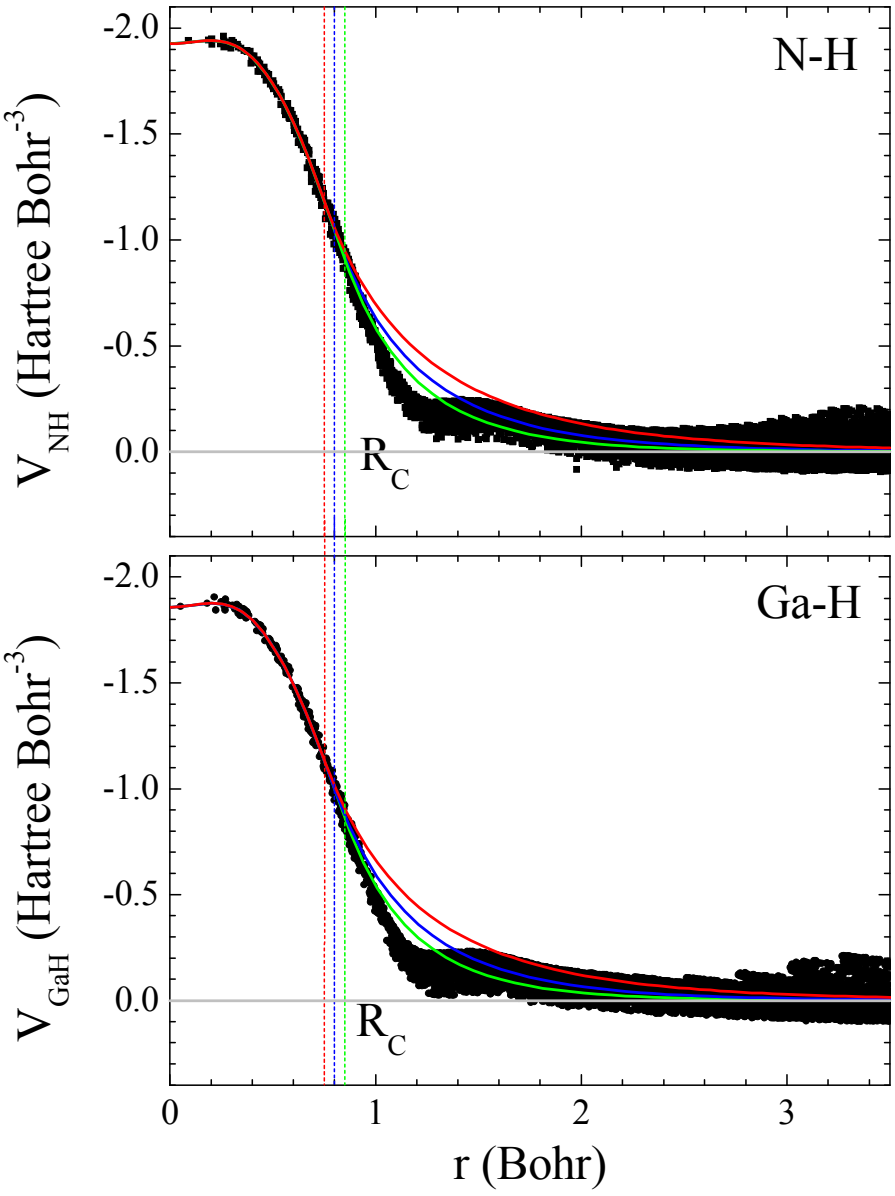

Figure B.2: Points representing the hydrogen pseudopotential attached to nitrogen (top) and gallium (bottom), in real space. The dispersion of values for given r is a consequence of the angular dependence of the potential. The fits performed with splines and the Yukawa-like potential of varying R_C are drawn with lines.

Appendix C

Arnoldi algorithm for the diagonalization of sparse matrices

Typically, the dimensions of the tight-binding Hamiltonian matrix of nanowires are in the range of 10^4 to 10^6. Although the LAPACK subroutines [253] can in principle be used with matrices of dimensions up to 10^5, its efficiency is dramatically reduced for such matrix sizes, and in addition, since these *direct methods* store the whole matrix, the computer memory is soon overflown.

The Arnoldi algorithm provides an optimal alternative approach, able of solving huge matrix eigenvalue problems (matrix dimensions above 10^4). The software that implements the Arnoldi algorithm is a free-license project, called ARPACK [254]. The Arnoldi algorithm belongs to the class of iterative methods for solving eigenvalue problems, where *solution* here has the narrower sense of obtaining, after a small number of iterations, a portion of the spectra, called *eigenvalues window*. Contrary to direct methods, which store all the elements of the matrix, the Arnoldi package use the operation of the matrix on a vector, extracting the information to solve the eigenvalue problem from the input vector image. Figure C.1 shows the scheme of the Arnoldi methods. The algorithm works better for *sparse* matrix (populated primarily with zeros), or *structured* matrix, where *structured* means that a product on a vector requires n operations rather than the usual order n^2. In this method we only store the vector and its image, and the matrix is defined by its action over an arbitrary vector. The absence of auxiliary storage makes the algorithm very fast for sparse matrix problems, with practically no limitation in the size of the matrix, thus converting it into a very suitable technique to solve the spectrum of very large Hamiltonians.

The operation of the Hamiltonian matrix on an input vector is defined as:

Arnoldi procedure

(1) $v_1 = v/\|v\|_2$ *for the starting vector* v
(2) **for** $j = 1, 2, ..., m$ **do**
(3) $w := Av_j$
(4) **for** $i=1, 2, ..., j$ **do**
(5) $h_{ij} = w^* v_i$
(6) $w := w - h_{ij} v_i$
(7) **end for**
(8) $h_{j+1,j} = \|v\|_2$
(9) **if** $h_{j+1,j} = 0$, **stop**
(10) $v_{j+1} = w/h_{j+1,j}$
(11) **end for**

Figure C.1: Flowchart of the Arnoldi algorithm. A detailed explanation of this and others methods can be found in Ref. [255].

$$\Psi_{out} = \boldsymbol{H} \cdot \Psi_{in}, \tag{C.1}$$

where most of the tight-binding Hamiltonian elements are zero due to the nearest neighbors approximation (even if we apply a second or third neighbors approximation, the matrix is very *sparse*). Moreover, in a semiconductor, we are interested in the values near the top of the valence band or the bottom of the conduction band. The ARPACK solvers use to give the lowest values of the spectra. Therefore, for obtaining the energies around a certain value E_0, we may shift the Hamiltonian matrix by means of:

$$\Psi_{out} = [\boldsymbol{H} - E_0 \boldsymbol{I}] \cdot \Psi_{in}, \tag{C.2}$$

being $\boldsymbol{I}$ the Identity matrix. Another variant of this procedure is the Folded Spectrum Method (FSM) [256] which starts from the operator $[\boldsymbol{H} - E_0 \boldsymbol{I}]^2$, and the eigenvalues are found by finding the minimum with the gradient conjugate techniques. This squared Hamiltonian can also be implemented in ARPACK, but one has to be careful since the product of two sparse matrix can lead to a dense matrix (populated primarily with non-zeros), and the efficiency of ARPACK in dense matrix problems is drastically reduced.

Bibliography

[1] J. Wu. *When group-III nitrides go infrared: New properties and perspectives.* J. Appl. Phys. **106**, 011101 (2009).

[2] J. Goldberger, R. He, Y. Zhang, S. Lee, H. Yan, H.-J. Choi, and P. Yang. *Single-crystal gallium nitride nanotubes.* Nature **422**, 599 (2003).

[3] M. H. Huang, S. Mao, H. Feick, H. Yan, Y. Wu, H. Kind, E. Weber, R. Russo, and P. Yang. *Room-temperature ultraviolet nanowire nanolasers.* Science **292**, 1897 (2001).

[4] Y. Cui, Q. Wei, H. Park, and C. M. Lieber. *Nanowire nanosensors for highly sensitive and selective detection of biological and chemical species.* Science **293**, 1289 (2001).

[5] Y. B. Tang, Z. H. Chen, H. S. Song, C. S. Lee, H. T. Cong, H. M. Cheng, W. J. Zhang, I. Bello, and S. T. Lee. *Vertically aligned p-type single-crystalline GaN nanorod arrays on n-type Si for heterojunction photovoltaic cells.* Nano Lett. **8**, 4191 (2008).

[6] P. Yang, R. Yan, and M. Fardy. *Semiconductor nanowire: What's next?* Nano Lett. **10**, 1529 (2010).

[7] M. S. Gudiksen, J. Wang, and C. M. Lieber. *Size-dependent photoluminescence from single indium phosphide nanowires.* The Journal of Physical Chemistry B **106**, 4036 (2002).

[8] A. I. Hochbaum, R. Chen, R. D. Delgado, W. Liang, E. C. Garnett, M. Najarian, A. Majumdar, and P. Yang. *Enhanced thermoelectric performance of rough silicon nanowires.* Nature **451**, 163 (2008).

[9] W. Lu and C. M. Lieber. *Semiconductor nanowires.* Journal of Physics D: Applied Physics **39**, R387 (2006).

[10] O. Jani, I. Ferguson, C. Honsberg, and S. Kurtz. *Design and characterization of GaN/InGaN solar cells.* Appl. Phys. Lett. **91**, 132117 (2007).

[11] C. Rivera, J. L. Pau, E. Munoz, P. Misra, O. Brandt, H. T. Grahn, and K. H. Ploog. *Polarization-sensitive ultraviolet photodetectors based on M-plane GaN grown on $LiAlO_2$ substrates.* Applied Physics Letters **88**, 213507 (2006).

[12] H. Morkoc. *Handbook of Nitride Semiconductors and Devices, Materials Properties, Physics and Growth* (Wiley-VCH, 2008).

[13] D. J. As, F. Schmilgus, C. Wang, B. Schottker, D. Schikora, and K. Lischka. *The near band edge photoluminescence of cubic GaN epilayers.* Appl. Phys. Lett. **70**, 1311 (1997).

[14] J. Schormann, D. J. As, K. Lischka, P. Schley, R. Goldhahn, S. F. Li, W. Loffler, M. Hetterich, and H. Kalt. *Molecular beam epitaxy of phase pure cubic InN.* Appl. Phys. Lett. **89**, 261903 (2006).

[15] J. Renard, G. Tourbot, D. Sam-Giao, C. Bougerol, B. Daudin, and B. Gayral. *Optical spectroscopy of cubic GaN in nanowires.* Appl. Phys. Lett. **97**, 081910 (2010).

[16] R. E. Algra, M. A. Verheijen, M. T. Borgstrom, L.-F. Feiner, G. Immink, W. J. P. van Enckevort, E. Vlieg, and E. P. A. M. Bakkers. *Twinning superlattices in indium phosphide nanowires.* Nature **456**, 369 (2008).

[17] B. V. Novikov, S. Y. Serov, N. G. Filosofov, I. V. Shtrom, V. G. Talalaev, O. F. Vyvenko, E. V. Ubyivovk, Y. B. Samsonenko, A. D. Bouravleuv, I. P. Soshnikov, N. V. Sibirev, G. E. Cirlin, and V. G. Dubrovskii. *Photoluminescence properties of GaAs nanowire ensembles with zincblende and wurtzite crystal structure.* Phys. Status Solidi-R **4**, 175 (2010).

[18] R. W. G. Wyckoff. *Crystal Structures*, vol. 1 (John Wiley and Sons, 1963).

[19] I. Vurgaftman and J. R. Meyer. *Band parameters for nitrogen-containing semiconductors.* J. Appl. Phys. **94**, 3675 (2003).

[20] W. Paszkowicz, R. Cerny, and S. Krukowski. *Rietveld refinement for indium nitride in the 105-295 K range.* Powder Diffr. **18**, 114 (2003).

[21] F. Bernardini and V. Fiorentini. *Spontaneous versus piezoelectric polarization in III-V nitrides: Conceptual aspects and practical consequences.* Phys. Status Solidi B-Basic Solid State Phys. **216**, 391 (1999).

[22] G. F. Koster. *Space Groups and Their Representations.* vol. 5 of *Solid State Physics*, 173 – 256 (Academic Press, 1957).

[23] C. Kittel. *Introducción a la Física del Estado Sólido* (Reverté, 1997), 3rd ed.

[24] T. Maruyama, Y. Miyajima, S. H. Cho, K. Akimoto, and H. Kato. *Angle-resolved photoemission study of the wurtzite GaN (0001).* Physica B: Condensed Matter **262**, 240 (1999).

[25] M. Tinkham. *Group Theory and Quantum Mechanics* (Dover, 2003).

[26] L. C. Lew Yan Voon, M. Willatzen, M. Cardona, and N. E. Christensen. *Terms linear in k in the band structure of wurtzite-type semiconductors.* Phys. Rev. B **53**, 10703 (1996).

[27] W.-T. Wang, C. L. Wu, S. F. Tsay, M. H. Gau, I. Lo, H. F. Kao, D. J. Jang, J.-C. Chiang, M.-E. Lee, Y.-C. Chang, C.-N. Chen, and H. C. Hsueh. *Dresselhaus effect in bulk wurtzite materials.* Appl. Phys. Lett. **91**, 082110 (2007).

[28] J. Wu, W. Walukiewicz, W. Shan, K. M. Yu, J. W. Ager, E. E. Haller, H. Lu, and W. J. Schaff. *Effects of the narrow band gap on the properties of InN.* Phys. Rev. B **66**, 201403 (2002).

[29] G. F. Koster, J. O. Dimmock, R. G. Wheeler, and H. Statz. *Properties of the Thirty-Two Point Groups* (MIT, 1963).

[30] C. Klingshirn. *Semiconductor Optics* (Springer Verlag, 2007).

[31] S. Nakamura and S. Chichibu. *Introduction to Nitride Semiconductors, Blue Laser Diodes, and Light Emitting Diodes* (CRC Press, 2000).

[32] S. L. Chuang and C. Chang. $\boldsymbol{k} \cdot \boldsymbol{p}$ *method for strained wurtzite semiconductors.* Phys. Rev. B **54**, 2491 (1996).

[33] B. Monemar. *Bound excitons in GaN.* Journal of Physics: Condensed Matter **13**, 7011 (2001).

[34] Y. Taniyasu and M. Kasu. *Surface 210 nm light emission from an AlN p–n junction light-emitting diode enhanced by A-plane growth orientation.* Appl. Phys. Lett. **96**, 221110 (2010).

[35] A. D. Andreev and E. P. O'Reilly. *Theory of the electronic structure of GaN/AlN hexagonal quantum dots.* Phys. Rev. B **62**, 15851 (2000).

[36] V. Bougrov, M. E. Levinshtein, S. L. Rumyantsev, and A. Zubrilov. *Properties of Advanced Semiconductor Materials GaN, AlN, InN, BN, Sic, SiGe* (John Wiley & Sons, 2001).

[37] L. Chen, B. J. Skromme, R. F. Dalmau, R. Schlesser, Z. Sitar, C. Chen, W. Sun, J. Yang, M. A. Khan, M. L. Nakarmi, J. Y. Lin, and H.-X. Jiang. *Band-edge exciton states in AlN single crystals and epitaxial layers.* Appl. Phys. Lett. **85**, 4334 (2004).

[38] R. Goldhahn, P. Schley, A. Winzer, M. Rakel, C. Cobet, N. Esser, H. Lu, and W. Schaff. *Critical points of the band structure and valence band ordering at the gamma point of wurtzite InN.* J. Cryst. Growth **288**, 273 (2006).

[39] P. Rinke, M. Winkelnkemper, A. Qteish, D. Bimberg, J. Neugebauer, and M. Scheffler. *Consistent set of band parameters for the group-III nitrides AlN, GaN, and InN.* Phys. Rev. B **77**, 075202 (2008).

[40] O. Brandt and K. H. Ploog. *Solid-state lighting: The benefit of disorder.* Nat. Mater. **5**, 769 (2006).

[41] C. J. Neufeld, N. G. Toledo, S. C. Cruz, M. Iza, S. P. DenBaars, and U. K. Mishra. *High quantum efficiency InGaN/GaN solar cells with 2.95 eV band gap.* Appl. Phys. Lett. **93**, 143502 (2008).

[42] H. T. Chou, D. Goldhaber-Gordon, S. Schmult, M. J. Manfra, A. M. Sergent, and R. J. Molnar. *Single-electron transistors in GaN/AlGaN heterostructures.* Appl. Phys. Lett. **89**, 033104 (2006).

[43] M. Shur and M. A. Khan. *GaN and AlGaN Ultraviolet Detectors.* In *Gallium Nitride (GaN) II* (edited by J. I. Pankove and T. D. Moustakas), vol. 57 of *Semiconductors and Semimetals* (Elsevier, 1998).

[44] T. L. Tansley and C. P. Foley. *Optical band gap of indium nitride.* J. Appl. Phys. **59**, 3241 (1986).

[45] V. Davydov, A. Klochikhin, R. Seisyan, V. Emtsev, S. Ivanov, F. Bechstedt, J. Furthmüller, H. Harima, A. Mudryi, J. Aderhold, O. Semchinova, and J. Graul. *Absorption and Emission of Hexagonal InN. Evidence of Narrow Fundamental Band Gap.* Phys. Status Solidi B-Basic Solid State Phys. **229**, R1 (2002).

[46] J. Wu, W. Walukiewicz, K. M. Yu, J. W. Ager III, E. E. Haller, H. Lu, W. J. Schaff, Y. Saito, and Y. Nanishi. *Unusual properties of the fundamental band gap of InN.* Appl. Phys. Lett. **80**, 3967 (2002).

[47] P. Rinke. *www.fhi-berlin.mpg.de* .

[48] I. Mahboob, T. D. Veal, L. F. J. Piper, C. F. McConville, H. Lu, W. J. Schaff, J. Furthmüller, and F. Bechstedt. *Origin of electron accumulation at wurtzite InN surfaces.* Phys. Rev. B **69**, 201307 (2004).

[49] J. Segura-Ruiz, N. Garro, A. Cantarero, C. Denker, J. Malindretos, and A. Rizzi. *Optical studies of MBE-grown InN nanocolumns: Evidence of surface electron accumulation.* Phys. Rev. B **79**, 115305 (2009).

[50] T. Nagata, G. Koblmüller, O. Bierwagen, C. S. Gallinat, and J. S. Speck. *Surface structure and chemical states of a-plane and c-plane InN films.* Appl. Phys. Lett. **95**, 132104 (2009).

[51] A. Janotti, D. Segev, and C. G. Van de Walle. *Effects of cation d states on the structural and electronic properties of III-nitride and II-oxide wide-band-gap semiconductors.* Phys. Rev. B **74**, 045202 (2006).

[52] A. Svane, N. E. Christensen, I. Gorczyca, M. van Schilfgaarde, A. N. Chantis, and T. Kotani. *Quasiparticle self-consistent GW theory of III-V nitride semiconductors: Bands, gap bowing, and effective masses.* Phys. Rev. B **82**, 115102 (2010).

[53] C. G. Van de Walle and D. Segev. *Microscopic origins of surface states on nitride surfaces.* J. Appl. Phys. **101**, 081704 (2007).

[54] A. I. Hochbaum and P. Yang. *Semiconductor nanowires for energy conversion.* Chem. Rev. **110**, 527 (2010).

[55] B. Amstatt, J. Renard, C. Bougerol, E. Bellet-Amalric, B. Gayral, and B. Daudin. *Quantum dot to quantum wire transition of m-plane GaN islands.* Phys. Rev. B **79**, 035313 (2009).

[56] P. Corfdir, P. Lefebvre, J. Ristic, P. Valvin, E. Calleja, A. Trampert, J. D. Ganiere, and B. Deveaud-Pledran. *Time-resolved spectroscopy on GaN nanocolumns grown by plasma assisted molecular beam epitaxy on Si substrates.* J. Appl. Phys. **105** (2009).

[57] J. Yoon, A. M. Girgis, I. Shalish, L. R. Ram-Mohan, and V. Narayanamurti. *Size-dependent impurity activation energy in GaN nanowires.* Appl. Phys. Lett. **94**, 142102 (2009).

[58] R. Songmuang, O. Landre, and B. Daudin. *From nucleation to growth of catalyst-free GaN nanowires on thin AlN buffer layer.* Appl. Phys. Lett. **91**, 251902 (2007).

[59] C. Adelmann, B. Daudin, R. A. Oliver, G. A. D. Briggs, and R. E. Rudd. *Nucleation and growth of GaN/AlN quantum dots.* Phys. Rev. B **70**, 125427 (2004).

[60] H. Morkoc. *III-Nitride semiconductor growth by MBE: Recent issues.* J. Mater. Sci.-Mater. Electron. **12**, 677 (2001).

[61] M. Henini (ed.). *Handbook of Self Assembled Semiconductor Nanostructures for Novel Devices in Photonics and Electronics* (Elsevier Science Ltd, 2008).

[62] E. Calleja, M. A. Sánchez-García, F. J. Sánchez, F. Calle, F. B. Naranjo, E. Muñoz, U. Jahn, and K. Ploog. *Luminescence properties and defects in GaN nanocolumns grown by molecular beam epitaxy.* Phys. Rev. B **62**, 16826 (2000).

[63] R. Calarco, R. J. Meijers, R. K. Debnath, T. Stoica, E. Sutter, and H. Lüth. *Nucleation and growth of GaN nanowires on Si(111) performed by molecular beam epitaxy.* Nano Lett. **7**, 2248 (2007).

[64] J. E. Northrup and J. Neugebauer. *Theory of GaN* $(10\bar{1}0)$ *and* $(11\bar{2}0)$ *surfaces.* Phys. Rev. B **53**, R10477 (1996).

[65] E. Calleja, J. Ristic, S. Fernández-Garrido, L. Cerutti, M. A. Sánchez-García, J. Grandal, A. Trampert, U. Jahn, G. Sánchez, A. Griol, and B. Sánchez. *Growth, morphology, and structural properties of group-III-nitride nanocolumns and nanodisks.* Phys. Status Solidi B-Basic Solid State Phys. **244**, 2816 (2007).

[66] O. Landre, R. Songmuang, J. Renard, E. Bellet-Amalric, H. Renevier, and B. Daudin. *Plasma-assisted molecular beam epitaxy growth of GaN nanowires using indium-enhanced diffusion.* Appl. Phys. Lett. **93**, 183109 (2008).

[67] C. Denker, J. Malindretos, F. Werner, F. Limbach, H. Schuhmann, T. Niermann, M. Seibt, and A. Rizzi. *Self-organized growth of InN-nanocolumns on p-Si(111) by MBE.* Physica Status Solidi C **5**, 1706 (2008).

[68] C. Bougerol, R. Songmuang, D. Camacho, Y. M. Niquet, R. Mata, A. Cros, and B. Daudin. *The structural properties of GaN insertions in GaN/AlN nanocolumn heterostructures.* Nanotechnology **20**, 295706 (2009).

[69] O. Landre, V. Fellmann, P. Jaffrennou, C. Bougerol, H. Renevier, A. Cros, and B. Daudin. *Molecular beam epitaxy growth and optical properties of AlN nanowires.* Appl. Phys. Lett. **96**, 061912 (2010).

[70] H. Li, W. Wang, B. Song, R. Wu, J. Li, Y. Sun, Y. Zheng, and J. Jian. *Catalyst-free synthesis, morphology evolution and optical property of one-dimensional aluminum nitride nanostructure arrays.* Journal of Alloys and Compounds **503**, L34 (2010).

[71] T. Stoica, R. Meijers, R. Calarco, T. Richter, and H. Lüth. *MBE growth optimization of InN nanowires.* J. Cryst. Growth **290**, 241 (2006).

[72] T. Stoica, R. J. Meijers, R. Calarco, T. Richter, E. Sutter, and H. Lüth. *Photoluminescence and intrinsic properties of MBE-grown InN nanowires.* Nano Lett. **6**, 1541 (2006).

[73] J. Grandal, M. A. Sanchez-Garcia, E. Calleja, E. Luna, and A. Trampert. *Accommodation mechanism of InN nanocolumns grown on Si(111) substrates by molecular beam epitaxy.* Appl. Phys. Lett. **91**, 021902 (2007).

[74] P. D. C. King, T. D. Veal, and C. F. McConville. *Nonparabolic coupled Poisson-Schrödinger solutions for quantized electron accumulation layers: Band bending, charge profile, and subbands at InN surfaces.* Phys. Rev. B **77**, 125305 (2008).

[75] E. Calleja, J. Grandal, M. A. Sánchez-García, V. Niebelschutz, M. Cimalla, and O. Ambacher. *Evidence of electron accumulation at nonpolar surfaces of InN nanocolumns.* Appl. Phys. Lett. **90**, 262110 (2007).

[76] L. Cerutti, J. Ristic, S. Fernandez-Garrido, E. Calleja, A. Trampert, K. H. Ploog, S. Lazic, and J. M. Calleja. *Wurtzite GaN nanocolumns grown on Si(001) by molecular beam epitaxy.* Appl. Phys. Lett. **88**, 213114 (2006).

[77] E. A. Stach, P. J. Pauzauskie, T. Kuykendall, J. Goldberger, R. He, and P. Yang. *Watching GaN nanowires grow.* Nano Lett. **3**, 867 (2003).

[78] T. Richter, H. L. R. Meijers, R. Calarco, and M. Marso. *Doping concentration of GaN nanowires determined by opto-electrical measurements.* Nano Lett. **8**, 3056 (2008).

[79] M. Niebelschutz, V. Cimalla, O. Ambacher, T. Machleidt, K. H. Franke, J. Ristic, J. Grandal, M. A. Sanchez-Garcia, and E. Calleja. *Space charged region in GaN and InN nanocolumns investigated by atomic force microscopy.* Phys. Status Solidi B-Basic Solid State Phys. **5**, 1609 (2008).

[80] T. Kuykendall, P. J. Pauzauskie, Y. Zhang, J. Goldberger, D. Sirbuly, J. Denlinger, and P. Yang. *Crystallographic alignment of high-density gallium nitride nanowire arrays.* Nat. Mater **3**, 524 (2004).

[81] V. A. Venables, G. D. T. Spiller, and M. Hanbucken. *Nucleation and growth of thin films.* Rep. Prog. Phys. **47**, 399 (1984).

[82] G. R. Yazdi, P. O. A. Persson, D. Gogova, R. Fornari, L. Hultman, M. Syvajarvi, and R. Yakimova. *Aligned AlN nanowires by self-organized vapor-solid growth.* Nanotechnology **20**, 1773 (2009).

[83] R. K. Paul, K.-H. Lee, B.-T. Lee, and H.-Y. Song. *Formation of AlN nanowires using Al powder.* Materials Chemistry and Physics **112**, 562 (2008).

[84] H. Yu, J. Li, R. A. Loomis, L.-W. Wang, and W. E. Buhro. *Two- versus three-dimensional quantum confinement in indium phosphide wires and dots.* Nat. Mater. **2**, 517 (2003).

[85] M. M. G. Alemany, X. Huang, M. L. Tiago, L. J. Gallego, and J. R. Chelikowsky. *The role of quantum confinement in p-type doped indium phosphide nanowires.* Nano Lett. **7**, 1878 (2007).

[86] K. Pemasiri, M. Montazeri, R. Gass, L. M. Smith, H. E. Jackson, J. Yarrison-Rice, S. Paiman, Q. Gao, H. H. Tan, C. Jagadish, X. Zhang, and J. Zou. *Carrier dynamics and quantum confinement in type II ZB-WZ InP nanowire homostructures.* Nano Lett. **9**, 648 (2009).

[87] O. Landré, D. Camacho, C. Bougerol, Y. M. Niquet, V. Favre-Nicolin, G. Renaud, H. Renevier, and B. Daudin. *Elastic strain relaxation in GaN/AlN nanowire superlattice.* Phys. Rev. B **81**, 153306 (2010).

[88] O. Hayden, G. Zheng, P. Agarwal, and C. Lieber. *Visualization of carrier depletion in semiconducting nanowires.* Small **3**, 2048 (2007).

[89] Y. Zhang, Wang, and A. Mascarenhas. *Quantum coaxial cables for solar energy harvesting.* Nano Letters **7**, 1264 (2007). PMID: 17408302.

[90] M. D. Kelzenberg, D. B. Turner-Evans, B. M. Kayes, M. A. Filler, M. C. Putnam, N. S. Lewis, and H. A. Atwater. *Photovoltaic measurements in single-nanowire silicon solar cells.* Nano Letters **8**, 710 (2008). PMID: 18269257.

[91] E. D. Minot, F. Kelkensberg, M. van Kouwen, J. A. van Dam, L. P. Kouwenhoven, V. Zwiller, M. T. Borgström, O. Wunnicke, M. A. Verheijen, and E. P. A. M. Bakkers. *Single quantum dot nanowire leds.* Nano Letters **7**, 367 (2007).

[92] J. M. Wagner and F. Bechstedt. *Properties of strained wurtzite GaN and AlN: Ab initio studies.* Phys. Rev. B **66**, 115202 (2002).

[93] G. Cicero, A. Ferretti, and A. Catellani. *Surface-induced polarity inversion in ZnO nanowires.* Phys. Rev. B **80**, 201304 (2009).

[94] K. Rezouali, M. A. Belkhir, and J. B. Bai. *Ab initio study of confinement and surface effects in AlN nanowires.* J. Phys. Chem. C **114**, 11352 (2010).

[95] T. Akiyama, A. J. Freeman, K. Nakamura, and T. Ito. *Electronic structures and optical properties of GaN and ZnO nanowires from first principles.* Journal of Physics: Conference Series **100**, 052056 (2008).

[96] D. J. Carter, J. D. Gale, B. Delley, and C. Stampfl. *Geometry and diameter dependence of the electronic and physical properties of GaN nanowires from first principles.* Phys. Rev. B **77**, 115349 (2008).

[97] A. Terentjevs, A. Catellani, and G. Cicero. *Nitrogen vacancies at InN* $(1\bar{1}00)$ *surfaces: A theoretical study.* Appl. Phys. Lett. **96**, 171901 (2010).

[98] A. Molina-Sánchez, A. García-Cristóbal, A. Cantarero, A. Terentjevs, and G. Cicero. *LDA+U and tight-binding electronic structure of InN nanowires.* Phys. Rev. B **82**, 165324 (2010).

[99] *http://www.abinit.org/.*

[100] *http://www.quantum-espresso.org/.*

[101] *http://www.icmab.es/siesta/.*

[102] *http://www.wien2k.at/.*

[103] A. Zunger. *Pseudopotential theory of semiconductor quantum dots.* Phys. Status Solidi B-Basic Solid State Phys. **224**, 727 (2001).

[104] A. Di Carlo. *Microscopic theory of nanostructured semiconductor devices: beyond the envelope-function approximation.* Semicond. Sci. Technol. **18**, R1 (2003).

[105] Y. M. Niquet, A. Lherbier, N. H. Quang, M. V. Fernández-Serra, X. Blase, and C. Delerue. *Electronic structure of semiconductor nanowires.* Phys. Rev. B **73**, 165319 (2006).

[106] A. Zunger. *Electronic-structure theory of semiconductor quantum dots.* MRS Bulletin **23**, 35 (1998).

[107] A. Zunger and L.-W. Wang. *Theory of silicon nanostructures.* Applied Surface Science **102**, 350 (1996). Proceedings of the International Symposium on Si Heterostructures: From Physics to Devices.

[108] R. Singh and G. Bester. *Nanowire quantum dots as an ideal source of entangled photon pairs.* Phys. Rev. Lett. **103** (2009).

[109] L. Zhang, J.-W. Luo, A. Zunger, N. Akopian, V. Zwiller, and J.-C. Harmand. *Wide inp nanowires with wurtzite/zincblende superlattice segments are type-ii whereas narrower nanowires become type-i: An atomistic pseudopotential calculation.* Nano Lett. **10**, 4055 (2010).

[110] A. Molina-Sánchez, A. García-Cristóbal, A. Cantarero, and G. Bester. *Semiempirical pseudopotential method in GaN nanowires: Method for the passivation of free-surfaces and electronic structure.* In preparation .

[111] G. Bester. *Electronic excitations in nanostructures: An empirical pseudopotential based approach.* J. Phys.-Condes. Matter **21** (2009).

[112] J. C. Slater and G. F. Koster. *Simplified LCAO method for the periodic potential problem.* Phys. Rev. **94**, 1498 (1954).

[113] A. Di Carlo. *Semiconductor nanostructures.* Phys. Status Solidi B-Basic Solid State Phys. **217**, 703 (2000).

[114] S. Schulz, S. Schumacher, and G. Czycholl. *Tight-binding model for semiconductor quantum dots with a wurtzite crystal structure: From one-particle properties to coulomb correlations and optical spectra.* Phys. Rev. B **73**, 245327 (2006).

[115] S. Schulz, S. Schumacher, and G. Czycholl. *Spin-orbit coupling and crystal-field splitting in the electronic and optical properties of nitride quantum dots with a wurtzite crystal structure.* Eur. Phys. J. B **64**, 51 (2008).

[116] M. P. Persson and H. Q. Xu. *Electronic structure of [100]-oriented free-standing InAs and InP nanowires with square and rectangular cross sections.* Phys. Rev. B **73**, 125346 (2006).

[117] M. P. Persson and A. Di Carlo. *Electronic structure and optical properties of free-standing [0001] oriented GaN nanowires and nanotubes.* J. Appl. Phys. **104**, 073718 (2008).

[118] D. Camacho-Mojica and Y.-M. Niquet. *Stark effect in GaN/AlN nanowire heterostructures: Influence of strain relaxation and surface states.* Phys. Rev. B **81**, 195313 (2010).

[119] A. Molina-Sánchez, A. García-Cristóbal, and A. Cantarero. *Anisotropy in the optical response of GaN and AlN nanowires.* In preparation .

[120] G. Bastard. *Wave Mechanics Applied to Semiconductor Heterostructures* (Halstead Press, New York, 1988).

[121] A. Zunger. *On the farsightedness (hyperopia) of the standard $\boldsymbol{k}\cdot\boldsymbol{p}$ model.* Physica Status Solidi A-Applied Research **190**, 467 (2002).

[122] C. Pryor. *Eight-band calculations of strained InAs/GaAs quantum dots compared with one-, four-, and six-band approximations.* Phys. Rev. B **57**, 7190 (1998).

[123] O. Stier, M. Grundmann, and D. Bimberg. *Electronic and optical properties of strained quantum dots modeled by 8-band $\boldsymbol{k}\cdot\boldsymbol{p}$ theory.* Phys. Rev. B **59**, 5688 (1999).

[124] J. M. Llorens. *Estructura Electrónica y Propiedades Ópticas de Puntos Cuánticos Auto-Organizados.* Ph.D. thesis, University of Valencia (2006).

[125] R. G. Parr and W. Yang. *Density-Functional Theory of Atoms and Molecules* (Oxford University Press, 1989).

[126] R. M. Dreizler and E. K. U. Gross. *Density Functional Theory* (Springer, 1990).

[127] R. Enderlein and N. J. M. Höring. *Fundamentals of Semiconductor Physics and Devices* (World Scientific Publishing Company, 1997).

[128] P. Hohenberg and W. Kohn. *Inhomogeneous electron gas.* Phys. Rev. **136**, B864 (1964).

[129] W. Kohn and L. J. Sham. *Self-consistent equations including exchange and correlation effects.* Phys. Rev. **140**, A1133 (1965).

[130] *http://nobelprize.org/.*

[131] M. C. Payne, M. P. Teter, D. C. Allan, T. A. Arias, and J. D. Joannopoulos. *Iterative minimization techniques for ab initio total-energy calculations: molecular dynamics and conjugate gradients.* Rev. Mod. Phys. **64**, 1045 (1992).

[132] L. M. Sandratskii and P. G. Guletskii. *Symmetrised method for the calculation of the band structure of noncollinear magnets.* J. Phys. D-Appl. Phys. **16**, L43 (1986).

[133] A. L. Fetter and J. D. Walecka. *Quantum Theory of Many-Particle Systems* (Dover Publications, 2003).

[134] J. P. Perdew and M. Levy. *Physical content of the exact Kohn-Sham orbital energies: Band gaps and derivative discontinuities.* Phys. Rev. Lett. **51**, 1884 (1983).

[135] L. J. Sham and M. Schlüter. *Density-functional theory of the energy gap.* Phys. Rev. Lett. **51**, 1888 (1983).

[136] F. Carlos, N. Fernando, and M. A. L. Miguel (eds.). *A Primer in Density Functional Theory* (Springer-Verlag, 2003).

[137] M. Städele, M. Moukara, J. A. Majewski, P. Vogl, and A. Görling. *Exact exchange Kohn-Sham formalism applied to semiconductors.* Phys. Rev. B **59**, 10031 (1999).

[138] V. I. Anisimov, F. Aryasetiawan, and A. I. Lichtenstein. *First-principles calculations of the electronic structure and spectra of strongly correlated systems: the LDA+U method.* J. Phys.-Condes. Matter **9**, 767 (1997).

[139] R. W. Godby, M. Schlüter, and L. J. Sham. *Self-energy operators and exchange-correlation potentials in semiconductors.* Phys. Rev. B **37**, 10159 (1988).

[140] F. Aryasetiawan and O. Gunnarsson. *The GW method.* Rep. Prog. Phys. **61**, 237 (1998).

[141] A. I. Liechtenstein, V. I. Anisimov, and J. Zaanen. *Density-functional theory and strong interactions: Orbital ordering in Mott-Hubbard insulators.* Phys. Rev. B **52**, R5467 (1995).

[142] M. Cococcioni and S. de Gironcoli. *Linear response approach to the calculation of the effective interaction parameters in the LDA+U method.* Phys. Rev. B **71**, 035105 (2005).

[143] V. I. Anisimov, J. Zaanen, and O. K. Andersen. *Band theory and Mott insulators: Hubbard U instead of Stoner I.* Phys. Rev. B **44**, 943 (1991).

[144] N. W. Ashcroft and N. D. Mermin. *Solid State Physics* (Harcourt College Publisher, 1976).

[145] D. Marx and J. Hutter. *Ab Initio Molecular Dynamics: Basic Theory and Advanced Methods* (Cambridge University Press, 2009).

[146] W. E. Pickett. *Pseudopotential methods in condensed matter applications.* Phys. Rep. **9**, 115 (1989).

[147] J. Grotendorst, S. Blügel, and D. Marx (eds.). *Computational Nanoscience: Do It Yourself!*, vol. 31 of *NIC* (2006).

[148] V. Heine. *Solid State Physics* (Academic, New York, 1970).

[149] J. C. Phillips and L. Kleinman. *New method for calculating wave functions in crystals and molecules.* Phys. Rev. **116**, 287 (1959).

[150] M. L. Cohen and J. Chelikowsky. *Electronic Structure and Optical Properties of Semiconductors* (Springer, 1989).

[151] L. Kleinman and D. M. Bylander. *Efficacious form for model pseudopotentials.* Phys. Rev. Lett. **48**, 1425 (1982).

[152] C. Herring. *A new method for calculating wave functions in crystals.* Phys. Rev. **57**, 1169 (1940).

[153] G. B. Bachelet, D. R. Hamann, and M. Schlüter. *Pseudopotentials that work: From H to Pu.* Phys. Rev. B **26**, 4199 (1982).

[154] N. Troullier and J. L. Martins. *Efficient pseudopotentials for plane-wave calculations.* Phys. Rev. B **43**, 1993 (1991).

[155] D. Vanderbilt. *Soft self-consistent pseudopotentials in a generalized eigenvalue formalism.* Phys. Rev. B **41**, 7892 (1990).

[156] D. J. Singh and L. Nordström. *Planewaves, Pseudopotentials and the LAPW method* (Springer, 2006).

[157] P. Giannozzi, S. Baroni, N. Bonini, M. Calandra, R. Car, C. Cavazzoni, D. Ceresoli, G. L. Chiarotti, M. Cococcioni, I. Dabo, A. D. Corso, S. de Gironcoli, S. Fabris, G. Fratesi, R. Gebauer, U. Gerstmann, C. Gougoussis, A. Kokalj, M. Lazzeri, L. Martin-Samos, N. Marzari, F. Mauri, R. Mazzarello, S. Paolini, A. Pasquarello, L. Paulatto, C. Sbraccia, S. Scandolo, G. Sclauzero, A. P. Seitsonen, A. Smogunov, P. Umari, and R. M. Wentzcovitch. *QUANTUM ESPRESSO: a modular and open-source software project for quantum simulations of materials.* Journal of Physics: Condensed Matter **21**, 395502 (2009).

[158] A. Rubio, J. L. Corkill, M. L. Cohen, E. L. Shirley, and S. G. Louie. *Quasiparticle band structure of AlN and GaN.* Phys. Rev. B **48**, 11810 (1993).

[159] L. C. O. Dacal. *Private Communication.*

[160] E. G. Gadret, G. O. Dias, L. C. O. Dacal, M. M. de Lima, C. V. R. S. Ruffo, F. Iikawa, M. J. S. P. Brasil, T. Chiaramonte, M. A. Cotta, L. H. G. Tizei, D. Ugarte, and A. Cantarero. *Valence-band splitting energies in wurtzite InP nanowires: Photoluminescence spectroscopy and ab initio calculations.* Phys. Rev. B **82**, 125327 (2010).

[161] A. Terentjevs, A. Catellani, D. Prendergast, and G. Cicero. *Importance of on-site corrections to the electronic and structural properties of InN in crystalline solid, nonpolar surface, and nanowire forms.* Phys. Rev. B **82**, 165307 (2010).

[162] P. D. C. King, T. D. Veal, C. F. McConville, F. Fuchs, J. Furthmüller, F. Bechstedt, J. Schörmann, D. J. As, K. Lischka, H. Lu, and W. J. Schaff. *Valence band density of states of zinc-blende and wurtzite inn from x-ray photoemission spectroscopy and first-principles calculations.* Phys. Rev. B **77**, 115213 (2008).

[163] M. L. Cohen and V. Heine. *The fitting of pseudopotentials to experimental data and their subsequent application.* vol. 24 of *Solid State Physics*, 37 – 248 (Academic Press, 1970).

[164] H. Fu. *Electric-field effect in InP quantum films.* Phys. Rev. B **64**, 075303 (2001).

[165] M. Califano, G. Bester, and A. Zunger. *Prediction of a Shape-Induced Enhancement in the Hole Relaxation in Nanocrystals.* Nano Lett. **3**, 1197 (2003).

[166] P. R. C. Kent, L. Bellaiche, and A. Zunger. *Pseudopotential theory of dilute III-V nitrides.* Semicond. Sci. Technol. **17**, 851 (2002).

[167] M. Goano, E. Bellotti, E. Ghillino, G. Ghione, and K. F. Brennan. *Band structure nonlocal pseudopotential calculation of the III-nitride wurtzite phase materials system. Part I. Binary compounds GaN, AlN, and InN.* J. Appl. Phys. **88**, 6467 (2000).

[168] K. Kim, P. R. C. Kent, A. Zunger, and C. B. Geller. *Atomistic description of the electronic structure of $In_xGa_{1-x}As$ alloys and InAs/GaAs superlattices.* Phys. Rev. B **66**, 045208 (2002).

[169] L.-W. Wang and A. Zunger. *Local-density-derived semiempirical pseudopotentials.* Phys. Rev. B **51**, 17398 (1995).

[170] S. P. Grabowski, M. Schneider, H. Nienhaus, W. Monch, R. Dimitrov, O. Ambacher, and M. Stutzmann. *Electron affinity of $Al_xGa_{1-x}N(0001)$ surfaces.* Appl. Phys. Lett. **78**, 2503 (2001).

[171] L. Bellaiche, A. Al-Yacoub, N. A. Modine, and E. D. Jones. *Successes and predictions of a pseudopotential approach in anion-mixed nitrides.* Progress in Semiconductor Materials for Optoelectronic Applications **692**, 9 (2002).

[172] J. Li and L.-W. Wang. *Deformation potentials of CdSe quantum dots.* Appl. Phys. Lett. **85**, 2929 (2004).

[173] J. R. Chelikowsky and M. L. Cohen. *Nonlocal pseudopotential calculations for the electronic structure of eleven diamond and zinc-blende semiconductors.* Phys. Rev. B **14**, 556 (1976).

[174] A. Zunger and M. L. Cohen. *First-principles nonlocal-pseudopotential approach in the density-functional formalism. II. Application to electronic and structural properties of solids.* Phys. Rev. B **20**, 4082 (1979).

[175] R. D. King-Smith, M. C. Payne, and J. S. Lin. *Real-space implementation of nonlocal pseudopotentials for first-principles total-energy calculations.* Phys. Rev. B **44**, 13063 (1991).

[176] H. Fu and A. Zunger. *Local-density-derived semiempirical nonlocal pseudopotentials for InP with applications to large quantum dots.* Phys. Rev. B **55**, 1642 (1997).

[177] M. S. Hybertsen and S. G. Louie. *Spin-orbit splitting in semiconductors and insulators from the ab initio pseudopotential.* Phys. Rev. B **34**, 2920 (1986).

[178] R. C. Casella. *Symmetry of wurtzite.* Phys. Rev. **114**, 1514 (1959).

[179] A. De and C. E. Pryor. *Predicted band structures of III-V semiconductors in the wurtzite phase.* Phys. Rev. B **81**, 155210 (2010).

[180] M.-Z. Huang and W. Ching. *A minimal basis semi-ab initio approach to the band structures of semiconductors.* Journal of Physics and Chemistry of Solids **46**, 977 (1985).

[181] D. Fritsch, H. Schmidt, and M. Grundmann. *Band-structure pseudopotential calculation of zinc-blende and wurtzite AlN, GaN, and InN.* Phys. Rev. B **67**, 235205 (2003).

[182] E. Silveira, J. A. Freitas, Jr., M. Kneissl, D. W. Treat, N. M. Johnson, G. A. Slack, and L. J. Schowalter. *Near-bandedge cathodoluminescence of an AlN homoepitaxial film.* Appl. Phys. Lett. **84**, 3501 (2004).

[183] P. O. Löwdin. *On the non-orthogonality problem connected with the use of atomic wave functions in the theory of molecules and crystals.* J. Chem. Phys. **18**, 365 (1950).

[184] N. A. Hill and K. B. Whaley. *Size dependence of excitons in silicon nanocrystals.* Phys. Rev. Lett. **75**, 1130 (1995).

[185] C. Delerue, M. Lannoo, and G. Allan. *Comment on "Size dependence of excitons in silicon nanocrystals".* Phys. Rev. Lett. **76**, 3038 (1996).

[186] N. A. Hill and K. B. Whaley. *Hill and Whaley Reply:.* Phys. Rev. Lett. **76**, 3039 (1996).

[187] S. Schulz, D. Mourad, and G. Czycholl. *Multiband description of the optical properties of zincblende nitride quantum dots.* Phys. Rev. B **80**, 165405 (2009).

[188] J. M. Jancu, F. Bassani, F. Della Sala, and R. Scholz. *Transferable tight-binding parametrization for the group-III nitrides.* Appl. Phys. Lett. **81**, 4838 (2002).

[189] T. Yang, S. Nakajima, and S. Sakai. *Electronic structures of wurtzite GaN, InN and their alloy Ga1-xInxN calculated by the tight-binding method.* Jpn. J. Appl. Phys. **34**, 5912 (1995).

[190] A. Kobayashi, O. F. Sankey, S. M. Volz, and J. D. Dow. *Semiempirical tight-binding band structures of wurtzite semiconductors AlN, CdS, CdSe, ZnS, and ZnO.* Phys. Rev. B **28**, 935 (1983).

[191] P. Vogl, H. P. Hjalmarson, and J. D. Dow. *A Semi-empirical tight-binding theory of the electronic structure of semiconductors.* Journal of Physics and Chemistry of Solids **44**, 365 (1983).

[192] M. Cardona and P. Y. Yu. *Fundamentals of Semiconductors* (Springer-Verlag, 1996).

[193] W. A. Harrison. *Electronic Structure and the Properties of Solids* (Dover, 1989).

[194] T. B. Boykin, G. Klimeck, R. C. Bowen, and F. Oyafuso. *Diagonal parameter shifts due to nearest-neighbor displacements in empirical tight-binding theory.* Phys. Rev. B **66**, 125207 (2002).

[195] G. H. Li, A. R. Goñi, C. Abraham, K. Syassen, P. V. Santos, A. Cantarero, O. Brandt, and K. Ploog. *Photoluminescence from strained InAs monolayers in GaAs under pressure.* Phys. Rev. B **50**, 1575 (1994).

[196] D. J. Chadi. *Spin-orbit splitting in crystalline and compositionally disordered semiconductors.* Phys. Rev. B **16**, 790 (1977).

[197] I. Vurgaftman, J. R. Meyer, and L. R. Ram-Mohan. *Band parameters for III-V compound semiconductors and their alloys.* J. Appl. Phys. **89**, 5815 (2001).

[198] M. Fox. *Optical Properties of Solids* (Oxford University Press, 2001).

[199] S. L. Chuang. *Physics of Optoelectronic Devices* (Wiley-Interscience, 1995).

[200] M. Virgilio and G. Grosso. *Quantum-confined Stark effect in Ge/SiGe quantum wells: A tight-binding description.* Phys. Rev. B **77**, 165315 (2008).

[201] S.-Y. Ren and W. A. Harrison. *Semiconductor properties based upon universal tight-binding parameters.* Phys. Rev. B **23**, 762 (1981).

[202] L. C. Lew Yan Voon and L. R. Ram-Mohan. *Tight-binding representation of the optical matrix elements: Theory and applications.* Phys. Rev. B **47**, 15500 (1993).

[203] M. Graf and P. Vogl. *Electromagnetic fields and dielectric response in empirical tight-binding theory.* Phys. Rev. B **51**, 4940 (1995).

[204] R. Mata, A. Cros, J. A. Budagosky, A. Molina-Sánchez, N. Garro, A. García-Cristóbal, J. Renard, S. Founta, B. Gayral, E. Bellet-Amalric, C. Bougerol, and B. Daudin. *Reversed polarized emission in highly strained a-plane GaN/AlN multiple quantum wells.* Phys. Rev. B **82**, 125405 (2010).

[205] Y.-N. Xu and W. Y. Ching. *Electronic, optical, and structural properties of some wurtzite crystals.* Phys. Rev. B **48**, 4335 (1993).

[206] L.-W. Wang and A. Zunger. *Solving Schrödinger's equation around a desired energy: Application to silicon quantum dots.* J. Chem. Phys. **100**, 2394 (1994).

[207] A. Zunger, A. Franceschetti, G. Bester, W. B. Jones, K. Kim, P. A. Graf, L.-W. Wang, A. Canning, O. Marques, C. Voemel, J. Dongarra, J. Langou, and S. Tomov. *Predicting the electronic properties of 3D, million-atom semiconductor nanostructure architectures.* Journal of Physics: Conference Series **46**, 292 (2006).

[208] P. A. Graf, K. Kim, W. B. Jones, and L.-W. Wang. *Surface passivation optimization using DIRECT.* J. Comput. Phys. **224**, 824 (2007).

[209] F. Bernardini and V. Fiorentini. *Polarization fields in nitride nanostructures: 10 points to think about.* Appl. Surf. Sci. **166**, 23 (2000).

[210] A. Molina, A. Garcia-Cristobal, and A. Cantarero. *Tight-binding study of the optical properties of GaN/AlN polar and nonpolar quantum wells.* Microelectronics Journal **40**, 418 (2009).

[211] S. Baskoutas and G. Bester. *Conventional optics from unconventional electronics in ZnO quantum dots.* The Journal of Physical Chemistry C **114**, 9301 (2010).

[212] A. Galindo and P. Pascual. *Quantum Mechanics I* (Springer-Verlag, 1990).

[213] C. Delerue, G. Allan, and M. Lannoo. *Theoretical aspects of the luminescence of porous silicon.* Phys. Rev. B **48**, 11024 (1993).

[214] M. Cruz, C. Wang, M. R. Beltran, and J. Tagüena-Martínez. *Morphological effects on the electronic band structure of porous silicon.* Phys. Rev. B **53**, 3827 (1996).

[215] M. Cruz, M. R. Beltran, C. Wang, J. Tagüena-Martínez, and Y. G. Rubo. *Supercell approach to the optical properties of porous silicon.* Phys. Rev. B **59**, 15381 (1999).

[216] F. Trani, D. Ninno, and G. Iadonisi. *Tight-binding formulation of the dielectric response in semiconductor nanocrystals.* Phys. Rev. B **76**, 085326 (2007).

[217] C. Echeverria-Arrondo, J. Perez-Conde, and A. K. Bhattacharjee. *Acceptor and donor impurities in GaN nanocrystals.* J. Appl. Phys. **104**, 044308 (2008).

[218] Y. M. Niquet, C. Delerue, G. Allan, and M. Lannoo. *Method for tight-binding parametrization: Application to silicon nanostructures.* Phys. Rev. B **62**, 5109 (2000).

[219] X. Huang, E. Lindgren, and J. R. Chelikowsky. *Surface passivation method for semiconductor nanostructures.* Phys. Rev. B **71**, 165328 (2005).

[220] C. L. dos Santos and P. Piquini. *Diameter dependence of mechanical, electronic, and structural properties of InAs and InP nanowires: A first-principles study.* Phys. Rev. B **81**, 075408 (2010).

[221] J. S. Thakur, Y. V. Danylyuk, D. Haddad, V. M. Naik, R. Naik, and G. W. Auner. *Influence of defects on the absorption edge of InN thin films: The band gap value.* Phys. Rev. B **76**, 035309 (2007).

[222] L. F. J. Piper, T. D. Veal, C. F. McConville, H. Lu, and W. J. Schaff. *Origin of the n-type conductivity of InN: The role of positively charged dislocations.* Appl. Phys. Lett. **88**, 252109 (2006).

[223] P. D. C. King, T. D. Veal, C. F. McConville, F. Fuchs, J. Furthmuller, F. Bechstedt, P. Schley, R. Goldhahn, J. Schormann, D. J. As, K. Lischka, D. Muto, H. Naoi, Y. Nanishi, H. Lu, and W. J. Schaff. *Universality of electron accumulation at wurtzite c- and a-plane and zinc-blende InN surfaces.* Appl. Phys. Lett. **91**, 092101 (2007).

[224] L. Colakerol, T. D. Veal, H.-K. Jeong, L. Plucinski, A. DeMasi, T. Learmonth, P.-A. Glans, S. Wang, Y. Zhang, L. F. J. Piper, P. H. Jefferson,

A. Fedorov, T.-C. Chen, T. D. Moustakas, C. F. McConville, and K. E. Smith. *Quantized electron accumulation states in indium nitride studied by angle-resolved photoemission spectroscopy.* Phys. Rev. Lett. **97**, 237601 (2006).

[225] C.-L. Wu, H.-M. Lee, C.-T. Kuo, C.-H. Chen, and S. Gwo. *Absence of Fermi-level pinning at cleaved nonpolar InN surfaces.* Phys. Rev. Lett. **101**, 106803 (2008).

[226] C. G. Van de Walle and J. Neugebauer. *First-principles calculations for defects and impurities: Applications to III-nitrides.* J. Appl. Phys. **95**, 3851 (2004).

[227] A. Janotti and C. G. Van de Walle. *Sources of unintentional conductivity in InN.* Appl. Phys. Lett. **92**, 032104 (2008).

[228] T. Richter, C. Blomers, H. Luth, R. Calarco, M. Indlekofer, M. Marso, and T. Schapers. *Flux quantization effects in InN nanowires.* Nano Lett. **8**, 2834 (2008).

[229] F. Werner, F. Limbach, M. Carsten, C. Denker, J. Malindretos, and A. Rizzi. *Electrical conductivity of InN nanowires and the influence of the native indium oxide formed at their surface.* Nano Lett. **9**, 1567 (2009).

[230] D. R. Khanal, W. Walukiewicz, J. Grandal, E. Calleja, and J. Wu. *Determining surface Fermi level pinning position of InN nanowires using electrolyte gating.* Appl. Phys. Lett. **95**, 173114 (2009).

[231] F. Chirico, A. Di Carlo, and P. Lugli. *Efficient self-consistent pseudopotential calculation of nanostructured devices.* Phys. Rev. B **64**, 045314 (2001).

[232] J. Segura-Ruiz. *Electronic and Vibrational States of InN and GaInN Nanocolumns.* Ph.D. thesis, University of Valencia (2009).

[233] J. Segura-Ruiz, A. Molina-Sánchez, N. Garro, A. García-Cristóbal, A. Cantarero, F. Iikawa, C. Denker, J. Malindretos, and A. Rizzi. *Inhomogeneous free-electron distribution in InN nanowires: Photoluminescence excitation experiments.* Phys. Rev. B **82**, 125319 (2010).

[234] S. Lazic, E. Gallardo, J. M. Calleja, F. Agulló-Rueda, J. Grandal, M. A. Sánchez-Garcia, E. Calleja, E. Luna, and A. Trampert. *Phonon-plasmon coupling in electron surface accumulation layers in InN nanocolumns.* Phys. Rev. B **76**, 205319 (2007).

[235] A. A. Klochikhin, V. Y. Davydov, I. Y. Strashkova, P. N. Brunkov, A. A. Gutkin, M. E. Rudinsky, H. Y. Chen, and S. Gwo. *Band bending of n-InN epilayers and exact solution of the classical Thomas-Fermi equation.* Physica Status Solidi-R **1**, 159 (2007).

[236] P. Y. Yu and M. Cardona. *Fundamentals of Semiconductors* (Springer, 1999).

[237] M. Tadić and Z. Ikonić. *Self-consistent electronic-structure calculation of rectangular modulation-doped $GaAs/Ga_{1-x}Al_xAs$ quantum wires.* Phys. Rev. B **50**, 7680 (1994).

[238] W. Walukiewicz, S. X. Li, J. Wu, K. M. Yu, J. W. Ager, E. E. Haller, H. Lu, and W. J. Schaff. *Optical properties and electronic structure of InN and In-rich group III-nitride alloys.* J. Cryst. Growth **269**, 119 (2004).

[239] S. Abe, T. Inaoka, and M. Hasegawa. *Evolution of electron states at a narrow-gap semiconductor surface in an accumulation-layer formation process.* Phys. Rev. B **66** (2002).

[240] J. Segura-Ruiz. *Privatte Communication.*

[241] M. Goano. *Algorithm 745. Computation of the complete and incomplete Fermi-Dirac integral.* ACM Trans. Math. Softw. **21**, 221 (1995).

[242] J. H. Luscombe, A. M. Bouchard, and M. Luban. *Electron confinement in quantum nanostructures: Self-consistent Poisson-Schrödinger theory.* Phys. Rev. B **46**, 10262 (1992).

[243] W. H. Press, B. P. Flannery, S. A. Teukolsky, and W. T. Vetterling. *Numerical Recipes: The Art of Scientific Computing* (Cambridge University Press, Cambridge (UK) and New York, 1992), 2nd ed.

[244] K. Mohseni and T. Colonius. *Numerical treatment of polar coordinate singularities.* J. Comput. Phys. **157**, 787 (2000).

[245] M. C. Lai. *A note on finite difference discretizations for Poisson equation on a disk.* Numer. Meth. Part Differ. Equ. **17**, 199 (2001).

[246] M. C. Lai and W. C. Wang. *Fast direct solvers for Poisson equation on 2D polar and spherical geometries.* Numer. Meth. Part Differ. Equ. **18**, 56 (2002).

[247] M. Zervos and L. F. Feiner. *Electronic structure of piezoelectric double-barrier InAs/InP/InAs/InP/InAs(111) nanowires.* J. Appl. Phys. **95**, 281 (2004).

[248] J. H. Luscombe and M. Luban. *Lateral confinement in quantum nanostructures: Self-consistent screening potentials.* Appl. Phys. Lett. **57**, 61 (1990).

[249] K. Oldham, J. Myland, and J. Spanier. *An Atlas of Functions: with Equator, the Atlas Function Calculator* (Springer, 2008), 2nd ed.

[250] C. S. Gallinat, G. Koblmuller, J. S. Brown, and J. S. Speck. *A growth diagram for plasma-assisted molecular beam epitaxy of In-face InN.* J. Appl. Phys. **102**, 064907 (2007).

[251] L. F. J. Piper, T. D. Veal, I. Mahboob, C. F. McConville, H. Lu, and W. J. Schaff. *Temperature invariance of InN electron accumulation.* Phys. Rev. B **70**, 115333 (2004).

[252] B. Arnaudov, T. Paskova, P. P. Paskov, B. Magnusson, E. Valcheva, B. Monemar, H. Lu, W. J. Schaff, H. Amano, and I. Akasaki. *Energy position of near-band-edge emission spectra of InN epitaxial layers with different doping levels.* Phys. Rev. B **69**, 115216 (2004).

[253] E. Anderson, Z. Bai, C. Bischof, S. Blackford, J. Demmel, J. Dongarra, J. Du Croz, A. Greenbaum, S. Hammarling, A. McKenney, and D. Sorensen. *LAPACK Users' Guide* (1999).

[254] R. B. Lehoucq, D. C. Sorensen, and C. Yang. *ARPACK Users' Guide: Solution of Large Scale Eigenvalue Problems with Implicitly Restarted Arnoldi Methods.* (1997).

[255] Z. Bai, J. Demmel, J. Dongarra, A. Ruhe, and H. van der Vorst. *Templates for the Solution of Algebraic Eigenvalue Problems: A Practical Guide* (2000).

[256] L. W. Wang and J. B. Li. *First-principles thousand-atom quantum dot calculations.* Phys. Rev. B **69**, 153302 (2004).